Engineering Journal

American Institute of Steel Construction

Third Quarter 2009 Volume 46, No. 3

ENGINEERING JOURNAL

AMERICAN INSTITUTE OF STEEL CONSTRUCTION

Dedicated to the development and improvement of steel construction, through the interchange of ideas, experiences and data.

ENGINEERING JOURNAL (ISSN 0013-8029) is published quarterly. Subscriptions: Members: one subscription, $20 per year, included in dues; Additional Member Subscriptions: $15 per year. Non-Members U.S., Canada, and Mexico: $40 per year, $110 for three years, single copy $15. International Members and Non-Members: $90 per year; $250 for three years; single copy $25. Published by the American Institute of Steel Construction at One East Wacker Drive, Suite 700, Chicago, IL 60601.

Periodicals postage paid at Chicago, IL and additional mailing offices. **Postmaster:** Send address changes to ENGINEERING JOURNAL in care of the American Institute of Steel Construction, One East Wacker Drive, Suite 700, Chicago, IL 60601.

Estimating Inelastic Drifts and Link Rotation Demands in EBFs

PAUL W. RICHARDS and BRANDON THOMPSON

The ductility of steel eccentrically braced frames (EBFs) depends on stable inelastic rotation of the links (Roeder and Popov, 1978). Experimental testing of ASTM A992 links has shown that well-stiffened shear-yielding links can accommodate large inelastic rotations without significant loss of strength (Okazaki et al., 2005). Current provisions require designers to detail links with appropriate stiffeners depending on the expected inelastic rotation demands (AISC, 2005). EBFs are unique, when compared to other ductile braced frames or special moment resisting frames, in that specific detailing (the link stiffener spacing) is directly related to the estimated inelastic deformation.

Typically, a designer will amplify elastic analysis results to estimate EBF link inelastic rotations. First, the displacements and story drifts are obtained from a static elastic analysis of the EBF under the equivalent lateral force. Next, elastic story drifts are multiplied by a deformation amplification factor, C_d, to estimate the inelastic story drifts (ICC, 2006). Finally, with the estimated inelastic story drifts, the designer estimates link inelastic rotations using simplified rigid-plastic relationships (Figure 1, for example).

Two issues may limit the accuracy of the practice just described. First, the definition of story drift in the provisions (ICC 2006) includes components from column deformations that are likely unrelated to link demands. Second, the deformation amplification factor, even if reasonable for computing inelastic roof drifts, may not be reasonable for computing inelastic story drifts. The first issue is discussed in the following paragraph, while the second is discussed in the following section.

It may be unreasonable to amplify the total elastic story drift by C_d to estimate the inelastic story drift in tall frames. Provisions define story drift as the relative lateral displacement of the top and bottom of a story, divided by the story height (ICC, 2006). When columns of a particular story experience axial deformation, frame "flexural" deformation increases story drifts for all stories above (see Figure 2, left). In contrast, brace and beam deformations at a particular story cause frame "shear" deformation and do not impact story drifts beyond that story (Figure 2, middle). The total story drift is greatest in the upper stories of tall frames because of frame flexural deformation. Therefore, link inelastic rotations will always be predicted to be greatest in the top stories of tall frames. Some engineers consider it overly conservative to amplify total elastic story drifts by C_d because inelastic story drifts (and link rotations) are related only to frame shear distortions (Horne et al., 1999).

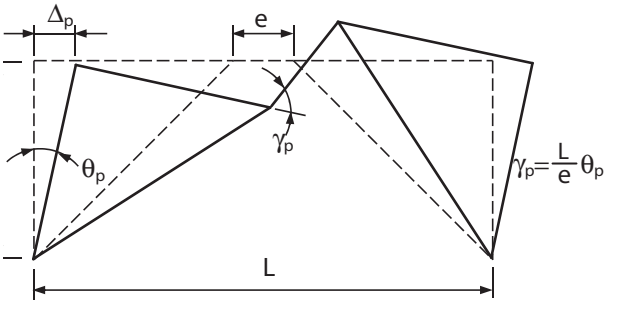

Fig. 1. Relationship between inelastic story drift and inelastic link rotation (AISC, 2005).

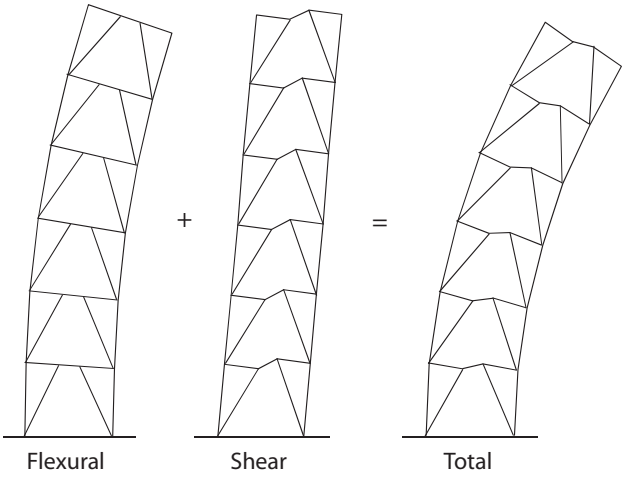

Fig. 2. Components of story and frame deformation.

Paul W. Richards is an assistant professor in the department of civil and environmental engineering, Brigham Young University, Provo, UT.

Brandon Thompson is a graduate student researcher in the department of civil and environmental engineering, Brigham Young University, Provo, UT.

DEFLECTION AMPLIFICATION FACTORS FOR ESTIMATING INELASTIC DRIFTS

Roof Drifts

A typical response envelope of base shear ratio (C) versus lateral drift (Δ) is shown in Figure 3. In design, the inelastic roof drift of the system (Δ_m, in Figure 3) is estimated by multiplying the elastic drift (Δ_s) by a deflection amplification factor (DAF). The deflection amplification factor DAF is:

$$\text{DAF} = \mu_s \, \Omega \tag{1}$$

where $\mu_s = \Delta_m/\Delta_y$ and $\Omega = C_y/C_s$ (Uang, 1991; Uang and Maarouf, 1994). If the equal displacement principle holds true ($\Delta_e = \Delta_m$), the deflection amplification factor DAF should be equal to C_e/C_s, which is the strength reduction factor, R, used in design.

Previous studies indicate that low-rise structures require greater DAFs than high-rise structures. For low-rise structures that fall in the acceleration amplification region of the response spectra, Δ_m tends to exceed Δ_e (Newmark and Hall, 1982). Uang and Maarouf (1994) found that a DAF of 1.2 times the R factor (1.2R) was appropriate for a 2-story EBF with a ductility demand of 5. However, for three taller systems in that study (6- to 13-story steel and concrete moment frames), appropriate DAFs were in the range of 0.7 to 0.9R. Karavasilis et al. (2007) investigated X-braced steel frames and had similar results; back calculated DAFs were about 1.3 times the ductility demand for 3-story frames, but 0.6 to 0.8 times the ductility demand for 6- to 20-story frames.

Values of the deformation amplification factor, C_d, in current provisions reflect engineering judgment and compromise. The history of drift requirements and deformation amplifications factors is summarized by Searer and Freeman (2004). Current U.S. provisions (ICC, 2006) specify a deformation amplification factor, C_d, for EBFs of 4, which is 0.5 to 0.6 times the R factor. This value applies to all EBFs regardless of building height. The 1997 UBC (ICBO, 1997) specified a deflection amplification factor of 0.7R. Amplification factors in this range (0.5 to 0.7R) appear reasonable for mid- to high-rise structures based on the studies cited earlier, but seem too low to accurately predict inelastic roof drifts in low-rise buildings.

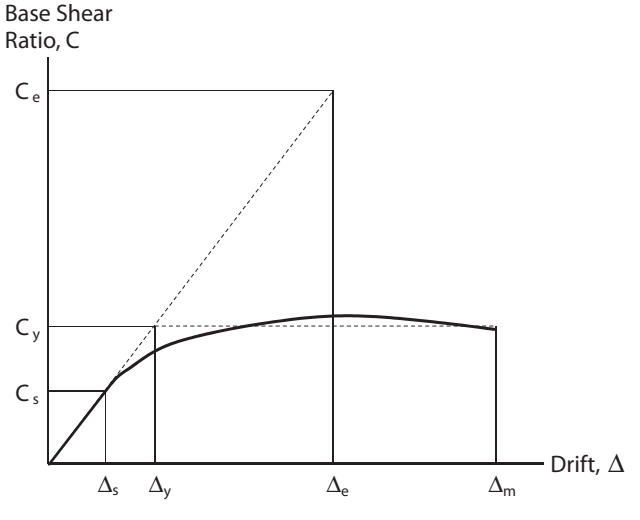

Fig. 3. General structural response envelope.

Story Drifts

The previous discussion on DAFs was in the context of predicting inelastic roof drifts. In practice, deformation amplification factors are commonly used for estimating inelastic story drifts because story drifts have prescribed limits (ICC, 2006). When the deformation amplification factors for roof drifts are extended directly to story drifts, the underlying assumption is that inelastic deformation is distributed evenly among the stories.

Because of weak stories, appropriate DAFs for predicting maximum story drifts are greater than those for predicting roof drifts. Uang and Maarouf (1994) found that deflection amplification factors to estimate maximum story drifts ranged from 1 to 1.5R for three buildings that had reasonable distribution of yielding, but was as high has 1.8R for a 6-story concrete building with a weak first story. In a much more exhaustive study of moment frames, Medina and Krawinkler (2005) found that maximum story drifts were 1.1 to 1.5 times the maximum roof drifts. This issue compounds the problems of using the current C_d factor to estimate story drifts in low-rise EBFs.

OBJECTIVE

This paper explores the accuracy of predicting EBF inelastic drifts and link rotations through amplification of elastic deformations. Inelastic drifts and rotations from nonlinear dynamic analyses of several EBFs are compared with those estimated by amplifying elastic deformations. Three approaches to developing better deformation amplification factors are investigated. Practical implications of the results are discussed and recommendations are made for improved EBF design.

EBF DESIGN AND ELASTIC DRIFTS

Design of Frames

Twelve EBF buildings were designed representing three heights (3-, 9-, and 18-story) and four strength levels. Building plan dimensions and floor masses matched those used in moment frame studies (Gupta and Krawinkler, 1999)

Table 1. Link Demand/Capacity Ratios and Frame Periods		
No. Stories	**Link D/C**	**Period (s)**
3	0.85	0.73
3	0.65	0.64
3	0.50	0.58
3	0.42	0.52
9	0.90	2.00
9	0.60	1.81
9	0.44	1.55
9	0.36	1.41
18	1.03	5.65
18	0.63	4.75
18	0.45	3.99
18	0.35	3.55

(see Figure 4). Seismic weights, W, for the 3-, 9-, and 18-story buildings were 7,160, 21,880, and 24,160 kips, respectively. Braced bays were located around the perimeter of the buildings. EBFs had two braces per bay. The 18-story buildings were 239 ft tall, just below the 240-ft maximum height allowed for braced frames (Seismic Design Category D, ICC, 2006).

Buildings were designed according to the 2006 IBC (ICC, 2006) equivalent lateral force procedure and AISC Seismic Provisions (2005). A Los Angeles, California, site was used for design with $S_{DS} = 1.11$ and $S_{D1} = 0.61$, where S_{DS} and S_{D1} are the site design spectral accelerations at 0.2 and 1.0 s in terms of gravity. S_{DS} and S_{D1} are based on the MCE × ⅔. The importance factor was taken as 1.0. The equivalent lateral forces for the 3-, 9-, and 18-story buildings were 0.134W, 0.056W, and 0.0342W, respectively.

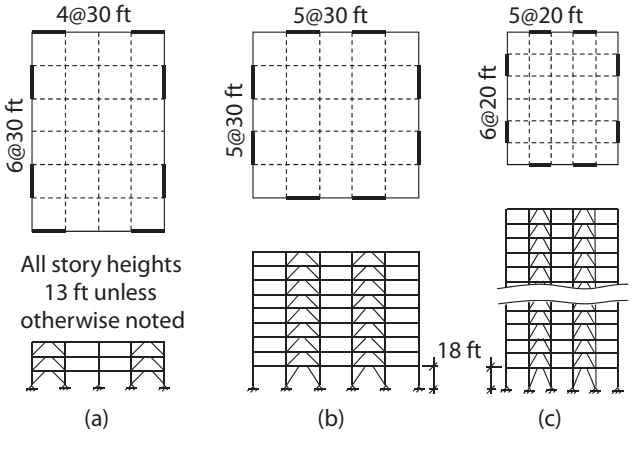

Fig. 4. Plan and elevation views of EBF buildings: (a) 3-story, (b) 9-story and (c) 18-story.

EBFs were designed for each of the buildings. To investigate the influence of strength, four designs were developed for each building height. For each design, a demand/capacity between 0.4 and 1.0 was selected for the links. Then links were sized to provide similar demand/capacity ratios at all floors (Popov et al., 1992). The average demand/capacity ratio (D/C ratio) for the links of each frame are indicated in Table 1. Frames with a D/C ratio relatively close to 1.0 represent typical designs, while those with a lower D/C are stronger than required to resist the equivalent lateral force. Member sizes for all frames can be found in Prinz (2007). As part of the design, elastic analysis under the equivalent lateral force was performed for each frame using the program RISA (RISA Technologies, 2005).

Elastic Drifts

Results from the elastic analyses provide some insight into the effect of frame strength on elastic story drifts. The elastic story drifts of each frame under the equivalent lateral force are shown in Figure 5. Total story drift is indicated with open squares, while solid squares indicate the component of the total drift caused by story shear distortion (Figure 2, middle). Equations for computing the story drifts components from model nodal displacements are developed in the Appendix. Frames with different D/C ratios had different member sizes and correspondingly different lateral stiffness. As frame stiffness increases (lower D/C ratios) elastic drifts decrease. Note that the shear component of the story drift is similar over the height each frame (Figure 5).

In Figure 5, a dashed line where drift equals 0.005 indicates an elastic story drift that will result in an estimated inelastic drift of 0.02 (4 × 0.005), which is the inelastic story drift limit for these frames. The 9-story frame with D/C = 0.90 and all of the 18-story frames have noncompliant story drifts in upper stories when typical procedures are used to estimate inelastic drift.

ADDITIONAL MODELING AND ANALYSIS

Techniques

Individual frames were modeled as two-dimensional systems using the nonlinear dynamic analysis program Ruaumoko (Carr, 2006). Standard beam elements with bilinear flexural-axial hinges at each end were used to represent beams and columns. Links were modeled with beam elements and springs in an arrangement that has been used and validated in previous EBF studies (Richards and Uang, 2006; Ramadan and Ghobarah, 1995). Columns at the base of the frames were considered fixed. Beam-column connections were considered rigid when a gusset plate would be present and pinned when not present.

Expected material strengths were specified for the ductile elements in the models, while nominal strengths were used for other members. EBF shear link elements had maximum strengths of $1.55V_n$ ($R_y = 1.1$, $\omega = 1.41$) based on experimental data for ASTM A992 shear links (Okazaki et al., 2005), where V_n is the nominal shear capacity of the link, R_y is the ratio between expected and nominal material strength, and ω is the strain hardening factor.

A single continuous column in each model represented all the gravity columns associated with the frame (one-fourth of the building). This representative column had stiffness and strength at each story corresponding to the sum of the gravity columns, assuming weak axis bending. Gravity loads corresponding to $1.2D + 0.5L$ (ICC, 2006) were applied to this column during the analyses, where D and L are dead and live load effects. This column was pinned at the base and constrained to match the frame displacements at each floor level.

Analyses

Modal and pushover analyses were performed for model characterization. The pushover analyses used the lateral force distribution prescribed by the equivalent lateral force procedure (ICC, 2006).

Dynamic analyses were performed using suites of ten earthquake records, primarily from California events (Tables 2 and 3). Earthquake records were scaled so that the mean spectral acceleration of the suite for a range of building periods was greater than the design spectra over the same range. Compared to period-independent scaling procedures, this method of scaling has been shown to result in reduced scatter of response data (Kurama and Farrow, 2003). The mean spectra of the scaled records are shown in Figure 6 with the design spectra. Different suites were used for the analysis of the 3- and 9-story and the 18-story frames (Tables 2 and 3) so that scaling factors greater than 3 were not required.

Rayleigh damping was used in the dynamic analyses with consideration of its potential problems. Ricles and Popov (1994) and Hall (2005) have demonstrated that Rayleigh damping may result in unrealistically high damping forces during time history analyses for some cases. To investigate the sensitivity of final results to damping assumptions, analyses were performed twice, first with 2% Rayleigh damping specified at the fundamental period and at a period of 0.2 s, and again with 0.5% damping specified at the same periods.

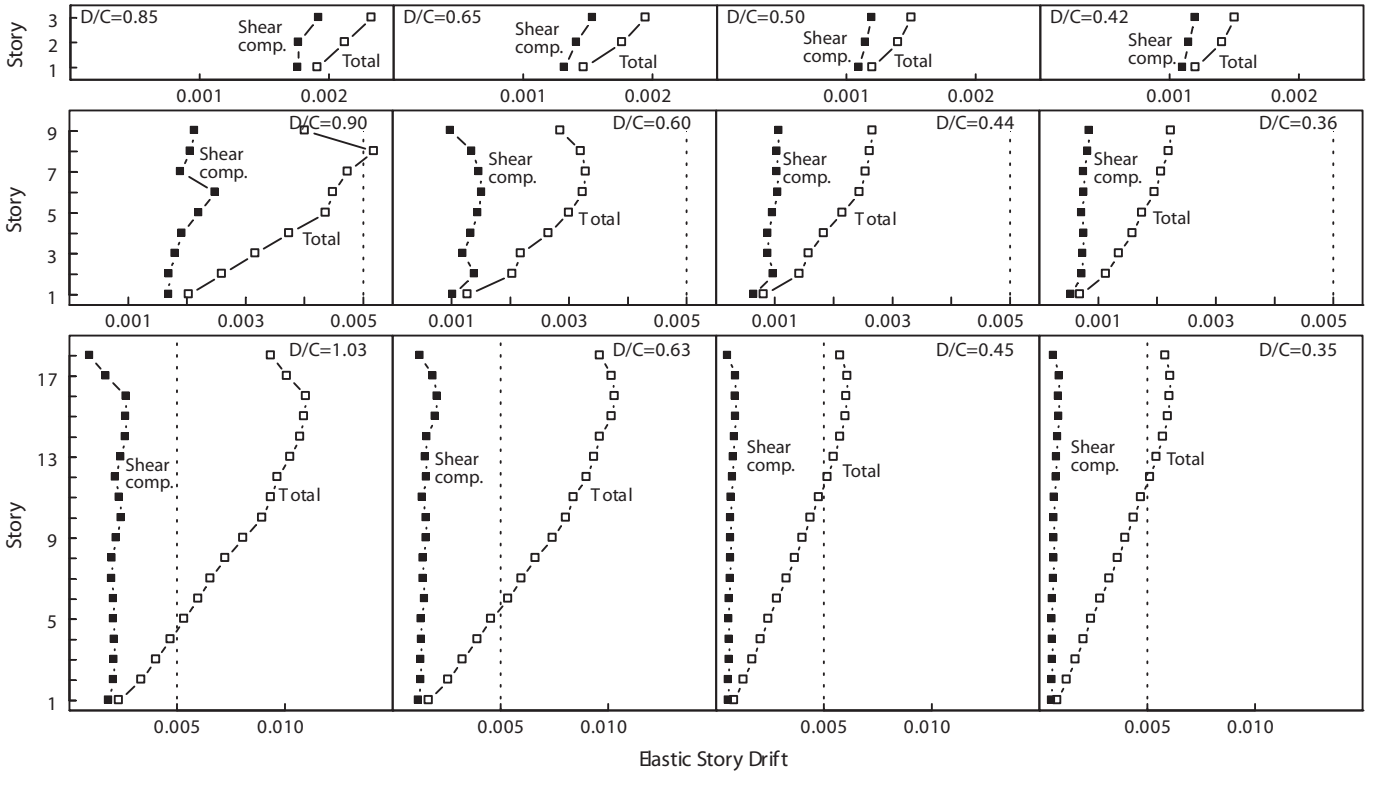

Fig. 5. Elastic story drifts under the equivalent lateral force.

Table 2. Earthquake Records Used for 3- and 9-Story Frame Analyses				
Record	**PGA[a] (g)**	***R*[b] (km)**	**Site[c]**	**Scale Factor**
1994 Northridge				
Canoga Park, NORTHR/CNP196[d]	0.42	15.8	D	2.06
90013 Beverly Hills, NORTHR/MUL279	0.52	19.6	C	1.07
90018 Hollywood, NORTHR/WIL180	0.25	25.7	C	1.85
90006 Sun Valley, NORTHR/RO3090	0.44	12.3	D	1.27
1989 Loma Prieta				
1656 Hollister Array, LOMAP/HDA255	0.28	25.8	D	2.20
Hollister City Hall, LOMAP/HCH180	0.22	28.2	D	1.54
Gilroy No. 3, LOMAP/GO3090	0.37	14.4	D	2.60
Gilroy No. 4, LOMAP/GO4090	0.21	16.1	D	2.53
1987 Superstition Hills				
Parachute Test Site, SUPERST/B-PTS225	0.46	0.7	C	1.02
Parachute Test Site, SUPERST/B-PTS315	0.38	0.7	C	2.02

a. Peak Ground Acceleration
b. Distance to fault rupture
c. NEHRP Site class
d. Designation in Pacific Earthquake Engineering Research (PEER) database

Table 3. Earthquake Records Used for 18-Story Frame Analyses				
Record	**PGA[a] (g)**	***R*[b] (km)**	**Site[c]**	**Scale Factor**
1999 Duzce, Turkey				
Duzce, DUSCE/DZC270[d]	0.54	8.2	D	0.86
1999 Chi-Chi, Taiwan				
TCU063, CHICHI/TCU063-N	0.13	10.4	D	0.90
CHY101, CHICHI/CHY101-N	0.44	11.4	D	0.59
1999 Kocaeli, Turkey				
Yarimca, KOCAILI/YPT060	0.27	2.6	D	0.83
Yarimca, KOCAILI/YPT330	0.35	2.6	D	0.97
1994 Northridge				
90056 Newhall, NORTHR/WPI046	0.46	7.1	C	1.28
1992 Landers				
24 Lucerne, LANDERS/LCN275	0.72	1.1	B	0.71
1979 Imperial Valley				
955 El Centro Array #4, IMPVALL/H-E04230	0.36	4.2	D	0.87
952 El Centro Array #5, IMPVALL/H-E05230	0.38	1.0	D	0.82
942 El Centro Array #6, IMPVALL/H-E06230	0.44	1.0	D	0.70

a. Peak Ground Acceleration
b. Distance to fault rupture
c. NEHRP Site class
d. Designation in Pacific Earthquake Engineering Research (PEER) database

Model Characterization

Results from the modal and pushover analyses provide a reasonable level of confidence in the designs and the models. The natural period of each frame is shown in Table 1 (last column). The approximate fundamental periods given by design provisions are 0.66, 1.41, and 2.55 s for the 3-, 9-, and 18-story frames, respectively (ICC, 2006). As expected, the natural period of the model frames are close-to or greater than the approximate periods. Results from the pushover analyses are given in Figure 7. The drift at yield is similar for all frames of a given geometry, despite large differences in strength.

RESULTS FROM NONLINEAR DYNAMIC ANALYSES

Damping

Drifts from the analyses with 2% damping will be discussed in the remainder of the paper. Compared with the models with 0.5% damping, the models with 2% damping had lower story drifts (around 20% lower for most stories, but as low as 50%), but greater maximum brace and column demands (around 5% greater for most columns, but as much as 10% greater). This is because relatively high link rotation velocities generate large damping forces, unrealistically increasing brace and column demands (Ricles and Popov, 1994). While 2% viscous damping may result in excess brace and column forces, it is believed to provide reasonable values for drifts (and link rotations).

Inelastic Roof Drifts

Roof drifts were computed using data from the nonlinear dynamic and static elastic analyses. For each frame, the roof drift from the dynamic analyses is the average of the maximum roof drift that occurred under each of the ten records. Average values are used since more than seven records were considered (ICC, 2006). The amplified elastic roof drift is the roof drift from the elastic analysis under the equivalent lateral force multiplied by the factor C_d/I. C_d/I was equal to 4.0 for all frames.

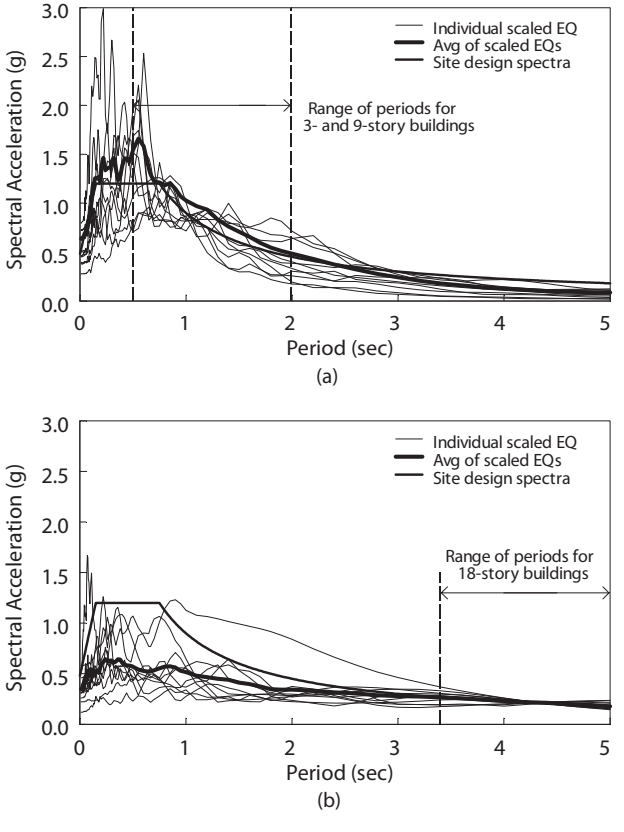

Fig. 6. Response spectra of earthquakes scaled for (a) 3- and 9-story buildings and (b) 18-story buildings.

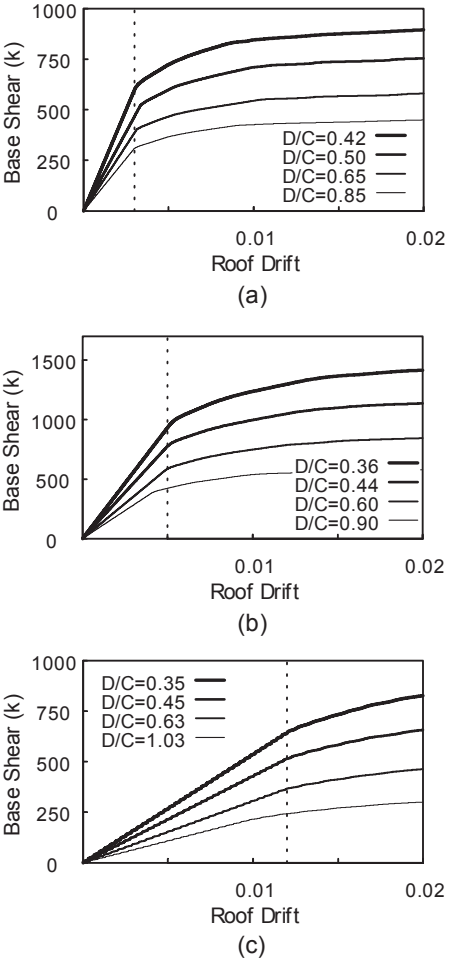

Fig. 7. Pushover analysis results: (a) 3-story, (b) 9-story and (c) 18-story.

Short and tall frames have different relationships between strength and roof drift. Figure 8 shows roof drift as a function of frame strength (D/C ratio) for the 3-, 9-, and 18-story frames. For the 3-story frames, there is an increase in roof drift as frame strength decreases (D/C ratio increases) (Figure 8). However, for the 9- and 18-story frames, roof drifts from the dynamic analyses are largely independent of frame strength. Estimating roof drifts by amplifying elastic drifts by a factor of 4.0 is somewhat unconservative for short frames and overly conservative for tall frames with D/C ratios near 1.0. This observation is consistent with the other studies that were discussed previously.

Inelastic Story Drifts

Story drifts were computed using data from the nonlinear dynamic and the linear static analyses (see Appendix). Story drifts from the dynamic analyses were computed as the average of the maximum story drifts for each floor from ten analyses (circles in Figure 9). Story drifts were estimated from the elastic analyses by amplifying the elastic story drifts by the factor C_d/I (triangles in Figure 9).

Maximum story drifts from the dynamic analyses occurred in the lower story of the 3-story frames (Figure 9, top row), and in the top few stories of the 9- and 18-story

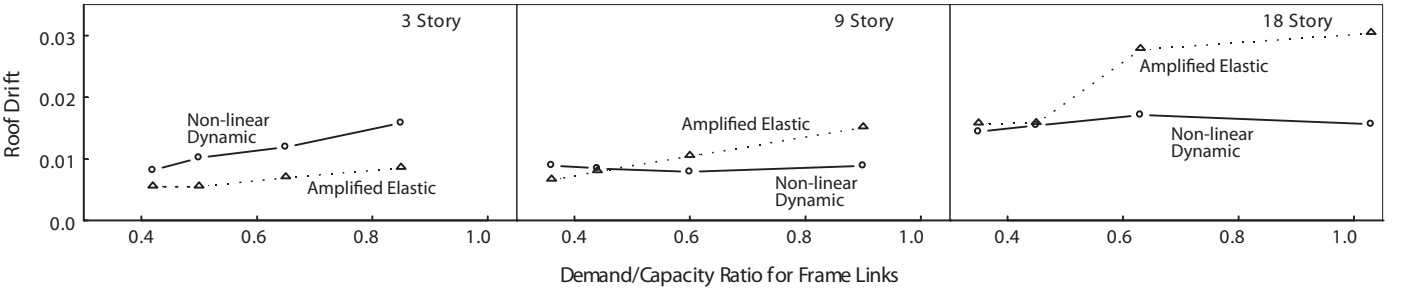

Fig. 8. Roof drifts computed from analyses.

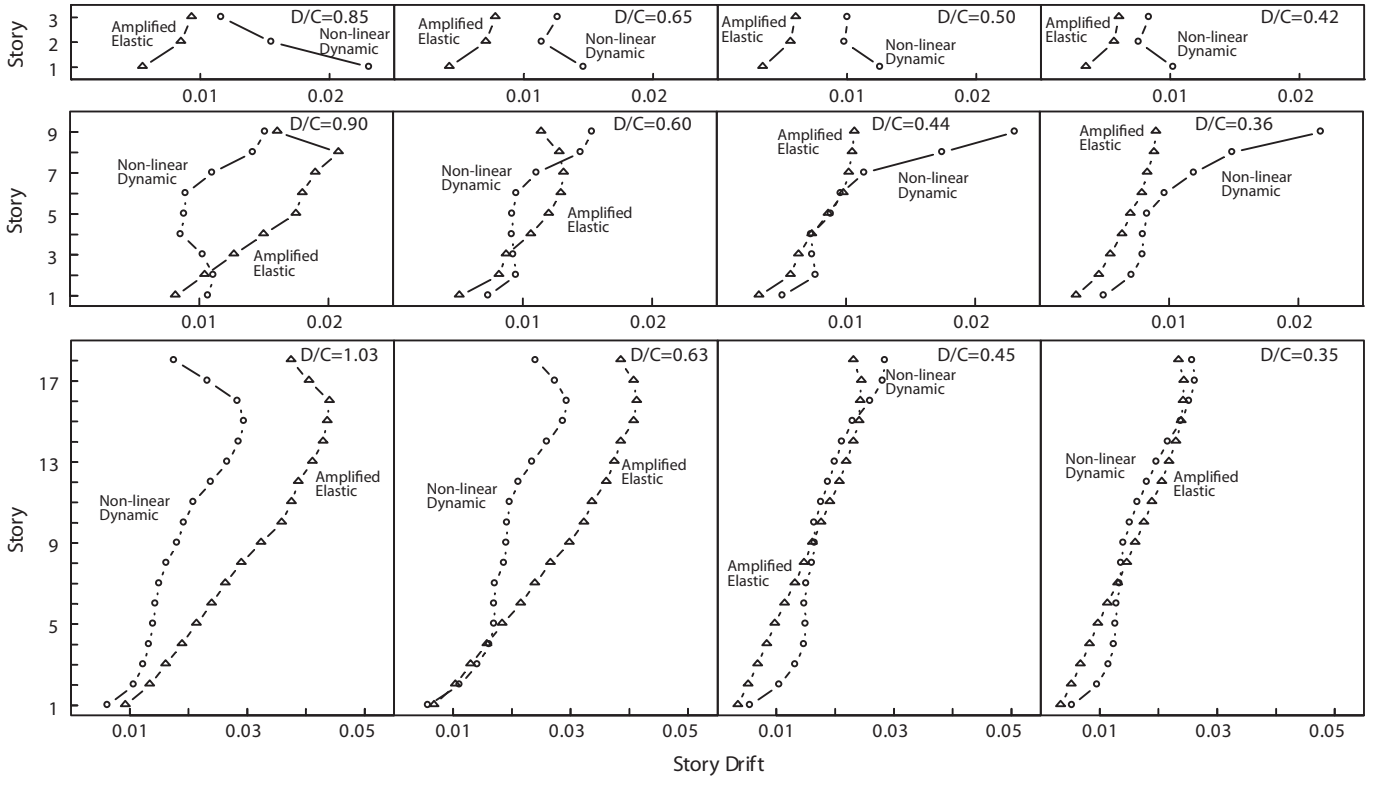

Fig. 9. Story drifts computed from analyses.

frames (Figure 9, middle and bottom rows). For the 3-story frames, the maximum story drift decreases as frame strength increases (D/C decreases); however, in the 9-story frames, the story drifts at the top of the frames increase as frame strength increases. It appears that reduced yielding at the base of the 9-story frames resulted in greater response in the upper stories. For the 18-story frames, maximum story drifts are similar for all D/C ratios.

Correlation between the amplified elastic story drifts and the dynamic analyses drifts improves as D/C ratios decrease. Considering Figure 9, correlation is quite poor for frames with D/C ratios closer to 1.0 (left side) but improves, and might be considered good, for taller frames with low D/C ratios (right side). This is because the stronger frames experience more of a first mode elastic response, giving a distribution of drifts more similar to the elastic analysis. Unfortunately, typical designs have D/C ratios closer to 1.0, placing them in the region of poor correlation. For the 3-story frames with D/C = 0.85, the amplified static drift at the first story was only 26% of that observed in the dynamic analyses (Figure 9). For the 9- and 18-story frames reasonable correlation was observed in the bottom stories; however, drifts in the upper stories from amplified elastic drifts were nearly two times the drifts from the dynamic analyses for 18-story frames with D/C close to 1.0.

Additional insights into the behavior of the frames can be gained by considering the portion of the drifts coming from story shear deformations. Figure 10 indicates the shear component of the maximum story drifts from the dynamic analyses with solid circles. The open circles are the total drift and have the same values as in Figure 10. For the 3- and 9-story frames, the majority of the drift for all stories is from story shear deformations; for the 18 story frame with D/C = 1.03, shear deformations account for at least half of the story drift for most stories. As might be expected, the percentage of drift from shear deformations in taller frames is much greater than that given by elastic analysis (compare Figure 10 and Figure 5).

Inelastic Link Rotation

Link rotations were computed using data from the nonlinear dynamic and the static elastic analyses (see Appendix). Link rotations from the dynamic analyses were computed as the average of the maximum link rotations for each floor from ten analyses (circles in Figure 11). Link rotations were estimated from the elastic analyses by multiplying the elastic story drifts by C_d/I to get an estimated inelastic drift and then multiplying that by L/e (see Figure 1).

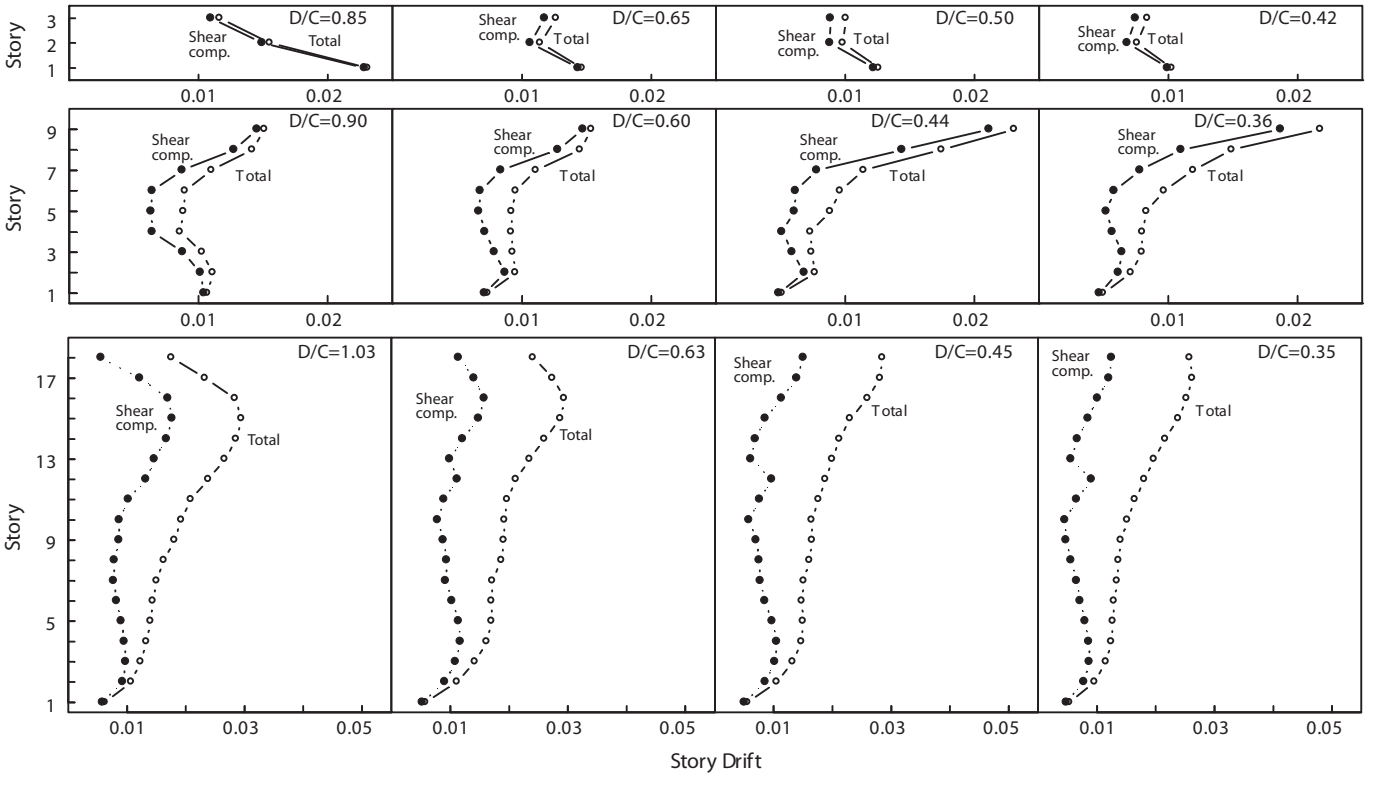

Fig. 10. Comparing shear component of story drift with the total story drift from dynamic analyses.

For most of the frames, the differences between the dynamic and amplified elastic values of link rotation are similar to the differences in story drifts (compare Figure 11 and Figure 9). When link lengths are the same at each floor, the relationship assumed by Figure 1 scales all of the drifts from Figure 9 by the same value. The greatest discrepancy between Figure 11 and Figure 9 is for stories in frames where the majority of the drift is not from shear deformations. For typical frames (with D/C near 1.0) the amplified elastic estimates of link rotation do not correspond well to those from the dynamic analyses; estimates are too low for the 3-story frames and too high for the others.

ALTERNATIVE METHODS OF ESTIMATING LINK INELASTIC ROTATION

Since the current approach for estimating link rotations appears inaccurate, three alternative methods for estimating link inelastic rotation were explored. The first is using a calibrated story-specific C_d factor to scale total elastic story drifts, and then compute link rotation using Figure 1. The second method is using a calibrated story-specific C_d factor to scale the shear component of story drift, and then compute link rotation using Figure 1. The third method is using a story-specific rotation amplification factor to scale elastic link rotations directly to yield inelastic link rotations.

Method 1

A calibrated deformation amplification factor can be computed by combining results from the nonlinear dynamic analyses with the static elastic analyses. The typical method of estimating link rotation is:

$$(\text{elastic drift}) \times C_d \times (L/e) = (\text{inelastic link rotation}) \qquad (2)$$

where C_d is constant. Analysis results were used to solve for C_d for each story of each frame given the elastic drift from the elastic analyses, and the inelastic link rotation from the dynamic analyses:

$$C_{d,\,calib} = (\text{inelastic link rotation})/[(\text{elastic drift}) \times (L/e)] \qquad (3)$$

The computed values of $C_{d,\,calib}$ are indicated in Figure 12(a). A value of 4.0 (currently used for design) is indicated by a dashed line in Figure 12(a).

From Figure 12(a) it is clear that no single value of C_d will give a reasonable estimate of link rotation for all stories of all frames. The present value of 4.0 gives reasonable

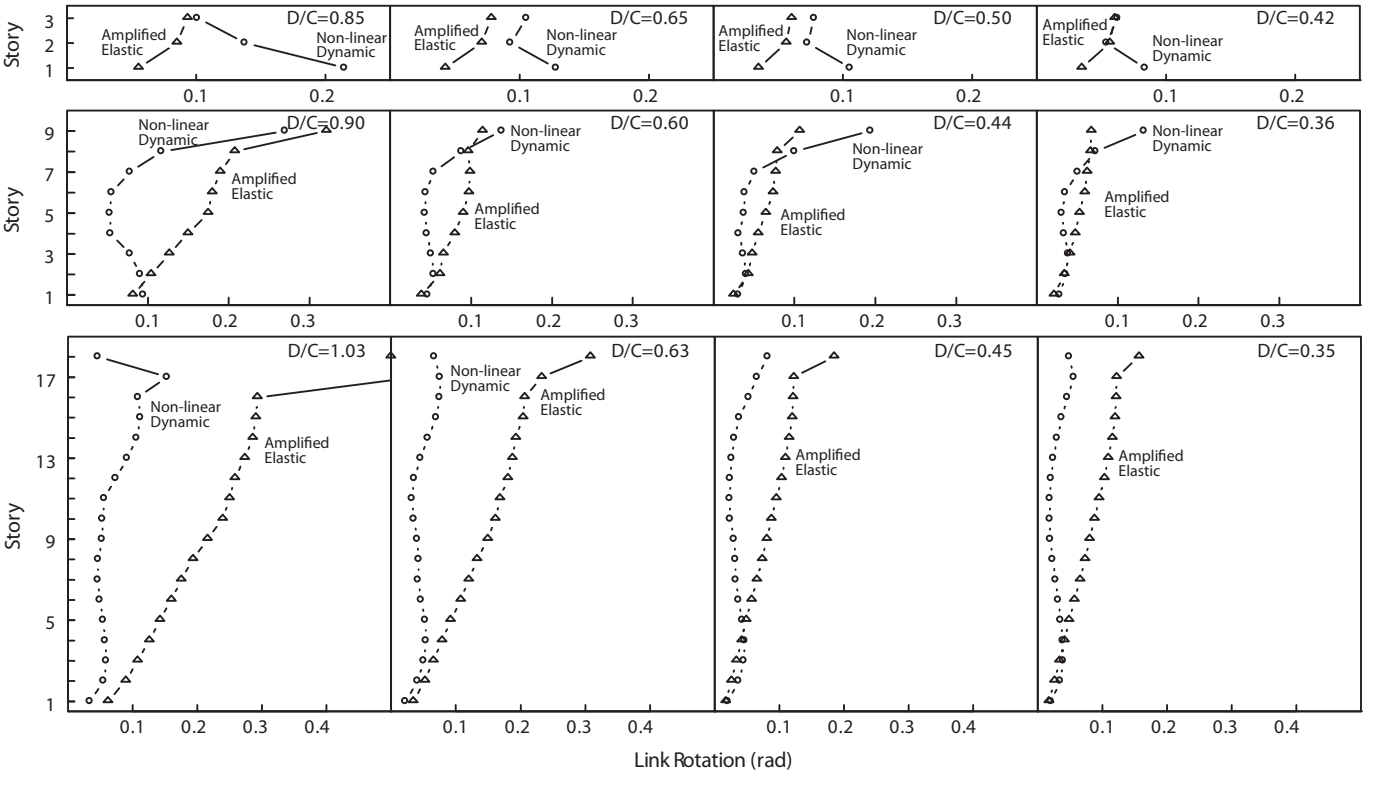

Fig. 11. Link rotations computed from analyses.

estimates of link rotations in the top two stories of the 3-story frames and in the bottom stories of the 9-story frames.

The grouping for the 9-story frames in Figure 12(a) gives a sense of the sensitivity of the results to frame geometry. The 9-story frame with D/C = 0.90 had links that were 3 ft long (except the top story), while the other 9-story frames had links that were 4 ft long (except top story). The frame with D/C = 0.90 has similar calibrated C_d factors as compared to the others, but it appears there is some sensitivity of the result to geometry. For the 3- and 18-story frames, similar link sizes were used for frames of all D/C ratios (except in the top stories of the 18-story frames), so differences in $C_{d,\ calib}$ are entirely due to strength.

Method 2

Another type of deformation amplification factor can be developed that scales only the shear component of the elastic story drift. This factor is computed as:

$$C_{d,\ shear} = (\text{inelastic link rotation}) / [(\text{shear component of elastic drift}) \times (L/e)]. \quad (4)$$

The computed values of $C_{d,\ shear}$ are indicated in Figure 12(b). In comparing Figure 12(b) with Figure 12(a), specifically the taller frames with the highest D/C ratios, values of $C_{d,\ shear}$ appear to have better vertical alignment than $C_{d,\ calib}$, making them better suited to be represented by a constant value. For example, a constant value of 5.0 for $C_{d,\ shear}$ might give a reasonably conservative estimate for link rotations for the 9- and 18-story frames of this study. Refer to Figure 4 and Prinz (2007) for the specific geometry and sizes for the frames that these factors are based on; in general, bay widths were 20 to 30 ft, bay heights were 13 ft, and link lengths were 3 to 4 ft.

Method 3

The third type of factor considered was a link rotation amplification factor (RAF) that would provide a direct estimation of link inelastic rotation from the link rotation of the elastic analysis. This factor, RAF was computed from the data as:

$$\text{RAF} = (\text{inelastic link rotation})/(\text{elastic link rotation}) \quad (5)$$

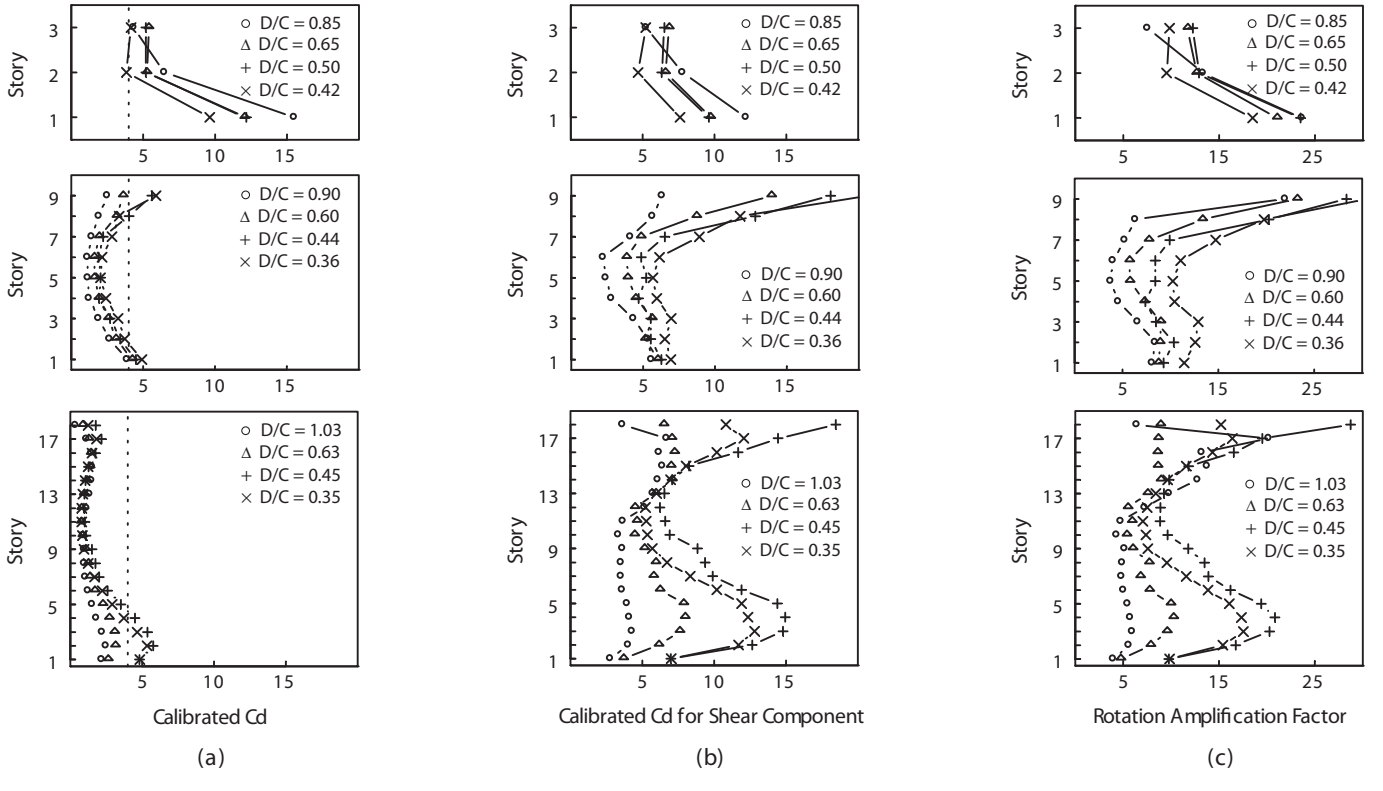

Fig. 12. Amplification factors for estimating inelastic deformations: (a) $C_{d,\ calib}$ for estimating link rotations using total elastic story drift, (b) $C_{d,\ shear}$ for estimating link rotations using the shear component of the elastic story drift, and (c) rotation amplification factor for estimating inelastic link rotations using elastic link rotations.

where inelastic link rotation came from the dynamic analyses. Values for the RAF are given in Figure 12(c). Values for this factor are less tightly grouped and appear more sensitive to frame strength. There appears to be no benefit to using the RAF instead of the $C_{d,\ shear}$.

SUMMARY AND PRACTICAL IMPLICATIONS

The ductility of steel eccentrically braced frames (EBFs) depends on stable inelastic rotation of the links. Links are sized and detailed so that inelastic rotation demands do not exceed inelastic rotation capacities. Typically, design engineers amplify elastic analysis results to estimate EBF link inelastic rotations. In this study, twelve EBFs (3-, 9-, and 18-story) were designed and investigated using time history analyses. Roof drifts, story drifts, and link rotations obtained from the time history analyses were compared with those estimated by amplifying elastic analysis results. In general, poor correlation was observed for most stories in typical frames. Three other methods for estimating inelastic link rotations were considered.

Low-rise EBFs will experience greater story drifts and link rotations than predicted by amplified elastic analysis. The value of the deformation amplification factor, C_d, is too low to accurately estimate inelastic drifts in low-rise buildings. Since inelastic drifts are underestimated, inelastic link rotations are also underestimated. Designers should keep this in mind when sizing links and determining appropriate stiffeners in low-rise buildings.

Mid to high-rise EBFs will experience much lower story drifts and link rotations than predicted by amplified elastic analysis. This is primarily due to the fact that elastic drifts which include the flexural component caused by column elongation are amplified.

Calibrated C_d factors are necessary for designers to reasonably estimate inelastic drifts and link rotations in EBFs. Results indicate that using a constant factor to scale the elastic shear deformation will yield more reasonable results for taller buildings than the present method of scaling total deformation. A factor of 5.0 was reasonable for the 9- and 18-story frames in this study with D/C near 1.0. The frames considered in the study had 20- to 30-ft bay widths, 13-ft typical bay heights, and link lengths of 3 to 4 ft. It appears the calibrated C_d factors are somewhat sensitive to EBF geometry, so this study is inadequate to recommend factors for general design.

ACKNOWLEDGMENTS

This work was possible due to the support of Brigham Young University. Matt Merrell, former student at Brigham Young University, assisted in the design of the frames used in the study. Reviewers provided helpful suggestions that significantly improved the paper. Their contribution is appreciated by the authors.

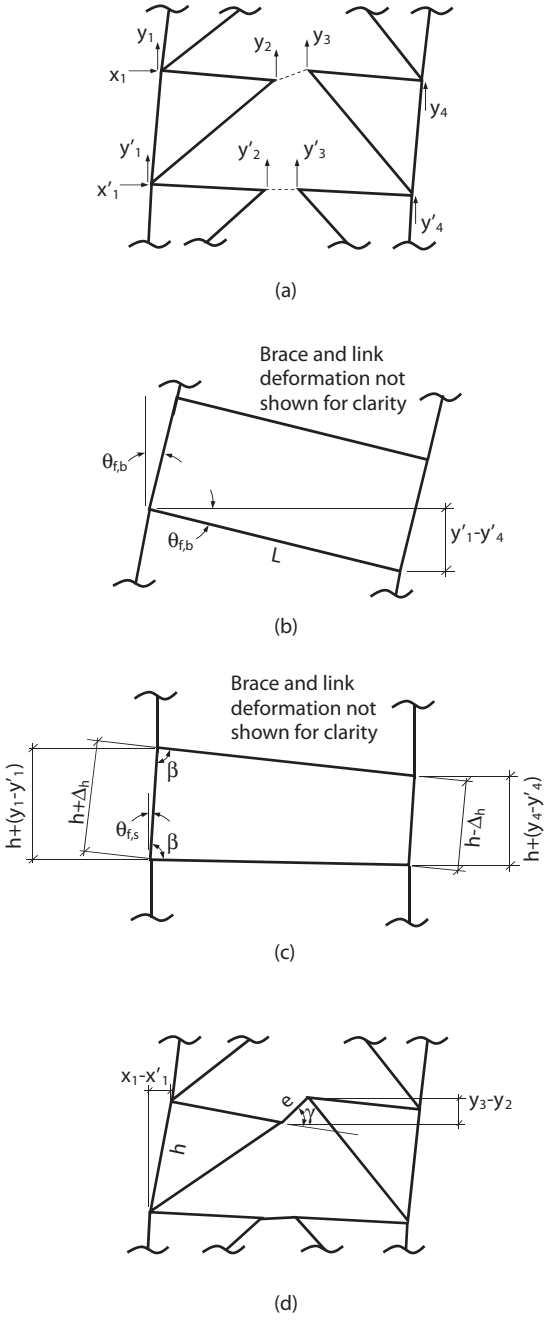

Fig. 13. Computing drift components and link rotations: (a) nodal displacements used for calculations; (b) component of story drift due to axial deformations in columns below; (c) component of story drift due to axial deformation in columns of story; (d) geometry for computing link rotations.

APPENDIX

Total story drifts and drift components were computed using nodal displacements from the analysis outputs. The six nodal displacements required to compute the components of drift for a story are x_1, y_1, y_4, x'_1, y'_1 and y'_4, as defined in Figure 13(a).

The total story drift, as defined by current provisions (ICC 2006), is:

$$\theta_T = (x_1 - x'_1)/h \tag{6}$$

where h is the story height. One component of this total story drift, is due to column shortening or elongation in the stories below, $\theta_{f,b}$. From the geometry shown in Figure 13(b), $\theta_{f,b}$ is:

$$\theta_{f,b} = \arcsin[(y'_1 - y'_4)/L] \tag{7}$$

Another component of the total story drift comes from column shortening or elongation in the story in question, $\theta_{f,s}$ [illustrated in Figure 13(c)]. From the geometry of Figure 13(c), $\theta_{f,s}$ is:

$$\theta_{f,s} = 90° - \beta \tag{8}$$

where

$$\beta = \arccos(\Delta_h/L) \tag{9}$$

From similar triangles in Figure 13(c),

$$(h + \Delta_h)/[h + (y_1 - y'_1)] = (h - \Delta_h)/[h + (y_4 - y'_4)] \tag{10}$$

which can be solved for Δ_h:

$$\Delta_h = h(R - 1)/(R + 1) \tag{11}$$

where

$$R = [h + (y_1 - y'_1)]/ [h + (y_4 - y'_4)] \tag{12}$$

Combining Equations 10 to 14, $\theta_{f,s}$ can be expressed in terms of nodal displacements:

$$\theta_{f,s} = 90° - \arccos\{[h(R - 1)]/[L(R + 1)]\} \tag{13}$$

Finally, the shear component of the total story drift, θ_s, is:

$$\theta_s = \theta_T - \theta_{f,b} - \theta_{f,s} \tag{14}$$

Link rotation, γ, was computed using nodal displacements x_1, x'_1, y_2 and y_3. From Figure 13(d) the relationship is:

$$\gamma = (y_3 - y_2)/e + (x_1 - x'_1)/h \tag{15}$$

REFERENCES

AISC (2005), *Seismic Provisions for Structural Steel Buildings*, American Institute of Steel Construction, Inc., Chicago.

Carr, A. (2004), *Ruaumoko Users Manual*, University of Canterbury, Christchurch, New Zealand.

Gupta, A. and Krawinkler, H. (1999), "Prediction of Seismic Demands for SMRFs with Ductile Connections and Elements," *Report SAC/BD-99/06*, SAC Joint Venture, Sacramento, CA.

Hall, J. (2005), "Problems Encountered from the Use (or misuse) of Rayleigh Damping," *Earthquake Engineering and Structural Dynamics*, Vol. 35, No. 5, 525–545.

Horne, J.P., Rubbo, A. and Malley, J.O. (2001), "AISC-LRFD Design and Optimization of Steel Eccentrically Braced Frames," *Proceedings of 70th Annual SEAOC Meeting*, San Diego, CA.

International Code Council (ICC) (2006), *International Building Code*, International Code Council, Inc., Whittier, CA.

International Conference Building Officials (ICBO) (1997), *Uniform Building Code*, International Conference Building Officials, Whittier, CA.

Karavasilis, T.L., Bazeos, N. and Beskos, D.E. (2007), "Estimation of Seismic Drift and Ductility Demands in Planar Regular X-Braced Steel Frames," *Earthquake Engineering and Structural Dynamics*, Vol. 36, No. 15, 2273–2289.

Kurama, Y.C. and Farrow, K.T. (2003), "Ground Motion Scaling Methods for Different Site Conditions and Structural Characteristics," *Earthquake Engineering and Structural Dynamics*, Vol. 32, No. 15, 2425–2450.

Medina, R.A. and Krawinkler, H. (2005), "Evaluation of Drift Demands for the Seismic Performance Assessment of Frames," *Journal of Structural Engineering*, Vol. 131, No. 7, 1003–1013.

Newmark, N.M. and Hall, W.J. (1982), *Earthquake Spectra and Design*, Earthquake Engineering Research Institute, El Cerrito, CA.

Okazaki, T., Arce, G., Ryu, H.-C. and Engelhardt, M.D. (2005), "Experimental Study of Local Buckling, Overstrength, and Fracture of Links in Eccentrically Braced Frames," *Journal of Structural Engineering*, Vol. 131, No. 10, 1526–1535.

Popov, E.P., Ricles, J.M. and Kasai, K. (1992), "Methodology for Optimum EBF Link Design," *Proceedings of the 10th World Conference on Earthquake Engineering*, Balkema, Rotterdam, Vol. 7, 3983–3988.

Prinz, G. (2007). *Impact of Beam Splicing on Seismic Response of Buckling Restrained Braced Frames, Masters Thesis* (advisor: P. Richards), Brigham Young University, Provo, UT.

Ramadan, T. and Ghobarah, A. (1995), "Analytical Model for Shear-Link Behavior," *Journal of Structural Engineering*, Vol. 121, No. 11, 1574–1580.

Richards, P. and Uang, C-M. (2006), "Testing Protocol for Short Links in Eccentrically Braced Frames," *Journal of Structural Engineering*, Vol. 132, No. 8, 1183–1191.

Ricles, J.M. and Popov, E.P. (1994), "Inelastic Link Element for EBF Seismic Analysis," *Journal of Structural Engineering*, Vol. 120, No. 2, 441–463.

RISA Technologies (2005), *RISA-2D Version 6.0 User's Guide*, Foothill Ranch, CA.

Roeder, C.W. and Popov, E.P (1978), "Eccentrically Braced Steel Frames for Earthquakes," *Journal of the Structural Division*, Vol. 104, No. ST3, 391–412.

Searer, G.R. and Freeman, S.A. (2004). "Design Drift Requirements for Long-Period Structures," *Proceedings of the 13th World Conference on Earthquake Engineering*, Vancouver, B.C. Canada.

Uang, C.-M. (1991). "Establishing R (or R_w) and C_d Factors for Building Seismic Provisions," *Journal of Structural Engineering* Vol. 117, No. 1, 19–28.

Uang, C.-M. and Maarouf, A. (1994), "Deflection Amplification Factor for Seismic Design Provisions," *Journal of Structural Engineering,* Vol. 120, No. 8, 2423–2436.

Experimental Study of Bolted Connection Strength at Elevated Temperatures

LIANG YU and KARL H. FRANK

ASTM A325 and A490 bolts are widely used on bolted connections in steel structures (ASTM A325-04, A490-04). Bolted connections are designed based upon their strength at ambient temperature; however, their strength at elevated temperatures is crucial to the performance of a structure during a fire. Understanding their behavior at elevated temperature is one of the keys to evaluate the fire resistance capability and fire safety of steel structures. In the Cardington series of fire tests, both fire protected and unprotected bolted beam-column connections failures were observed but not investigated thoroughly (Cardington Fire Test Report, 1998). Some research work has been focused on the stiffness variation of bolt connections at elevated temperatures. Theoretical models and FE simulations have been carried out (Liu, 1996; Silva et al., 2001; Al-Jabri, 2004). Little experimental work has been done to investigate the ultimate capacity of bolt connections at elevated temperature.

A research program was started in 2002 to study the ultimate capacity of bolted connections at elevated temperatures by the authors, which included large amounts of experimental work on both the bolts and the connections. As part of this study, the stiffness and shear strength of A325 and A490 bolts with temperature was investigated (Yu and Frank, 2009). The results of the connection tests which investigated the bearing and block shear capacity limit states are presented in this paper. Residual slip load capacity of fully tightened A490 bolt connection after exposure to different elevated temperatures was also presented.

TEST SETUP AND SPECIMEN DESIGN

Single-Bolt Connection

The single-bolt connection was designed to study the bearing capacity of steel plate at elevated temperature. Figure 1 shows the dimensions of the connection plates. The connection was made with two pieces of ⅜-in.-thick ASTM A572 Grade 50 steel plates and one ⅞-in.-diameter, 3-in.-long A325 bolt. The ASTM A572 Grade 50 steel had measured dynamic yield strength of 57.1 ksi and dynamic ultimate tensile strength of 78.6 ksi at ambient temperature. ("Dynamic" means the cross head of the test machine moved continuously at a constant speed without any pause.) The bolt was installed by hand to compact the connection and lightly tightened to minimize the clamping force and friction force that could be generated between the connected plates. An ASTM F436 washer was installed under the ASTM A563 Grade DH nut. The 1⁹⁄₁₆-in. holes in both the top and bottom plates were used to connect the test connection to the loading clevises with a pin and were designed not to fail. The ¹⁵⁄₁₆-in. bolt hole in the bottom plate was designed to have bearing failure at ambient temperature. Two end distances, ⅞ in. and 1⁵⁄₁₆ in., were tested in the temperature range up to 800 °C (1472 °F). These two end distances, named as 1.0*d* and 1.5*d*, corresponded to the edge distances of 1.0 and 1.5 times the nominal diameter of the A325 bolt.

Figure 2 shows the single-bolt connection test setup. The test system consists of an electric furnace, two stainless steel loading clevises, load frame, hydraulic ram, and data acquisition equipment. The furnace has a heating capacity of 800 °C (1472 °F). Figure 3 shows the heating time temperature curve of the furnace with ASTM standard fire heating curve (ASTM, E119-00a). The average heating rate is about 3.6 °F/min (2.0 °C/min). Because the strength of low carbon steels is insensitive to the time exposed to elevated

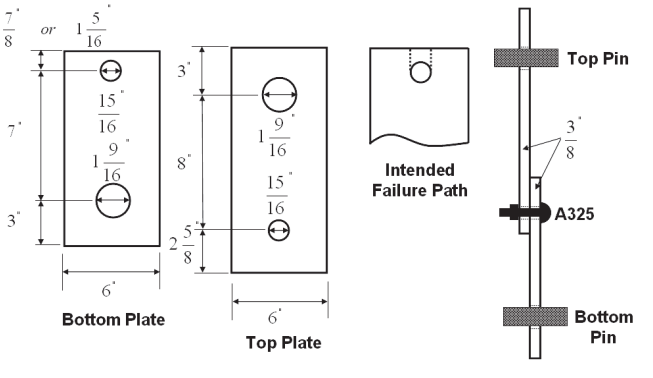

Fig. 1. Design of single-bolt connection (1 in. = 25.4 mm).

Liang Yu is a senior engineer for Deepflex, Inc., Houston, TX.

Karl H. Frank is a professor in the department of civil, architectural and environmental engineering, University of Texas at Austin.

temperatures, it is believed that the test results presented here are comparable to other similar tests performed at different heating rates. Two Type K thermocouple wires are inserted between connection plates to monitor the specimen temperature during test. The resolution of temperature readings is ±0.1 °C (0.18 °F). Furnace temperature is set to maintain specimen temperature at the desired level. Machine vision technology similar to that used by Spyrou and Davison was adapted to measure connection deformation, which is defined as the relative movement of connection plates (Spyrou and Davison, 2001). Figure 4 shows the visual targets—two pair of punch marks orthogonally oriented—and the connection deformation under load. The load is measured by a 200-kip load cell with ±0.1% accuracy.

Twenty-one single bolt connections were tested at temperatures from ambient temperature to 800 °C (1472 °F). All the tests were constant temperature tests and loaded quasi-statically. The connection was installed in the furnace at ambient temperature and heated to the desired temperature level before loading started. Once the desired specimen temperature was reached and the specimen had reached thermal equilibrium, the temperature in the furnace was kept constant. The axial tension load was then applied gradually until failure occurred.

Two-Bolt Connection

Two-bolt connections were designed to investigate block shear capacity at elevated temperature, as shown in Figure 5. The connection was made with three pieces of ½-in.-thick ASTM A572 Grade 50 steel plates and two ⅞-in.-diameter, 3-in.-long A490 bolts. The Grade 50 steel had measured dynamic yield strength of 56.3 ksi and dynamic ultimate strength of 73.0 ksi at ambient temperature. The 1$^{9}/_{16}$-in. holes were used to connect the specimen to the stainless loading clevises. The 3-in.-long A490 bolts were cut and rethreaded from 7-in.-long A490 bolts from the same manufactured lot that had been tested for shear capacity at elevated temperatures (Yu and Frank, 2009). ASTM F436 washer and ASTM A563 Grade DH nut were used. All the bolts were snug tightened. The higher strength A490 bolts were used in these specimens to produce a block shear failure rather than a bolt shear failure.

The loading test set up was the same as the single-bolt connection test shown in Figure 2. Ten connections were tested. Seven of them were constant temperature tests and the other three were tests under constant load. The constant temperature test procedure on two-bolt connections was the same as that of the single-bolt connection tests. In constant load test, the tension load in specimen connection was maintained while the furnace temperature was increased slowly until failure occurred. Specimen temperature, load and deformation are all recorded during the test.

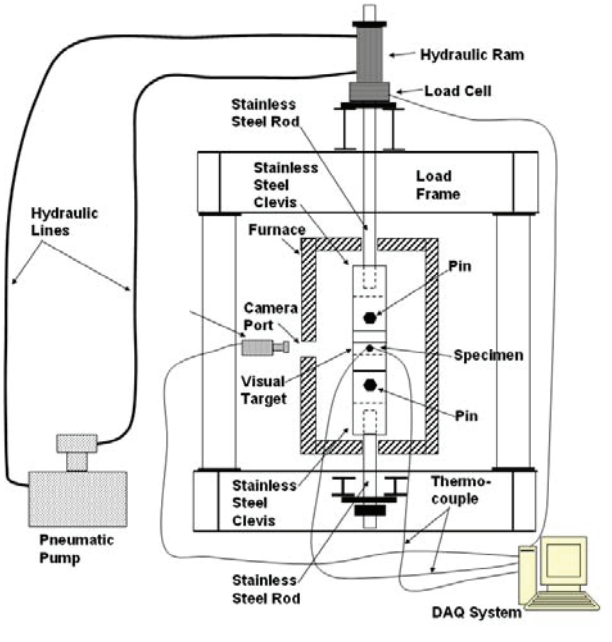

Fig. 2. Single-bolt connection test setup.

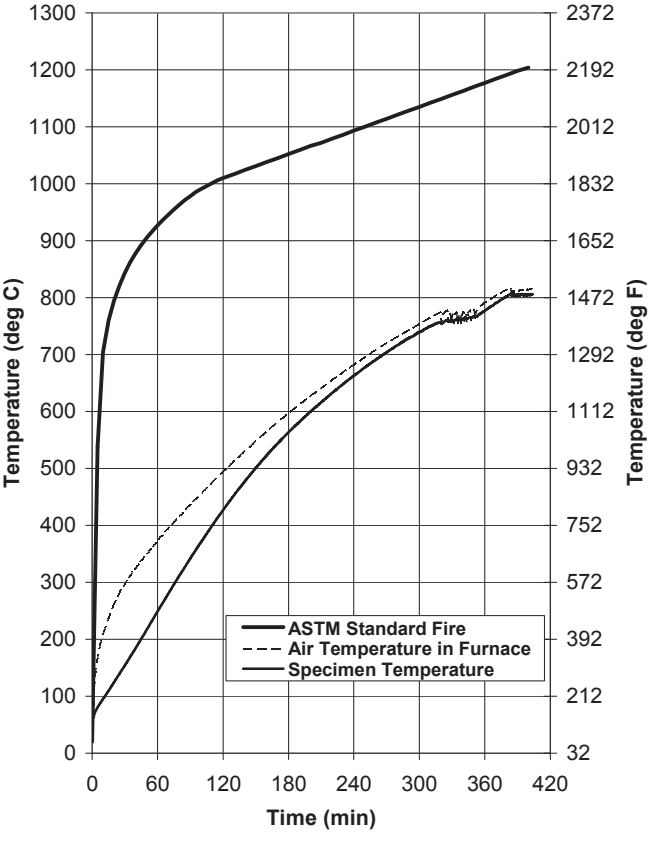

Fig. 3. Heating time temperature curve of the electric furnace.

Slip Load Test

A standard test method for determining the slip load of bolted connection is defined in the RCSC *Specification for Structural Joints Using ASTM A325 or A490 Bolts* (Appendix A, AISC 2005). The specimens used for the slip load test had the same geometry as the standard compression test specimen given by AISC. The clamping force was provided by a tension control A490 bolt. The pretension force in the A490 bolt used in the specimens was determined by tightening the A490 bolt on a Skidmore load cell. The average of three results was used as the estimated initial clamping force in all the specimens. The steel plates were sand blasted on both surfaces to produce surfaces with uniform slip coefficients on each plate.

The specimens were bolted together at ambient temperature. Nine connections were made in each batch and three were randomly picked as control samples which were not heated. The other six specimens were heated to desired temperature levels in the furnace and cooled outside of the furnace. After the connections temperature reach ambient temperature, they were tested to determine their slip loads.

TEST RESULTS

Single-Bolt Connection

Figure 6 shows the failure mode and failure paths of the single-bolt connections with 1.0*d* end distance. The tests are labeled using the first letter of their title followed by the test temperature. For example, the label SC-T300-D10 refers to *s*ingle-bolt *c*onnection at a *t*emperature of *300* degrees Celsius with an end distance *D* of *1.0* times the nominal diameter of the bolt. Specimens failed in bearing at all the temperatures except 700 °C (1292 °F). As test temperature increased from ambient temperature to 500 °C (932 °F), the bearing failure paths changed from parallel to flared fracture path. At 600 °C (1112 °F), bearing capacity was very close to the shear capacity of bolt. The bolt had under gone considerable shear deformations as shown in the Figure 6(g). At 700 °C (1292 °F), the connection failed by bolt shear with significant bearing deformations around the bolt hole. At 800 °C (1472 °F), a bearing failure occurred with very little shearing deformation on the bolt shank.

Figure 7 shows the load deformation curves of 1.0*d* single-bolt connections at elevated temperatures. From ambient temperature to 300 °C (572 °F), the load capacity of the single-bolt connections increases with temperature while deformation capacity decreases. From 300 °C (572 °F) to 500 °C (932 °F), load capacities of the connections begin to drop and deformation capacities of the connection are less than those at ambient temperature. From 600 °C (1112 °F) to 800 °C (1472 °F), load capacity drops significantly and the deformation capacity increases.

Figure 8 shows the failure mode and failure paths of the single-bolt connections with 1.5*d* end distance. From ambient temperature to 300 °C (572 °F), the 1.5*d* connection failures were similar to connection with a 1.0*d* end distance. Between 300 °C (572 °F) and 400 °C (752 °F), the failure mode changed from bearing failure to a shear failure of the bolt. The amount of bearing deformation at the bolt hole after the test indicates the shear capacity of bolt is close to bearing capacity of plate at 400 °C (752 °F) and 800 °C (1472 °F). At 500 °C (932 °F), 600 °C (1112 °F) and 700 °C (1292 °F), the amount of bearing deformation is very small, indicating the bearing capacity of the bolt hole is much higher than shear capacity of the bolt.

Figure 9 shows the load deformations curves of single-bolt 1.5*d* connections at elevated temperatures. Connection stiffness drops slightly at 100 °C (212 °F), compared with that at ambient temperature. Connection stiffness then increases at 200 °C (392 °F) and goes back down at 300 °C (572 °F). Due to the failure mode change from bearing failure to bolt shear

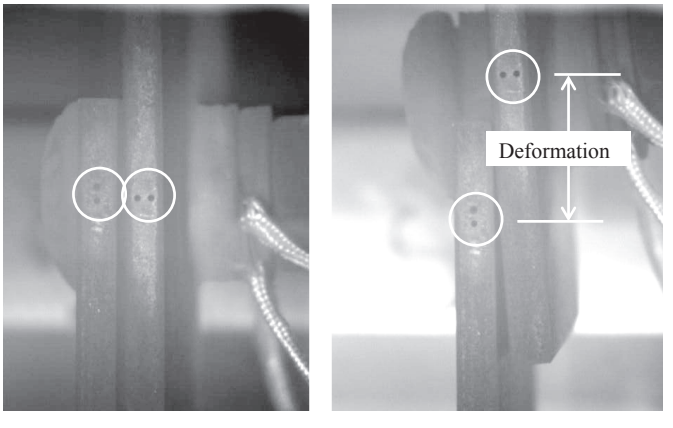

Fig. 4. Visual targets on single-bolt connection plates and connection deformation.

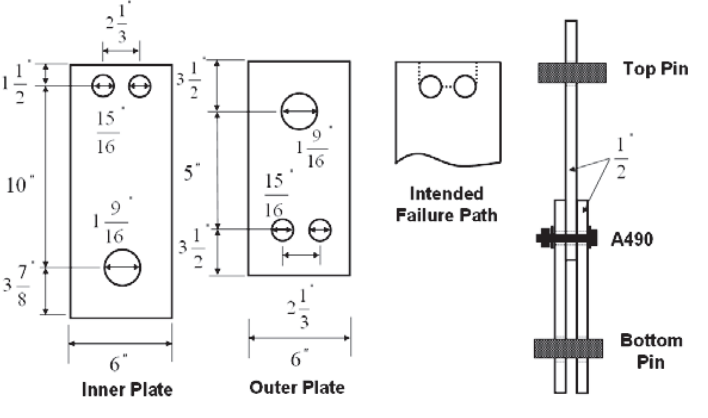

Fig. 5. Design of two-bolt connection (1 in. = 25.4 mm).

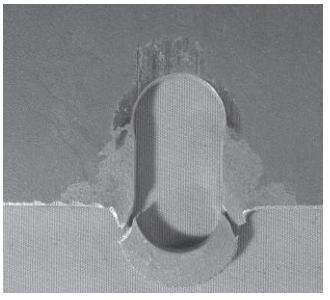

(a) SC-T25-D10 (25 °C, 77 °F)

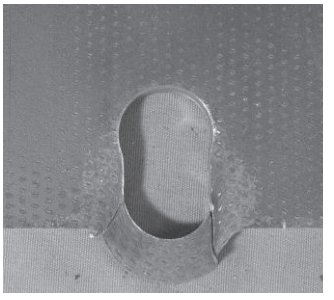

(b) SC-T100-D10 (100 °C, 212 °F)

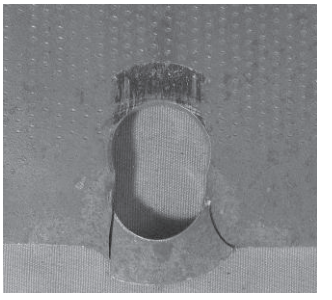

(c) SC-T200-D10 (200 °C, 392 °F)

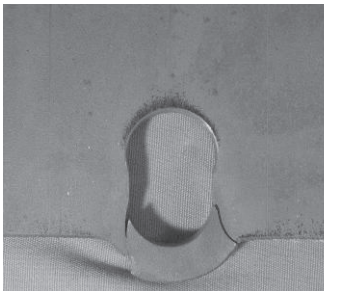

(d) SC-T300-D10 (300 °C, 572 °F)

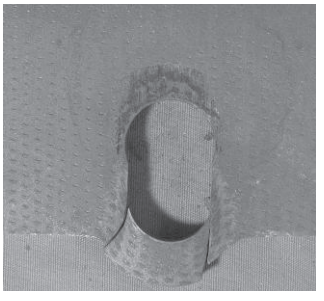

(e) SC-T400-D10 (400 °C, 752 °F)

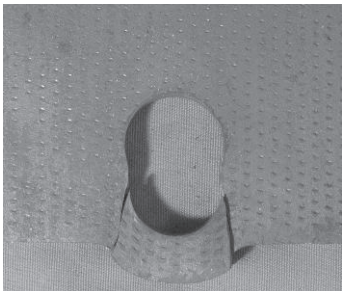

(f) SC-T500-D10 (500 °C, 932 °F)

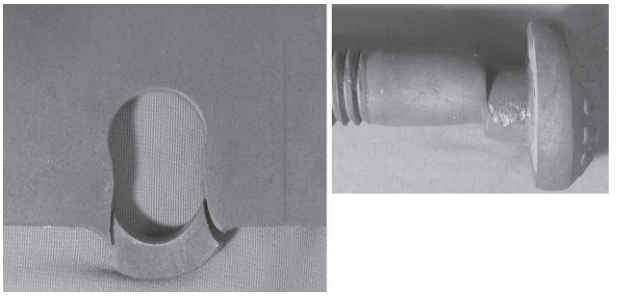

(g) SC-T600-D10 and half-sheared bolt (600 °C, 1112 °F)

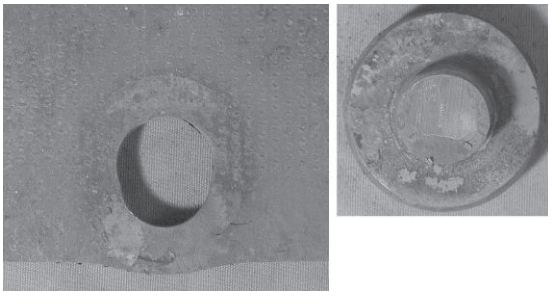

(h) SC-T700-D10 and sheared bolt section (700 °C, 1292 °F)

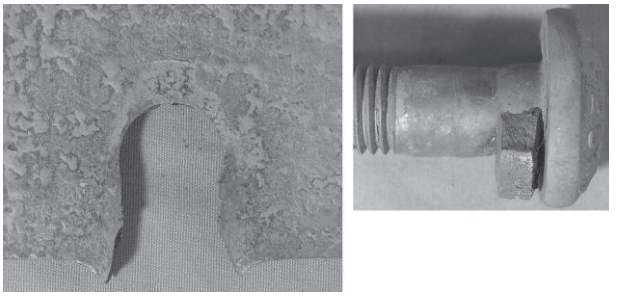

(i) SC-T800-D10 and intact bolt after test (800 °C, 1472 °F)

Fig. 6. Single-bolt connections ($L_e = 1.0d$) failures at different temperatures.

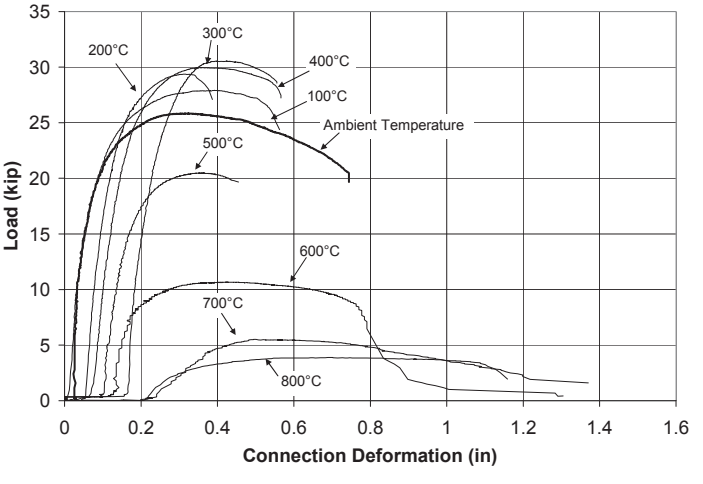

Fig. 7. Load deformation curves of single-bolt $L_e = 1.0d$ connection at elevated temperatures (1 kip = 4.448 kN).

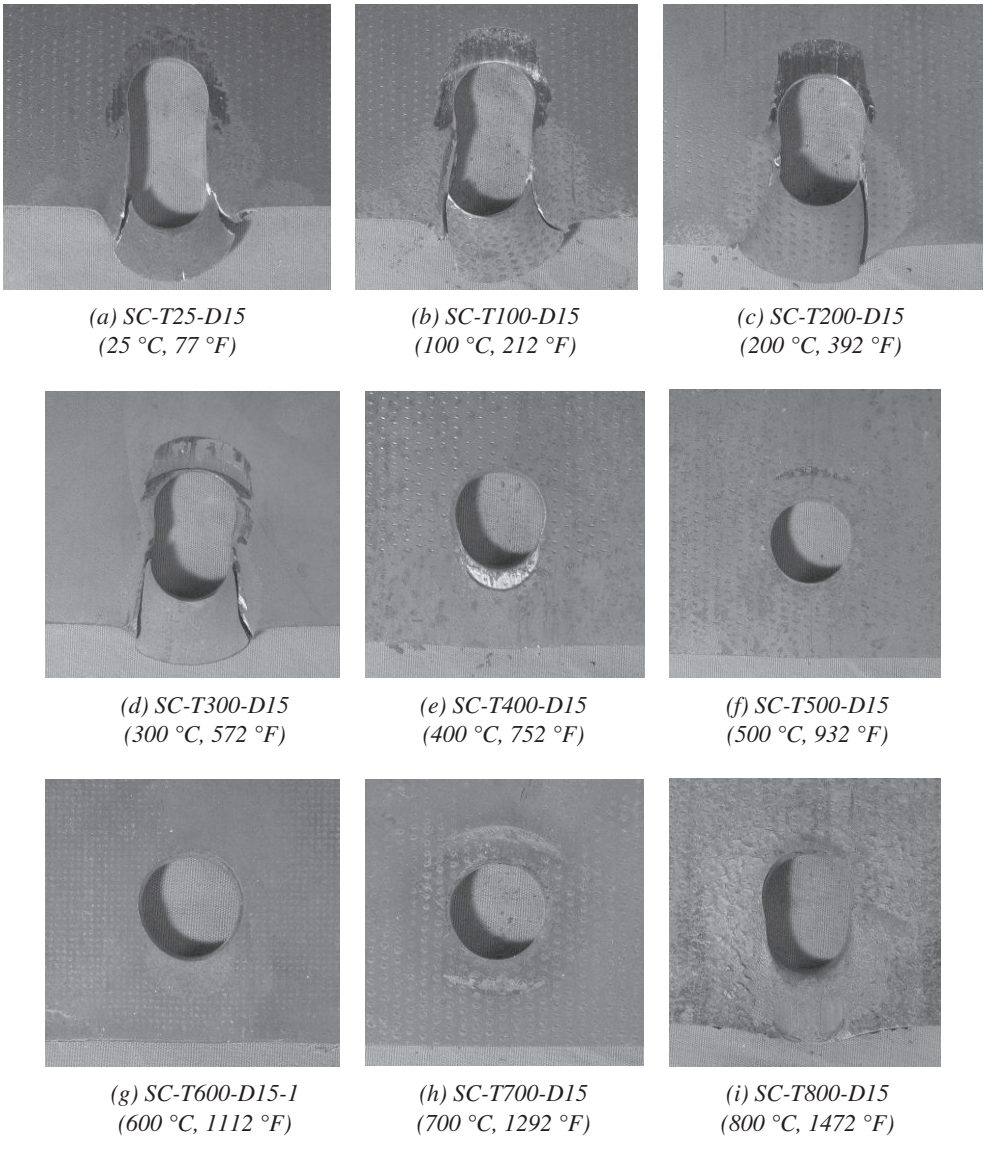

(a) SC-T25-D15 (25 °C, 77 °F)

(b) SC-T100-D15 (100 °C, 212 °F)

(c) SC-T200-D15 (200 °C, 392 °F)

(d) SC-T300-D15 (300 °C, 572 °F)

(e) SC-T400-D15 (400 °C, 752 °F)

(f) SC-T500-D15 (500 °C, 932 °F)

(g) SC-T600-D15-1 (600 °C, 1112 °F)

(h) SC-T700-D15 (700 °C, 1292 °F)

(i) SC-T800-D15 (800 °C, 1472 °F)

Fig. 8. Single-bolt connections (L_e = 1.5d) failures at different temperatures.

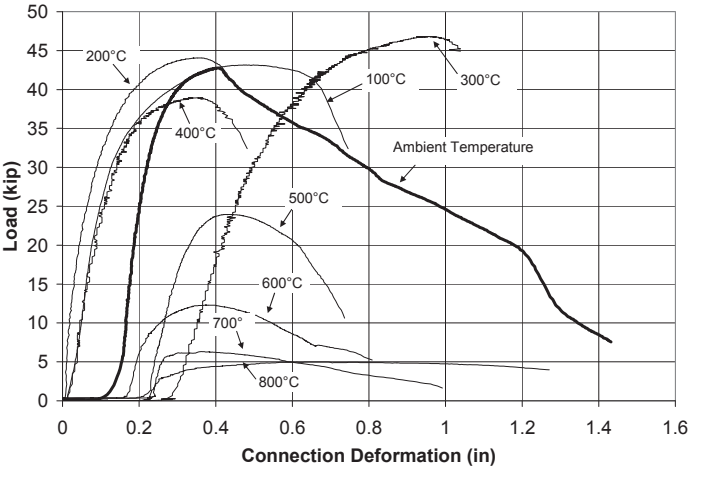

Fig. 9. Load deformation curve of single-bolt L_e = 1.5d connection at elevated temperatures (1 kip = 4.448 kN).

failure at 400 °C (752 °F), the connection stiffness at 400 °C (752 °F), 500 °C (932 °F) and 600 °C (1112 °F) are higher than the stiffness at 300 °C (572 °F). The deformation capacity of tested connections increased due to the increased ductility of the bolts from 500 °C (932 °F) to 700 °C (1292 °F). The very large deformation capacity at 800 °C (1472 °F) was the combination of bolt ductility and bearing deformation on the plate.

Figure 10 is a plot of the load capacities of the connections at different temperature levels. From ambient temperature to 300 °C (572 °F), the capacities of the single-bolt connections with 1.0*d* and 1.5*d* end distances increase with the temperature by approximately 5 kips, a 15 to 20% increase. The capacity of 1.0*d* connection drops slightly by about 2%—from 300 °C (572 °F) to 400 °C (752 °F). However, the capacity of 1.5*d* connection drops significantly as the failure mode changed from bearing failure of the steel plate to the shear failure of A325 bolt. From 400 °C (752 °F) to 800 °C (1472 °F), the capacity of 1.5*d* connection is controlled by the shear capacity of the A325 bolt. In the same temperature range, bearing failure is still the controlling failure mode in 1.0*d* connection except at 700 °C (1292 °F). The shear capacity of the ⅞-in. A325 bolt is close to the bearing capacity 1.0*d* connection from 600 °C (1112 °F) to 800 °C (1472 °F). The structural steels and high-strength bolts have different strength reduction rates with temperature. The high-strength bolt is quenched and tempered while the structural steel is hot rolled. The bolt loses its strength rapidly above 300 °C (572 °F) when the test temperature exceeds the tempering temperature of the bolt (Honeycombe, 1981; DeGarmo, 1979; Kirby, 1995; Yu and Frank, 2009). In Appendix 4 of the AISC *Specification*, structural steel is assumed to have no reduction in strength until it temperature exceeds 400 °C (752 °F) (AISC, 2005).

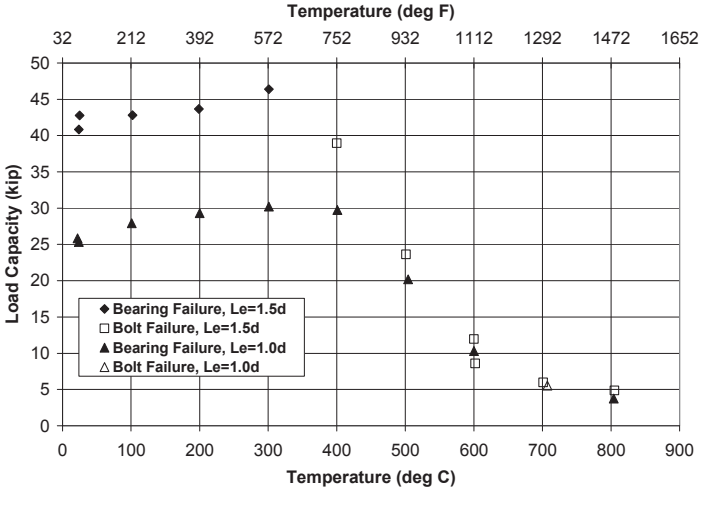

Fig. 10. Load capacities of single-bolt connections at elevated temperatures (1 kip = 4.448 kN).

Two-Bolt Connections

Figure 11 shows the results of the two-bolt connections tested at constant temperatures from 300 °C (572 °F) to 800 °C (1472 °F). The room temperature test was conducted as part of a companion study at the laboratory (Brown et al., 2007). At 300 °C (572 °F), the test connection has almost the same capacity as it does at ambient temperature. From 400 °C (752 °F) to 700 °C (1292 °F), the connection capacity almost drops linearly with its temperature, from 104 kips to 21 kips. The rate of decrease in connection capacity is less from 700 °C (1292 °F) to 800 °C (1472 °F). There is only an 8-kip-decrease in capacity at these high temperatures. It is also noticed that there is no increase in strength at 300 °C (572 °F) and 400 °C (752 °F), which was found in the bearing tests. Figure 12 shows the load deformation curves for the two-bolt connections in the constant temperature tests. As temperature increases, connection stiffness decreases and ductility increases.

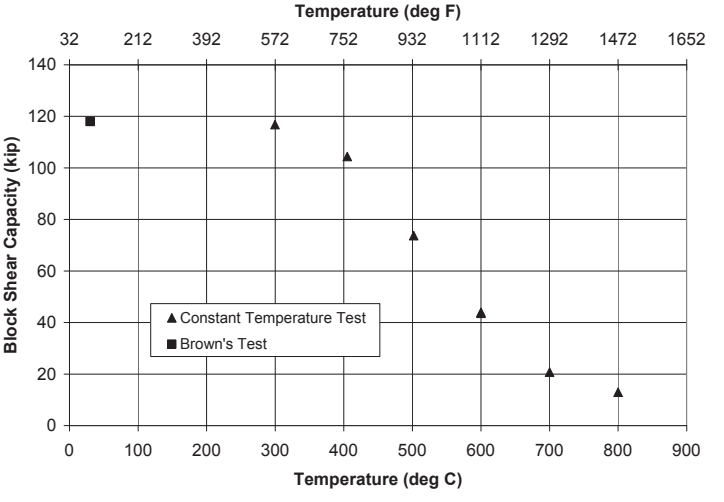

Fig. 11. Two-bolt connection constant temperature test results (1 kip = 4.448 kN).

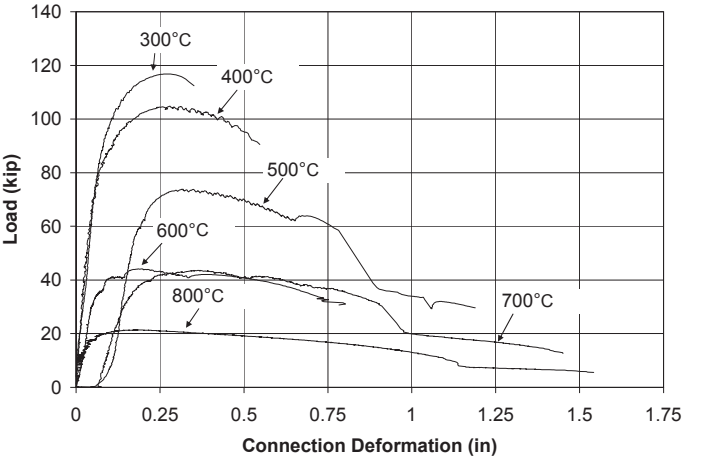

Fig. 12. Load deformation curves of two-bolt connection constant temperature tests (1 kip = 4.448 kN).

Figure 13 shows the block shear failures and the condition of the bolts after the tests. At 300 °C (572 °F), the ASTM A572 Grade 50 structural steel is in the blue brittle range (where the ductility of steel drops significantly) and an unusual half net section fracture-block shear failure occurred. At 400 °C (752 °F), normal block shear failure occurs. Right after the middle tensile part fractures, shear failure occurs on both shear paths. From 500 °C (932 °F) to 800 °C (1472 °F), the block failure can be divided into two phases: tensile failure first and then shear failure. The gap between the failed ends of tensile part indicated the connection still carries load by shear after the tensile ligament between the holes fractured. After a large amount of shear deformation, the material included in block shear fails in tension at two tips. At temperatures lower than 500 °C (932 °F), the A490 bolts has no significant deformation, which indicates the A490 bolt's shear capacity is much higher than block shear capacity of the plate. However from 600 °C (1112 °F) to 800 °C (1472 °F), larger deformations are found on the bolt shank, which indicates the difference between bolt shear capacity and block shear capacity of plate is small.

Constant load tests were performed to simulate the behavior of bolted connections in a fire event. Figure 14 shows the time-temperature and time-deformation curves of constant load tests. Three load levels, 33 kips, 60 kips and 75 kips, are tested. All the connections show very small deformation increase until its temperature reaches a critical level. The connection deformation then starts to increase quickly, and connection failure occurs a few seconds later. The failure temperature was taken as the temperature when the connection ceases to carry the load. Due to the limitations of the electric furnace, the connections are exposed to high

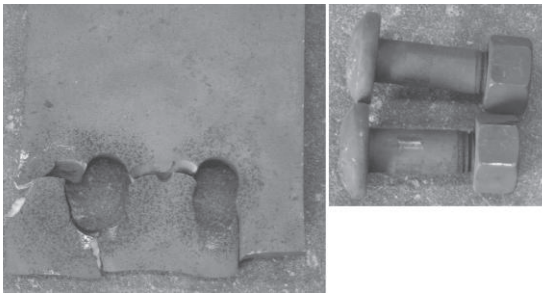

(a) TC-T300-CT (300 °C, 572 °F)

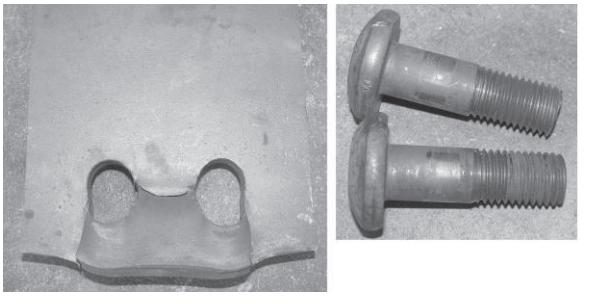

(b) TC-T400-CT (400 °C, 752 °F)

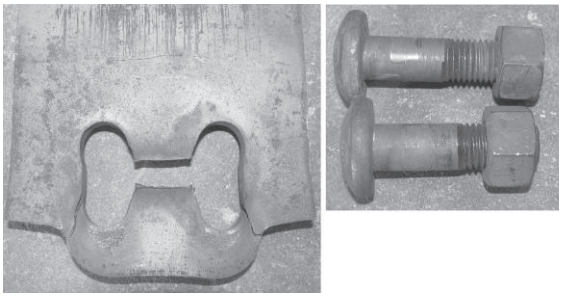

(c) TC-T500-CT (500 °C, 932 °F)

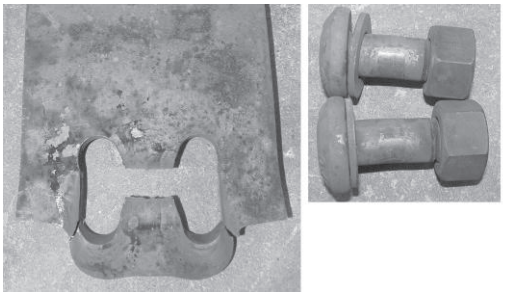

(d) TC-T600-CT (600 °C, 1112 °F)

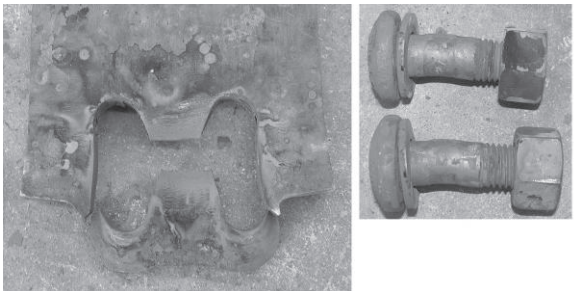

(e) TC-T700-CT (700 °C, 1292 °F)

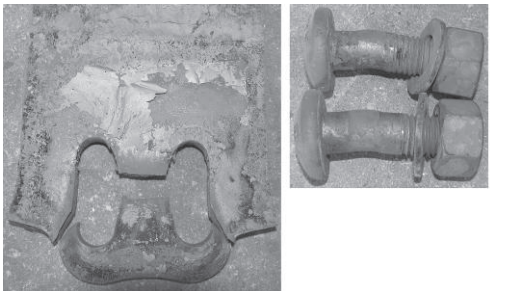

(f) TC-T800-CT (800 °C, 1472 °F)

Fig. 13. Block shear failures at different temperature levels (constant temperature tests).

Table 1. Tension Force in A490 Bolt after Shearing of Spline				
Bolt No.	**Bolt 1**	**Bolt 2**	**Bolt 3**	**Average**
Tension force (kips)	57.0	58.0	57.0	57.3

temperature for a longer time—more than 2 to more than 3 hours—than they would experience in the ASTM standard fire test or in an actual fire with the connection unprotected. The time at a particular temperature would be less in the ASTM test than in these tests. No significant deformation occurred in these sustained load tests until the connection was within 50 ºC (90 ºF) of the failure temperature. Any creep effects would be less in the ASTM standard fire test protocol due to its rapid temperature increase relative to these tests.

Figure 15 shows the constant temperature test results plotted with the constant load test results. The two types of tests produced the same strengths. Therefore, it appears that the test results are not influenced by the heating and loading path taken during the tests. The effect of the load sustained at lower temperatures did not significantly influence the strength or deformation of the connection. Based upon these results, it is apparent the constant temperature test results can be used to estimate the behavior of bolted connections regardless of the time-temperature history the connection experiences during a fire event.

Slip Load of Fully Tightened A490 Bolt Connection

The pretension force in tension control A490 bolts used in the test specimens was measured with a Skidmore load cell. The test results are shown in Table 1.

Three batches of connections were tested. Before making a connection, all the steel plates were blasted using a fine sand blasting medium to provide a uniform surface to minimize the variance among connections within the batch. The preparation was not intended to duplicate the surface roughness of a commercially blasted surface. In each batch, three connections were randomly picked as the control samples and were tested without being heated. The loss of slip resistance was determined by comparing the control test results to the results of the heated connections. Among the nine control connections, seven results were between 30 kips and 40 kips. The test results show a good consistency across test batches with two exceptions: a low load of 26.6 kips and a high load of 54.0 kips. The average slip load of each batch of the control tests, neglecting the two outliers, was between 31.4 to 33.3 kips. These slip loads correspond to a slip coefficient of 0.27 to 0.29, using the average bolt tension determined in the Skidmore load cell.

Figure 16 gives the absolute slip loads of the heated connections tested after cooled to ambient temperature. From ambient temperature to 400 °C (752 °F), the slip load increased from about 35 kips to 50 kips. Therefore, slip connections maintain their slip capacity after being exposed to a temperature lower than 400 °C (752 °F). However, the slip capacity dropped significantly from 400 °C (752 °F) to 800 °C (1472 °F).

The reason for a slip resistance increase from ambient temperature to 400 °C (752 °F) might be due to the increase in the surface roughness due to oxidization and the bolt tension evidently remaining constant. During the heating and cooling phases, the connection underwent expansion and shrinkage. That might have resulted in a better contact between the surfaces. The rapid drop above 400 °C (752 °F) is probably due to a loss of bolt tension. From the shear tests

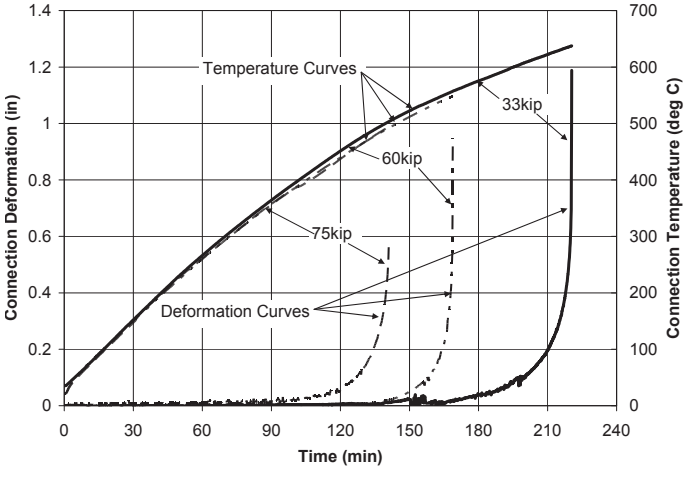

Fig. 14. Time-deformation and time-temperature curves of constant load tests (1 in. = 25.4 mm, 1 kip = 4.448 kN).

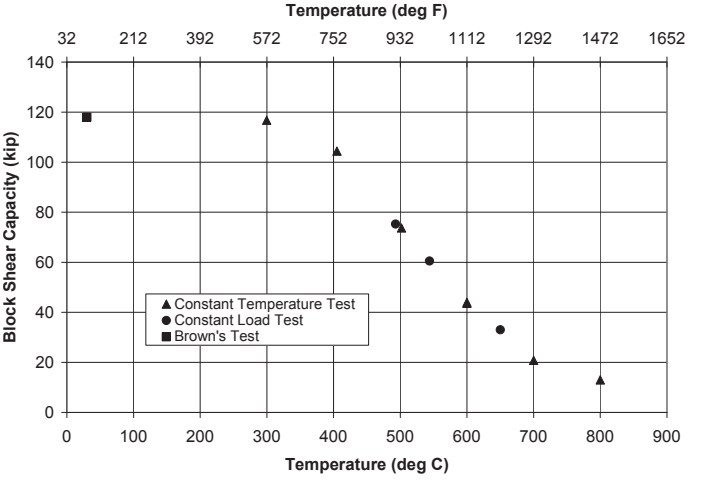

Fig. 15. Constant load test vs. constant temperature test (1 kip = 4.448 kN).

on A490 bolts at elevated temperature, the shear capacity of A490 bolt drops by 40% at 500 °C (932 °F) when compared with its shear capacity at ambient temperature (Yu and Frank, 2009). It is reasonable to estimate A490 bolt's tensile capacity drops by the same amount. From the mill test report, the tensile strength of this A490 bolt is 75.4 kips. At 500 °C (932 °F), the estimated tensile strength is 45.2 kips. The original pretension force is 57.3 kips, which is greater than estimated tensile strength of 45.2 kips at 500 °C (932 °F). Therefore, A490 bolt stretches plastically. After cooling to ambient temperature, the elongated bolt will have a reduced tension load, which would result in a loss of the slip capacity of the connection.

Figure 17 shows post-test slip surfaces of the connections that had been heated to different temperatures and cooled to ambient temperature before being tested for the slip capacity. On the slip surface of the control connections, slip marks are small. After the connection was heated to 100 °C (212 °F) and 200 °C (392 °F), large slip marks concentrate near the bolt hole, where high clamping force acts. This indicates better contact of the steel plate surfaces due to expansion and shrinkage in heating and cooling. At 300 °C (572 °F), there are more slip marks on the surfaces. These specimens had the highest slip load. At 400 °C (752 °F), slip marks reduce and are similar to the 100 °C (212 °F) connection. From 500 °C (932 °F) to 800 °C (1472 °F), slip marks almost disappear. This is consistent with the conclusion that A490 bolt loses most of its pretension force after experiencing temperature higher than 400 °C (752 °F).

COMPARISON WITH AISC SPECIFICATIONS

The bearing and block shear test results were normalized by dividing the strengths at elevated temperatures by the strength at room temperature. The results were compared with the strength reductions of structural steels given in Table A-4.2.1 of the Appendix 4 of the AISC *Specification*, as shown in Figures 18 and 19. The results of the bearing test with bearing failures agree with the strength reduction factors in the AISC *Specification*. The AISC values overestimate the strength of connections, which failed by bolt shear failure. The heat-treated bolts have a rapid drop in strength when their temperature exceeds the tempering temperature during manufacture process, which results in a change from bearing failure to bolt shear failure. The block shear strength tests shown in Figure 19 all fall below the AISC strength curve. The block shear strength of the two-bolt connections during a fire would be overestimated using the AISC strength values at temperatures between 750 and 1300 °F (400 and 700 °C). If lower-strength A325 bolts had been used in these two-bolt connections, the strength would have been even lower since the test load exceeds the shear capacity of the A325 bolts. Both the strength of the bolts and plate material at the elevated temperature must be considered in determining the strength of the connection during a fire.

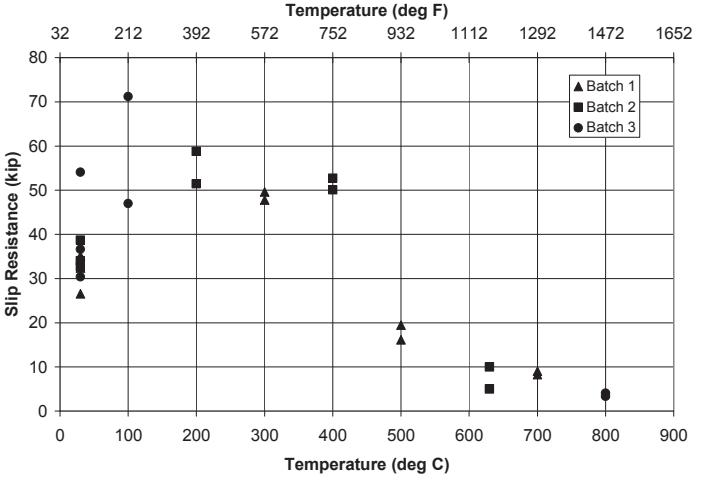

Fig. 16. Slip load vs. temperature (1 kip = 4.448 kN).

CONCLUSION

Single A325 bolt connections with two end distances, 1.0 and 1.5 times of the nominal bolt diameter, were tested at temperatures up to 800 °C (1472 °F). A 10 to 20% bearing capacity increase was found on all specimens at 300 °C (572 °F). As known from the milling process, steels exhibit a strength increase along with a ductility decrease around this temperature. A thorough explanation will involve the knowledge of metallurgy. For 1.0*d* connections, significant bearing capacity loss was found between 400 °C (752 °F) and 800 °C (1472 °F). On 1.5*d* connections, failure mode changed from bearing failure to shear failure of the bolt between 300 °C (572 °F) and 400 °C (752 °F). Above 400 °C (752 °F), load capacity of these connections was controlled by the shear capacity of the A325 bolts. Understanding this failure mode change is extremely important for improving the load capacity of bolted connections at elevated temperatures. At ambient temperature, the capacity of the tested connections was controlled by bearing strength of the bolt hole. However, at temperatures above 300 °C (572 °F), the shear capacity of the bolt becomes the controlling limit. Under such situation, increasing the end distance of bolt hole or plate thickness will not increase the load capacities of the connections.

Block shear capacity of bolted connections at elevated temperature was studied on two-bolt connections. Significant reduction on block shear capacity was found between 400 °C (752 °F) and 800 °C (1472 °F). Test results from constant load tests agree well with those from constant temperature tests. This indicates the constant temperature test results can be used to estimate the behavior of bolted connections regardless of the time-temperature history that the connection experiences during a fire event.

The residual slip load capacity of fully tightened A490 bolt connections was investigated. Up to 50% slip load capacity increase is found on the connections that were exposed to a temperature between 100 °C (212 °F) and 400 °C (752 °F). However, a 50% slip load capacity loss occurs after the exposure to 500 °C (932 °F). Further decrease is found after the specimen was exposed to temperatures between 500 °C (932 °F) and 800 °C (1472 °F). In addition, 400 °C (752 °F) is a key temperature in assessing the slip load capacity of A490 bolt after a fire. Connections heated below this temperature retain their slip capacity after a fire, while connections heated above this temperature have a reduced slip load capacity.

These findings provide an insight into the design of bolted connections at elevated temperatures and assess fire damage on bolt connections. The capacity of bolt connections

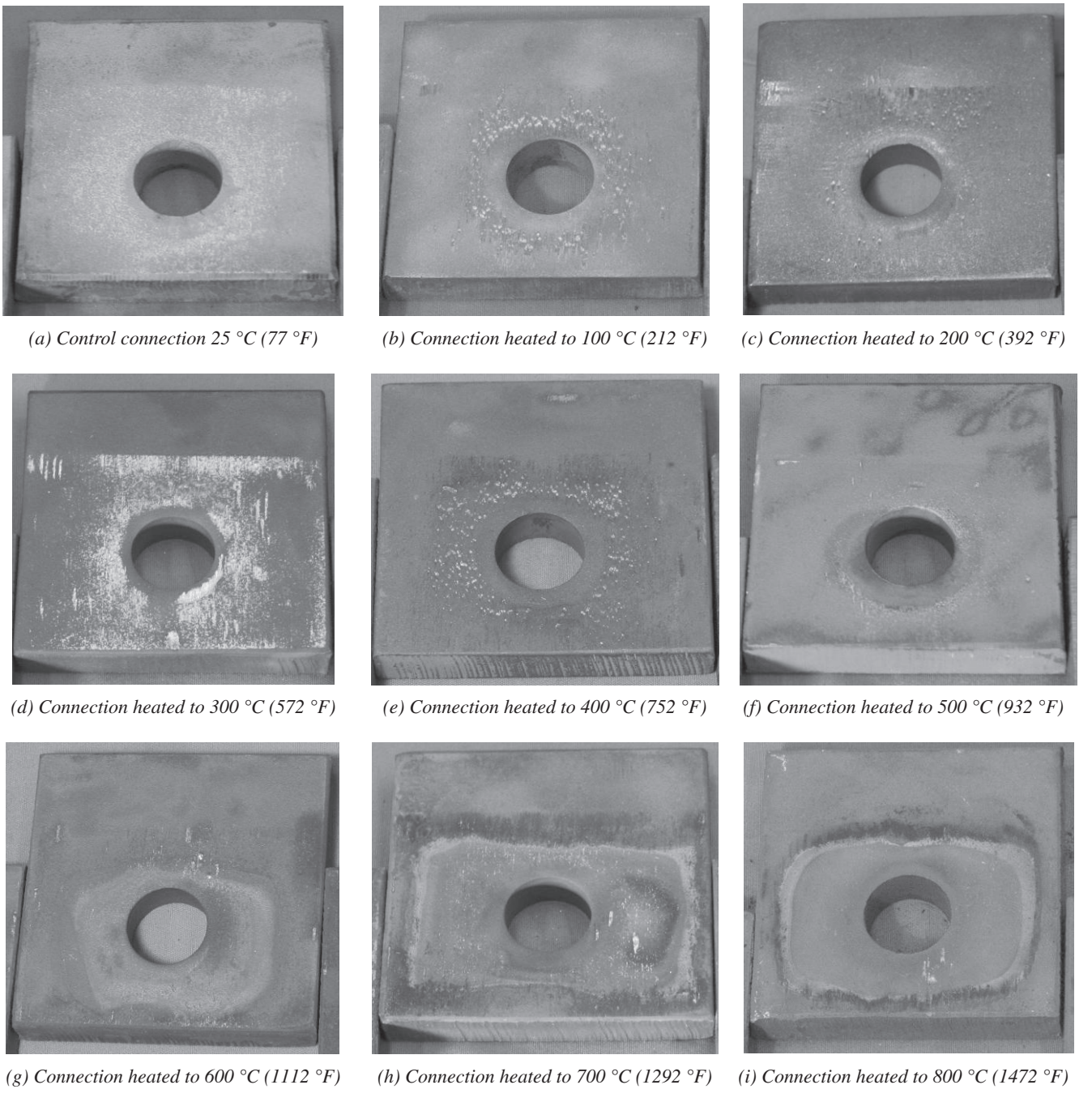

(a) Control connection 25 °C (77 °F) *(b) Connection heated to 100 °C (212 °F)* *(c) Connection heated to 200 °C (392 °F)*

(d) Connection heated to 300 °C (572 °F) *(e) Connection heated to 400 °C (752 °F)* *(f) Connection heated to 500 °C (932 °F)*

(g) Connection heated to 600 °C (1112 °F) *(h) Connection heated to 700 °C (1292 °F)* *(i) Connection heated to 800 °C (1472 °F)*

Fig. 17. Slip surface of connections after heated to different temperature levels and tested at room temperature.

are generally controlled by the bearing or block shear failure in the steel plates at temperatures below 300 °C (572 °F) because the heat-treated bolts have higher strength than structural steels; however, when exposed to temperatures above 300 °C (572 °F), the bolts lose their strength at a much higher rate than structural steels. The capacity of bolted connections becomes controlled by the strength of bolts rather than the steel plates. In other words, increasing the bolt end distance may not help the connection strength at temperatures above 300 °C (572 °F). For slip critical connections with fully tightened bolts, the load capacity can be greatly reduced after exposure to a temperature above 400 °C (752 °F).

The material strength reduction factors given in Appendix 4 of the AISC *Specification* follow the trend of the test results. However, the strength of the block shear tests was lower than the AISC strength reduction factors. The AISC strength values overestimated the strength of the bearing tests, which failed by bolt shear as well.

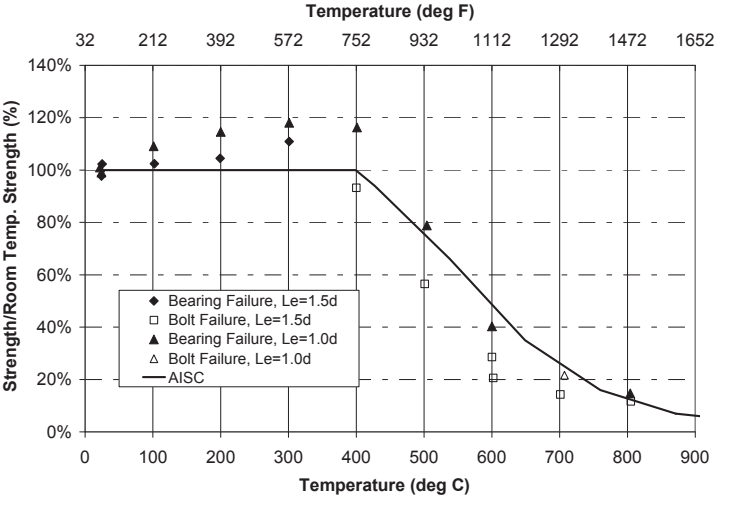

Fig. 18. Comparisons of bearing tests with AISC Appendix 4.

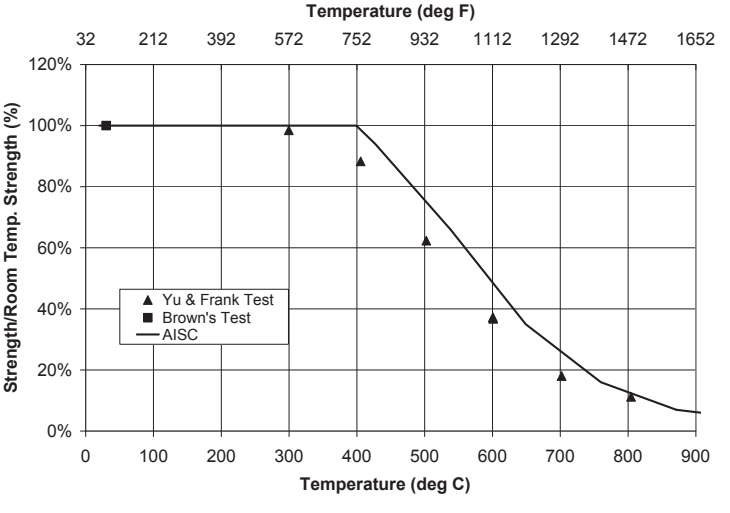

Fig. 19. Comparisons of block shear tests with AISC Appendix 4.

REFERENCES

AISC (2005), *Steel Construction Manual,* 13th Ed., American Institute of Steel Construction, Inc., Chicago.

Al-Jabri, K.S. (2004), "Component-Based Model of the Behavior of Flexible End-Plate Connections at Elevated Temperatures," *Composite Structures*, Vol. 66, 215–221.

American Society for Testing and Materials (ASTM) A325-04, *Standard Specification for Structural Bolts, Steel, Heat Treated, 120/105 ksi Minimum Tensile Strength.*

American Society for Testing and Materials (ASTM), A490-04, *Standard Specification for Structural Bolts, Alloy Steel, Heat Treated, 150 ksi Minimum Tensile Strength.*

American Society for Testing and Materials (ASTM), ASTM E119-00a, *Standard Test Methods for Fire Tests of Building Construction and Materials.*

British Steel Swinden Technology Center (1998), *Cardington Fire Test Report—The Behavior of Multi-storey Steel Framed Building Subject to Fire Attack, Experimental Data.*

Brown, Lubitz, Cekov, Frank and Keating (2007), *Evaluation of Influence of Hole Making Upon the Performance of Structural Steel Plates and Connections,* Center for Transportation Research, University of Texas at Austin, Report FHWA/TX-07/0-4624-1.

Da Silva, Luis Simoes, Santiago, Aldina and Vila Real, Paulo (2001), "A Component Model for the Behavior of Steel Joints at Elevated Temperatures," *Journal of Constructional Steel Research*, Vol. 57, 1169–1195.

DeGarmo, E. Paul (1979), *Materials and Processes in Manufacturing,* 5th Ed., Macmillan Publishing Co., Inc.

Honeycombe, R.W.K. (1981), *Steels Microstructures and Properties,* Metallurgy and Materials Science Series.

Kirby, B.R. (1995), "The Behavior of High-Strength Grade 8.8 Bolts in Fire," *Journal of Construction Steel Research*, Vol. 33, 3–38.

Liu, T.C.H. (1996), "Finite Element Modeling of Behavior of Steel Beams and Connections in Fire," *Journal of Constructional Steel Research*, Vol. 36, 181–199.

Spyrou, S. and Davison, J.B. (2001), "Displacement Measurement in Studies of Steel T-stub Connections," *Journal of Constructional Steel Research*, Vol. 57, 647–659.

Yu, L. (2006), *Behavior of Bolted Connection During and After a Fire*, Ph.D. Dissertation, University of Texas at Austin, Ferguson Structural Engineering Lab.

Yu, L. and Frank, K.H. (2009), "Shear Behavior of A325 and A490 High Strength Bolts in Fire and Post Fire," *Engineering Journal*, AISC, Vol. 46, No. 2.

Collapse Performance of Low-Ductility Chevron Braced Steel Frames in Moderate Seismic Regions

ERIC M. HINES, MARY E. APPEL and PETER J. CHEEVER

Prior to 1978, seismic design practice in the United States distinguished moderate seismic regions from high seismic regions through the application of lower design acceleration levels (SEAOC, 1960; Rojahn, 1995). In 1978 the Applied Technology Council's document ATC-3-06 proposed further differentiation between moderate and high seismic regions by regulating structural systems and detailing requirements according to Seismic Design Category (SDC) (ATC, 1978). Since the publication of ATC-3-06, detailing requirements have grown more numerous and stringent for buildings in high seismic regions (SDC D or higher); however, they have not influenced building design in low and moderate seismic regions (SDC C or lower) as heavily. Thus, it has generally been accepted that buildings in low and moderate seismic regions may be designed both for lower maximum considered earthquake (MCE) forces and less ductility than their counterparts in high seismic regions. Current model codes adhere to this philosophy by assigning different height limits to recognized structural systems in each SDC (ICC, 2006; ASCE, 2005). Each recognized system is assigned a response modification factor (*R*-factor), which applies to all SDCs.

Language in the 1992 AISC *Seismic Provisions* (AISC, 1992) clearly exempted most buildings in SDC A, B, and C from seismic detailing requirements. This exemption generated the unintended consequence that some engineers designed buildings in low and moderate seismic regions with high *R*-factors, but without providing appropriate detailing. The 1997 AISC *Seismic Provisions* clarified the intention of the SDC exemptions by specifying that "Systems designed and detailed to meet the requirements in the LRFD *Specification* but not the requirements of Part I" of the AISC *Seismic Provisions* should be designed with $R = 3$ (AISC, 1997a). Although this provision was originally intended to ensure a minimum design level for low-ductility systems, its ability to ensure collapse resistance similar to more ductile systems with higher *R*-factors has not been proven.

These historical circumstances motivate fundamental questions concerning seismic collapse behavior in moderate seismic regions.

1. How much ductility, how much strength, and how much reserve capacity are actually required for a building to survive an MCE event in a moderate seismic region?

2. In particular, can an inherently low-ductility system such as a concentric chevron braced steel frame be designed to survive moderate seismic demand with a high level of confidence?

3. Should such systems even be evaluated according to the concepts of ductility and capacity design?

4. How can we articulate a design philosophy for low-ductility systems in moderate seismic regions that aims to ensure safety against collapse while allowing engineers as much freedom as possible to design creatively and economically?

DESIGN PHILOSOPHY FOR MODERATE SEISMIC REGIONS

The absence of a clearly expressed low-ductility design philosophy for moderate seismic regions makes $R = 3$ appear to be an attractive option for the design of such systems. Further investigation reveals, however, that the literature is relatively silent on the adequacy of $R = 3$. In comparison to well-developed design philosophies such as ductility and capacity design, isolation, and supplemental damping, $R = 3$ offers little insight into structural behavior. A design philosophy for low-ductility systems in moderate seismic regions should encourage the development of structural systems according to well-established principles rather than prescriptive requirements. The analyses presented in this paper indicate that collapse vulnerability of an $R = 3$ system depends heavily on the capacity of its gravity framing to act as a reserve system. While conclusions regarding the safety of $R = 3$ in general remain beyond the scope of this paper, the studies presented herein yield some insight into reserve

Eric M. Hines is a professor of practice in the department of civil and environmental engineering, Tufts University, Medford, MA and an associate at LeMessurier Consultants, Cambridge, MA.

Mary E. Appel is a structural engineer at BSA Life Structures, Indianapolis.

Peter J. Cheever is an executive vice president at LeMessurier Consultants, Cambridge, MA.

system performance and other important characteristics of a low-ductility design philosophy. Such a philosophy should respond to the following observations:

1. Socioeconomic Impact

    a. Emphasize collapse prevention over economic loss (Luft and Simpson, 1979).

    b. Encourage owners, designers, and builders to develop creative approaches based on fundamental principles rather than follow prescriptive requirements that can, under certain circumstances, diminish rather than improve collapse performance.

2. Moderate Seismic Hazard

    a. Design event return periods are much longer than most high seismic regions (Bell and Lamontagne, 2002).

    b. Variability of possible earthquake magnitudes is higher than in most high seismic regions (Hines et al., 2009).

    c. Spectral acceleration values are generally higher than model codes in the low period range, and lower than model codes in the high period range (Leyendecker et al., 2000).

    d. Ground motions propagated through specific soil columns may produce response spectra that differ significantly from code prescribed values (Sorabella 2006, Appel 2008).

3. Low-Ductility Systems

    a. Member design of lateral force resisting systems (LFRSs) is often governed by wind forces and stiffness considerations.

    b. Potential variations in capacity of low-ductility systems are higher than variations in high-ductility systems.

    c. Taller buildings and moment frame structures often perform in the elastic range, even under ground motions whose spectral accelerations are more than twice the levels prescribed by model codes.

    d. Most buildings contain substantially more gravity framing than assigned directly to the primary LFRS. This gravity framing may be harnessed effectively and economically as a reserve system.

    e. Small amounts of ductility in the primary or reserve LFRS can increase collapse capacity substantially.

A design philosophy for low-ductility structures in moderate-seismic regions should draw not only on concepts of strength and ductility, but also elastic flexibility and reserve capacity to address the needs of individual structures. For instance, ordinary moment resisting frames (OMRFs) owe much of their robust behavior in moderate seismic regions to their elastic flexibility (Nelson, 2007). Collapse of low-ductility braced frames can be prevented by providing a flexible reserve system that is activated after brace fracture (Hines and Appel, 2007). Eccentric braced frames with longer links are well-suited to achieve moderate levels of ductility in the primary LFRS while allowing greater flexibility for coordination with architectural openings (Engelhardt and Popov, 1989). This paper focuses explicitly on low-ductility chevron braced steel frames and the consequences of enhancing their reserve capacity.

Results presented in this paper show that moment connecting a portion of the gravity framing for a building braced with chevron concentric-braced frames (CBFs) can increase collapse capacity substantially. Such reserve systems would require little to no increase in tonnage, and they would allow reductions in seismic story shear and overturning forces on the primary LFRS. This has the potential to reduce foundation costs. The reserve systems discussed in this paper provide stability primarily through their elastic flexibility and secondarily through their ductility. Overall, ductility demand on these reserve systems was observed to be very low, in the range of OMRFs. While moment connections do carry additional cost, this cost is typically lower than the cost of increased tonnage associated with moment frames as primary LFRS (as much as four times the tonnage of a CBF for equivalent stiffness). A hypothesis resulting from this study is that reserve systems for CBFs can be designed with OMRF connections and without consideration of either strong-column/weak-beam behavior or strong panel zone behavior. The force levels to which such reserve systems should be designed is beyond the scope of this introductory paper and should be the subject of future discussion.

The concept of a reserve system is well established in other contexts, such as higher ductility dual systems; the ASCE 7 general provision for redundancy, requiring stability of the lateral system even if an individual member is compromised; and the $R = 3$ concept itself. $R = 3$ clearly implies that the damaged primary system, gravity framing, façade and nonstructural components of a building possesses sufficient reserve capacity to prevent collapse under earthquake forces in an acceptable number of cases. The $R = 3$ criterion also implies that a response modification factor of 3 ensures the appropriate design force level for a given primary LFRS. Following a historical description of how this issue came to light in Boston, this study compares the effectiveness of primary LFRS strength versus reserve LFRS strength in improving collapse prevention performance.

HISTORICAL MOTIVATION FOR A CASE STUDY OF CHEVRON BRACED STEEL FRAMES IN BOSTON

The poor inelastic system performance of concentric chevron braced frames has been clearly demonstrated and discussed for decades, mostly in context of high seismic demands (Anderson, 1975; SEAONC, 1982; Shibata and Wakabayashi, 1983a, 1983b; Uang and Bertero, 1986; Khatib et al., 1988; Nakashima and Wakabayashi, 1992; Tremblay and Robert, 2000, 2001; Tremblay, 2001; Kim and Choi, 2004). From other structural design perspectives, however, chevron braced frames can be very attractive. Like most braced frames, they have a very high stiffness-to-weight ratio. They are generally symmetric, and they accommodate a variety of architectural openings. They are also statically determinate and assume gravity loads only from the floor which they support. These attractive attributes contrast starkly against their potentially poor seismic performance. Thus, they are interesting candidates for study in moderate seismic regions where the building community generally considers seismic concerns secondary to more conventional structural design concerns such as architectural coordination, stiffness and cost.

Historical aspects of the Massachusetts State Building Code make the Boston area particularly appropriate for this discussion of strength, ductility and reserve capacity. Since the 1970s, engineers, seismologists and public officials have worked to prepare Boston and other cities in Massachusetts for a destructive seismic event similar to the 1755 Cape Ann Earthquake. The success of these previous efforts, drawing heavily from the Seismic Design Decision Analysis project at MIT, was evidenced both in the creation and adoption of the "first seismic criteria developed specifically for a jurisdiction in the eastern United States" (Luft and Simpson, 1979) and in the Hazus Pilot Study conducted for Boston in the late 1990s (EQE, 1997). Luft and Simpson summarized the philosophical conclusions of this work as follows:

> The primary finding of these studies was that the probable maximum earthquake intensities for Massachusetts are as large as those for Zone 3 regions in California, but have much longer return periods. Because of the long return periods for destructive earthquakes, it was found that the cost to society of the earthquake-resistant design is considerably greater than the projected savings in damage and loss of life due to an earthquake. Nevertheless, the committee felt that society would insist on reasonable measures to mitigate the number of casualties from a major seismic event. It was therefore considered necessary to develop a set of criteria which would minimize the projected loss of life resulting from such an event, without causing construction costs to increase by an unacceptable amount. (p. 1)

These conclusions distinguished seismic design philosophy in Massachusetts from the contemporary SEAOC provisions for California by placing exclusive emphasis on protection against loss of life in an extreme event and ignoring the need to minimize the cost of damage in minor and moderate earthquakes (SEAOC, 1974).

Thirty years later, the philosophy described by Luft and Simpson remains valid for moderate seismic regions, where most building owners and occupants are unlikely to experience a major seismic event during their lifetime. In the meantime, however, this philosophy has experienced an interesting historical twist that deserves new attention. In the 1970s it was clear to the Massachusetts seismic committee that the least costly way to protect new building stock was to require design and detailing at an acceptable level of ductility. In light of seismic provisions issued since the 1990s to protect chevron braced frames in high seismic regions, however, it has become clear that the alternative $R = 3$ approach in SDC A, B and C results in chevron braced steel frames that are less expensive than the ordinary concentrically braced frame (OCBF) criteria listed in any edition of the AISC *Seismic Provisions*. This comparison came to light in Massachusetts because the sixth edition of the Massachusetts State Building Code required the 1992 AISC *Seismic Provisions* to apply to Seismic Design Category C (Massachusetts, 1996).

The contrast between $R = 3$ and the OCBF is demonstrated most clearly with the 2002 and 2005 AISC *Seismic Provisions* (AISC, 2002, 2005b). For instance, Section 14.2 of the 2002 *Provisions* required an overstrength factor of $\Omega = 2.0$ to be applied to all members and connections in an OCBF where $R = 5$, with the exception that brace connections should be designed for the expected tensile strength $R_y F_y A_g$ of the braces. The effective R-factor for such a frame was thus 2.5, less than 3.0. Coupling these higher forces with the more stringent connection requirements, the 2002 OCBF design was clearly more expensive than an $R = 3$ design.

In order to demonstrate this difference in detail, Gryniuk and Hines (2004) developed $R = 3$ and 2002 AISC OCBF designs for an eight-story student residence facility at the Wentworth Institute of Technology in Boston. These two designs were submitted to several fabricators for comparative pricing. Representative values from this study, demonstrating an 82% increase in lateral system cost, are reported in Table 1.

Similarly, simple calculations for a nine-story OCBF according to the 2005 AISC *Seismic Provisions* estimated a 70% increase in brace, beam and column tonnage over a comparable $R = 3$ design. The R-factor related to the 2005 OCBF was reduced from 5 to 3.25 in accordance with model code revisions, and the amplification of member forces was eliminated, making the OCBF member forces approximately 8% lower than the $R = 3$ design. The *b/t* requirement for hollow structural sections (HSS) and the capacity design requirements for columns and beams in a chevron configuration, however, kept the weight of the system significantly higher. Thus, it has become clear that, for the chevron CBF

Table 1. 2004 Cost Comparison of R = 3 and R = 5 Chevron Concentrically Braced Steel Frames According to the 2002 *AISC Seismic Provisions*			
	Lateral System		
(1)	R = 3 (2)	OCBF 2002 (3)	OCBF %Inc (4)
Tons	73.38	154.75	110%
Material	$52,942	$115,803	119%
Freight	$8,219	$17,239	110%
Drafting	$53,029	$67,817	28%
Shop	$160,740	$354,780	121%
Erection	$120,100	$164,500	37%
Total	$395,030	$720,139	82%
Bms., Cols., Brcs.	248 pcs.	248 pcs.	
Draft Hrs.	920	1119	22%
Shop Hrs.	2679	5913	121%

configuration, an R = 3 design is more attractive than an OCBF with respect to construction cost and design effort in SDC A, B and C. This does not necessarily mean that an R = 3 chevron CBF design will safely conform to the seismic design philosophy for moderate seismic regions summarized by Luft and Simpson in 1979. Rather, it legitimates the question as to whether increased ductility is really the most economical approach to ensuring collapse resistance in moderate seismic regions.

DESIGN AND MODELING OF BRACED FRAME BUILDINGS

Chevron braced frames were designed for 3-, 6-, 9- and 12-story building configurations. For each configuration, separate designs were developed assuming R = 2 (R2), R = 3 (R3) and R = 4 (R4) with no seismic detailing, but accounting for some lateral capacity in the gravity system. The 12-story/R4 design was not included in this study since it resulted in smaller design forces than required by wind loads. A fourth design was developed for each configuration as a low-ductility dual system, with a primary braced frame system designed to resist wind only, and a relatively light moment frame reserve system (referred to here as a wind plus reserve system or WRS). OCBF designs according to the AISC seismic provisions were not included because the focus of this study was on chevron CBF R = 3 systems and their reliance on reserve capacity. Each of the 15 designs assumed the plan geometry of the SAC 9-story building (SAC, 2000b), with two braced frames per side. Consistent with the SAC 9-story building, each configuration assumed a first-story height of 18 ft, with 13-ft story heights above. See Figure 1 for a plan view and typical bracing elevations for the R2, R3 and R4 designs.

The frames were designed for Boston, Massachusetts in accordance with IBC 2006 and ASCE 7-05 using Load Resistance Factor Design (LRFD). The wind loads were determined using Exposure B. The seismic loads were determined using Site Class D and Seismic Design Category B, assuming no increase to the fundamental period as allowed by Section 12.8.2 of ASCE 7-05. Figure 2 plots

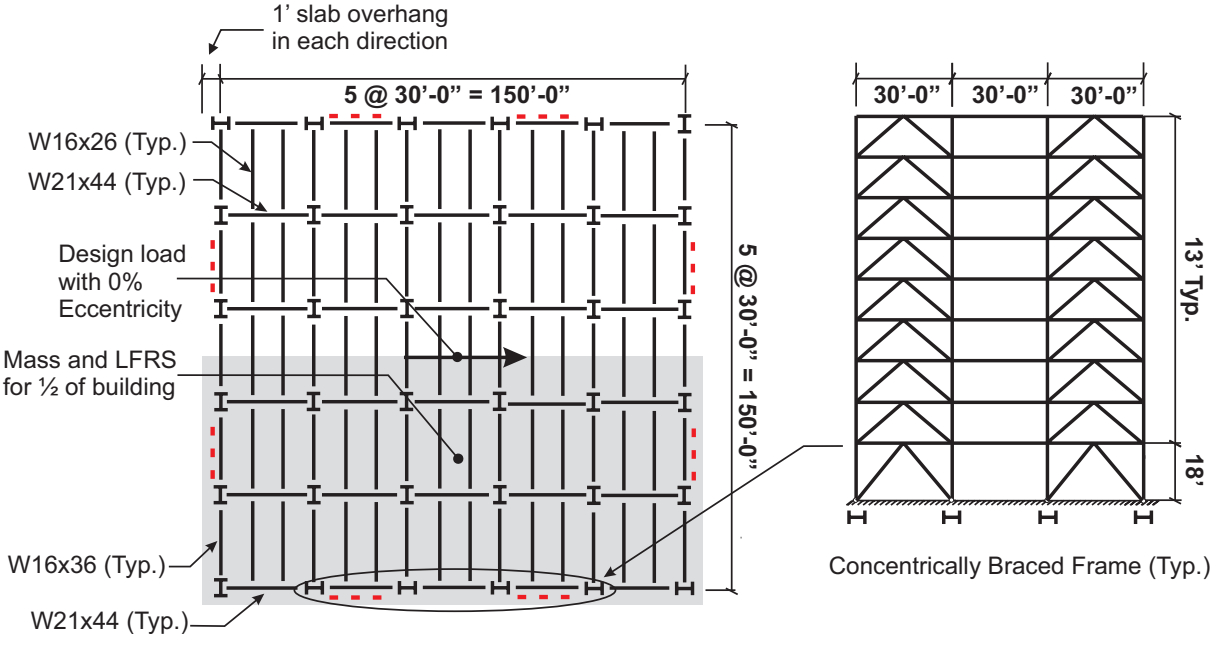

Fig. 1. R3 Plan view and 9-story braced frame elevation.

Table 2. R3 Design Member Sizes						
Story (1)		Brace (2)	Girder (3)	Column (4)	Int. Grav. Col. (5)	Corner Col. (6)
3 Story 0.099(W)	R		W21x44			
	3	HSS 6x6x¼	W21x44	W12x40	W12x40	W12x40
	2	HSS 7x7x¼	W21x44	W12x40	W12x40	W12x40
	1	HSS 8x8x¼		W12x53	W12x53	W12x53
6 Story 0.066(W)	R		W21x44			
	6	HSS 6x6x¼	W21x44	W12x40	W12x40	W12x40
	5	HSS 6x6x¼	W21x44	W12x40	W12x40	W12x40
	4	HSS 7x7x¼	W21x44	W12x53	W12x53	W12x40
	3	HSS 8x8x¼	W21x44	W12x53	W12x53	W12x40
	2	HSS 8x8x¼	W21x44	W12x87	W12x87	W12x53
	1	HSS 8x8x5/16		W12x87	W12x87	W12x53
9 Story 0.050(W)	R		W21x44			
	9	HSS 6x6x¼	W21x44	W12x40	W12x50	W12x40
	8	HSS 6x6x¼	W21x44	W12x40	W12x50	W12x40
	7	HSS 7x7x¼	W21x44	W12x40	W12x50	W12x40
	6	HSS 7x7x¼	W21x44	W12x72	W12x72	W12x40
	5	HSS 8x8x¼	W21x44	W12x72	W12x72	W12x40
	4	HSS 8x8x¼	W21x44	W12x87	W12x87	W12x45
	3	HSS 8x8x¼	W21x44	W12x87	W12x87	W12x45
	2	HSS 8x8x¼	W21x44	W12x152	W12x136	W12x72
	1	HSS 9x9x5/16		W12x152	W12x136	W12x72
12 Story Design Base Shear = 0.040(W)	R		W21x44			
	12	HSS 5x5x¼	W21x44	W14x48	W14x48	W14x48
	11	HSS 6x6x¼	W21x44	W14x48	W14x48	W14x48
	10	HSS 7x7x¼	W21x44	W14x53	W14x61	W14x48
	9	HSS 7x7x¼	W21x44	W14x53	W14x61	W14x48
	8	HSS 7x7x¼	W21x44	W14x74	W14x82	W14x48
	7	HSS 8x8x¼	W21x44	W14x74	W14x82	W14x48
	6	HSS 8x8x¼	W21x44	W14x109	W14x109	W14x53
	5	HSS 8x8x¼	W21x44	W14x109	W14x109	W14x53
	4	HSS 8x8x¼	W21x44	W14x120	W14x109	W14x61
	3	HSS 8x8x5/16	W21x44	W14x120	W14x109	W14x61
	2	HSS 8x8x5/16	W21x44	W14x176	W14x145	W14x82
	1	HSS 9x9x5/16		W14x176	W14x145	W14x82

approximate base shear versus story height for wind and R3 earthquake loads according to these assumptions for buildings up to 18 stories. The close proximity of design earthquake and wind forces in this graph demonstrates the common experience in moderate seismic regions that wind can control member design, while seismic requirements control detailing. This is seldom the case in high seismic regions. Figure 2 also shows that the threshold at which wind forces control a design can vary depending on LRFD and Allowable Strength Design (ASD) approaches. For buildings that are not square, wind forces in the short direction control at lower heights.

Table 2 lists the member sizes for each R3 design. Brace sizes are listed in Column (2). All braces were designed as square HSS, slotted and field welded to gusset plates, as shown in Figure 3. All braces were selected to have a minimum thickness of ¼ in. Column (3) in Table 2 lists the braced frame girders. Column (4) lists the braced frame columns, designed to carry both gravity loads and overturning forces. Column (5) lists the interior gravity frame columns, and Column (6) lists corner columns, designed to carry gravity loads only. All beams and girders were designed assuming full composite action. The girders spanning between gravity frame columns were designed as W21×44s for vibration control. Spandrel girders were designed as W21×44s to meet deflection requirements. Although the gravity system was not designed explicitly for lateral loads, its lateral capacity was considered in the two dimensional (2D) analysis of the buildings by allowing these members to reach $0.20M_p$ with an elastic stiffness of $0.50EI$, based on a simplified interpretation of test results reported by Liu and Astaneh (2000). Gravity frame beams were designed as W16×26s and spandrel beams were designed as W16×36s, however, these beams were not modeled since the analyses assumed 2D seismic forces parallel to the girders.

Accounting for the expected yield strength and expected end fixity of the tube braces, the frame designs resulted in connections that fractured before the braces buckled. For this reason, brace buckling hysteresis and fracture life were not modeled. Instead the analytical model assumed elastic brace behavior up to fracture with little to no brace capacity thereafter (see Appendix). Table 3 compares the expected brace strength to the connection capacity for each R3 design. As a matter of convention, the R2, R4 and WRS designs were also assumed to experience connection fracture prior to brace buckling for all cases. Column (2) in Table 3 lists the computed LRFD axial brace force using ASCE 7-05 load combinations. Column (3) lists HSS members selected for an unbraced length between work points assuming an effective length factor for the brace of $K = 1.0$. The expected buckling strength of the braces [Column (4)] was calculated assuming an expected yield strength of R_yF_y = (1.3)(46 ksi) = 60 ksi, and using an effective length factor of $K = 0.7$. Column (5) lists the weld size used, representing one of four welds used for the connection shown in Figure 3.

Weld lengths were assumed to be at least the width of the HSS, consistent with requirements for plates in section J2.2b in the AISC *Specification* (AISC, 2005a) and similar recommendations extended to HSS in the AISC *Hollow Structural Section Connection Manual* (AISC, 1997b). Column (6) in Table 3 lists the assumed fracture capacity of the four welds listed in Column (5). For example the 3-story/R3 third story weld size listed in Column (5) is calculated as (0.6)(70 ksi)(3⁄16 in.)(0.707)(4)(6 in.) = 134 kips.

The wind plus reserve system (WRS) was designed with a primary chevron braced frame to resist wind only and two three-bay moment frames in each direction. See Figure 4 for the locations of the braced frames and moment frames, and see Table 4 for typical member sizes of the WRS designs. In order to change as few members as possible in the analytical model, the moment frames were constructed by moment connecting the existing spandrel girders in the braced frame. This "design" should be understood in diagrammatic and analytical terms only. In an actual building, complications might arise from attempting to moment connect large gusset plate connections without prequalified detailing. From an analytical point of view, imagining the new moment connections outside of the existing gravity framing system allowed the gravity beam contributions to remain identical between the two models. This study emphasized analytical comparisons of strength variations in primary and reserve LFRS, not the detailed implementation of an actual reserve system.

For the WRS design, the size of the braced frame columns was increased slightly to carry additional bending moments and to avoid extremely weak panel zones. The braced frame

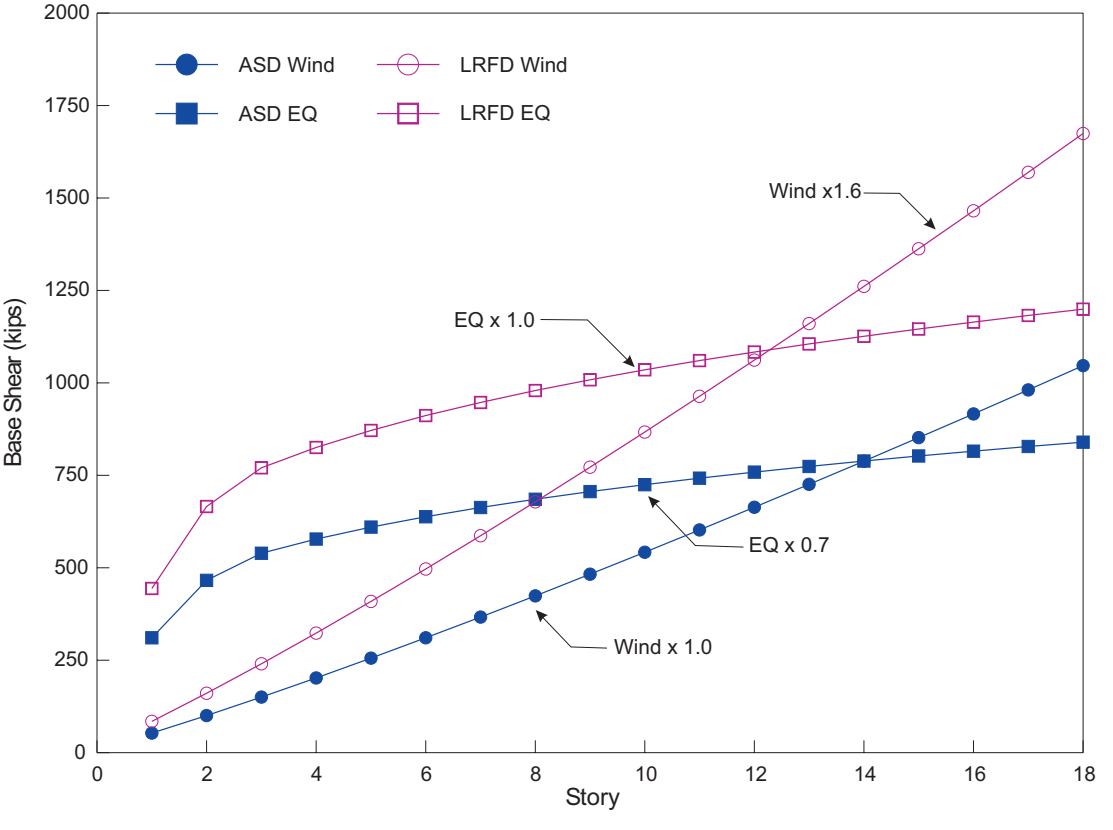

Fig. 2. R3 seismic and wind base shears with respect to story height.

Table 3. R3 Design Brace Sizes and Connection Forces

Story (1)		Design Load (2)	Brace (3)	Expected Strength (4)	Weld (×4) (5)	Weld Capacity (6)
3 Story	3	81 k	6x6x¼	201 k	3⁄16"x6"	134 k
	2	121 k	7x7x¼	268 k	¼"x7"	208 k
	1	158 k	8x8x¼	302 k	¼"x8"	238 k
6 Story	6	63 k	6x6x¼	201 k	3⁄16"x6"	134 k
	5	99 k	6x6x¼	201 k	3⁄16"x6"	134 k
	4	125 k	7x7x¼	268 k	¼"x7"	208 k
	3	153 k	8x8x¼	332 k	¼"x8"	238 k
	2	167 k	8x8x¼	332 k	¼"x8"	238 k
	1	197 k	8x8x5⁄16	371 k	¼"x9"	267 k
9 Story	9	62 k	6x6x¼	201 k	3⁄16"x6"	134 k
	8	95 k	6x6x¼	201 k	3⁄16"x6"	134 k
	7	119 k	7x7x¼	268 k	¼"x7"	208 k
	6	140 k	7x7x¼	268 k	¼"x7"	208 k
	5	158 k	8x8x¼	332 k	¼"x8"	238 k
	4	172 k	8x8x¼	332 k	¼"x8"	238 k
	3	182 k	8x8x¼	332 k	¼"x9"	267 k
	2	189 k	8x8x¼	332 k	¼"x9"	267 k
	1	218 k	9x9x5⁄16	453 k	¼"x10"	297 k
12 Story	12	57 k	5x5x¼	134 k	3⁄16"x5"	111 k
	11	87 k	6x6x¼	201 k	3⁄16"x6"	134 k
	10	110 k	7x7x¼	268 k	3⁄16"x7"	156 k
	9	130 k	7x7x¼	268 k	¼"x7"	208 k
	8	148 k	7x7x¼	268 k	¼"x7"	208 k
	7	163 k	8x8x¼	332 k	¼"x8"	238 k
	6	176 k	8x8x¼	332 k	¼"x8"	238 k
	5	186 k	8x8x¼	332 k	¼"x9"	267 k
	4	194 k	8x8x¼	332 k	¼"x9"	267 k
	3	200 k	8x8x5⁄16	409 k	¼"x9"	267 k
	2	204 k	8x8x5⁄16	409 k	5⁄16"x8"	297 k
	1	233 k	9x9x5⁄16	453 k	5⁄16"x9"	334 k

Table 4. WRS Design Member Sizes

Story (1)		Brace (2)	Girder (3)	Column (4)	Panel Zone Reduction (5)
3 Story	R		W21x44		$0.29M_p$
	3	HSS 5x5x¼	W21x44	W12x40	$0.29M_p$
	2	HSS 5x5x¼	W21x44	W12x40	$0.43M_p$
	1	HSS 6x6x¼		W12x72	
6 Story	R		W21x44		$0.29M_p$
	6	HSS 5x5x¼	W21x44	W12x40	$0.29M_p$
	5	HSS 5x5x¼	W21x44	W12x40	$0.37M_p$
	4	HSS 5x5x¼	W21x44	W12x50	$0.37M_p$
	3	HSS 6x6x¼	W21x44	W12x50	$0.57M_p$
	2	HSS 6x6x¼	W21x44	W12x96	$0.57M_p$
	1	HSS 7x7x¼		W12x96	
9 Story	R		W21x44		$0.34M_p$
	9	HSS 5x5x¼	W21x44	W12x53	$0.34M_p$
	8	HSS 5x5x¼	W21x44	W12x53	$0.34M_p$
	7	HSS 6x6x¼	W21x44	W12x53	$0.43M_p$
	6	HSS 6x6x¼	W21x44	W12x72	$0.43M_p$
	5	HSS 6x6x¼	W21x44	W12x72	$0.52M_p$
	4	HSS 7x7x¼	W21x44	W12x87	$0.52M_p$
	3	HSS 7x7x¼	W21x44	W12x87	$0.97M_p$
	2	HSS 7x7x¼	W21x50	W12x152	$0.84M_p$
	1	HSS 8x8x¼		W12x152	
12 Story	R		W21x44		$0.38M_p$
	12	HSS 5x5x¼	W21x44	W14x48	$0.38M_p$
	11	HSS 5x5x¼	W21x44	W14x48	$0.42M_p$
	10	HSS 6x6x¼	W21x44	W14x61	$0.42M_p$
	9	HSS 6x6x¼	W21x44	W14x61	$0.61M_p$
	8	HSS 6x6x¼	W21x44	W14x109	$0.61M_p$
	7	HSS 7x7x¼	W21x44	W14x109	$0.61M_p$
	6	HSS 7x7x¼	W21x44	W14x109	$0.61M_p$
	5	HSS 7x7x¼	W21x44	W14x109	$0.81M_p$
	4	HSS 8x8x¼	W21x44	W14x120	$0.81M_p$
	3	HSS 8x8x¼	W21x50	W14x120	$0.89M_p$
	2	HSS 8x8x¼	W21x62	W14x176	$0.67M_p$
	1	HSS 9x9x5⁄16		W14x176	

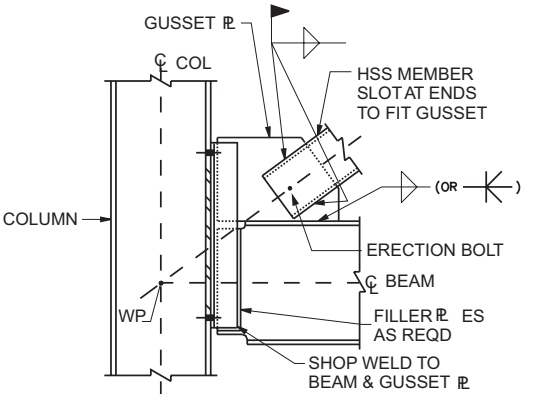

Fig. 3. Gusset plate connections. Note, the connection does not conform to the 2t brace-to-gusset plate requirement Fig. C-I-13.2 (AISC,2005b).

columns were initially designed to carry the gravity loads plus the overturning from wind only. They were then enhanced to withstand 0.01*g* acceleration, consistent with the minimum seismic force specified in Section 12.8.1.1 of ASCE 7-05. This load was distributed as an inverted triangle, assuming all braces had fractured and assuming no consideration for panel zone capacity. Since panel zone capacity ultimately controlled the strength of these reserve moment frames, beam yield strengths were reduced for analysis to the values listed in Column (5) of Table 4. In the taller configurations, the member size of the second-story braced/moment frame girder was increased for additional capacity. In addition to the reserve system, the WRS models were constructed to account for gravity framing reserve capacity in the same way as the R2, R3 and R4 designs. Furthermore, one line of gravity columns was rotated to act in the strong direction.

Table 5. Design Weight Comparison					
		R2	R3	R4	WRS
3 Story	Lateral System Weight (tons)	53	44	42	44
	% Difference	22.3%	—	–3.7%	1.0%
6 Story	Lateral System Weight (tons)	107	98	93	94
	% Difference	9.3%	—	–5.1%	–4.3%
9 Story	Lateral System Weight (tons)	191	168	157	168
	% Difference	14.1%	—	–6.1%	0.3%
12 Story	Lateral System Weight (tons)	284	244	—	258
	% Difference	16.1%	—	—	5.4%

Table 5 compares the weights of the 15 lateral system designs, showing that in all cases the WRS designs are lighter than the R2 designs and very similar the to the R3 designs.

Reserve system first yield capacities of the models were assessed based on pushover analyses assuming control forces distributed as an inverted triangle and are reported in Table 6. Figure 5 shows the moment diagram for the 6-story/R3 pushover analysis. Note that the gravity framing provided enough stiffness to cause the braced frame columns to bend about their strong axis, effectively mobilizing column strength and stiffness at the first floor for columns assumed pin-connected to adjacent beams. Hence, even a modest reserve system can be expected to afford higher capacity than calculated simply according to beam yield strength.

Table 6. Reserve System First-Yield Capacities			
		R3	WRS
No. of Stories	3	58 k	113 k
	6	80 k	132 k
	9	83 k	171 k
	12	85 k	176 k

Detailed discussion of the analytical models and ground motion suite can be found in the Appendix to this paper.

ANALYTICAL RESULTS

Collapse capacities of low-ductility structural systems are particularly sensitive to variations in both ground motion and building system characteristics. Furthermore, rock motions and soil amplification characteristics can vary greatly for a given MCE scenario. For these reasons, reliability-based performance assessments, such as described in FEMA-350 (SAC, 2000a) and ATC-63 (ATC, 2008), are particularly well-suited to evaluate the collapse capacities of low-ductility systems. The Appendix to this paper includes detailed discussion of both FEMA-350 and ATC-63 approaches to collapse performance assessment and explains why the ATC-63 approach was favored for these low-ductility systems. The Appendix also describes modifications to the ATC-63 approach that were necessary for accommodating special characteristics of the Eastern North America (ENA) suite and the low-ductility systems.

This section discusses structural behavior observed during analysis of these systems. Once the braces were assumed

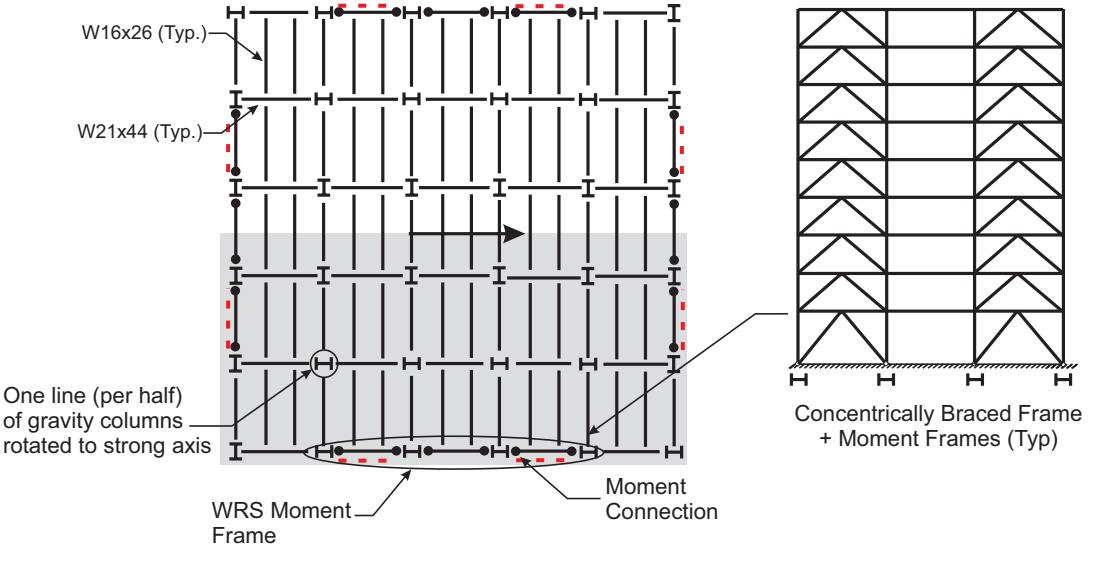

Fig. 4. WRS building plan and braced frame elevation.

to fracture, these systems experienced severe stiffness and strength discontinuities. System performance was highly dependent on ground motion characteristics. Different ground motions would fracture braces at different levels in different sequences, resulting in a variety of behaviors that are too complicated to characterize intuitively or simply. In spite of the complex behavior exhibited by these systems, however, some interesting behavioral trends did emerge out of both the analyses and the performance assessment process. Not only elastic higher mode effects, but also dynamically changing modes due to brace fracture were observed to affect collapse performance. Collapse performance was also observed to depend on building height, primary LFRS strength, and reserve LFRS strength.

Incremental dynamic analyses (IDAs) (Vamvatsikos and Cornell, 2002) were run for each of the 15 models under the 15 motions discussed in the Appendix, for a total 225 IDAs. Figure 6 shows the IDA results for the 9-story/R3 configuration. Starting at a scale factor (SF) of 1.0, the ground motion (GM) acceleration amplitudes for each IDA was scaled up

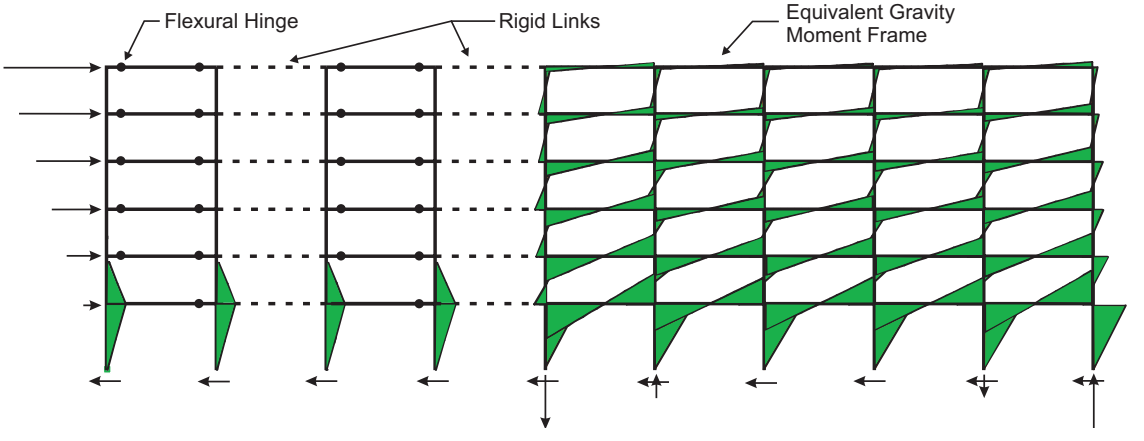

Fig. 5. Pushover analysis moment diagram for the 6-story/R3 reserve system.

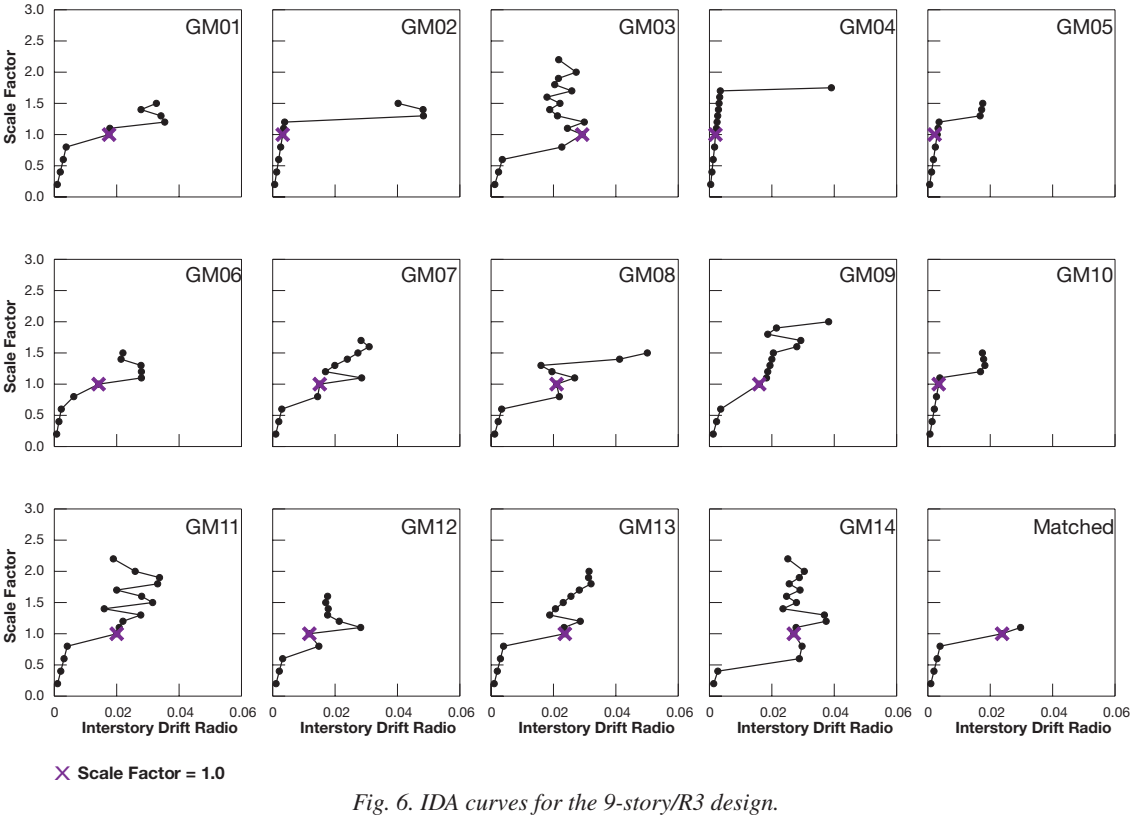

Fig. 6. IDA curves for the 9-story/R3 design.

Table 7. Collapse Table

	Design Value	Ground Motion														
		1	2	3	4	5	6	7	8	9	10	11	12	13	14	Matched
3 Story	WRS	6.8	6.8	5.8	4.5	5.0	4.5	4.5	2.8	5.4	8.0	4.5	5.8	6.0	4.5	3.0
	R4	1.2	1.9	(0.8)	1.7	1.5	1.6	2.8	2.0	2.4	(0.8)	1.6	1.8	2.4	1.0	1.2
	R3	(0.8)	1.1	(0.8)	1.3	(0.8)	1.4	3.0	1.0	1.2	1.2	1.3	(0.6)	1.4	(0.8)	(0.8)
	R2	(0.6)	2.4	1.3	1.4	1.6	1.2	1.8	1.1	(0.8)	1.7	1.7	1.7	1.5	(0.8)	1.3
6 Story	WRS	4.5	5.3	3.5	3.0	3.0	3.0	5.0	3.0	5.4	5.8	1.9	3.0	3.5	2.0	1.6
	R4	1.5	1.7	1.2	1.2	(0.6)	1.5	2.2	1.2	(0.9)	1.4	1.3	1.2	1.1	(0.8)	(0.6)
	R3	1.0	1.3	1.7	1.4	(0.8)	1.3	3.0	1.3	1.3	1.4	1.3	1.7	(0.9)	(0.4)	(0.8)
	R2	1.3	1.5	1.1	1.3	1.1	(0.8)	4.0	2.6	1.6	1.2	1.5	1.7	1.2	(0.6)	1.1
9 Story	WRS	4.5	6.0	5.0	3.5	3.5	3.0	4.5	1.8	5.8	5.2	6.0	4.0	4.5	2.6	1.2
	R4	1.2	1.9	1.3	1.5	1.3	(0.8)	1.4	1.5	1.5	1.2	3.0	1.4	1.3	1.2	(0.8)
	R3	1.5	1.5	1.5	1.7	1.5	2.2	1.8	1.5	2.0	1.5	2.2	1.6	2.0	2.2	1.1
	R2	2.6	2.6	2.8	2.6	1.4	1.5	3.0	2.2	4.0	1.7	1.4	3.5	2.0	1.4	1.3
12 Story	WRS	4.5	3.5	1.9	2.2	2.8	3.0	2.6	2.0	5.0	5.4	5.0	2.6	4.0	1.9	1.8
	R3	1.2	2.6	1.8	1.4	1.1	2.2	2.8	2.0	2.0	1.1	1.0	1.8	(0.8)	1.2	1.0
	R2	2.0	3.0	2.4	3.5	1.7	1.3	2.6	2.0	1.6	1.1	1.3	1.3	1.3	1.3	1.4

by increments of 0.1 until the model either collapsed or became numerically unstable, and it was scaled down until the model responded in the linear range. Some models required certain motions to be scaled down in order to arrive at their collapse capacity. Collapse capacity was recorded in terms of scale factor at the increment just prior to collapse. Note that incrementing SF rather than the spectral acceleration at the first natural period (S_{aT1}) was a modification to the ATC-63 process. The Appendix discusses this modification further.

Collapse capacities for each analysis are reported in Table 7, with a circle around analysis cases resulting in collapse at a scale factor of 1.0. Cases such as the 6-story/R3/GM1, with a collapse capacity of 1.0, survived the unscaled ground motion, but then collapsed when the ground motion was scaled to 1.1. Four models collapsed under the spectral matched motion, shown in Figure A-8 in the Appendix and listed in the column labeled "Matched" in Table 7. The highest IDA scale factor under this motion for the R2, R3 and R4 system designs was 1.4 for the 12-story/R2 design. IDA scale factors for the WRS designs under the matched motion ranged from 1.2 for the 9-story configuration to 3.0 for the 3- and 6-story configurations. Relatively poor performance under this motion suggests that the suite of motions used for this study should not be considered overly conservative. Furthermore, the choice of ground motions and soil amplification characteristics are essential to the collapse assessment of these systems. See the Appendix of this paper and Hines et al. (2009) for further discussion of ground motion suite selection for ENA.

The circled values in Table 7 give an immediate impression that the 3- and 6-story configurations were more vulnerable to collapse than the 9- and 12-story configurations. The 3-story/R3 model collapsed under 6 of the 15 unscaled ground motions (40%), whereas the 6-story/R3 model collapsed under 4 of the 15 unscaled ground motions (27%). The 9-story/R3 did not collapse under any unscaled ground motions and 12-story/R3 models collapsed under only one unscaled motion.

It is difficult to distinguish significant behavioral differences among the R2, R3 and R4 models for the 3- and 6-story configurations. For instance, the 3-story/R4 model

collapsed under only two motions (13%), outperforming not only the 3-story/R3, but also the 3-story/R2 (three collapses = 20%). Such an observation suggests that collapse capacity may not always increase in proportion to strength. There may even be configurations, as demonstrated here, where an R3 design produces greater vulnerability than either a stronger or a weaker design.

Table 7 demonstrates the subtle relationship between design strength and collapse vulnerability via comparison of different designs under the same motion. For the 6-story configuration, GM5 collapsed only the weaker R3 and R4 designs. On the other hand, GM6 collapsed the stronger R2 design but spared the two weaker designs. In certain cases, the survival of a weaker design next to the collapse of a stronger design under the same ground motion can be understood by examining how initial damage protected the weaker design from subsequent stronger pulses by moving the building's natural periods out of the range of these pulses. For instance, the 6-story/R4 design experienced early damage at approximately 8 seconds into GM6, as shown in Figure 7. The first story drift record in Figure 7 shows that although the R4 model reached a drift of almost 3% as a result of this damage, the model righted itself under subsequent shaking. Conversely, the R2 design easily withstood the potentially damaging pulse at 8 seconds, only to collapse under much stronger shaking at 22 seconds.

The only 9-story configurations to collapse at SF = 1.0 were the R4 design under GM6 and the Matched motion, suggesting that for the taller configurations, increased strength played a role in mitigating collapse vulnerability. The 12-story/R3 design was observed to collapse under GM13 at the tenth story, demonstrating that taller buildings can become vulnerable to higher mode effects. This observation is consistent with observations from hundreds of analyses not reported in this paper on designs with lower brace capacities at higher stories (Appel, 2008). Brace connection capacities for the designs featured in this paper were specified according to fillet weld lengths equal to or in excess of the width of the brace. Table 3 demonstrates that the expected weld capacity in Column (6) typically far exceeded the demand on the brace in Column (2). For instance, for the 9-story/R3 model, Table 3 lists the seventh-story expected weld capacity as 208 kips, 1.75 times higher than the 119 kip design demand, whereas it lists the first-story expected weld capacity as 297 kips, only 1.36 times higher than the 218 kip design demand. Previous studies on designs with expected weld capacities uniformly proportional to design brace demands yielded more collapses in the upper stories and more uniform damage to the primary system. More uniformly distributed damage in the primary LFRS could serve to increase collapse capacity provided an appropriate reserve system is in place.

For all configurations, the WRS design significantly outperformed the strength designs experiencing no collapses at a scale factor of 1.0 and reaching median scale factors above 4.0. Figures 11 through 14 clearly demonstrate the robustness of the WRS designs in comparison to their strength design counterparts. The Appendix discusses these figures in greater detail. Figures 8 through 10 compare damage and collapse behavior of the 6-story/R3 and WRS designs. Figure 8 shows that the 6-story/R3/GM5 case experienced first brace fracture at the fifth story at around 7.6 seconds, with first-story brace fracture occurring at around 19.9 seconds in the negative direction. Subsequent pulses in the positive direction also fractured a second-story brace and yielded the second-story gravity frame prior to collapsing the model at the first story. Figure 9 shows that the 6-story/WRS/GM5 case also experienced first brace fracture at higher stories close to 7.5 seconds, with first-story brace fracture at around 15.4 seconds. No yielding of the reserve system and relatively low inelastic drifts, less than 0.5%, were observed. Figure 10 shows that the 6-story/WRS/GM5×2 case experienced more pronounced inelastic behavior when the GM5 accelerations were scaled to 2.0 times their original values.

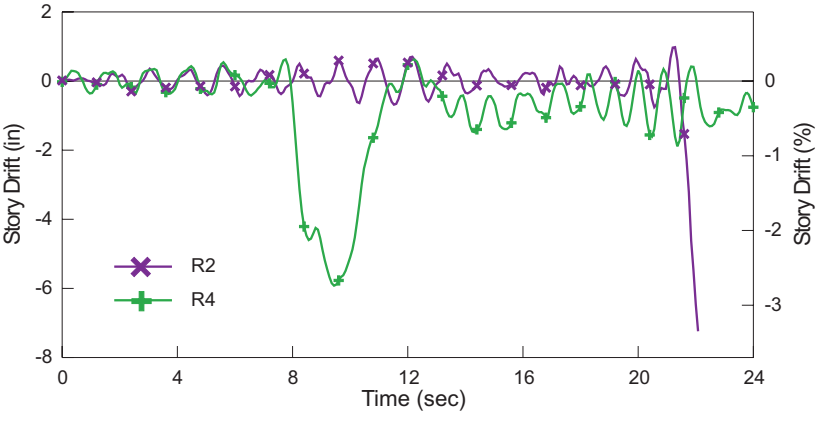

Fig.7. First-story drift for the 6-story/R2 and R4 models under GM6.

An additional brace fractured at the fifth story and reserve system beams were observed to yield at the second and fifth stories. Figure 10 demonstrates the need for some ductility in the reserve system. More ductile reserve systems allow IDAs to be scaled to higher levels. The same may also be said of stronger reserve systems, which are still significantly more flexible than the primary system. How reserve systems should be designed for strength and ductility presents itself as a major question for future research concerning low-ductility systems.

Collapse Performance Assessment

Figures 11 through 14 show not only the improvement to collapse capacity provided by the WRS designs for every configuration, but also the relative similarity between the R2, R3 and R4 designs. Note that the symbols in these figures are used to differentiate between curves. They do not represent experimental data points. For taller configurations, Figure 13 and Figure 14 demonstrate the beneficial effects of added strength, while they also show less difference between the R2 and WRS designs. Probability of collapse can be read for each design as the point where its fragility curve crosses the vertical line at an SF of 1.0. Figure 11 shows that the 3-story/R2, R3 and R4 designs appear to have collapse probabilities ranging from 30% to 48%, while the WRS design appears to have a collapse probability of less than 2%. While this study does not necessarily satisfy the further consideration required by ATC-63 for average and upper bound collapse probabilities for a set of "Index Archetype Configurations," the WRS results do generally fall under the recommended 10% threshold (ATC, 2008, p. 2-9). Figure 12 shows that the 6-story/R2, R3 and R4 designs appear to have collapse probabilities of about 40%, while the WRS curve shows a collapse probability of less than 10%. For the 9-story/R2, R3 and R4 designs, Figure 13 shows collapse probabilities ranging from 18% to 39%, while the WRS curve shows a collapse probability of 5%. Finally, Figure 14 shows collapse probabilities for the 12-story/R2 and R3 designs as 30% and 35%, while the WRS curve shows a collapse probability of 11%. While Table 7 lists only one collapse for the 12-story configuration at SF = 1.0, the WRS fragility curve in Figure 14 shows less dramatic improvement over the R2 and R3 designs. This can be explained by observing which stories collapsed at the maximum IDA increment for the various designs.

Tables 8 through 11 summarize the IDA results at the increment prior to collapse for each of the configurations. The "Scale Factor" rows in these tables present the same data as Table 7; however, these tables also list the story that collapsed and the maximum drift reached on this story at the increment before the collapse occurred. Note that the drift reported may not be the maximum drift, since it relates to

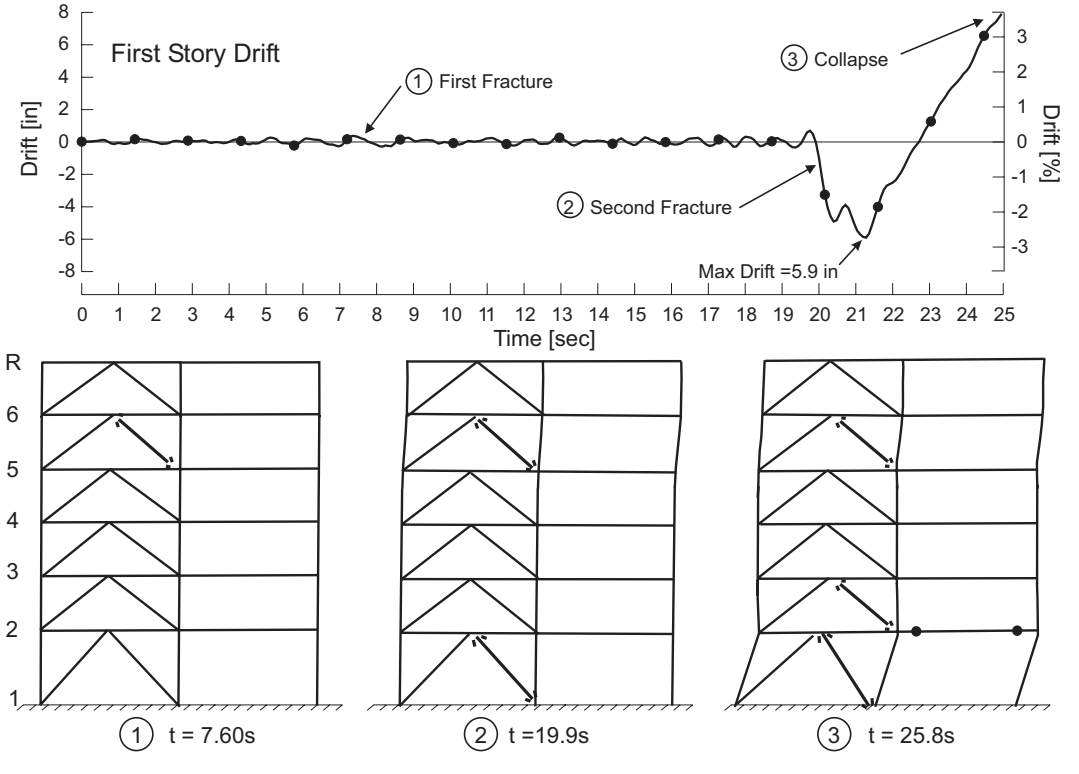

Fig. 8. Collapse behavior for 6-story/R3/GM5.

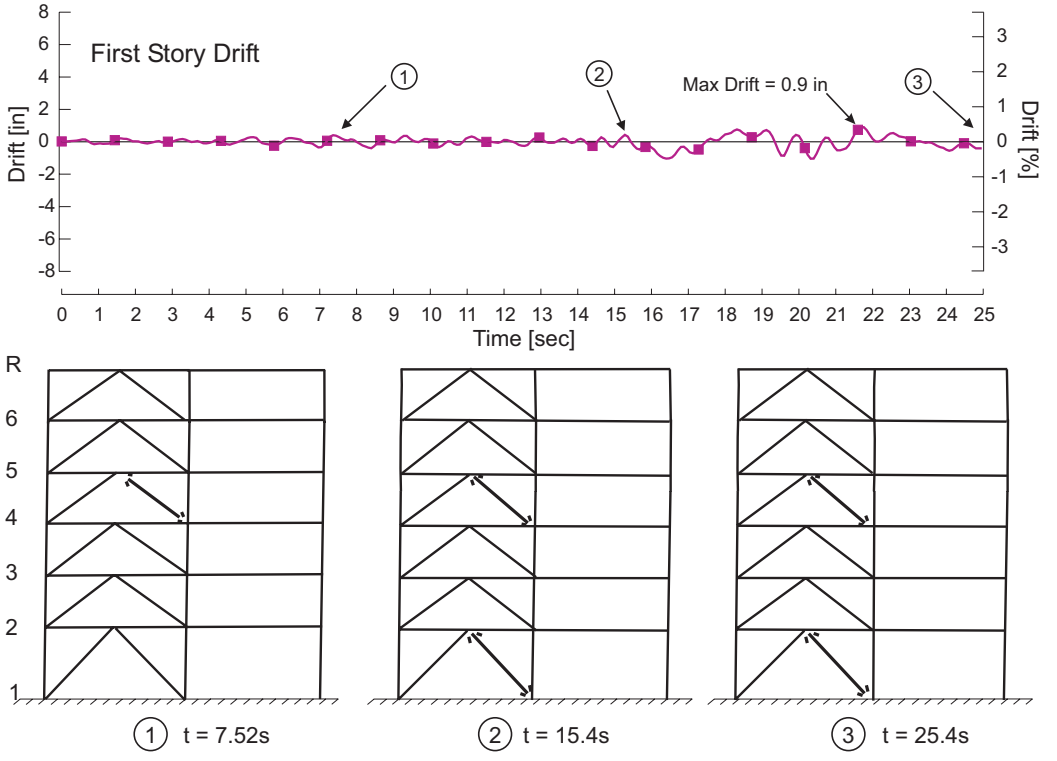

Fig. 9. Behavior for 6-story/WRS/GM5.

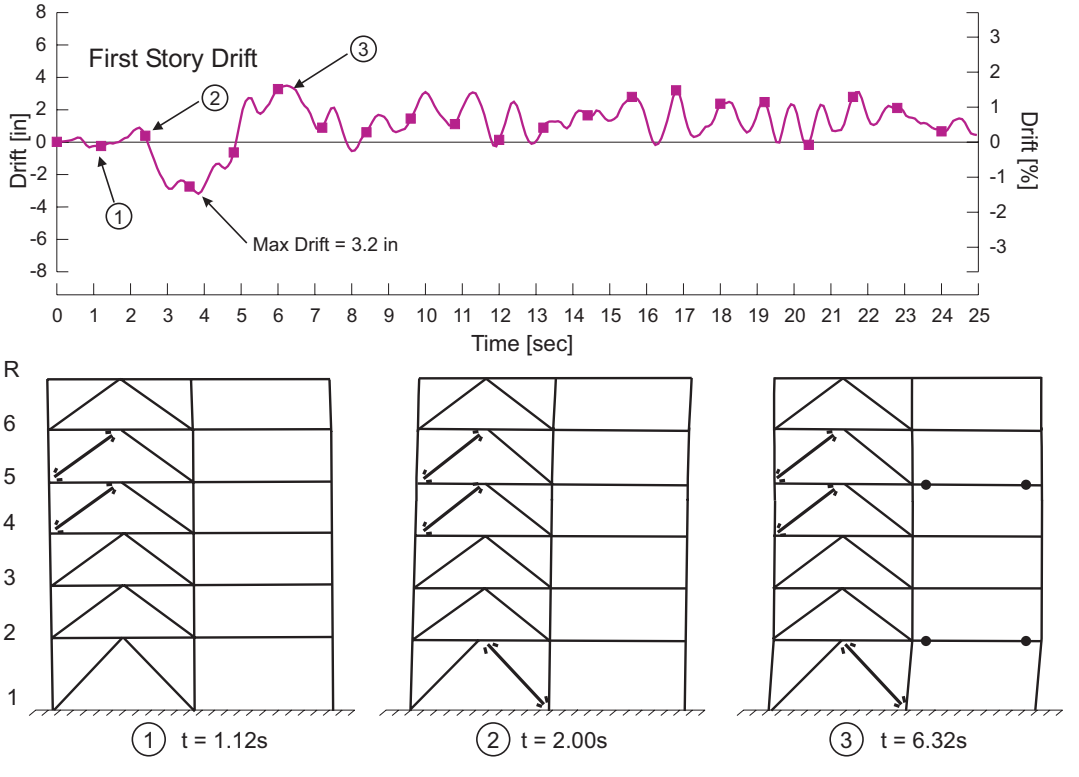

Fig. 10. Behavior for 6-story/WRS/GM5/SF = 2.0.

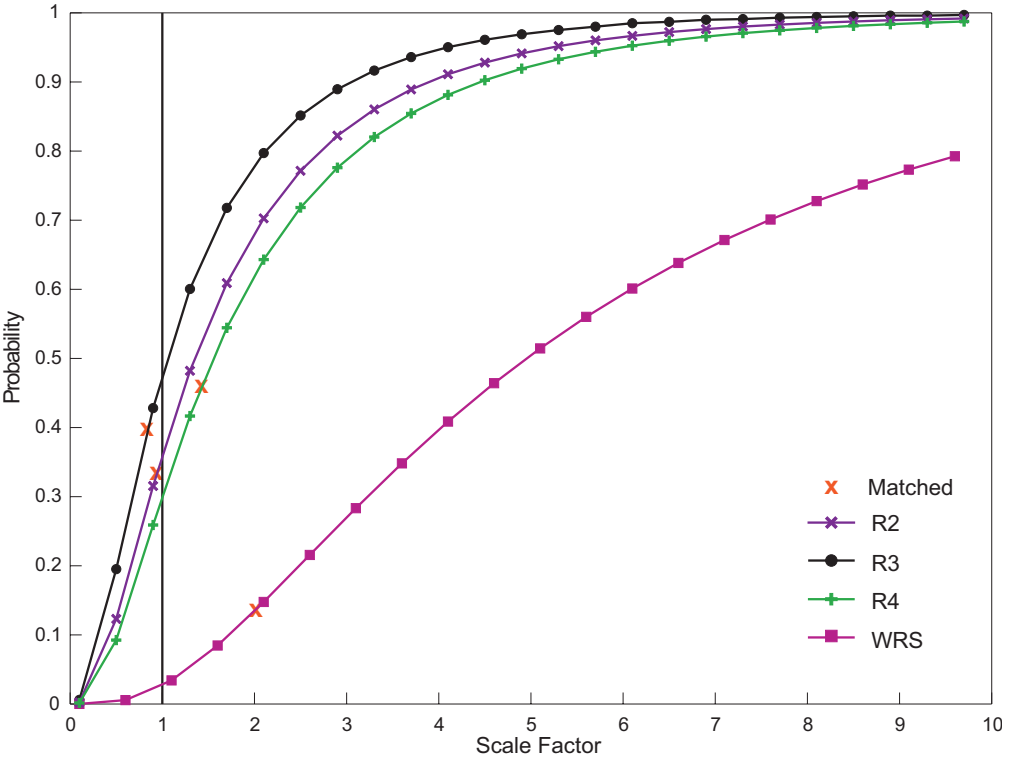

Fig. 11. 3-story fragility curves.

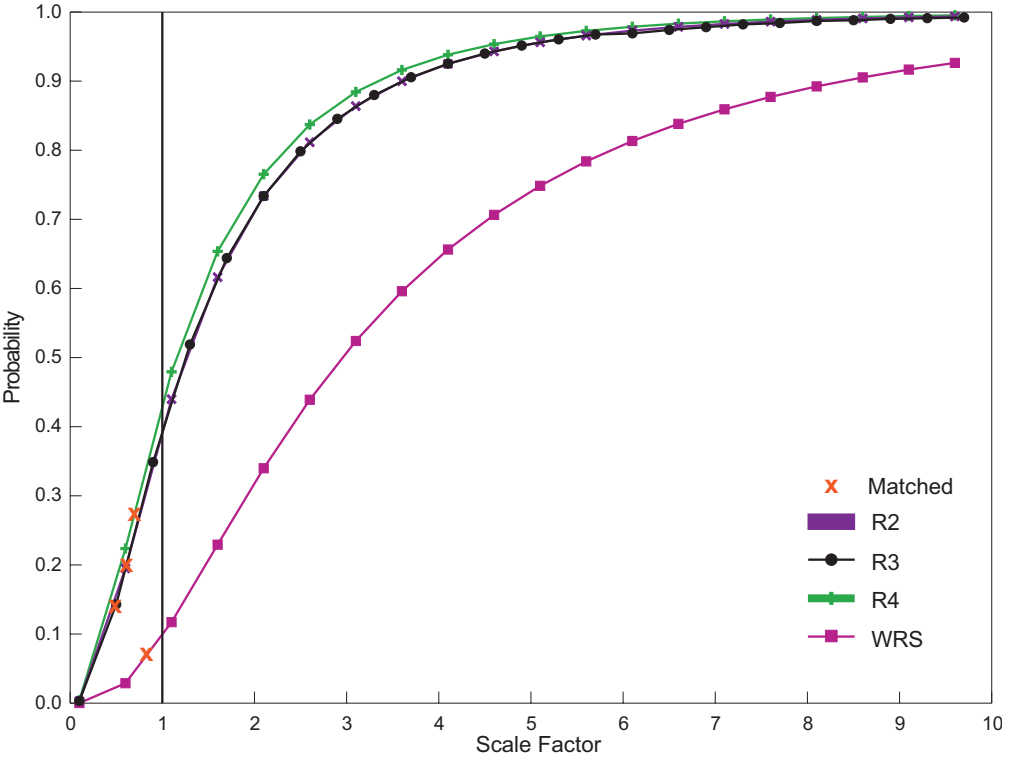

Fig. 12. 6-story fragility curves.

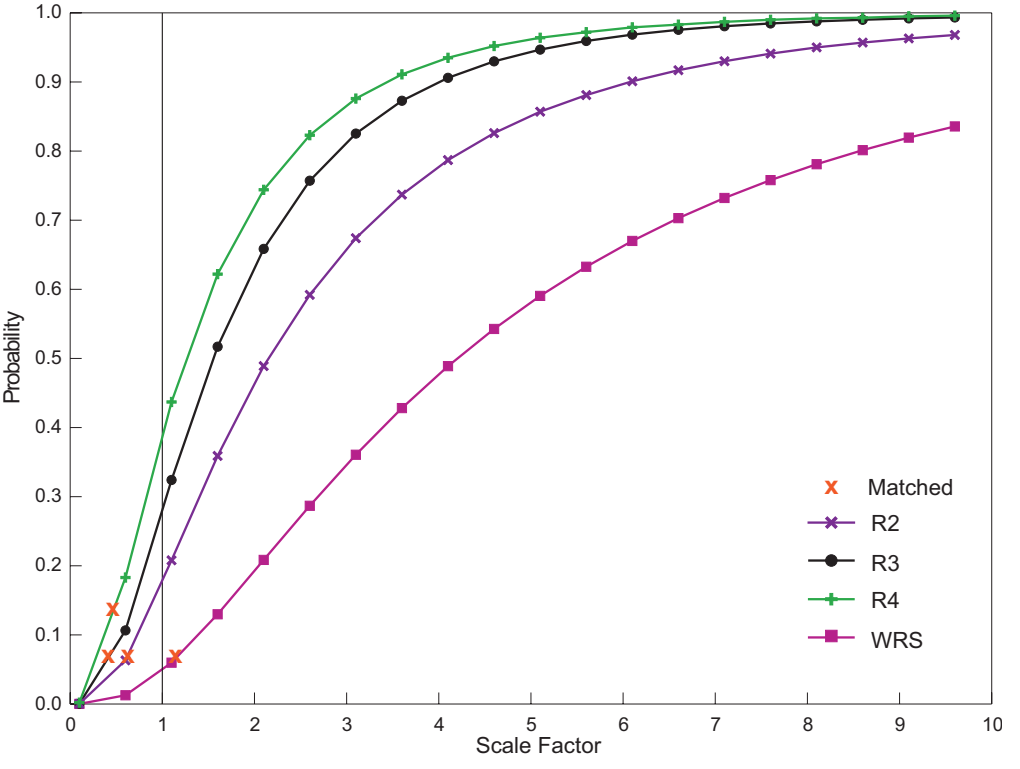

Fig. 13. 9-story fragility curves.

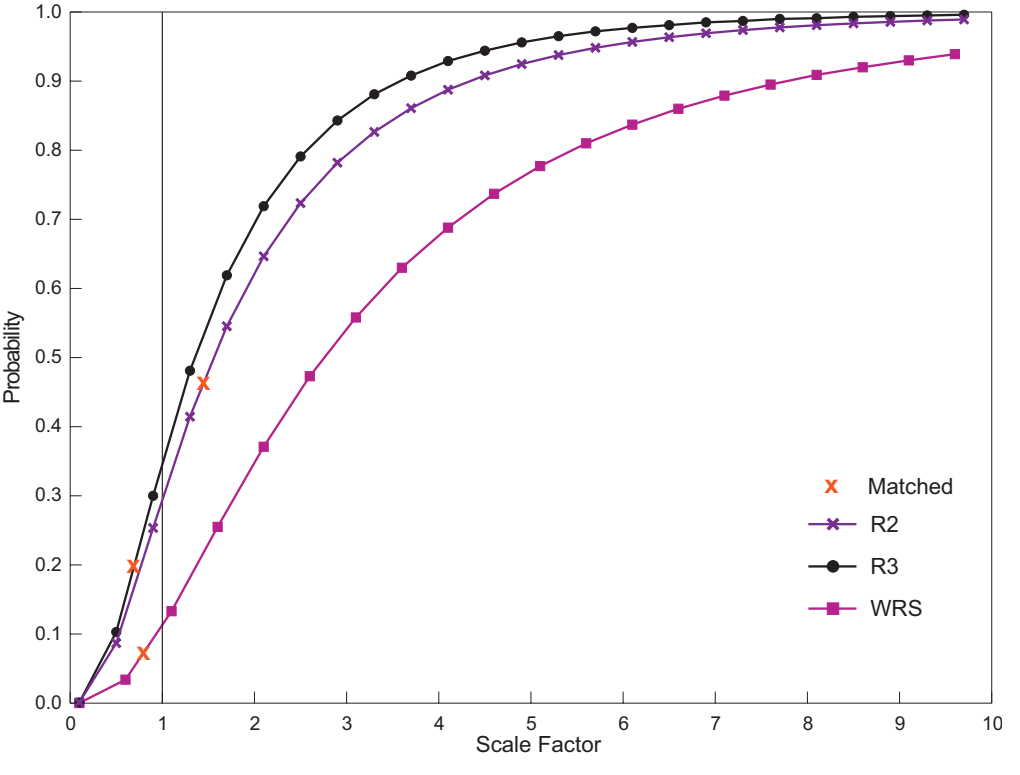

Fig. 14. 12-story fragility curves.

Table 8. 3-Story Collapse Summary

Design Value		Ground Motion														
		1	2	3	4	5	6	7	8	9	10	11	12	13	14	Matched
R2	Story	1	1	1	3	1	3	1	1	3	3	1	1	1	1	1
	Scale Factor	0.6	2.4	1.3	1.4	1.6	1.2	1.8	1.1	0.8	1.7	1.7	1.7	1.5	0.8	1.3
	Drift	.011	.055	.031	.027	.039	.027	.023	.021	.016	.029	.024	.037	.019	.038	.032
R3	Story	1	1	1	1	1	1	1	1	1	1	1	1	1	1	1
	Scale Factor	0.8	1.1	0.8	1.3	0.8	1.4	3.0	1.0	1.2	1.2	1.3	0.6	1.4	0.8	0.8
	Drift	.032	.018	.015	.027	.016	.035	.038	.028	.030	.012	.044	.026	.017	.037	.002
R4	Story	1	1	1	1	1	1	1	1	1	1	1	1	1	1	1
	Scale Factor	1.2	1.9	0.8	1.7	1.5	1.6	2.8	2.0	2.4	0.8	1.6	1.8	2.4	1.0	1.2
	Drift	.031	.019	.025	.022	.022	.027	.029	.028	.014	.021	.020	.022	.026	.036	.023
WRS	Story	1	1	1	1	1	1	1	1	1	1	1	1	1	1	1
	Scale Factor	6.8	6.8	5.8	4.5	5.0	4.5	4.5	2.8	5.4	8.0	4.5	5.8	6.0	4.5	3.0
	Drift	.037	.044	.038	.022	.042	.026	.030	.030	.018	.026	.021	.035	.043	.026	.044

Table 9. 6-Story Collapse Summary

Design Value		Ground Motion														
		1	2	3	4	5	6	7	8	9	10	11	12	13	14	Matched
R2	Story	5	1	6	1	1	4	1	1	1	4	1	1	1	1	1
	Scale Factor	1.3	1.5	1.1	1.3	1.1	0.8	4.0	2.6	1.6	1.2	1.5	1.7	1.2	0.6	1.1
	Drift	.037	.009	.013	.034	.011	.005	.031	.038	.035	.029	.030	.055	.036	.022	.005
R3	Story	5	1	1	1	1	1	1	1	1	5	1	1	1	1	1
	Scale Factor	1.0	1.3	1.7	1.4	0.8	1.3	3.0	1.3	1.3	1.4	1.3	1.7	0.9	0.4	0.8
	Drift	.023	.023	.027	.035	.023	.040	.014	.017	.028	.018	.033	.029	.012	.014	.018
R4	Story	1	1	1	1	1	5	1	1	1	1	1	1	1	1	1
	Scale Factor	1.5	1.7	1.2	1.2	0.6	1.5	2.2	1.2	0.9	1.4	1.3	1.2	1.1	0.8	0.6
	Drift	.016	.017	.017	.016	.003	.019	.026	.025	.011	.028	.018	.035	.047	.030	.003
WRS	Story	1	1	1	1	1	1	1	1	1	1	1	1	1	1	1
	Scale Factor	4.5	5.0	3.5	3.0	3.0	3.0	5.0	3.0	5.4	5.8	1.9	3.0	3.5	2.0	1.6
	Drift	.015	.023	.022	.026	.021	.024	.048	.027	.033	.022	.017	.029	.024	.021	.047

Table 10. 9-Story Collapse Summary																
Design Value		Ground Motion														
		1	2	3	4	5	6	7	8	9	10	11	12	13	14	Matched
R2	Story	8	1	1	1	8	7	1	1	1	1	9	1	8	7	1
	Scale Factor	2.6	2.6	2.8	2.6	1.4	1.5	3.0	2.2	4.0	1.7	1.4	3.5	2.0	1.4	1.3
	Drift	.057	.035	.018	.027	.031	.031	.028	.027	.030	.026	.027	.023	.026	.046	.005
R3	Story	8	1	1	1	8	1	1	1	9	1	8	8	1	1	1
	Scale Factor	1.5	1.5	1.5	1.7	1.5	2.2	1.8	1.5	2.0	1.5	2.2	1.6	2.0	2.2	1.1
	Drift	.033	.040	.022	.028	.050	.022	.039	.018	.038	.018	.019	.018	.031	.025	.030
R4	Story	7	1	1	1	7	1	1	1	1	7	1	1	1	1	1
	Scale Factor	1.2	1.9	1.3	1.5	1.3	0.8	1.4	1.5	1.5	1.2	3.0	1.4	1.3	1.2	0.8
	Drift	.027	.018	.017	.026	.018	.017	.004	.031	.022	.042	.020	.018	.018	.019	.021
WRS	Story	1	1	1	1	1	1	1	1	1	1	1	1	1	1	1
	Scale Factor	4.5	6.0	5.0	3.5	3.5	3.0	4.5	1.8	5.8	5.2	6.0	4.0	4.5	2.6	1.2
	Drift	.027	.031	.035	.036	.024	.022	.039	.030	.021	.024	.017	.034	.024	.019	.020

Table 11. 12-Story Collapse Summary																
Design Value		Ground Motion														
		1	2	3	4	5	6	7	8	9	10	11	12	13	14	Matched
R2	Story	1	9	1	1	1	12	11	11	11	11	1	11	11	1	1
	Scale Factor	2.0	3.0	2.4	3.5	1.7	1.3	2.6	2.0	1.6	1.1	1.3	1.3	1.3	1.3	1.4
	Drift	.041	.029	.019	.032	.028	.028	.028	.020	.023	.028	.043	.016	.051	.043	.029
R3	Story	11	1	11	12	1	1	1	11	1	1	1	1	10	1	11
	Scale Factor	1.2	2.6	1.8	1.4	1.1	2.2	2.8	2.0	2.0	1.1	1.0	1.8	0.8	1.2	1.0
	Drift	.022	.023	.011	.017	.027	.026	.020	.036	.021	.023	.026	.015	.017	.017	.014
WRS	Story	1	1	1	1	1	1	1	1	1	1	1	1	1	1	1
	Scale Factor	4.5	3.5	1.9	2.2	2.8	3.0	2.6	2.0	5.0	5.4	5.0	2.6	4.0	1.9	1.8
	Drift	.015	.024	.022	.017	.024	.018	.014	.032	.015	.022	.018	.018	.022	.024	.014

the story that collapsed in the next increment, and not the story with maximum drift in the increment reported. Table 11 lists all maximum IDA increment collapses on the first story for the 12-story/WRS model, whereas it lists 8 out of 15 collapses at higher stories for the R2 design and 6 out of 15 collapses at higher stories for the R3 design. The WRS design still outperformed both R2 and R3 designs, and effectively prevented collapses at upper stories due to higher mode effects. The strength and stiffness of the WRS reserve system were, however, insufficient to allow IDA amplification levels similar to shorter buildings. This can be explained by the large P–Δ effects at the first story under the heavy weight of the 12-story structure. Even though shear forces between the first and second stories were lower in proportion to total weight for the 12-story configurations, lack of fixity at the column bases and increased story height made the reserve system more vulnerable to P–Δ effects and less able to handle amplified forces and deformations after brace fracture. In fact, Tables 8 through 11 list all IDA maximum increment collapses for the WRS on the first story, demonstrating that this problem of a soft story in the reserve system ultimately proved to limit all of the WRS designs. For taller configurations, the problem became more pronounced due to higher gravity loads. Such a result makes intuitive sense, and is certainly familiar from experience with more ductile systems in high seismic regions. This result leads to three questions about reserve systems that should direct further investigation:

1. For taller structures, how effective are primary system strength and reserve system strength and stiffness at the lower stories in preventing collapse?

2. Performance of reserve systems for individual structures can be improved by tuning based on nonlinear dynamic analysis, but can simpler, more realistic tuning methods be developed?

3. Would it be advantageous not to specify minimum weld requirements for upper story braces?

The third question arises out of previous work where model brace fracture capacities were based on brace design forces, rather than on minimum weld lengths. These analyses allowed more uniform damage throughout the structure and concentrated more maximum increment IDA collapses in the upper stories, where P–Δ effects were smaller than the lower stories and where increases in reserve system strength and stiffness are potentially less costly. These three questions help to emphasize that while this study has indicated the possibility of improved performance with reserve systems, it has neither demonstrated ideal reserve system designs nor determined the minimum acceptable capacity for reserve systems. The reserve system is a broad and flexible concept that appears essential to the design of low-ductility structures in moderate seismic regions, but it requires further investigation to be developed for general use in design.

CONCLUSIONS

Moderate seismic regions are distinguished from high seismic regions in three basic ways.

1. Collapse prevention, rather than potential economic loss, drives lateral system design.

2. Ground motions for moderate seismic regions differ significantly from their high seismic counterparts.

3. Wind loads and stiffness considerations often govern system choice and member design.

In light of these differences it is reasonable to talk about an independent seismic design philosophy for low-ductility structures in moderate seismic regions. At the heart of this philosophy, the concepts of reserve capacity and elastic flexibility should complement more well-established concepts of strength, ductility and capacity design. Such a philosophy should provide engineers with maximum flexibility for developing new structural systems based on first principles. This paper focused specifically on the concept of reserve capacity and its ability to enhance collapse performance for chevron braced steel frames not specifically detailed for seismic resistance.

R = 3 designs for 3-, 6-, 9- and 12-story building configurations under 2% in 50-year earthquake loads calculated according to IBC 2006 were assessed to have an approximately 30% chance of collapse for a typical Site Class D location in Boston, Massachusetts. Two major assumptions in this study violated ATC-63 recommendations for collapse performance assessment (ATC, 2008):

1. The gravity system provided reserve capacity (p. 1-4).

2. Suite ARS values were allowed to be uniformly lower than their IBC 2006 counterparts at the building fundamental period (p. A-11).

The R = 3 models would have demonstrated less robust collapse performance without these two assumptions.

At the same time, conventional faith in the collapse resistance of low-ductility steel structures appears to be well founded. For instance, Yanev et al. (1991) noted that the performance of steel structures has been excellent in previous earthquakes, with very few actual collapses. Steel building collapses were generally concentrated in the 1985 Mexico City earthquake, where most steel frames had been constructed out of built-up sections rather than rolled shapes. No steel structures were observed to collapse during the Northridge earthquake (Bruneau et al., 1995), and the only steel braced frames structures that collapsed during the

Kobe earthquake had been braced with rods, angles and flat bars (Tremblay et al., 1996). Nevertheless, the literature is relatively silent both on why these low-ductility buildings designed for high seismic regions survived and on whether such anecdotes constitute reliable assurance that a provision such as $R = 3$ will prevent future collapses. Large-scale test data related to the performance of sections and details typically used for building design in moderate seismic regions, as well as large-scale shaking table tests related to the collapse of low-ductility frames are only sparsely addressed in the literature to date.

In this study, the $R = 3$ models' resistance to collapse appears to have derived more from their inherent elastic reserve capacity than from their inherent ductility. Changes in primary LFRS strength, explored for $R = 2$ and $R = 4$ designs neither significantly improved nor significantly degraded collapse performance. In fact, the 3-story/R4 model outperformed both of the stronger designs. Changes to the reserve system capacity, however, uniformly improved collapse performance. The familiar concept of reserve capacity is widely accepted for high-ductility dual systems, and it is implied in the $R = 3$ provision itself. As a philosophical concept, reserve systems have the potential to increase safety, reduce construction cost, and encourage innovation in LFRS design. With so much riding on reserve systems, they should be recognized formally and designed explicitly.

Further investigation of these questions requires more complete understanding of low-ductility structural details and their effects on system collapse performance. Bruneau et al. (1995) noted that 4 out of 11 CBFs observed after the Northridge earthquake experienced some form of anchor bolt yielding or failure. Gravity column splices could also hasten collapse if they act as weak links during the engagement of the gravity frame as a reserve system. Conversely, gusset plate connections could be designed to provide significant strength and ductility via moment frame action after brace fracture.

We recognize the multiple uncertainties associated with the study presented in this paper and feel that questions related to the collapse performance of $R = 3$ chevron braced steel frames will remain difficult to answer definitively. In spite of these uncertainties, however, it is our opinion that these analyses demonstrate the potential for reserve systems to improve $R = 3$ collapse performance significantly. In fact, an appropriate reserve system could allow the primary LFRS to be designed for wind only, effectively reducing overturning demands on a building's foundation.

The models presented in this paper were created from the same template, varying only in configuration, member sizes and the extent of reserve system. Assumptions regarding nonlinear material and geometric behavior were uniform for all models. Therefore, the improvement in analytical collapse performance achieved through more robust reserve systems was interpreted as insight into actual physical behavior. While it is possible to debate the reserve capacity assumed in these models for gravity framing or gusset plate connections, it is likely that the concept of a reserve system itself is quite reasonable. Ideally, future research will encourage the development of typical details for gusset plate connections that allow them to be included fully in the reserve system. If it can be clearly understood how much reserve capacity is required to ensure adequate collapse performance, then a structural designer may be able to create a reserve system via typical gusset plate details without adding more moment connections. Additional reserve system capacity may only be necessary in the weakest areas of a structure, allowing such a system to be tuned for efficiency. Philosophical emphasis should be placed on the need for a reliable reserve system. The manner in which a particular system is to be achieved should remain the responsibility of the designer.

In response to the lack of literature discussing the $R = 3$ criterion and low-ductility collapse performance under moderate seismic excitation in general, this study has called attention to questions that fall outside the general conceptual framework for design in high seismic regions:

1. What are the relationships among strength, ductility, elastic flexibility, reserve capacity, damage and collapse for low-ductility systems?

2. How can understanding of these relationships be used to develop an appropriate design philosophy for low-ductility systems in moderate seismic regions?

Such a philosophy should ensure safety, promote economy and allow designers maximum flexibility to develop creative structures that resist collapse. We hope that our discussion of the reserve system concept will serve as a useful step toward defining this philosophy.

ACKNOWLEDGMENTS

Funding for this work was provided jointly by the American Institute of Steel Construction, LeMessurier Consultants, the Structural Steel Fabricators of New England, the Boston Society of Architects, and the Boston Society of Civil Engineers. The authors would like to thank M.C. Gryniuk for his work in developing the original Ruaumoko braced frame models that were modified for this study and for helping to select an appropriate hysteresis rule for fracturing braces; R.A. Henige, LeMessurier Consultants, for his input on the building design and analysis; S. Sorabella and L.G. Baise, Tufts University, for their work on developing the ground motion suite; R. Leon for his helpful comments regarding analysis of OCBF systems; and the AISC Research Advisory Committee for their many helpful comments on earlier drafts.

Table A-1. Modeling Assumptions			
	Assumption	**Conservative or Unconservative**	**Comments**
1	2D behavior	Unconservative	Torsional behavior can amplify force and deformation demands.
2	No nonstructural components	Unconservative/ Conservative	Unconservative if such elements serve to concentrate stiffness and attract loads to vulnerable parts of the building, or reduce the period of the structure. Conservative if such elements provide reserve capacity.
3	No flexural stiffness or strength of gusset plate connections	Conservative	Gusset plate-to-column connections are not expected to behave reliably in a ductile manner. While it may be possible for them to provide reserve capacity before fracturing, this reserve capacity is not well understood.
4	No buckling of columns	Unconservative	Stronger braces and connections could overload columns.
5	Perfect anchorage of column bases	Unconservative/ Conservative	Unconservative if yielding of anchor rods results in displacement of the building column on top of a concrete pier; conservative if yielding of anchor rods allows the primary LRFS to rock before experiencing significant damage.
6	Strong column splices	Unconservative	The column splices are allowed to develop the full flexural strength of the smallest member.
7	Gravity frame girders have $0.50EI$, yield at $0.2M_p$, and have high ductility	Conservative	According to Liu and Astaneh (2000), 30% to 40% capacity is only available for certain size members and for the load direction where the slab goes into compression. The capacity drops to approximately 18% at relatively low levels of inelastic rotation. See further discussion later.
8	The SAC building geometry is highly regular	Unconservative	This level of regularity in a building system cannot be considered typical, especially in a moderate-to-low-seismic region.
9	Braced frame columns bent about strong axis and gravity columns bent about weak axis; gravity girders (not beams) to be oriented parallel to direction of loading	Conservative/ unconservative	All columns were allowed to yield in flexure as beam-columns. For an R3 system, a designer theoretically assumes no responsibility for the orientation and contribution of the gravity framing as a reserve system.
10	The models do not lose all brace capacity immediately after reaching their designated fracture force	Unconservative	This assumption was necessary to ensure reliable numerical convergence. See further discussion that follows.

APPENDIX

Design and Modeling of Braced Frame Buildings

Half of each building configuration (Figure 1 and Figure 4) was modeled using the nonlinear analysis software Ruaumoko-2D (Carr 2004). The braced frames were connected by rigid links to a moment frame representing the inherent lateral capacity of the gravity framing (Figure 5). Table A-1 lists major assumptions applied consistently throughout the study. These assumptions are neither uniformly conservative nor uniformly unconservative.

Assuming that the girders yield at $0.20M_p$ (assumption 7) could be unconservative, because the gravity loads on the girders did not require their connection to be developed over the full depth of the W21×44. Liu and Astaneh's (2000) tests, however, generally assumed full depth connections. The gravity framing and reserve systems were modeled with bilinear plastic hinging mechanisms in the beams and columns (Figure A-1). Each girder modeled in the gravity frame represented two girders in order to capture the two lines of gravity framing. Girder yield moment capacity was therefore (50 ksi)(0.2)(95.4 in^3)(2) = 1910 kip-in.

Due to large discontinuities in strength and stiffness between damaged and undamaged frames, it was difficult to get these systems to converge numerically. The braces were modeled using the Ruaumoko model for the Matsushima

strength reduction hysteresis rule (Matsushima, 1969). The braces were assumed not to lose all brace capacity immediately after reaching their designated fracture force, rather they assumed a constant yield plateau prior to the first reversal of force. After the first reversal this yield plateau was abandoned and the brace was assumed to degrade to 5% of its previous strength. Each further reversal prompted an additional 95% degradation, effectively modeling zero capacity after the first excursion. While such yielding is unrealistic for braces prone to fracture, it did not appear to have a major impact on system performance. Figure A-2 represents a typical case where such yielding appears significant in the context of a hysteresis loop, but seems less so when observed as a function of time (Figure A-3, Figure A-4).

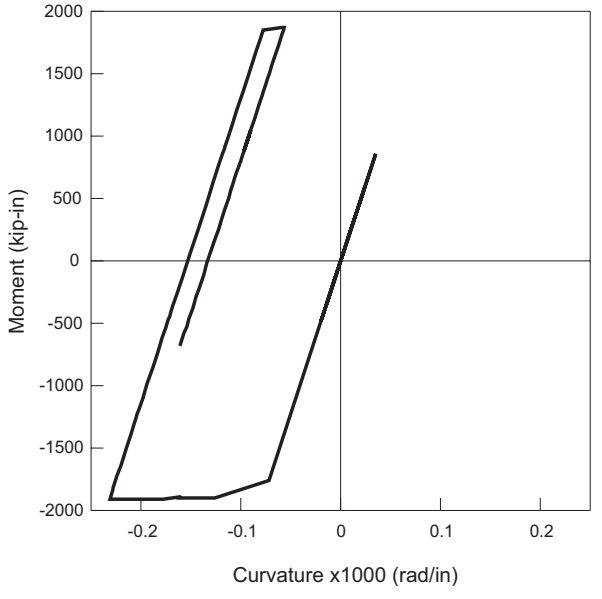

Fig. A-1. A 6-story/R3/GM3 second-floor bilinear hysteresis loop representing two gravity girders.

Figure A-3 plots force as a function of time for similar braces in three different structures: R3 with the brace hysteresis rule described earlier, designated *R3*; R3 with a bilinear brace hysteresis rule, designated *bilinear*; and the WRS system. As Figure A-3 shows, the two R3 structures demonstrated similar elastic behavior up to first-fracture/first-yield at approximately 4.7 seconds. The displacement response histories for these same situations are shown in Figure A-4. The R3 brace continued to resist force for approximately 1 second thereafter, before reaching a steady state of effectively zero force. The bilinear brace continued to resist force, without experiencing significant yielding. The WRS brace closely followed both R3 braces in the elastic range up to first fracture, continuing to resist force for approximately 1 second thereafter before reaching a steady state of zero force. While this short period of residual brace capacity may not represent physical behavior, it accounts for only a fraction of the total response over time and is less alarming

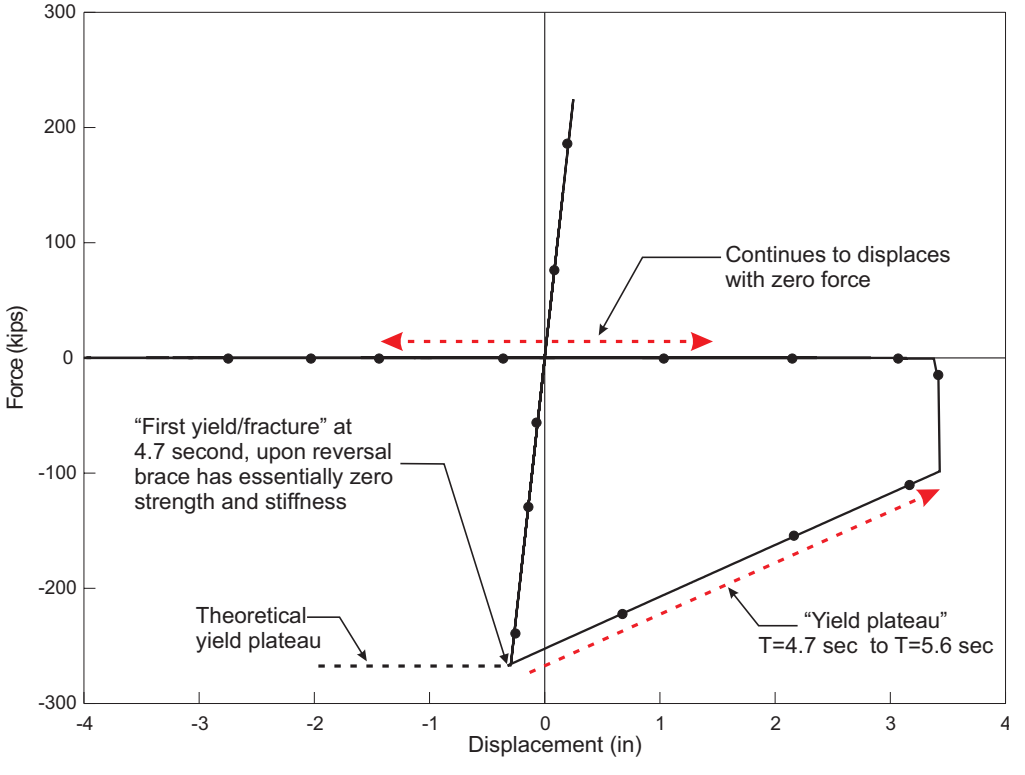

Fig. A-2. A 6-story/R3/GM3 first-story brace hysteresis loop.

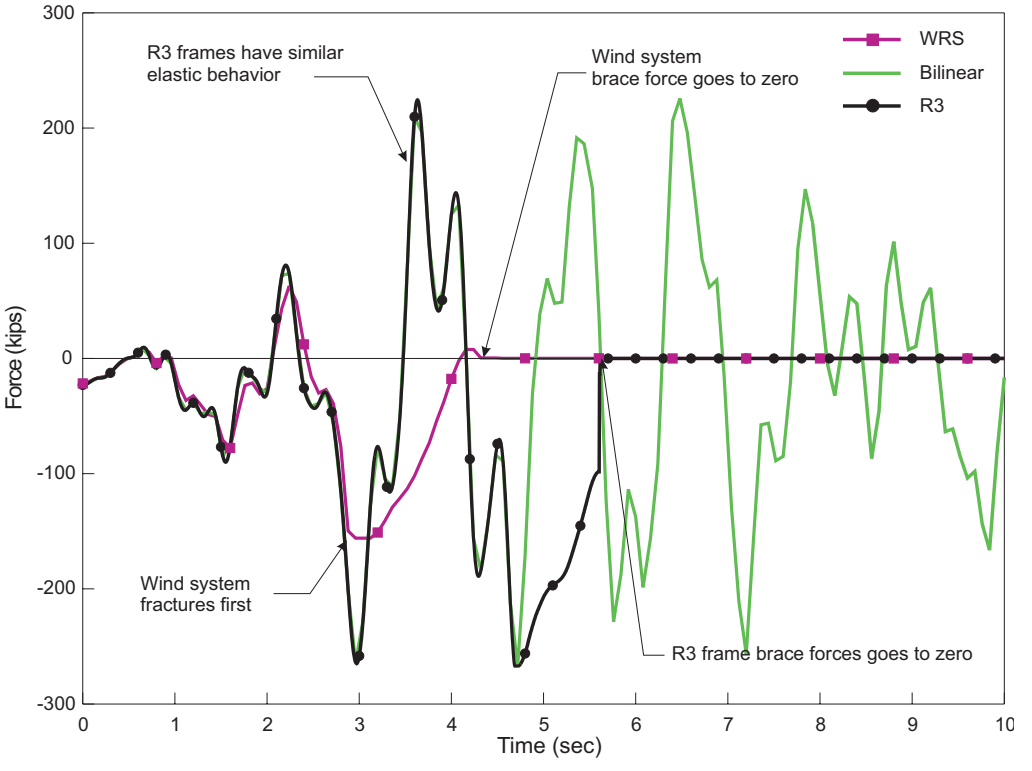

Fig. A-3. A 6-story/R3/GM3 first-story brace force versus time.

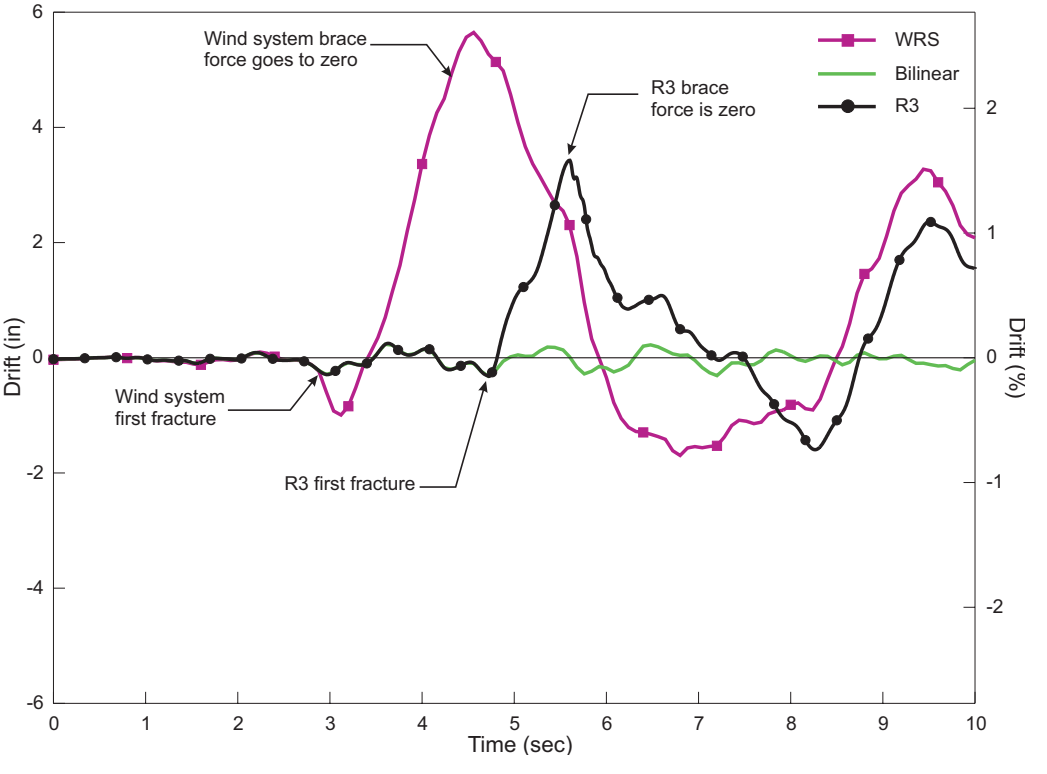

Fig. A-4. A 6-story/R3/GM3 first-story brace displacement.

Table A-2. Ground Motion Records				
Earthquake	GM	Record	Magnitude	Distance [km]
Mammoth Lakes	1	ER-A-LVL000	6.0	19.7
	2	ER-A-LVL090		
Tabas	3	ER-FER-L1	7.4	94.4
	4	ER-FER-T1		
Landers	5	ES-H05000	7.3	69.5
	6	ES-H05090		
Kocaeli	7	ER-MCD000	7.4	62.3
	8	ER-MCD090		
San Fernando	9	ES-SJC033	6.6	104
	10	ES-SJC303		
Northridge	11	ER-SOR225	6.7	54.1
	12	ER-SOR315		
Morgan Hill	13	ER-CLS220	6.2	22.7
	14	ER-CLS310		

when viewed as a function of time than as hysteretic behavior. Such a plateau probably protected most models from collapsing under a single pulse by requiring brace forces to reverse before allowing any loss in capacity. Though the plateau is unrealistic, it represents a modeling compromise made for the sake of numerical convergence and should be assessed as slightly unconservative. For further information regarding the design and analysis of these models, see Appel (2008).

Boston Ground Motion Suite

Strong motion records for moderate seismic regions are often too scarce to assemble adequate suites of ground motions for performance assessments. These limited data require either the development of artificial ground motions or the adaptation of records from measured events in higher seismic regions. Furthermore, the lack of data implies that uncertainty related to earthquake magnitude and distance is probably greater in moderate seismic regions than in high seismic regions. For instance, Figure A-5 shows the 1-Hz deaggregation of seismic hazard for Boston and for a location in Los Angeles. The LA hazard appears to derive from only two major sources and a few minor sources, whereas the Boston hazard derives from a multitude of separate sources. This variability in possible earthquake magnitudes is typical for the Eastern North America (ENA) seismic hazard.

The suite of ground motions used in this study was developed such that the average acceleration response spectrum (ARS) curve for 14 motions matched the IBC 2006 MCE for Site Class B. Every motion in the suite was required to match or exceed at least one U.S. Geological Survey (USGS) uniform hazard spectrum (UHS) point at T = 0.0, 0.1, 0.2, 0.3, 0.5, 1.0 or 2.0 seconds without scaling. Table A-2 lists the selected 14 ground motions recorded from seven different earthquake sources. In anticipation of future three-dimensional (3D) simulations, an orthogonal pair of motions was selected from each earthquake. For this two-dimensional (2D) study, all 14 motions were applied independently. Figure A-6 compares the selected suite of 14 unscaled ground motions to the UHS points. The Site Class B ARS values were allowed to be as great as 2.0 times or as small as 0.5 times any of the UHS points. Allowing this variation was thought to capture approximately 90% of the hazard represented by the USGS deaggregations (Sorabella, 2006). The Site Class B motions were amplified using the program Equivalent-linear Earthquake site Response Analysis (Bardet and Ichii, 2000), assuming a typical Boston soil profile (Johnson, 1989; Sorabella, 2006). Figure A-7 compares the ARS of the 14 motions with the average ARS and the IBC 2006 Site Class D MCE. Figure A-7 shows resonance of the soil column at approximately 0.9 second, and significantly lower spectral accelerations for all motions for $T > 2.0$ seconds. For this reason, a 15th motion was created artificially to match the Site Class D MCE as closely as possible. Figure A-8 compares the ARS of the spectral compatible motion, created using the program SIMQKE (Carr, 2004), to the Site Class D MCE as well as the 14 ground motion suite average. See Hines et al. (2009) for further discussion of issues related to the selection of ENA ground motion suites.

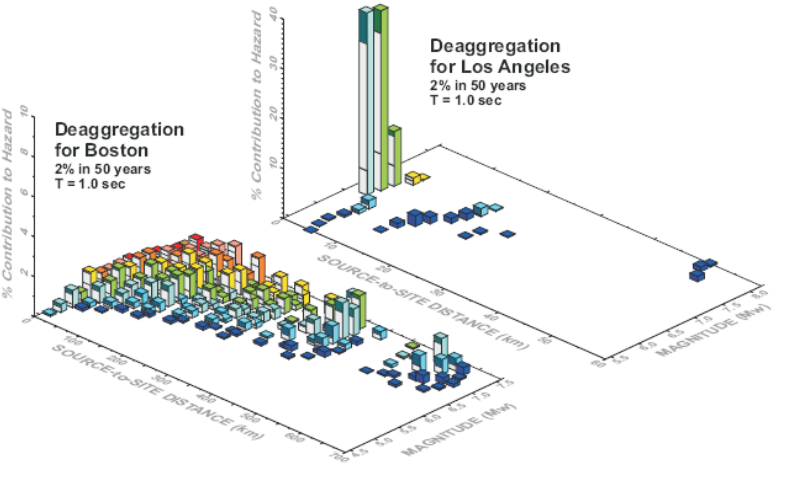

Fig. A-5. A 2% in 50-year (Frankel et al., 2002) deaggregation for Boston and LA at T = 1.0 s. (adapted from files downloaded from http://www.usgs.gov)

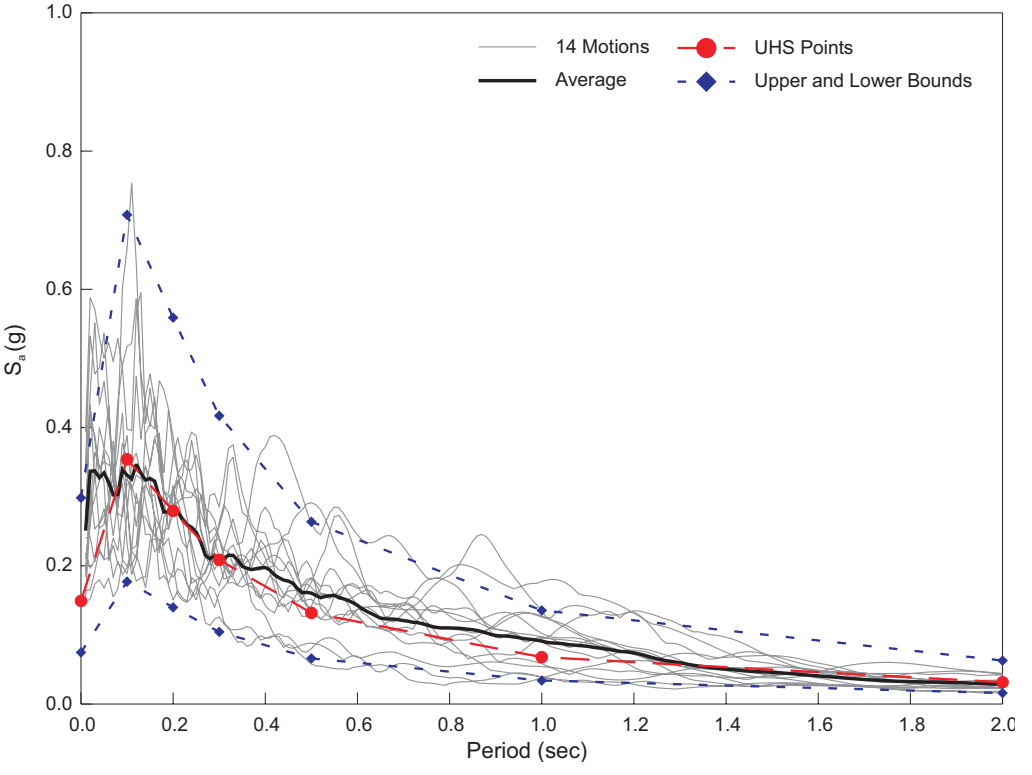

Fig. A-6. Selected 2002 14 ground motion suite—Site Class B.

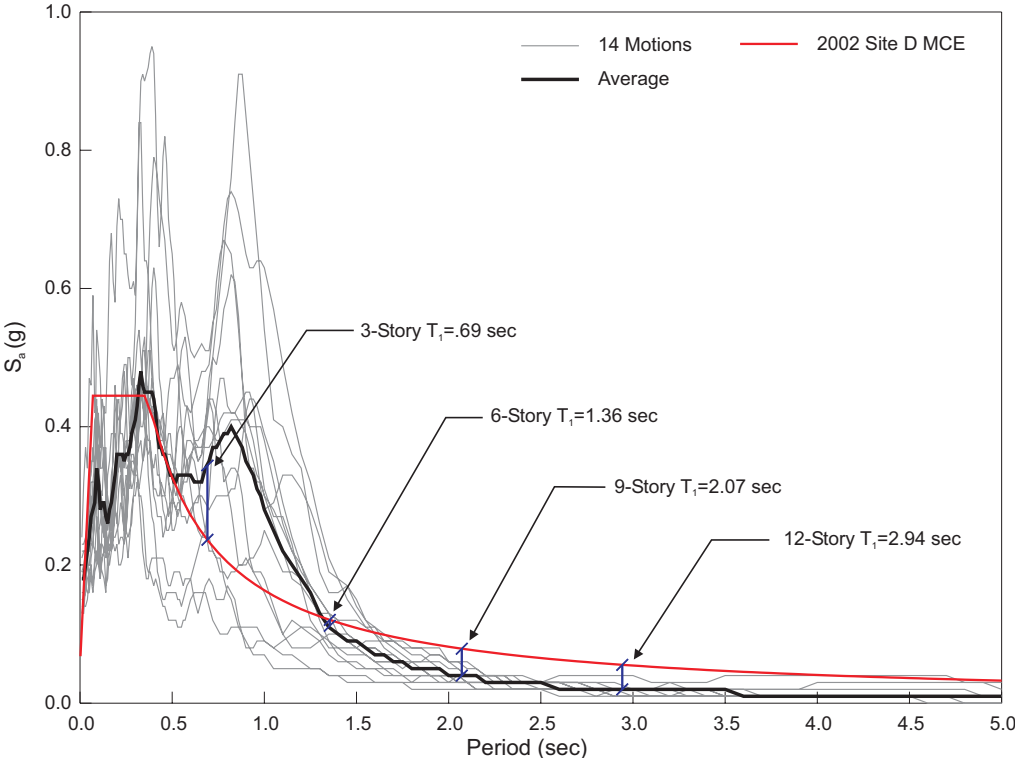

Fig. A-7. The 14 ground motion suite amplified through Site Class D soil column.

Performance Assessment: FEMA-350 versus ATC-63

The methods proposed in FEMA-350 (SAC, 2000a) and ATC-63 (ATC, 2008) differ substantially in their characterization of system demand and capacity and provide very different assessments for particular low-ductility buildings. After introducing the principal difference between these two methods—developed to assess higher ductility systems in high seismic regions—results for this study are presented according to a modified version of the ATC-63 method.

The FEMA-350 approach (SAC, 2000a; Cornell et al., 2002; Yun et al., 2002; Lee and Foutch, 2002) assumes that maximum interstory drift is the best indicator of collapse demand and capacity. This assumption is consistent with the general understanding that nonlinear structural behavior under seismic loads is more accurately assessed according to displacements than according to forces. For the purposes of the FEMA-350 approach, however, interstory drifts were assumed to be linearly related to spectral acceleration (Cornell et al., 2002). The use of displacements as engineering demand parameters (EDPs) to evaluate collapse has recently come under criticism, based on the observation that these EDP demands "become very sensitive to small perturbations when the system is close to collapse" (Ibarra and Krawinkler, 2005, p. 282).

For low-ductility systems, this problem is compounded in the assessment of the drift demand parameter, *D*. Since low-ductility systems either remain elastic or experience significant drift demands once the primary lateral system degrades, the EDP for interstory drift, *D*, can exhibit values that vary by an order of magnitude between ground motions. This wide variation results in a demand randomness factor, γ_r, that is commonly 2 or higher, leading to very low confidence in collapse capacity. Ironically, the confidence can be increased for a given assessment simply by removing the lowest drift demands from the assessment. This is illustrated by an example for the 9-story/R3 model.

The maximum interstory drift demands and capacities are given in Table A-3, for the 9-story/R3 model and the resulting demand and capacity factors reflecting randomness, based on the logarithmic standard deviations, β, of these values are listed in Table A-4. For the purposes of this example, the β values for uncertainty are assumed to be 0.400, reflecting an increased level of uncertainty associated with the analysis of low-ductility braced frame systems when compared to the moment frame systems for which the procedure was originally calibrated.

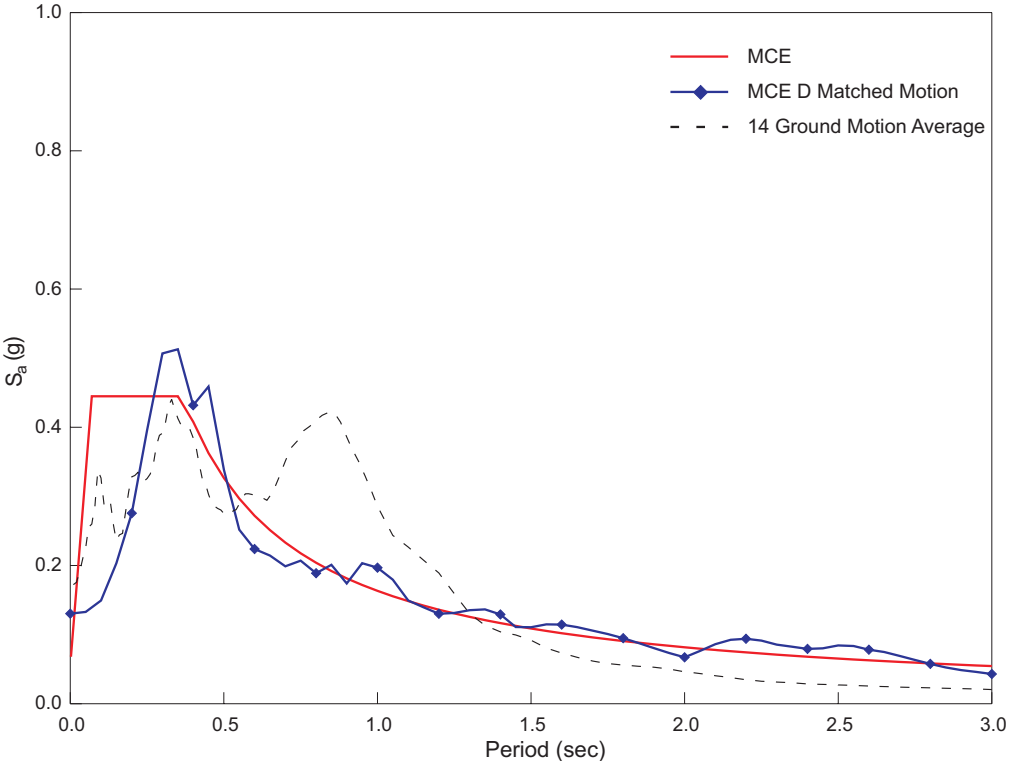

Fig. A-8. Matched motion ARS comparison.

Table A-3. Maximum Interstory Drift Demands and Capacities for 15 Ground Motions		
Motion	**Demand**	**Capacity**
GM1	0.018	0.033
GM2	0.003	0.040
GM3	0.014	0.022
GM4	0.015	0.028
GM5	0.021	0.050
GM6	0.029	0.022
GM7	0.002	0.039
GM8	0.003	0.018
GM9	0.016	0.038
GM10	0.003	0.017
GM11	0.020	0.019
GM12	0.012	0.018
GM13	0.024	0.031
GM14	0.027	0.025
Matched	0.024	0.030
Median	**0.0160**	**0.0283**

Combination of these values results in

$$\lambda = \frac{\gamma_R \gamma_U D}{\varphi_R \varphi_U C} = \frac{(1.85)(1.12)(0.0160)}{(0.918)(0.890)(0.0283)} = 1.43 \qquad (1)$$

where

γ_R = demand variability factor
γ_U = analysis uncertainty factor
D = median maximum drift demand for the unscaled motion
φ_R = resistance factor accounting for random behavior
φ_U = resistance factor accounting for uncertainty in analytic modeling
C = median maximum drift capacity according to IDAs

which yields $K_x = -0.22$ and a confidence of 41%.

Note, however, that GM2, 7, 8 and 10 produced demand drifts measuring in tenths of a percent, while the remaining ten motions produced demand drifts over 1% (Table A-3). Such low drift demands reflect the tendency of the system to perform in the elastic range under these ground motions at a scale factor (SF) of 1.0. Since Table A-3 reports only four such instances, the median demand, $D = 0.0160$, is still in the higher range of values. Equation 1 shows that $\gamma_R = 1.85$ has the most significant effect on confidence level. If these four motions are removed from the assessment, the median demand increases, but not enough to offset the increase in confidence. Combination of these values results in a confidence of 65%. (See Tables A-5 and A-6 pn page 175).

Table A-4. Demand and Capacity Factors per FEMA-350 Assessment for 15 Ground Motions			
Demand		**Capacity**	
β_{DR}	0.916	β_{CR}	0.343
γ_R	1.85	φ_R	0.918
β_{DU}	0.400	β_{CU}	0.400
γ_U	1.12	φ_U	0.890

The addition of more ground motions to the suite would probably not result in greater accuracy if the distribution continues to bifurcate between elastic and inelastic behavior, as shown in Figure 6. Such behavior distinguishes low-ductility braced frame systems from their higher ductility counterparts, whose transition into the inelastic range is generally expected to be smoother. If, for some reason, the median demand value fell into the elastic range, the resulting confidence would be unconservatively high. It could be argued that the effects of this bifurcation on the FEMA-350 approach could be mitigated by scaling the ground motions to the code spectral value at the first natural period, S_{aT1}, as recommended. The ATC-63 approach, however, demonstrated little sensitivity to the wide variety allowed within the suite and was therefore better suited to incorporate uncertainty related to earthquake intensity.

In addition to the sensitivity mentioned by Ibarra and Krawinkler (2005), this drift demand sensitivity motivates the assessment of collapse capacity according to earthquake intensity rather than drift demand and capacity. Since the models and incremental dynamic analyses used to assess collapse earthquake intensity are the same used for assessing interstory drifts, there is no danger in abandoning the "displacement-based" FEMA-350 approach in favor of an intensity-based parameter. Sensitivity to displacement behavior is preserved in the IDAs. Figure 6 shows the IDA curves for the 9-story/R3 model and demonstrates that variation in behavior can be observed either in terms of drift, or in terms of ground motion intensity. The IDA curve for GM4 shows that the model stayed in the elastic range until SF = 1.7 and just before collapse. Compare this result to the curve for GM11, where at SF = 1.0. The model already experienced inelastic behavior; however, it did not collapse until SF = 2.2. Note that almost every IDA curve exhibits a plateau between elastic and inelastic behavior, where the transition is made from primary LFRS to reserve LFRS.

Since drift demands appear bifurcated rather than lognormally distributed for the low-ductility LFRS in question, and since ground motion intensity, expressed in spectral acceleration, S_a, or SF gives at least as good an indication of

Table A-5. Maximum Interstory Drift Demands and Capacities for 11 Ground Motions		
Motion	**Demand**	**Capacity**
GM1	0.018	0.033
GM3	0.014	0.022
GM4	0.015	0.028
GM5	0.021	0.050
GM6	0.029	0.022
GM9	0.016	0.038
GM11	0.020	0.019
GM12	0.012	0.018
GM13	0.024	0.031
GM14	0.027	0.025
Matched	0.024	0.030
Median	**0.0200**	**0.0283**

Table A-6. Demand and Capacity Factors per FEMA-350 Assessment for 11 Ground Motions			
Demand		**Capacity**	
β_{DR}	0.288	β_{CR}	0.312
γ_R	1.06	φ_R	0.931
β_{DU}	0.400	β_{CU}	0.400
γ_U	1.12	φ_U	0.890

variability in collapse capacity as interstory drift, it is attractive to use an approach more similar to ATC-63. This approach focuses on spectral acceleration as an intensity measure and avoids discussing drift demands all together. IDA results are represented in the form of cumulative distribution functions, or fragility curves. These fragility curves provide not only a numerical indication but also visual indication of a particular system's resistance to collapse (see Figures 11 through 14).

Figure A-9 shows fragility curves for the 9-story/R3 and WRS models in terms of S_{a1}, with a collapse probability for the R3 model of close to 70%. In this figure, the smooth fragility curve is a cumulative distribution function based on the median and lognormal standard deviation of the experimental data points. The high probability of collapse reflects a characteristic of the ground motion suite that may provide further reason to differentiate the assessment of low-ductility systems in moderate seismic regions from high ductility systems in high seismic regions. Figure A-7 shows that the

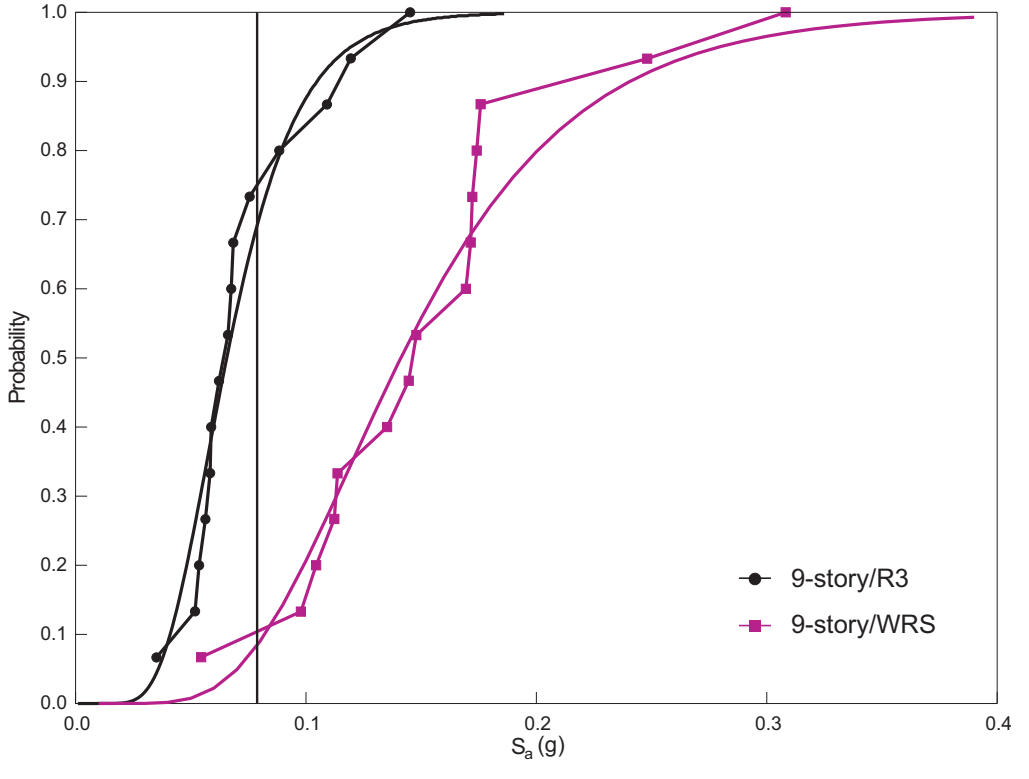

Fig. A-9. The 9-story/R3 and WRS fragility curves as a function of S_a.

average S_{a1} (T_1 = 2.07 seconds) value for the suite falls well below the MCE value given by IBC 2006 for Site Class D. These low spectral accelerations in the first mode are considered to be more realistic and more consistent with the state of the art related to ENA ground motions than the IBC 2006 curve (Sorabella, 2006; Hines et al., 2009). This phenomenon, combined with the presence of higher mode effects due to ARS spikes at lower periods suggests that evaluating fragility based on SF rather than S_a may be more realistic for low-ductility systems in moderate seismic regions. Using SF is similar to using S_{aT1} for the suite average rather than for the IBC MCE. Note that the IDAs in this assessment did not account for the fact that less soil amplification would be expected for larger motions due to nonlinear soil behavior. In order to take this into account, it would perhaps be more accurate to increment the rock motion and reevaluate the nonlinear soil column analysis at each increment. Such a procedure is beyond the scope of the present work. For now, it can be assumed that this part of the assessment is conservative since it does not take into account decreasing soil amplification with increasing intensity of bedrock ground motions. Figure A-10 shows the 9-story/R3 fragility curve in terms of SF, which is normalized to 1 for the original Site Class D suite.

The fragility curves in Figure A-9 express implicitly another characteristic of the suite used for this assessment. As discussed previously, no rock motions were scaled prior to their inclusion in the suite so as to allow maximum realistic variation in ground motion characteristics. Based on this suite, there is legitimate concern that the fragility curves merely reflect the level of variation allowed in choosing the rock motions. If this were the case, then the smallest motions would have the largest scale factors and the largest motions would have the smallest scale factors. In order to address this concern, Figure A-10 also shows normalized S_a values for each motion and for each of the first three modes ordered in the same manner as the values composing the fragility curves. S_a values were normalized for each mode by dividing the S_a for that mode (first, second or third) and ground motion (GM 1-14 or "Matched) by the S_a value for the same mode as defined by the IBC 2006 MCE ARS curve. Strict correlation with variations in rock motion intensity would imply a negative slope to each of the normalized S_a curves. While some general negative slope can be discerned for each set of S_a values, it is overwhelmed by variations in the normalized S_a values themselves. This demonstrates that higher mode effects and record-to-record (RTR) variability without respect to variations in *M-R* values provide for substantial variation in the collapse scale factors between ground motions. Similar variations in second and third mode normalized S_a values can be observed in Figure A-11 for the 9-story/WRS model.

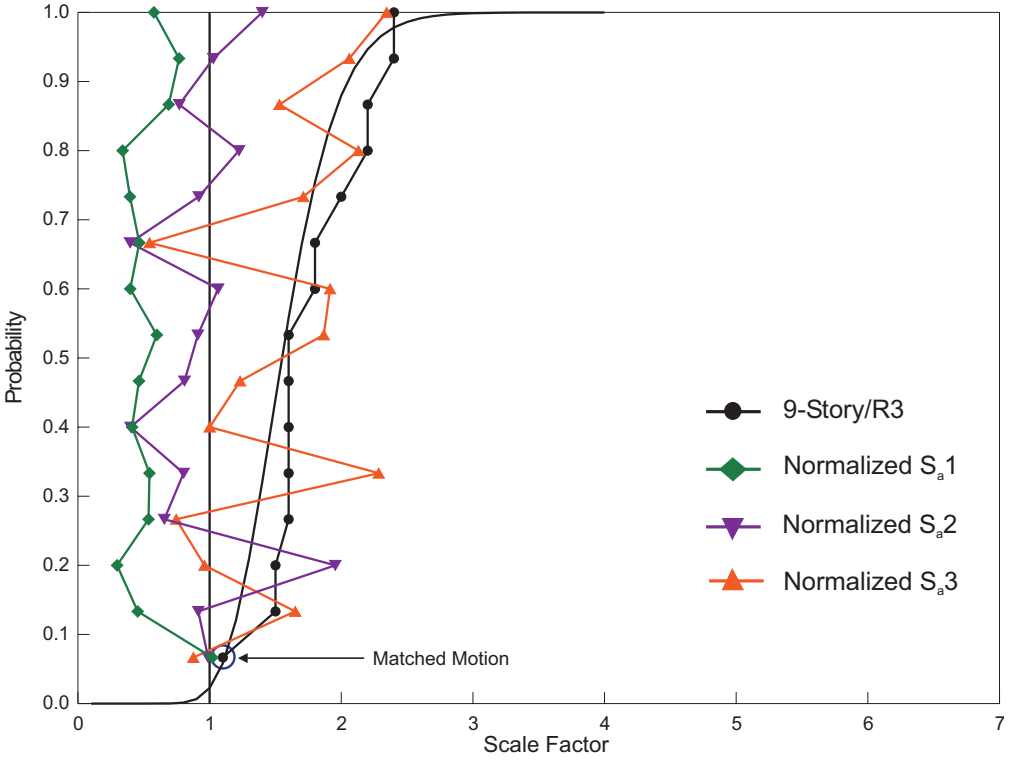

Fig. A-10. The 9-story/R3 fragility curve as a function of SF.

Figure A-10 and Figure A-11 reinforce the observation from Figure A-9 that the WRS design improved collapse resistance significantly beyond the R3 design. Figures 11 through 14 depict final fragility curves for each model as lognormal distributions based on the median scale factors from the suite of 15 motions and a uniform standard deviation of

$$\beta_{TOT} = \sqrt{\beta_{RTR}^2 + \beta_{DR}^2 + \beta_{TD}^2 + \beta_{MDL}^2} \quad (2)$$
$$= \sqrt{0.4^2 + 0.4^2 + 0.4^2 + 0.4^2} = 0.8$$

where

β_{TOT} = total system collapse uncertainty
β_{RTR} = record-to-record collapse uncertainty
β_{DR} = design requirements-related collapse uncertainty
β_{TD} = test data-related collapse uncertainty
β_{MDL} = modeling-related collapse uncertainty

These values are recommended by Chapters 5 and 7 of ATC-63 for an assessment considered to be "good." For comparison to the ATC-63 values, Table A-7 lists β_{RTR} values calculated from the 15 analysis cases for each model, and the resulting β_{TOT} value. β_{RTR} = 0.40 was used in lieu of the values reported in Table A-7 for three reasons: consistency with ATC-63, similarity between the calculated β_{RTR} values and the ATC-63 recommended value, and the ATC-63 value derives from a significantly greater number of analysis cases. It may be appropriate to modify the ATC-63 β_{RTR} value for low-ductility systems in moderate seismic regions; however, such a decision should be based on more than 15 ground motions.

Table A-7. Calculated β_{RTR} Values

	β	R2	R3	R4	WRS
3 Story	RTR	0.365	0.385	0.385	0.286
	Total	0.790	0.799	0.799	0.756
6 Story	RTR	0.447	0.447	0.354	0.390
	Total	0.830	0.830	0.785	0.802
9 Story	RTR	0.383	0.212	0.314	0.463
	Total	0.798	0.731	0.767	0.839
12 Story	RTR	0.411	0.386	—	0.389
	Total	0.812	0.740	—	0.801

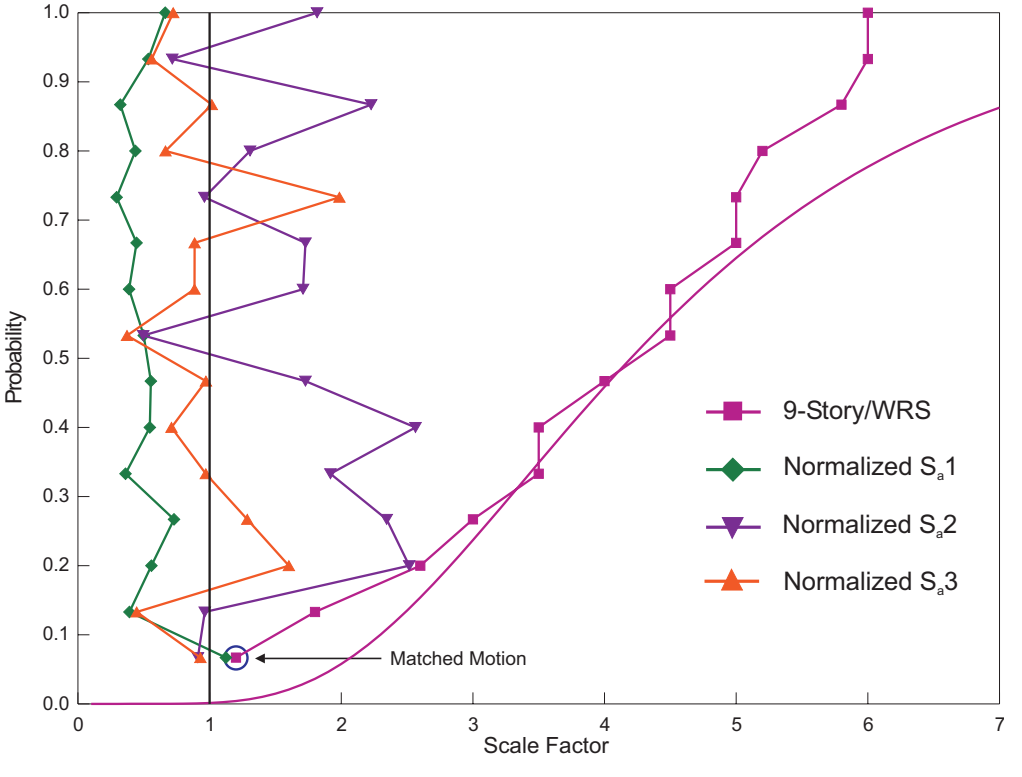

Fig. A-11. The 9-story/WRS fragility curve as a function of SF.

ABBREVIATIONS

ARS	acceleration response spectrum
ASD	Allowable Strength Design
ATC	Applied Technology Council
CBF	concentric braced frame
CUREE	Consortium of Universities for Research in Earthquake Engineering
EDP	engineering demand parameter
ENA	Eastern North America
FEMA	Federal Emergency Management Agency
GM	ground motion
HSS	hollow structural section
LFRS	lateral force resisting system
LRFD	Load Resistance Factor Design
IDA	incremental dynamic analysis
M-R	magnitude-distance
MCE	maximum considered earthquake
OCBF	ordinary concentric braced frame
OMRF	ordinary moment resisting frame
RTR	record-to-record (variability)
SAC	SEAOC-ATC-CUREE
SDC	Seismic Design Category
SEAOC	Structural Engineering Association of California
SF	scale factor
UHS	uniform hazard spectrum
WRS	wind plus reserve system

SYMBOLS

A_g	=	section gross area
b/t	=	width/thickness
C	=	median maximum drift capacity from IDAs
D	=	median maximum drift demand from IDAs
F_y	=	yield stress
K	=	effective length factor
K_x	=	Gaussian variate
M_p	=	plastic moment capacity
R	=	response modification factor
Ry	=	ratio of expected yield stress to specified minimum yield stress
S_a	=	spectral acceleration
S_{aT1}	=	spectral acceleration at the first natural period of a structure
W	=	building seismic weight
β (beta)	=	logarithmic standard deviation
β_{CR}	=	beta for aleatory uncertainty associated with structure capacity (FEMA-350)
β_{CU}	=	beta for epistemic uncertainty associated with structure capacity (FEMA-350)
β_{DR}	=	beta for aleatory uncertainty associated with structure demand (FEMA-350)
β_{DR}	=	beta for design requirements related to collapse uncertainty (ATC-63)
β_{DU}	=	beta for epistemic uncertainty associated with structure demand (FEMA-350)
β_{RTR}	=	beta for record-to-record variability (ATC-63)
β_{MDL}	=	beta for modeling uncertainty (ATC-63)
β_{TD}	=	beta for uncertainty related to test data (ATC-63)
β_{TOT}	=	beta for total system collapse uncertainty (ATC-63)
γ_r	=	demand variability factor (FEMA-350)
γ_u	=	analysis uncertainty factor (FEMA-350)
ϕ_r	=	resistance factor accounting for random (aleatory) behavior (FEMA-350)
ϕ_u	=	resistance factor accounting for uncertainty in analytical modeling
Ω	=	system overstrength factor

REFERENCES

AISC (1992), *Seismic Provisions for Structural Steel Buildings*, American Institute of Steel Construction, Inc., Chicago.

AISC (1997a), *Seismic Provisions for Structural Steel Buildings*, American Institute of Steel Construction, Inc., Chicago.

AISC (1997b), *Hollow Structural Sections, Connections Manual*, American Institute of Steel Construction, Inc., Chicago.

AISC (2002), *Seismic Provisions for Structural Steel Buildings*, ANSI/AISC 341-02, American Institute of Steel Construction, Inc., Chicago, May 21.

AISC (2005a), *Specification for Structural Steel Buildings*, ANSI/AISC 360-05, American Institute of Steel Construction, Inc., Chicago, March 9.

AISC (2005b), *Seismic Provisions for Structural Steel Buildings*, ANSI/AISC 341-05, American Institute of Steel Construction, Inc., Chicago, March 9, with Supplement No. 1, November 15.

Anderson, J.C. (1975), "Seismic behavior of K-Braced Frames," *Journal of the Structural Division*, ASCE, Vol. 101, No. 10.

Appel, M.E. (2008), *Design and Performance of Low-Ductility Chevron Braced Frames under Moderate Seismic Demands*, Masters Thesis, Department of Civil and Environmental Engineering, Tufts University, Medford, MA.

ASCE (2005), *Minimum Design Loads for Buildings and Other Structures*, ASCE/SEI 7-05, American Society of Civil Engineers, Reston, VA.

ATC (1978), *Tentative Provisions for the Development of Seismic Regulations for Buildings*, ATC-3-06, Applied Technology Council, NBS Special Publication 510, NSF Publication 78-8, U.S. Government Printing Office, Washington, D.C.

ATC (2008), Quantification of Building Seismic Performance Factors, ATC-63 Project Report—90% Draft, FEMA P695, Applied Technology Council, Redwood City, CA, April.

Bardet, J.P., Ichii, K. and Lin, C.H. (2000), *A Computer Program for Equivalent-Linear Earthquake Site Response Analyses of Layered Soil Deposits*, Department of Civil Engineering, University of Southern California, August, 40 pp.

Bell, G.R. and Lamontagne, A.S. (2002), "Use of Total Hazard in Examining Seismic Risk Considerations in Building Design," *EERI 7th National Conference on Earthquake Engineering*, Boston, July 21–25.

Bruneau, M., Tremblay, R., Timler, P. and Filliatrault, A. (1995), "Performance of Steel Structures during the 1994 Northridge Earthquake," *Canadian Journal of Civil Engineering*, Vol. 22, pp. 338–360.

Carr, A.J. (2004), *Ruaumoko Manual Volumes 1 & 2*, University of Canterbury, Christchurch, New Zealand, 333 pp.

Cornell, C.A, Jalayer, F., Hamburger, R.O. and Foutch, D.A. (2002), "Probabilistic Basis for 2000 SAC Federal Emergency Management Agency Steel Moment Frame Guidelines," *Journal of Structural Engineering*, ASCE, April, pp. 526–533.

Engelhardt. M.D. and Popov, E.P. (1989), Behavior of Long Links in Eccentrically Braced Frames, UCB/EERC-89/01, Earthquake Engineering Research Center, University of California at Berkeley, Richmond, CA.

EQE International (1997), Second Pilot Test Study of the Standardized Nationally Applicable Loss Estimation Methodology, Boston, Massachusetts, Final Report, Prepared for the National Institute of Building Sciences, March.

Frankel, A., Petersen, M.D., Mueller, C., Haller, K.M., Wheeler, R.L., Leyendecker, E.V., Wesson, R.L., Harmsen, S.C., Cramer, C.H., Perkins, D.M. and Rukstales, K.S. (2002), Documentation for the 2002 Update of the National Seismic Hazard Maps, United States Geological Survey, Open-File Report 02-420, Denver.

Gryniuk, M.C. and Hines, E.M. (2004), Safety and Cost Evaluation of a Steel Concentrically Braced Frame Student Residence Facility in the Northeastern United States, Preliminary Report to the American Institute of Steel Construction, LeMessurier Consultants, Cambridge, MA, December.

Hines, E.M and Appel, M.E. (2007), "Behavior and Design of Low-Ductility Braced Frames," *ASCE Structures Congress*, Long Beach, CA, May.

Hines, E.M., Sorabella, S. and Baise, L.G. (in review 2009), "Ground Motion Suite Selection for Eastern North America," *Journal of Structural Engineering,* ASCE.

ICC (2006), *International Building Code*, International Code Council, Falls Church, VA.

Ibarra, L. and Krawinkler, H (2005), Global Collapse of Frame Structures under Seismic Excitation, Blume Center Technical Report No. 152, Stanford University, Palo Alto, CA, August, 349 pp.

Johnson, E.J. (1989), "Geotechnical Characteristics of the Boston Area," *Civil Engineering Practice*, Boston Society of Civil Engineers Section/ASCE, Vol. 4, pp. 53–64.

Kim, J. and Choi, H. (2004), "Response Modification Factors of Chevron-Braced Frames," *Engineering Structures*, Vol. 27, pp. 285–300.

Khatib, I.F., Mahin, S.A. and Pister, K.S. (1988), Seismic Behavior of Concentrically Braced Steel Frames, UCB/EERC Report 88/01, Earthquake Engineering Research Center, University of California, Berkeley, Richmond, CA, January.

Lee, K. and Foutch, D.A (2002), "Seismic Performance Evaluation of Pre-Northridge Steel Frame Buildings with Brittle Connections," *Journal of Structural Engineering*, ASCE, Vol. 28, No. 4, April, pp. 546–555.

Leyendecker, E.V., Hunt, R.J, Frankel, A.D and Rukstales, K.S (2000), "Development of Maximum Considered Earthquake Ground Motion Maps," *Earthquake Spectra*, Vol. 16, No. 1, February, pp. 21–40.

Liu, J. and Astaneh-Asl (2000), "Cyclic Testing of Simple Connections Including Effects of Slab," *Journal of Structural Engineering*, ASCE, Vol. 126, No. 1, pp. 32–39.

Luft, R.W. and Simpson, H. (1979), "Massachusetts Earthquake Design Requirements," *ASCE Convention and Exposition*, Boston, Preprint 3567, April 2–6.

Massachusetts (1996), *The Massachusetts State Building Code: 780 CMR Sixth Edition.* Massachusetts State Board of Building Regulations and Standards, Boston.

Matsushima, Y. (1969), "Discussion of Restoring Force Characteristics of Buildings, the Damage from Tokachi-oki Earthquake" Report, Annual Meeting, Architectural Institute of Japan, August, pp. 587–588 (in Japanese).

Nakashima, M. and Wakabayashi, M. (1992), "Analysis and Design of Steel Braces and Braced Frames in Building Structures," in *Stability and Ductility of Steel Structures under Cyclic Loading*, Fukumoto, Y. and Lee, G.C. editors, CRC Press, Boca Raton, FL, pp. 309–321.

Nelson, T.A. (2007), "Performance of a 9-Story Low-Ductility Moment Resisting Frame under Moderate Seismic Demands," Masters Thesis, Department of Civil and Environmental Engineering, Tufts University, Medford, Massachusetts.

Rojahn, C. (1995), Structural Response Modification Factors, ATC-19, Applied Technology Council, Redwood City, CA.

SAC (2000a), Recommended Seismic Design Criteria for New Steel Moment-Frame Buildings, FEMA-350, Federal Emergency Management Agency, Washington, D.C.

SAC (2000b), State of the Art Report on Systems Performance of Steel Moment Frames Subject to Earthquake Ground Shaking, FEMA 355C, Federal Emergency Management Agency, Washington, D.C.

SEAOC (1960), Recommended Lateral Force Requirements and Commentary, Seismology Committee, Structural Engineers Association of California, San Francisco.

SEAOC (1974), Recommended Lateral Force Requirements and Commentary, Seismology Committee, Structural Engineers Association of California, San Francisco.

SEAONC (1982), Earthquake Resistant Design of Concentric and K-Braced Frames, Structural Engineers Association of Northern California, Research Committee, July.

Shibata, M. and Wakabayashi, M. (1983a), "Ultimate Strength of K-Type Braced Frame," *Transactions of the Architectural Institute of Japan*, No. 326, pp. 1–9, (in Japanese).

Shibata, M. and Wakabayashi, M. (1983b), "Experimental Study on the Hysteretic Behavior of K-Type Braced Frame Subjected to Repeated Load," *Transactions of the Architectural Institute of Japan*, No. 326, pp. 10–16 (in Japanese).

Sorabella, S. (2006), *Ground Motion Selection for Boston, Massachusetts*, Masters Thesis, Department of Civil and Environmental Engineering, Tufts University, Medford, Massachusetts.

Tremblay, R. (2001), "Seismic Behavior and Design of Concentrically Braced Steel Frames," *Engineering Journal*, AISC, Vol. 38, No. 3, 3rd Quarter, pp. 148–166.

Tremblay, R., Bruneau, M., Nakashima, M., Prion, G.L., Filliatrault, A. and DeVall, R. (1996), "Seismic Design of Steel Buildings: Lessons from the 1995 Hyogo-ken Nanbu Earthquake," *Canadian Journal of Civil Engineering*, Vol. 23, pp. 727–756.

Tremblay, R. and Robert, N. (2000), "Seismic Design of Low- and Medium-Rise Chevron Braced Steel Frames," *Canadian Journal of Civil Engineering*, Vol. 27, pp. 1192–1206.

Tremblay, R. and Robert, N. (2001), "Seismic Performance of Low- and Medium-Rise Chevron Braced Steel Frames," *Canadian Journal of Civil Engineering*, Vol. 28, pp. 699–714.

Uang, C.M. and Bertero, V. (1986), Earthquake Simulation Tests and Associated Studies of a 0.3-Scale Model of a Six-Story Concentrically Braced Steel Structure, UCB/EERC-86/10, Earthquake Engineering Research Center, University of California at Berkeley, Richmond, CA, December.

Vamvatsikos, D. and Cornell, C.A. (2002), "Incremental Dynamic Analysis," *Earthquake Engineering and Structural Dynamics*, 31, pp. 491–514.

Yanev, P.I., Gillengerten, J.D., and Hamburger, R.O. (1991), *The Performance of Steel Buildings in Past Earthquakes.* American Iron and Steel Institute and EQE Engineering, Inc.

Yun, S.Y., Hamburger, R.O., Cornell, C.A., and Foutch, D. (2002), "Seismic Performance Evaluation of Steel Moment Frames, *Journal of Structural Engineering*, ASCE, Vol. 128, No. 4, April, pp. 534–545.

Experimental Evaluation of Kaiser Bolted Bracket Steel Moment-Resisting Connections

SCOTT M. ADAN and WILLIAM GIBB

The Kaiser bolted bracket (KBB) is a new beam-to-column moment connection that consists of proprietary cast high-strength steel brackets that are fastened to the flanges of a beam and then bolted to a column. This fully restrained connection is designed to eliminate field welding in steel moment frame construction.

The cast Kaiser brackets are manufactured in a variety of sizes and are proportioned to develop the probable maximum moment capacity of the connecting beam. Depending on fabrication preference the brackets can be either fillet welded [Figure 1(a) or bolted to the beam Figure 1(b)]. When subjected to cyclic inelastic loading, yielding and plastic hinge formation occur primarily in the beam near the end of the bracket, thereby eliminating inelastic deformation demands at the face of the column.

This paper summarizes the development of bolted bracket connections and presents the results of seven full-scale KBB tests. These tests were conducted to evaluate the connection for both the retrofit of existing and the construction of new steel moment frames. More specifically, the tests were intended to assess the ductility of the connection under cyclic inelastic loading and to qualify their performance with respect to the requirements of ANSI/AISC 341, *Seismic Provisions for Structural Steel Buildings* (AISC, 2005a), hereafter referred to as the AISC *Seismic Provisions*.

BACKGROUND

In the aftermath of the 1994 Northridge, California, earthquake, damage to steel moment frame connections spawned concern for the reliability of established design and construction procedures. Widespread damage was observed in beam-to-column joints that experienced rotation levels well below the plastic moment capacity of the framing members. Failures included nonductile fractures of the bottom girder flange-to-column flange complete-joint-penetration (CJP) groove welds, cracks in beam flanges and cracks through the column section (Tremblay et al., 1995; Youssef et al., 1995; FEMA, 2000). The fractures were caused by poor welding procedures, including the use of filler metals with inherent low toughness, uncontrolled deposition rates and inadequate quality control; connection design and detailing that led to larger moment-frame members, less system redundancy and higher strain demands on the connections; the use of higher strength girders, leading to unintentional undermatching of the welds; and a number of other connection detailing and construction practices that were typical prior to the earthquake (FEMA, 2000). In an attempt to ensure satisfactory earthquake performance, more stringent qualifications for fully restrained moment connections were imposed.

Subsequent to the earthquake, a significant amount of research activity was initiated on the behavior of fully restrained connections. Some of the research objectives were focused specifically on providing a bolted repair method for moment frame connections damaged during the earthquake. Implementation of a bolted repair has advantages that come from eliminating the health and fire hazards associated with welding in an occupied building. Eliminating field welding can also reduce costs associated with weld fabrication and inspection.

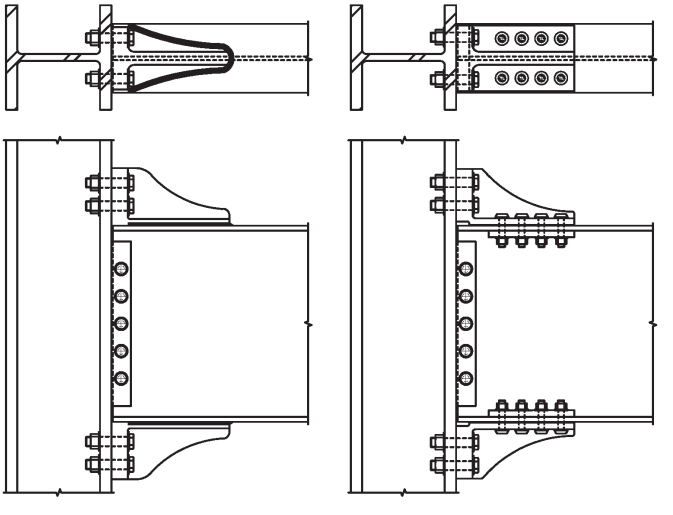

(a) Fillet welded to the beam. *(b) Bolted to the beam*

Fig. 1. Typical Kaiser bolted bracket moment-resisting connection.

Scott M. Adan is a structural engineer at Simpson Gumpertz & Heger Inc., San Francisco, CA.

William Gibb is the president of Steel Cast Connections, LLC, Seattle, WA.

A research program was initiated at Lehigh University with the objective of developing an economically viable bolted connection repair that could restore damaged moment connections to their original fully rigid condition. The program developed two repair schemes using high-strength bolts to attach a bracket between the flanges of a beam and a column. In the first scheme, the brackets were fabricated from either a stiffened angle or from thick welded plates. In the second scheme, the bracket consisted of pipes welded to a horizontal bracket plate.

The effectiveness of the repair schemes were demonstrated experimentally at Lehigh University where a total of eight tests were performed (Kasai et al., 1998). The first four specimens utilized relatively lightweight wide flange beam (W16×40) and column (W12×65) sections, identical to specimens tested by Anderson and Linderman (1991) with a clear span-to-depth ratio of 15. The haunch brackets were fabricated from a trimmed W14×145 section and fitted with a welded vertical stiffener plate. The beams, columns and brackets were A572 Grade 50 steel. The connecting fasteners were high-strength pretensioned A490 bolts.

The subsequent four test specimens utilized heavier wide flange beam (W36×150) and column (W14×426) sections, identical to specimens tested by Engelhardt and Sabol (1994) with a clear span-to-depth ratio of 10. The columns were A572 Grade 50 and the beams were A36 steel. The haunch brackets were fabricated from thick welded steel plates and connected with A490 bolts.

On five of the specimens, brackets were connected to both top and bottom beam flanges. The other three specimens being configured with brackets bolted only to the bottom flange, the top flange being connected with a high notch toughness CJP weld. This revised configuration was intended to investigate the effects of repairing only a fractured bottom flange. When a beam flange was connected with a bracket, the associated flange was not welded to the column, simulating a fractured condition.

On six of the specimens, thick steel washers or clamp plates were positioned on the opposite side of the connected beam flange in order to prevent ductile fracture through the net area. The clamp plates maintain the stability of the flange when inelastic buckling occurs outside the connected region.

Additionally, on three of the specimens, a thin brass washer plate was inserted between the bracket and the beam flange. In previous research, Grigorian et al. (1993) had used a thin brass plate as a friction-based seismic energy dissipator. Although not intended to dissipate energy in the bolted bracket connection, the brass plate provides a smooth slip mechanism at the bracket-to-beam interface.

All eight tested specimens exceeded the AISC *Seismic Provisions* (AISC, 2005a) special moment frame (SMF) qualifying requirements. At higher levels of interstory drift, flange local buckling outside the bracket region was observed to increase strains in the outermost bracket bolt holes. In the lighter specimens without the clamp plates, this increased strain caused necking and fracture through the flange net area. When configured with the clamp plates, the identical specimens exceeded the required interstory drift requirement without failure, and the tests were subsequently halted to prevent damage to the apparatus.

In the heavier specimens configured without the thin brass washer plates, energy released through the beam-bracket slip-stick mechanism caused loud, intermittent bursts of noise, particularly at high levels of inelastic drift. Fracture occurred through the flange net area at the outermost bolt holes. Upon inspection, evidence of abrading was observed between the beam and bracket contact surfaces. When the identical specimen was configured with the thin brass washer plates, deformation and fracture occurred outside the connected region through the flange gross area at a higher level of interstory drift. Noise levels were reduced and no evidence of abrading was observed.

Based on the initial eight Lehigh tests, the research concluded that the bolted bracket was capable of restoring the capacity of weakened or damaged moment connections. The haunch brackets directed yielding and inelastic beam deformation away from the column face and outside the connected region.

Although testing demonstrated that the thin brass washer and clamp plates were not essential in achieving the qualifying level of interstory drift, the research concluded that the plates could enhance ductile behavior and prevent net area fracture. The thin brass washer plate in particular was attributed with providing a smooth slip mechanism between the bracket and beam flange (Kasai et al., 1998).

To further demonstrate the effectiveness of the bolted bracket connection repair, six additional tests were performed at Lehigh University (Gross et al., 1999). The additional tests sought to obtain data on interior or two-sided connections that included the presence of a concrete slab.

In order to investigate the effects of repairing only a fractured bottom flange, the specimens were configured with brackets fastened only to the beam bottom flange. However, unlike prior tests, the top flange was fastened with a pre-Northridge CJP weld using filler metals without rated notch toughness and the backer bar was left in place. The bottom flange haunch brackets were fabricated from welded plates and attached with both a thin brass washer plate at the bracket slip interface and clamp plates opposite the connected bracket. The clear span-to-depth ratio of the specimens varied between 8 and 10. The beam, column and brackets were all A572 Grade 50 steel.

The first four specimens showed poor inelastic drift performance developing early fractures in the top flange CJP weld. In order to enhance the performance of the remaining two specimens, a double angle (trimmed from a W36×256 section) was bolted to the beam top flange and to the

Table 1. Kaiser Bolted Bracket Proportions						
Bracket Designation	Bracket Length, L_{bb} in. (mm)	Bracket Height, h_{bb} in. (mm)	Bracket Width, b_{bb} in. (mm)	Number of Column Bolts, n_{cb}	Column Bolt Gage, g in. (mm)	Column Bolt Diameter in. (mm)
W3.0	16 (406)	5½ (140)	9 (229)	2	5½ (140)	1⅜ (35)
W3.1	16 (406)	5½ (140)	9 (229)	2	5½ (140)	1½ (38)
W2.0	16 (406)	8¾ (222)	9 (229)	4	6 (152)	1⅜ (35)
W2.1	18 (457)	8¾ (222)	9½ (241)	4	6½ (165)	1½ (38)
W1.0	25½ (648)	12 (305)	9½ (241)	6	6½ (165)	1½ (38)
B2.1	18 (457)	8¾ (222)	10 (254)	4	6½ (165)	1½ (38)
B1.0	25½ (648)	12 (305)	10 (254)	6	6½ (165)	1½ (38)
B1.0C	28¾ (730)	12 (305)	10 (254)	6	6½ (165)	1⅝ (41)

column face using A490 bolts. Both of the enhanced specimens exceeded the AISC *Seismic Provisions* (AISC, 2005a) SMF qualifying requirements.

The research concluded that with adequately proportioned brackets, a repaired connection can redirect the flange tension force, thereby reducing the stress in the flange welded joints. In addition, the global study concluded that the presence of a concrete floor slab was beneficial to specimen performance by enhancing beam stability and delaying strength degradation (Gross et al., 1999).

CAST KAISER BOLTED BRACKET DEVELOPMENT

Following the successful completion of the Lehigh bolted bracket testing, research objectives focused on utilizing a high-strength casting as a replacement for the welded plate bracket. Fabrication of the plate brackets required a significant amount of skilled labor and rigorous inspection, while a one-piece casting could be manufactured in a quality consistent process, with little or no skilled labor.

In accordance with the design provisions outlined by Gross et al. (1999), two cast bracket configurations were developed and the concept was patented with the United States Patent and Trademark Office. The first configuration or W-series bracket is shop fillet-welded to a beam flange. As shown in Figure 2, the horizontal flanges of the W-series brackets are tapered to permit the application of a connecting fillet-weld to the beam flange.

The second configuration or B-series brackets are bolted to a beam flange. As shown in Figure 3, the horizontal flange of the B-series brackets are cast with two rows of parallel bolt holes. While initially intended for the repair of damaged moment connections, the bolted B-series may also be used in new moment frame construction, where a bolted application can facilitate fabrication. Once connected, the design intent is to promote yielding and plastic hinge formation in the beam at the end of the connected brackets.

Based on recommendations from the Steel Founder's Society of America (SFSA), the bracket cast steel specification was designated A148 Grade 80/50, the predecessor to the current specification of A958 Grade SC8620 class 80/50 (ASTM, 2006). The cast steel material has a nominal yield and tensile strength of 50 ksi (354 MPa) and 80 ksi (566 MPa), respectively.

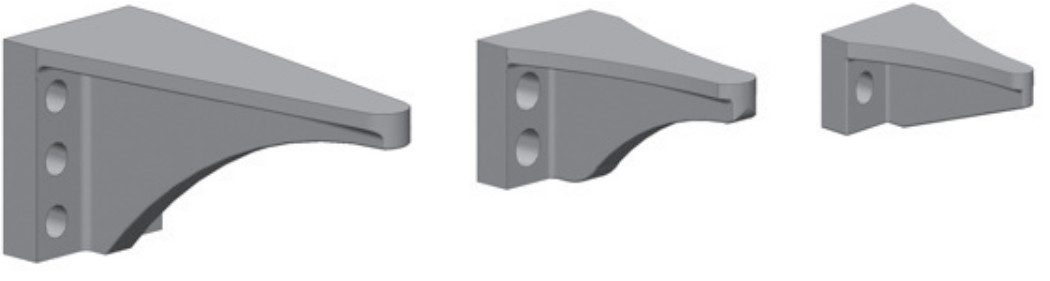

(a) Six-bolt W1.0 *(b) Four-bolt W2.1/W2.0* *(c) Two-bolt W3.1/W3.0*

Fig. 2. W-series bracket.

Table 2. W-Series Bracket Design Proportions						
Bracket Designation	Column Bolt Edge Distance, d_e in. (mm)	Column Bolt Pitch, p_b in. (mm)	Bracket Stiffener Thickness, t_s in. (mm)	Bracket Stiffener Radius, r_v in. (mm)	Bracket Horizontal Radius, r_h in. (mm)	Minimum Fillet Weld Size in. (mm)
W3.0	2½ (64)	None	1 (25)	n.a.	28 (711)	½ (13)
W3.1	2½ (64)	None	1 (25)	n.a.	28 (711)	⅝ (16)
W2.0	2¼ (57)	3½ (89)	2 (51)	12 (305)	28 (711)	¾ (19)
W2.1	2¼ (57)	3½ (89)	2 (51)	16 (406)	38 (965)	⅞ (22)
W1.0	2 (51)	3½ (89)	2 (51)	28 (711)	n.a.	⅞ (22)

Table 3. B-Series Bracket Design Proportions						
Bracket Designation	Column Bolt Edge Distance, d_e in. (mm)	Column Bolt Pitch, p_b in. (mm)	Bracket Stiffener Thickness, t_s in. (mm)	Bracket Stiffener Radius, r_v in. (mm)	Number of Beam Bolts, n_{bb}	Beam Bolt Diameter in. (mm)
B2.1	2 (51)	3½ (89)	2 (51)	16 (406)	8	1⅛ (29)
B1.0	2 (51)	3½ (89)	2 (51)	28 (711)	12	1⅛ (29)
B1.0C	2 (51)	3½ (89)	2 (51)	32 (813)	14	1¼ (32)

The A958 specification imposes a number of requirements beyond identifying the casting steel material. The specification requires the castings be produced in conjunction with a heat treatment process that includes normalizing and stress relieving and requires each batch of steel meet strict mechanical and chemical composition properties. These properties include the specified tensile and yield strengths, as well as elongation and area reduction limitations.

Following production, visual inspection and nondestructive quality control measures are performed on the castings. The nondestructive measures include tensile, radiographic, ultrasonic and magnetic particle testing.

Connection detailing for the Kaiser brackets is shown in Figure 4. The corresponding bracket proportions are summarized in Table 1. The design proportions for the W- and B-series bracket configurations are further summarized in Tables 2 and 3, respectively. In order to accommodate attachment of a fillet weld to the W-series brackets, the beam flange must be at least 6 in. (152 mm) wide. When specifying the B-series brackets, to prevent beam flange tensile rupture, the beam flange must be at least 9 in. (254 mm) wide.

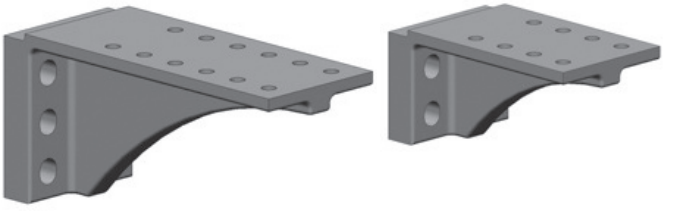

(a) Six-bolt B1.0/B1.0C *(b) Four-bolt B2.1*

Fig. 3. B-series bracket.

As shown in Figures 2(b), 2(c) and 3(a), a dual designation is associated with each of the depicted brackets. The difference between the two designations is the column bolt diameter, the bracket length, or both as indicated in Table 1.

The fasteners connecting the bracket to the beam and column are high-strength pretensioned A490, F2280 or A354 grade BD bolts. In the B-series brackets, when retrofitting an existing connection, the bracket-to-column bolt hole is cast with a standard bolt diameter and the bracket-to-beam bolts holes are cast 1/16 in. (2 mm) smaller than the nominal bolt diameter. Otherwise, the bracket-to-column holes are cast vertically short-slotted for field installation tolerance.

The matching bolt holes in the column and beam flanges are drilled ⅛ in. (3 mm) and 1/32 in. (1 mm) larger than the nominal bolt diameter, respectively. For the B-series, the bracket is typically used as a template to drill the beam flange bolt holes and simultaneously chase the holes in the casting. The strict tolerance on the beam flange bolt holes reduces the potential for connection slip.

For the W-series brackets, the filler metal used to weld the bracket to the beam flange requires rated notch toughness

in accordance with Section 7.3b of the AISC *Seismic Provisions* (AISC, 2005a).

When necessary, finger shims are used to fill the gap between the column flange and the bracket. However, the use of finger shims is subject to the limitations of RCSC *Specification for Structural Joints Using ASTM A325 and A490 Bolts* (RCSC, 2004).

The beam shear tab is a single plate connected to the column flange using a two-sided fillet weld, a two-sided partial-joint-penetration (PJP) groove weld or CJP groove weld. The shear tab is fastened to the beam with A325 bolts.

The thick rear flange of the bracket is designed to eliminate prying action in the bolts. However, prying action is still a design consideration in the connecting column flange.

As shown in Figure 4, the connection of the bracket to the column increases the effective panel zone depth. The increase in depth increases the area of the panel zone and can reduce or, in some cases, eliminate the need for doubler plates in accordance with the requirements of the AISC *Seismic Provisions* (AISC, 2005a).

Continuity plates have been a feature for many code prequalified moment connections. These stiffeners, positioned horizontally on each side of the column, are welded to the flanges and to the web. The use of continuity plates is dictated by the need to satisfy code prescribed limit states for the flange and web of the column. In a bolted connection, the configuration of the fasteners can impede the ability of the stiffeners to effectively address these limit states. The design intent for the KBB connection is to satisfy the prescribed limit states without continuity plates.

CONNECTION EXPERIMENTAL EVALUATION

The effectiveness of the KBB moment-resisting connection has been demonstrated experimentally at both Wyle Laboratories (Norco, California) and at the University of California, San Diego (UCSD). At Wyle Labs, a total of six tests were performed in 1998. Three of the tests were performed to obtain approval from the California Office of Statewide Healthcare Planning and Development (OSHPD) for a hospital moment frame retrofit project and the remaining three to obtain general approval from Los Angeles County for a variety of planned new moment frame projects. At UCSD, a test was performed in July 2005 to determine if the connection was a viable alternative for a moment frame retrofit project in Oakland, California (Newell and Uang, 2006).

Test Matrix

The experimental evaluation involved the testing of seven full-scale KBB connection subassemblies. The test matrix is shown in Table 4, and the details of the specimens are summarized and discussed herein. The test specimens included a wide range of

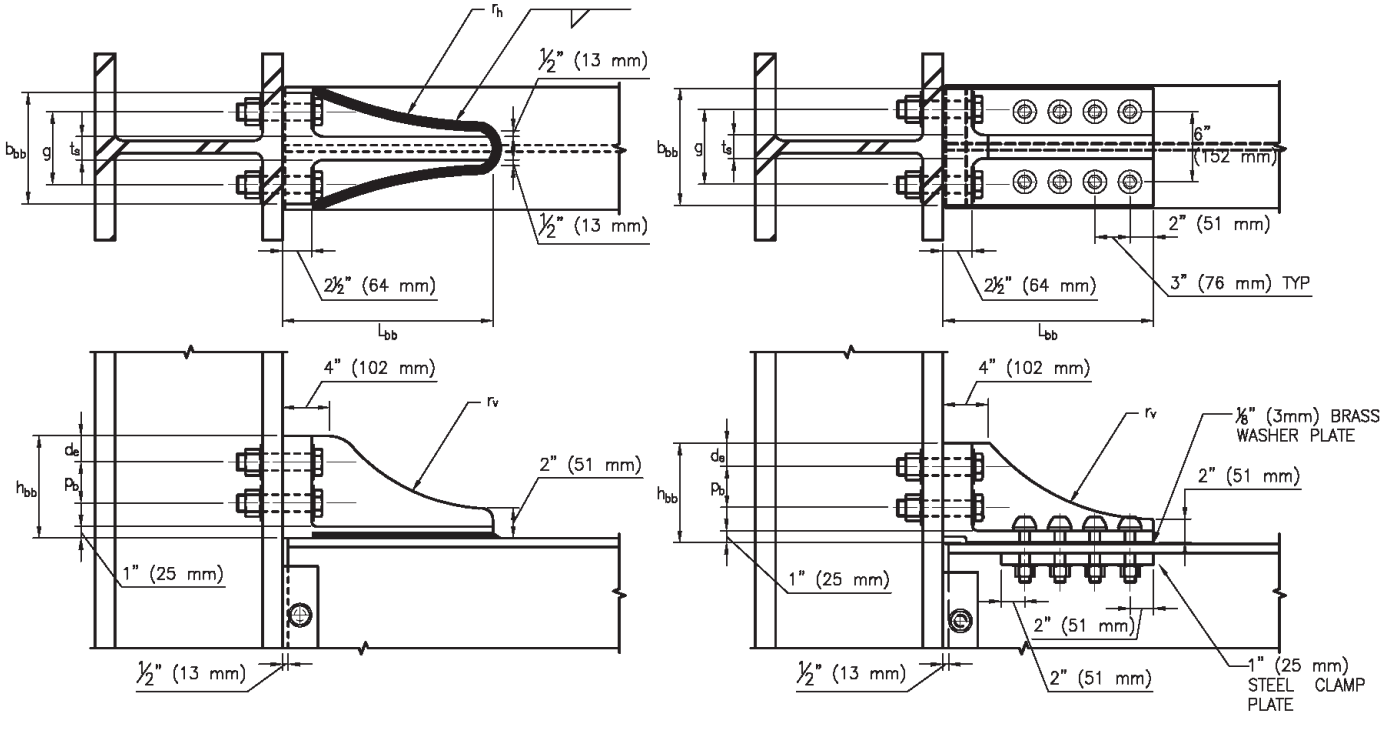

(a) W-series *(b) B-series*

Fig. 4. Kaiser bolted bracket connection detailing.

Table 4. Test Specimen Matrix

Specimen Designation	Column Size	Beam Size	Bracket Size	Column Type	Floor Slab	Span-to-Depth Ratio	$\Sigma M^*_{pc} / \Sigma M^*_{pb}$	Panel Zone $\phi_v R_v / R_u$	Continuity Plates t_{cf}/t_{req}	Loading Sequence
HH-5	Box[a]	W33×130	B1.0	Interior	No	11	0.8	1.0	1.4	ATC-24
HH-5A	Box[a]	W33×130	B1.0	Exterior	No	11	1.3	2.1	1.4	ATC-24
HH-6	W14×233	W30×108	B2.1	Exterior	No	12	1.7	1.1	1.0	ATC-24
HH-7	W14×233	W18×55	W3.1	Exterior	No	20	5.2	2.1	1.4	ATC-24
HH-8	W14×233	W30×108	W2.1	Exterior	No	12	1.7	1.1	1.0	ATC-24
HH-9	W14×132	W24×55	W3.1	Exterior	No	15	2.3	1.1	0.9	ATC-24
UCSD-3	W27×281[b]	W36×210	B1.0C	Interior	Yes	10	0.9	0.6	0.9	AISC-341

[a] Built-up box column: 15⅝ in. (397 mm) square by 1½ in. (38 mm) thick, 288 lb/ft (432 kg/m) total weight
[b] Panel zone strengthened with a ⅜–in. (10–mm) doubler plate (one side) and ⅝–in. (16–mm) continuity plates (both sides)

conditions and applications. Two of the specimens, HH-5 and UCSD-3, represented an interior moment frame column, with one specimen, HH5A, representing a three-sided condition when attached in conjunction to the column of specimen HH-5. One of the specimens, UCSD-3, had a composite concrete floor slab. In this test, to facilitate instrumentation, the concrete slab was blocked out around the brackets. In four of the test specimens, HH5, HH-5A, HH-6 and USCD-3, the bracket was bolted to the beam. These four specimens represented existing moment frame connections under consideration for retrofitting using the bolted bracket. The remaining specimens, HH-7, HH-8 and HH-9, were fillet-welded to the beam to represent new moment frame connections under consideration for construction.

The specimen column sizes ranged from a W14×132 to a W27×281 and included a square box column. The specimen beam sizes ranged from a W18×55 to a W36×210. All of the specimens had nominal steel yield strengths of 50 ksi (345 MPa). The cast Kaiser bracket sizes ranged from a W3.1 to a B1.0C. Each basic bracket size was represented. The clear span-to-depth ratio of the specimens varied between 10 and 20.

Included in Table 4 are the column-beam moment ratios prescribed by the AISC *Seismic Provisions* (AISC, 2005a). The criteria require the columns to be generally strong enough to force flexural yielding in the beam, thereby avoiding the formation of single-story mechanism. Two of the specimens, HH-5 and UCSD-3, both representing existing conditions, did not satisfy the criteria. The criteria are satisfied when the ratio of the sum of the column nominal flexural capacity, ΣM^*_{pc}, to the sum of the beam expect flexural capacity, ΣM^*_{pb}, is greater than 1.0 for each specimen, where the flexural capacities are extrapolated to the intersection of the beam and column centerline in accordance with the AISC *Seismic Provisions* (AISC 2005a).

Also included in Table 4 are the column panel zone (PZ) ratios prescribed by the AISC *Seismic Provisions* (AISC, 2005a). The criteria require minimum strength to prevent excessive column PZ distortion, where the strength, R_v, and the demand, R_u, are defined in accordance with the AISC *Seismic Provisions* (AISC, 2005a).

For reference purposes, Table 4 also includes the continuity plate criteria outlined in AISC *Prequalified Connections for Special and Intermediate Steel Moment Frames for Seismic Applications* (AISC, 2005c), hereafter referred to as the AISC *Prequalified Connections*. The criteria require minimum column flange thickness, t_{cf}, to prevent local flange buckling and to help distribute beam flange forces to the column web.

In order to evaluate the performance of the connection without continuity plates, the wide flange column specimens at Wyle Labs were tested without the stiffeners, with the condition for specimen HH-9 being unconservative. In specimen UCSD-3, continuity plates were provided at the same level as the beam flange.

Material Properties

The beams and columns for specimens HH-5 through HH-9 were fabricated from A572 Grade 50 steel. The beams and column for UCSD specimen were fabricated from A992 steel. The Kaiser bolted brackets were fabricated from A148 Grade 80/50 or 90/60 steel. Table 5 shows the measured static yield and tensile strengths, elongations, heat numbers and material suppliers for the test members. The mechanical properties were determined from tensile coupon tests and certified mill test reports. The cast steel tensile coupons or keel blocks were taken from the same heat as the representative casting in accordance with ASTM standards (ASTM, 2006). Fillet welds connecting the W-series bracket to the

Table 5. Steel Mechanical Properties

Member	Size	Steel Grade	Location	Yield Strength[a] ksi (MPa)	Tensile Strength[a] ksi (MPa)	Elong-ation[a] (%)	Heat Number	Supplier
Column	Box	A572 Gr. 50	Flange	58.2 (402)	85.9 (592)	[18]	2C7673	Geneva
Column	W14×233	A572 Gr. 50	Flange	46.5 (321)	65.7 (453)	[24]	70731	Kawasaki
Column	W14×132	A572 Gr. 50	Not taken	[57.0 (393)]	[76.0 (524)]	[28]	1-44900	Kawasaki
Column	W27×281	A992	Flange	54.4 (375)	74.6 (515)	33	234974	Nucor-Yamato
Column	W27×281	A992	Web	57.2 (395)	75.1 (518)	34	234974	Nucor-Yamato
Beam	W33×130	A572 Gr. 50	Flange	53.6 (370)	73.0 (504)	[22]	83254	Nucor-Yamato
Beam	W30×108	A572 Gr. 50	Flange	55.7 (384)	75.0 (518)	[25]	2-40010	Kawasaki
Beam	W30×108	A572 Gr. 50	Flange	53.0 (366)	67.0 (462)	[25]	2-40010	Kawasaki
Beam	W24×55	A572 Gr. 50	Flange	51.0 (352)	71.0 (490)	[26]	102958	Nucor-Yamato
Beam	W18×55	A572 Gr. 50	Not taken	[56.0 (386)]	[70.0 (483)]	[29]	3-5006	Chaparral
Beam	W36×210	A992	Flange	52.0 (359)	73.0 (504)	34	226190	Nucor-Yamato
Beam	W36×210	A992	Web	67.6 (466)	77.0 (531)	26	226190	Nucor-Yamato
Bracket	B1.0	A148 Gr. 80/50	Keel block	60.0 (414)	87.0 (600)	25	8/21/97-H3	Varicast
Bracket	W3.1	A148 Gr. 80/50	Keel block	61.0 (421)	88.0 (607)	22	12/31/97-H7	Varicast
Bracket	B2.1	A148 Gr. 80/50	Keel block	61.3 (423)	87.9 (607)	24	12/06/97-H3	Varicast
Bracket	W2.1	A148 Gr. 80/50	Keel block	73.9 (510)	102.9 (710)	22	H-3781	Pacific Steel
Bracket	B1.0C	A148 Gr. 90/60	Keel block	73.8 (365)	96.4 (90.0)	22	6336	North Star

[a] Values in brackets are based on Certified Mill Test Reports, others from coupon testing

beam were made from rated notch toughness E71-T8 filler metal. Further details regarding material properties for the UCSD specimen are reported in Newell and Uang (2006).

Test Subassemblage, Loading Protocol and Instrumentation

The subassemblage for the tests performed at Wyle Labs positioned the specimens in a horizontal plane just above the test floor as shown in Figure 5. The ends of the columns had pin-connected boundary conditions, using cylindrical bearings to simulate inflection points at the column mid-height in the prototype frame. The actuator attachment was made near the end of each beam through a load transfer assembly and lateral supports were provided along the beams as shown. The Kaiser brackets were attached to the beam and column specimens as indicated in Figure 4. The W-series brackets were fillet welded to the beam using a weld procedure specification (WPS) qualified for the combination of cast and rolled materials.

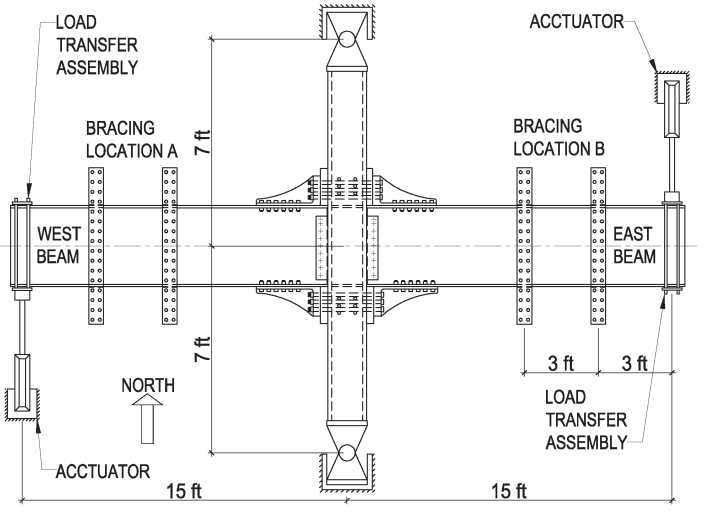

Fig. 5. Wyle Labs horizontally positioned experimental test setup. (Note: 1 ft = 305 mm)

Table 6. Summary of Test Results					
Specimen Designation	Maximum Interstory Drift Angle (% rad)	Maximum Inelastic Drift Angle (% rad)	Maximum Column Face Moment Ratio, M_{cf}/M_p	Maximum Plastic Hinge Moment Ratio, M_{ph}/M_p	Test Failure Mode
HH-5	6.1	4.7	1.51	1.25	No failure, maximized actuator stroke
HH-5A	6.8	5.1	1.55	1.29	No failure, maximized actuator stroke
HH-6	4.6	3.0	1.22	1.09	No failure, slip in the test apparatus
HH-7	4.8	3.1	1.37	1.24	Flange gross area fracture
HH-8	5.6	4.6	1.31	1.18	No failure, excessive buckling in specimen
HH-9	6.9	6.0	1.38	1.25	No failure, maximized actuator stroke
UCSD-3	4.0	3.0	1.35	1.11	Bracket-to-column bolt tensile rupture

The subassemblage for the test performed at UCSD positioned the specimen in a vertical plane. Pins were provided at the ends of the beams and at the top and bottom of the column to simulate inflection points. The actuator attachment was made at the top of the column through a load transfer assembly. Further details regarding the subassemblage including lateral bracing, steel column guides, composite floor connections and other details is reported by Newell and Uang (2006).

The specimens were tested by imposing a prescribed quasi-static cyclic story drift history. At UCSD, the loading history was based on the protocol specified in Appendix S of the AISC *Seismic Provisions* (AISC, 2005a). In this sequence deformations consist of six cycles each of 0.375, 0.5 and 0.75% story drift, followed by four cycles of 1.0% story drift and two cycles each of 1.5, 2, 3, 4 and 5% story drift.

At Wyle Labs, the loading history was based on the protocol specified in ATC 24 (ATC, 1992), which is considered acceptable by the AISC *Seismic Provisions* (AISC, 2005a). In this sequence, deformations are applied to the test specimen, up to the completion of the test, to produce three cycles each of loading at $0.25\delta_y$, $0.68\delta_y$, δ_y, $2\delta_y$, $3\delta_y$, followed by two cycles each of loading at $4\delta_y$, $5\delta_y$, $6\delta_y$, where δ_y is the deformation value at the first significant yield of the test specimen.

The testing was terminated when a fracture occurred, resulting in a significant loss of beam capacity; when the testing apparatus became unstable; or after reaching the equivalent story drift of $6\delta_y$, where $6\delta_y$ was the maximum stroke the actuator could accommodate.

As reported by Newell and Uang (2006), the test specimen at UCSD was instrumented to enable measurement of the applied loads, strains in the beams, column, brackets and panel zone, in addition to panel zone and bracket deformation. The beams, column and panel zone in the connected region were whitewashed prior to testing to provide visual indication of the occurrence of yielding during testing. The test specimens at Wyle Labs were instrumented to enable measurement of the applied loads, strains in the beams, column, brackets and panel zone. The panel zone deformation was not instrumented.

Test Results

All the specimens tested at Wyle Labs exceeded the AISC *Seismic Provisions* (AISC, 2005a) SMF qualifying 4.0% interstory drift angle without significant strength degradation. The UCSD test specimen met the requirement but subsequently experienced an unexpected nonductile connection failure. A summary of the response for each specimen is shown in Table 6, including the maximum interstory drift angle, the corresponding maximum inelastic drift angle, maximum column face moment ratio, maximum plastic hinge moment ratio and the test failure mode.

The interstory drift angle was computed by taking the beam tip displacement and dividing by the distance to the column centerline. The inelastic drift angle was calculated by taking the inelastic portion of the tip deflection and dividing by the distance to the face of the column. The beam column face moment, M_{cf}, was computed by taking the maximum force applied at the beam tip multiplied by the distance to the column face. The beam plastic hinge moment, M_{ph}, was computed by taking the maximum force applied at the beam tip multiplied by the distance to the end of the bracket. The column face and plastic hinge moment ratios are calculated by dividing the respective moment by the corresponding beam nominal plastic moment, M_p.

Figure 6 (pp. 190–191) shows plots of the applied load versus beam tip displacement for each specimen tested at Wyle Labs. The corresponding beam moment and interstory drift angle are also shown on the plots. The 4.0% interstory drift angle is shown with vertical dashed lines and the 80%

nominal plastic moment is shown with horizontal dashed lines corresponding to the AISC *Seismic Provisions* (AISC, 2005a) strength degradation requirement. As indicated in Figure 6, each of the specimens underwent a gradual deterioration of strength following the onset of local flange and web buckling of the beam. This gradual reduction in strength typically occurred after about 3.0 to 4.0% drift.

Specimens HH-5 and HH-5a were erected and tested separately on the opposing faces of the same built-up box column. As mentioned previously, the test was intended to represent an interior three-sided moment connection. A 1¾-in. (44-mm) spacer plate was positioned between the HH-5A beam flange and the brackets to offset the bolt holes projecting through the column. The hysteretic plots are shown in Figures 6(a), 6(b) and 6(c) for specimen HH-5 east beam, HH-5 west beam and HH-5A orthogonal beam, respectively. The slight pinching observed in the plots can be attributed to the slip-bearing behavior of the bolted beam flange connection. Following some amount of initial slip, subsequent hardening due to bolt bearing is observed. In specimen HH-5, panel zone yielding was observed in the column. Strain gauges were observed to be in the yield range at an interstory drift angle of approximately 3.3% drift. The same level of panel zone strain was not observed in the single-sided specimen HH-5A.

The tests were halted at 6.1% and 6.8% drift for specimen HH-5 and HH-5A, respectively, after the maximum actuator stroke was reached. At this level of rotation, a distinct plastic hinge had formed near the far end of the brackets as shown in Figures 7(a) and (b) (p. 192) for specimen HH-5 and HH-5A, respectively. Figure 7(c) shows a close-up of the beam flange near the end of the bracket in specimen HH-5 east, highlighting the ability of the thin brass washer and clamp plates to mitigate net area fracture. This detailing prevents flange buckling and abrading from distorting the first row of bolts as exhibited in earlier bolted bracket testing (Kasai et al., 1998).

Specimens HH-6 and HH-8 both used the same size beam and column. For specimen HH-6, the B-series brackets were bolted to the beam flange, and for specimen HH-8, the W-series brackets were welded to the beam flange. The test for specimen HH-6 was halted at approximately 4.6% drift to prevent damage to the test apparatus due to beam flange local buckling and column base anchorage bolt slip.

As shown in Figure 8(a) (p. 192), a 2-in. (50-mm) crack in the bracket-to beam fillet weld of specimen HH-8 was observed near the nose of the bracket at approximately 3.3% drift. Following a short pause, the test was continued with no observance of further crack growth. At approximately 5.6% drift, the test was halted to prevent damage to the apparatus due to excessive beam buckling. In both specimens HH-6 and HH-8, a plastic hinge was formed in the beam near the far end of the brackets. Figure 8(b) shows the hinge in specimen HH-8 at the end of the test.

Specimens HH-7 and HH-9 both had W-series brackets welded to the beam. The hysteretic plots are shown in Figures 6(e) and 6(g) for specimen HH-7 and HH-9, respectively. As shown in Figure 6(e), the combined strong column-weak beam and high PZ ratios focused the majority of the inelastic rotation into the beam. The test for specimen HH-7 was terminated at approximately 5.9% drift following gross area fracture in the beam flange. As shown in Figure 8(c), the fracture occurred approximately 3 in. (76 mm) from the end of the bracket in the same general vicinity where local inelastic buckling and low cyclic fatigue had weakened the lange.

The test for specimen HH-9 was halted at approximately 6.9% drift after the maximum actuator stroke was reached. At this level of rotation, a plastic hinge had formed in the beam near the far end of the brackets. Figure 9 (p. 193) shows the hinge in specimen HH-9 at the end of the test.

Specimen UCSD-3 represented an existing interior connection with a composite slab. During the test, as reported by Newell and Uang (2006), yielding in the column panel zone and in both the beam and column flanges was initially observed at approximately 0.75% drift. The column doubler plate had noticeably buckled at approximately 3.0% drift. On the first positive excursion to 4.0% drift, one of the lower bracket-to-column bolts ruptured. Despite the rupture and after a brief pause, the test was continued. On the first negative excursion to 4.0% drift, a bracket-to-column bolt on the opposite lower beam subsequently ruptured. Upon completion of the second full cycle of 4.0% drift, all the remaining lower bracket-to-column bolts ruptured, and the attaching bottom flange CJP weld fractured. Following the test, the remaining upper bolts were removed and observed to have been bent where the threaded portion of the bolt was in contact with the column flange.

Evaluation of Test Results

As indicated in Table 6, the specimen maximum plastic hinge moment ratios were similar to or less than the factor of 1.27 prescribed by AISC *Prequalified Connections* (AISC, 2005c) to account for both material overstrength, R_y, and strain hardening, C_{pr}.

Following a significant amount of inelastic strain, specimen HH-7 failed by gross area ductile fracture of the beam flange near the end of the bracket. While the cyclic loading of the remaining specimens at Wyle Labs was halted prior to fracture, given the observed cyclic inelastic strains, had the testing continued, flange gross area fracture would have been expected in these specimens as well.

As mentioned previously, the test specimens were instrumented with strain gauges to enable measurement of inelastic behavior in each of the connection components, including the beam and column flanges, the panel zone and the brackets. The component normalized tensile strains at 4.0%

Table 7. Component Normalized Tensile Strains at 4% Interstory Drift									
Specimen Designation	Beam Flange Net Area	Beam Flange Gross Area	Column Flange Net Area	Column Flange Gross Area	Panel Zone	Bracket Stiffener Edge	Bracket Heel	$\frac{\Sigma M^*_{pc}}{\Sigma M^*_{pb}}$	Panel Zone $\phi_v R_v / Ru$
HH-5	6.5	3.5	1.5	1.2	0.4	4.2	0.9	0.8	1.0
HH-5A	6.5	3.5	0.5	0.7	0.2	3.3	1.0	1.3	2.1
HH-6	5.0	3.6	0.5	No Gauge	0.2	0.6	0.5	1.7	1.1
HH-7	Not bolted	7.0	0.2	0.2	0.1	0.5	0.4	5.2	2.1
HH-8	Not bolted	5.0	No Gauge	0.2	0.3	1.2	0.3	1.7	1.1
HH-9	Not bolted	4.0	0.4	0.4	0.8	0.5	0.3	2.3	1.1
UCSD-3	20.0	6.0	20	4.0	15.0	1.0	0.3	0.9	0.6

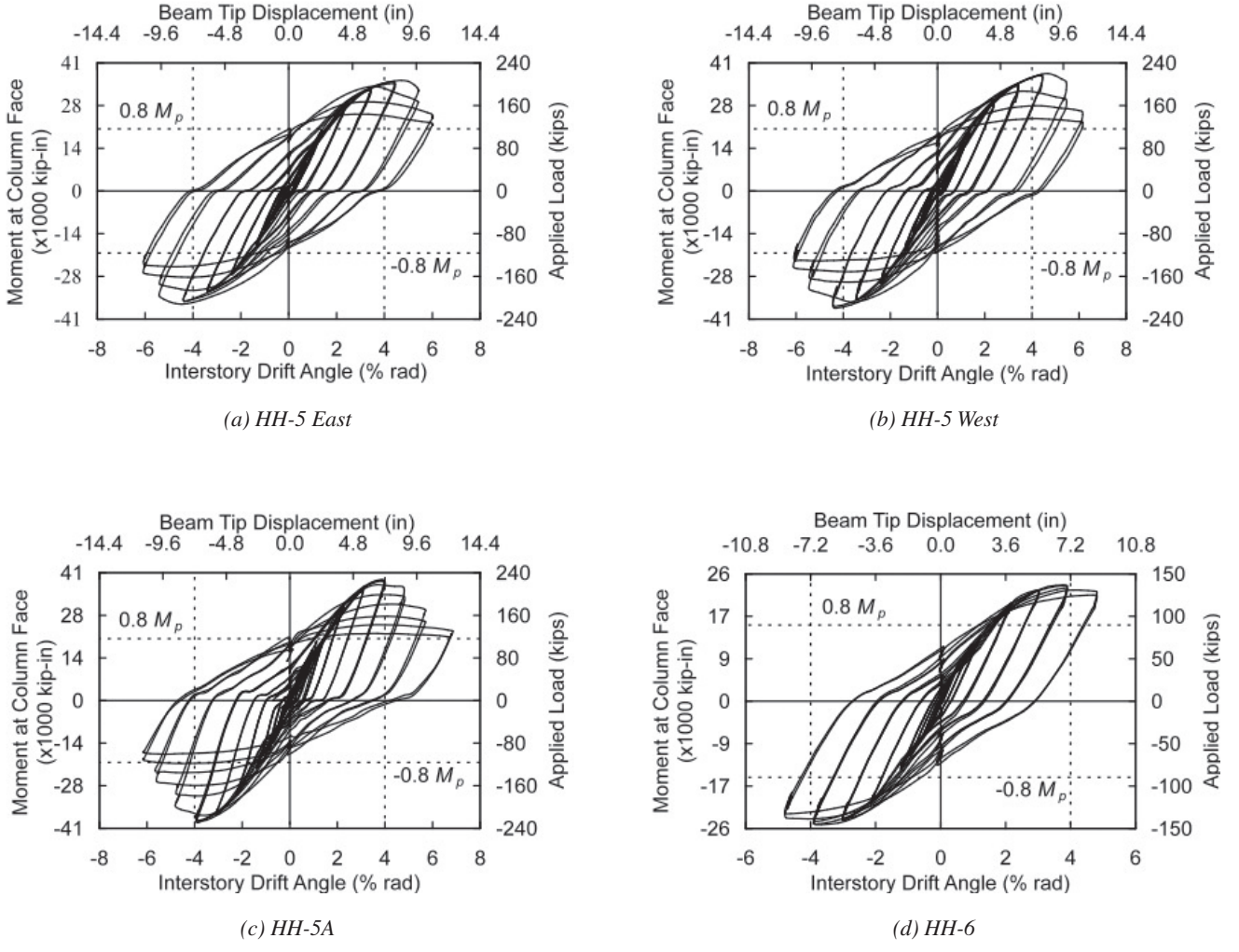

(a) HH-5 East

(b) HH-5 West

(c) HH-5A

(d) HH-6

Fig. 6. Applied load versus beam tip displacement—Wyle Labs specimens. (Note: 1 kip = 4.44 kN; 1 in. = 25.4 mm)

interstory drift are show in Table 7. In this table, the calculated column-beam and PZ ratios are repeated from Table 4 to compare with the measured strains. Although not totally inclusive of all inelastic contributions, these values indicate how each primary component contributed to the total inelastic behavior of the connection. For example, the calculations and strain measurements for specimen HH-7 indicate that virtually all the plastic rotation was developed within the beam; essentially no inelastic behavior was observed or recorded in the column, panel zone or brackets.

Each of the cast bracket stiffeners were instrumented on the free edge and near the junction of the vertical and horizontal flange (heel). As shown in Table 7, inelastic tensile strain in the brackets was limited to locations on the free edge. Following the completion of each test, no visible signs of distress to the stiffeners or to any other portion of the brackets were detected.

As described previously, and as shown in Figure 8(a), the bracket fillet weld in specimen HH-8 developed a 2-in. (50-mm) crack at the nose of the bracket. Despite the incident, the test was continued with no further observed crack growth. It is believed that the high toughness weld metal was a key factor that prevented the growth of the crack. Following the test, the procedure used to fillet weld the bracket to the beam was modified to avoid terminating weld passes near the bracket nose. Apparently, the specimen HH-8 weld passes had been terminated in this region. During the subsequent tests for specimens HH-7 and HH-9, no cracks were observed in the fillet welds made with the revised procedure.

Both column and beam flange bolt slip was observed in the test specimens. Figures 6(a) through 6(d) of the hysteretic plots show varying levels of pinching due to beam bolt slip. Column bolt slip is also evident in the hysteretic plots,

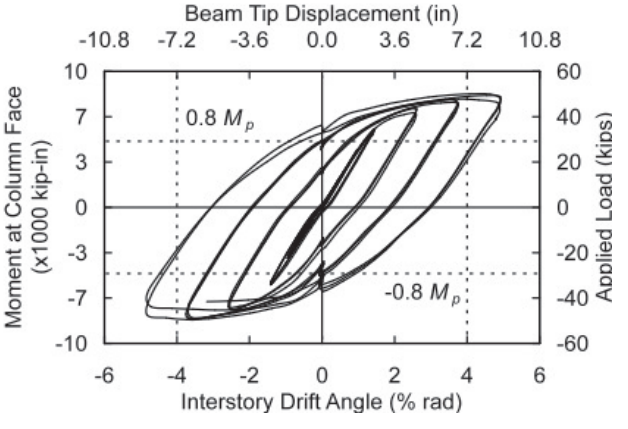

(e) HH-7

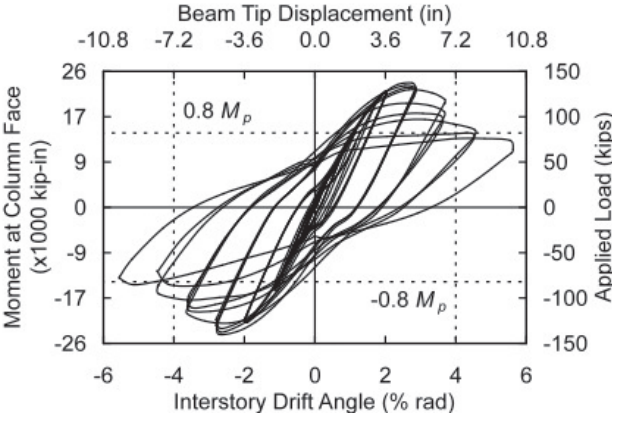

(f) HH-8

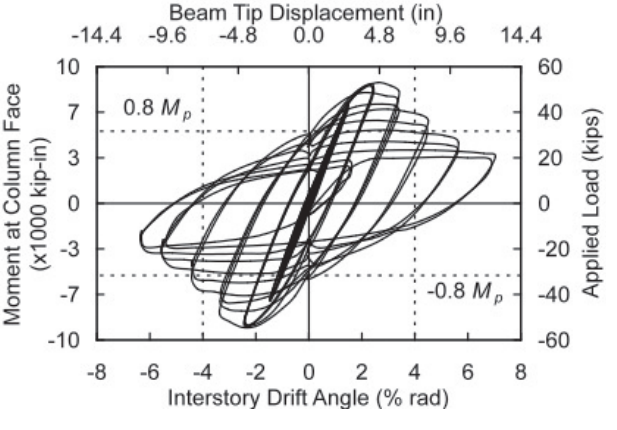

(g) HH-9

Fig. 6. (cont.) Applied load versus beam tip displacement—Wyle Labs specimens. (Note: 1 kip = 4.44 kN; 1 in. = 25.4 mm)

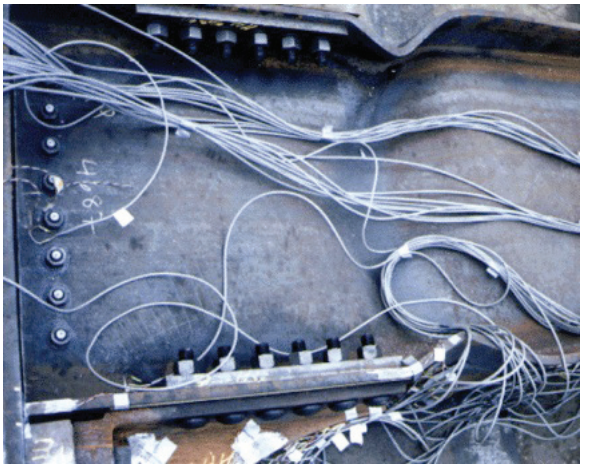

(a)

(b)

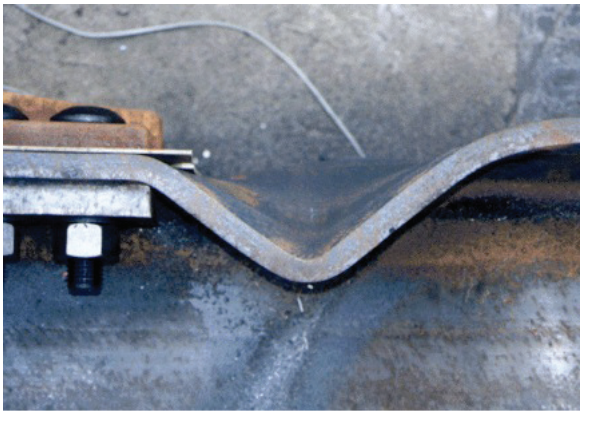

(c)

Fig. 7. Photographs of specimens at the end of testing: (a) HH-5 east beam hinge formation; (b) HH-5A hinge formation; (c) HH-5 east beam flange local buckling.

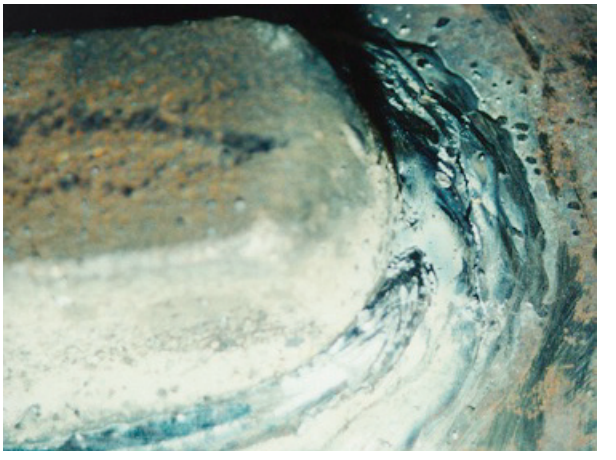

(a)

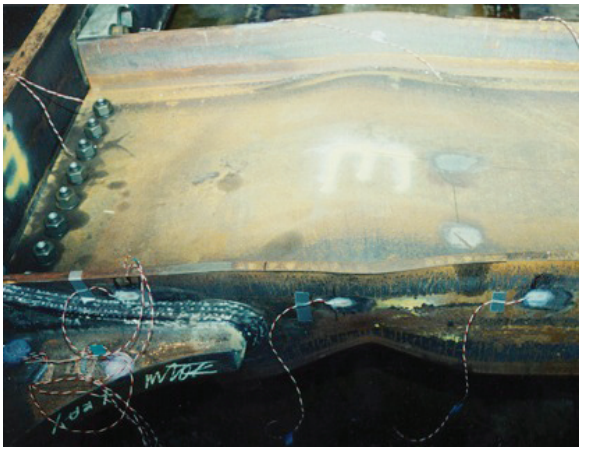

(b)

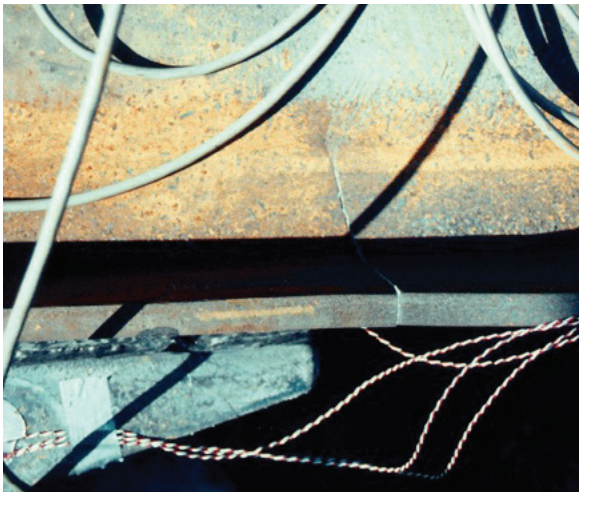

(c)

Fig. 8. Photographs of specimens at the end of testing: (a) HH-8 fillet weld crack close up; (b) HH-8 hinge formation; (c) HH-7 flange gross area fracture.

although less pronounced. In bolted connections, some amount of limited and controlled slip can be a desirable phenomenon. As a result of slippage, the stiffness of the structure decreases, the period elongates, and the energy dissipation and damping increase, all positive benefits. However, excessive slip can result in larger than expected story drifts. To limit and control slip, the B-series bracket specifies the use of smaller-diameter drilled beam bolt holes. Because the brackets can be either fastened to the beam in a fabrication shop or drilled in-place using the bracket as a template, the controlled conditions permit the strict tolerance required by the smaller-diameter hole.

In the Wyle Labs wide flange columns specimens, the tests were intended to evaluate the performance of the connection without continuity plates. In those specimens, the absence of continuity plates did not appear to promote local flange buckling or lead to other detrimental effects.

In specimen UCSD-3, significant yielding was observed and recorded in the panel zone. Analysis of the test data for specimen UCSD-3 indicated that between one-half and two-thirds of the total plastic rotation was developed by panel zone yielding, with the remainder developed by yielding in the beams and columns, particularly in the flange net areas (Newell and Uang, 2006). As shown in Table 7, measured inelastic strain in the panel zone was significant. Given the panel zone yielding and the observed bending in the remaining bracket-to-column bolts, deformation of the connecting column likely caused bolt tensile force levels to increase above their ultimate strength and fail. As indicated by the AISC *Steel Construction Manual* (AISC, 2005d), hereafter referred to as the AISC *Manual*, this prying action phenomenon can significantly increase the tensile force in a bolt.

Fig. 9. Photograph of hinge formation at the end of testing specimen HH-9.

Subsequent analysis of specimen UCSD-3 also determined several unintentional column limit state deficiencies. As indicated in Table 7, the column strength was significantly lower than that of the attaching beams. This condition can promote the formation of a hinge in the column, typically just below the level of the stiffened region. Table 4 indicates the column was also susceptible to local flange buckling. Although equipped with a continuity plate, the position of the bracket below the stiffener does not adequately limit flange buckling due to the offset distance. Finally, analysis of the column indicated the flange bolt holes did not satisfy the tensile rupture limit state provisions of AISC 360 *Specification for Structural Steel Buildings* (AISC, 2005b). Had the column satisfied these critical limit state design provisions, a more desirable ductile failure mode would have been anticipated. Although the specimen satisfied the SMF requirements for drift and strength, as part of this evaluation, the results are not considered justification to prequalify the specimen column, beam and bracket combination.

The presence of a composite floor slab on specimen UCSD-3 did not appear to promote the bolt fracture or lead to other detrimental effects. On the contrary, the presence of the slab was beneficial to specimen performance by enhancing beam stability and delaying strength degradation despite the high levels of recorded inelastic strain.

Although specimen UCSD-3 incorporated the use of a deep column section, the majority of bolted bracket specimens have been tested with W14 columns. In previous testing of RBS connections with deeper column sections, Ricles et al. (2004) concluded that the deeper columns do not behave substantially different from W14 columns and that no special consideration or bracing was needed when a slab is present.

The limited number of tests conducted in this program is insufficient to prequalify beams larger than those tested at Wyle Labs. However, the results can be used to develop design provisions for equivalent sized beam and bracket combinations. Those provisions, currently under development, will be the focus of a future paper.

SUMMARY AND CONCLUSIONS

An experimental study was performed to investigate the Kaiser bolted bracket steel moment-resisting connection. The study included a review of historical bolted bracket tests and the evaluation of seven full-scale specimens using a high-strength cast steel bracket. The parameters investigated in the experimental program included (1) column size, (2) beam size, (3) bracket size, (4) bracket connections, (5) and clear span-to-depth ratios. The conclusions that follow are based on the test results of this study.

1. For new construction, the KBB connection is able to satisfy the criteria in Appendix S of the AISC *Seismic Provisions* (AISC, 2005a) for qualifying a connection for use in a special moment frame. The connection directs yielding and inelastic beam deformation away from the column face and outside the connected region.

2. For existing connections, the KKB connection is capable of improving the capacity of weakened or damaged moment connections. A bottom-only bracket configuration is not recommended when used in conjunction with low notch toughness (pre-Northridge) CJP weld connecting the top flange.

3. For the range of column sizes investigated in this study, it is recommended that deep and box columns be considered for prequalification. Based on the similarity in performance to that of the RBS connection, the expected column sizes would include an equivalent depth up to a W36 section. The use of box columns participating in orthogonal moment frames is also recommended. There was insufficient testing to determine if box column depths deeper than 16 in. (406 mm) should be considered.

4. For the range of W14 column sections investigated in this study, the lack of continuity plates did not have a significant effect on performance. It is recommended that the stiffeners be eliminated when the column flange thickness satisfies local flange buckling limit state requirements. There was insufficient testing to determine if deeper column sections can tolerate the removal of continuity plates. Therefore, in deeper sections, continuity plates are recommended at the same elevation as that of the beam flanges.

5. For the range of beam and bracket sizes investigated in this study, it is recommended that beam sizes be limited to an equivalent beam depth of a W33 section and a maximum beam weight of 130 lb/ft (195 kg/m) with a clear span-to-depth ratio of 8 or greater.

6. For bolted connections, deformation of the connecting column flange can increase the tensile force in the bolt above that due to the direct tensile force alone. It is recommended that the prying action specification requirements of the AISC *Manual* (AISC, 2005d) be considered when calculating the size of the fastener.

7. To avoid the formation of discontinuities in the fillet welds connecting the W-series bracket to the beam flange, it is recommended that weld passes should not be stopped or started within 2 in. (51 mm) of the bracket nose and should be continuous around the nose. In addition, the use of a high toughness weld metal is recommended.

8. In the B-series brackets, beam net area fracture, common in bolted flange connections, can be mitigated with special detailing including the use of a thin brass washer plate at the bracket-to-beam interface and clamp plates opposite the connected bracket.

9. Connection slip in beams with bolted flange connections can be controlled and limited with a strict tolerance on the drilled bolt hole diameter.

ACKNOWLEDGMENTS

The research in this paper was partially provided with the financial support of Steel Cast Connections (www.steelcast-connections.com) of Seattle, Washington, which is the current patent holder of the Kaiser bolted bracket. The authors wish to thank Mr. Ian C. Hodgson of Lehigh University for providing information on the initial bracket testing performed at Lehigh University; Mr. David Bleiman of Rutherford & Chekene, whose work at IFC Kaiser Engineering led to the development of the Kaiser brackets and who supervised the testing performed at Wyle Labs; Dr. Chia-Ming Uang and Mr. James Newell of the University of California, San Diego, who supervised the testing performed at UCSD; and Mr. Ronald Hamburger of Simpson Gumpertz & Heger, who provided a technical review of this manuscript.

The writers are solely responsible for the accuracy of statements or interpretation contained in this publication. No warranty is offered with regard to the results, findings and recommendations contained herein by Steel Cast Connections, LLC. The organization and authors do not assume any legal liability or responsibility for the accuracy, completeness or usefulness of any of the information, product or processes included in this publication.

REFERENCES

AISC (2005a), *Seismic Provisions for Structural Steel Buildings,* AISC/ANSI 341-05, American Institute of Steel Construction Inc., Chicago.

AISC (2005b), *Specification for Structural Steel Buildings,* AISC/ANSI 360-05, American Institute of Steel Construction Inc., Chicago.

AISC (2005c), *Prequalified Connections for Special and Intermediate Steel Moment Frames for Seismic Applications,* AISC/ANSI 358-05, American Institute of Steel Construction, Chicago.

AISC (2005d), *Steel Construction Manual,* 13th ed., American Institute of Steel Construction, Chicago.

ATC (1992), *Guidelines for Cyclic Seismic Testing of Components of Steel Structures,* ATC-24, Applied Technology Council, Redwood City, CA.

ASTM (2006), "Standard Specification for Steel Castings, Carbon and Alloy, with Tensile Requirements, Chemical Requirements Similar to Standard Wrought Grades," ASTM Standard A958-00 (Reapproved 2006), American Society for Testing and Materials, West Conshohocken, PA.

Anderson, J.C. and Linderman, R.R. (1991), "Post Earthquake Repair of Welded Moment Connections," *Report No. CE 91-04*, Department of Civil Engineering, University of Southern California, Los Angeles.

Engelhardt, M.D. and Sabol, T.A. (1994), "Testing of Welded Steel Moment Connections in Response to the Northridge Earthquake," *Northridge Steel Update*, American Institute of Steel Construction, Chicago.

FEMA (2000), *Recommended Seismic Design Criteria for New Moment-Resisting Steel Frame Structures,* Report No. FEMA 350, Federal Emergency Management Agency, Washington, DC.

Grigorian, C.E., Yang, T.S. and Popov, E.P. (1992), "Slotted Bolted Connection Energy Dissipators," *EERC Report No. 92/10*, Earthquake Engineering Research Center, University of California, Berkeley, CA.

Gross, J.L., Engelhardt, M.D., Uang C.M., Kasai, K. and Iwankiw, N.R. (1999), "Modification of Existing Welded Steel Moment Frame Connections for Seismic Resistance," *AISC Design Guide No. 12*, American Institute of Steel Construction, Chicago.

Kasai, K., Hodgon, I. and Bleiman, D. (1998), "Rigid-Bolted Repair Methods for Damaged Moment Connections," *Engineering Structures,* Vol. 20, No. 4–6, pp. 521–532.

Newell, J. and Uang, C.M. (2006), "Cyclic Testing of Steel Moment Connections for the CALTRANS District 4 Office Building Seismic Rehabilitation," *UCSD Report No. SSRP-05/03*, University of California, San Diego.

RCSC (2005), *Specification for Structural Joints Using ASTM A325 or A490 Bolts,* Research Council on Structural Connections, Chicago.

Ricles, J.M., Zhang, X., Lu L.W. and Fisher, J. (2004), "Development of Seismic Guidelines for Deep-Column Steel Moment Connections," *ATLSS Report No. 04-13*, Lehigh University, Bethlehem, PA.

Tremblay, R., Timlez, P., Bruneau, M. and Filiatrault, A. (1995), "Performance of Steel Structures During the 1994 Northridge Earthquake," *Canadian Journal of Civil Engineering,* Vol. 22.

Youssef, N.F.G., Bonowitz, D. and Gross, J.H. (1995), "A Survey of Steel Moment-Resisting Frame Buildings Affected by the 1994 Northridge Earthquake," *Report No. NISTIR 5625*, National Institute of Standards and Technology, Gaithersburg, MD.

Experimental Investigation of Fillet-Welded Joints Subjected to Out-of-Plane Eccentric Loads

AMIT M. KANVINDE, GILBERT Y. GRONDIN, IVAN R. GOMEZ and YUKAY KWAN

Fillet-welded connections are popular in civil engineering construction due to their economy (minimal surface preparation is required prior to welding) and strength, and various aspects of their response have been studied extensively over the past five decades. Building on the early studies of Ligtenburg (1968), Clark (1971) and Butler and Kulak (1971), subsequent research efforts (e.g., Butler, Pal and Kulak, 1972; Miazga and Kennedy, 1986, 1989; Lesik and Kennedy, 1990) have led to the development of strength prediction approaches for welded connections loaded concentrically as well as eccentrically. Design considerations based on these approaches have been implemented in current North American design specifications (AISC, 2005; CISC, 2007).

Within this overall theme of research on fillet-welded connections, this paper focuses on the response of eccentrically loaded fillet welds where the load is not in the plane of the weld group, such as illustrated schematically in Figure 1(a). This type of weld group and loading configuration is described as a "special-case" in current weld design tables provided by the American Institute of Steel Construction (Table 8-4, *Steel Construction Manual*, AISC, 2005). Referring to the illustration in Figure 1(a), these joints resist the applied load through the development of stresses in the welds as well as bearing stresses over the contact surface of the attached plates. However, as discussed in this and the subsequent section, approaches adopted in current design practice (AISC, 2005) do not incorporate all aspects of behavior that control the strength of these joints. The design table adopted by AISC (Table 8-4, *Steel Construction Manual*, AISC, 2005) is based on the method of the instantaneous center (IC) of rotation (Tide, 1980). This IC method, as applied in development of the current design table, relies on the principle that at the strength limit state, the weld group rotates about a center of rotation, resulting in compatible deformations for all segments of the weld. Contingent on these deformations, the stresses in the weld segments are determined through a load-deformation relationship such as the one proposed by Lesik and Kennedy (1990). While the assumptions underlying the design table are consistent with the response of eccentrically loaded lap joints, they are questionable when applied to eccentrically loaded joints where the applied load is not in the plane of the weld group. Specifically, two issues are of concern. First, the eccentrically loaded configuration shown in Figure 1(a) produces a root notch at the unfused interface of the plates. Previous studies (e.g., Ng et al., 2002; Pham, 1983; Kanvinde et al., 2008) indicate that such a root notch, perpendicular to the direction of the bending stresses in the connection, produces a crack-like effect, possibly reducing both the strength and the ductility of the welds with respect to values implicitly assumed in the design table. This flaw, subjected to Mode I (crack opening) loads, is of greater concern as compared to a similar flaw in lap joints, which is subjected to Mode II (shear) loads. The second, and perhaps a more important issue, pertains to bearing in the region of compression between the connected plates. The design table is based on an approach that disregards this effect (Tide, 1980), leading to an inappropriate representation of the stress distribution in the welded joint. The reliance on this approach may be due to the relative lack of experimental data from welds loaded eccentrically out of plane. In fact, in addition to the current study, only two other documented test programs

Amit M. Kanvinde is an assistant professor of civil and environmental engineering, University of California, Davis.

Gilbert Y. Grondin is a professor of civil and environmental engineering, University of Alberta, Edmonton.

Ivan R. Gomez is a graduate student researcher in civil and environmental engineering, University of California, Davis.

YuKay Kwan is a graduate student researcher in civil and environmental engineering, University of Alberta, Edmonton.

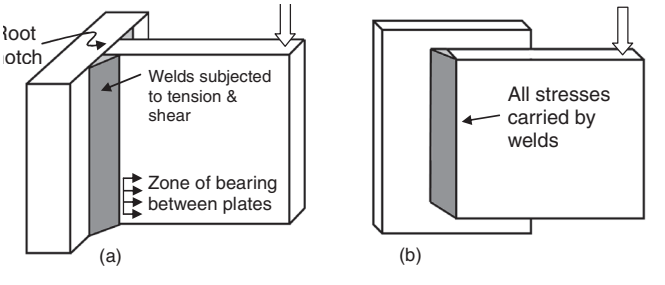

Fig. 1. Welded connection subjected to (a) out-of-plane eccentric load and (b) in-plane eccentric load.

(Dawe and Kulak, 1972, 1974; Beaulieu and Picard, 1985) have investigated this situation experimentally. Motivated by these issues, the main objectives of this paper are to (1) obtain a data set of test results of sufficient size to conduct a meaningful statistical analysis of the strength characteristics of welded connections loaded with out-of-plane eccentricity, (2) evaluate the effect of various parameters (under a wider range of values) on this strength in a systematic way, and (3) assess the applicability and level of safety provided by current design practice.

To realize these objectives, the main experimental basis for this paper is a series of 60 bend tests on cruciform specimens (such as shown in Figure 2) that evaluate the effect of a range of parameters, including weld size, weld metal toughness, load eccentricity and plate bearing width. The tests presented here are part of a comprehensive parent study that also included experiments and investigations of the effect of the weld root notch on the tensile strength and ductility of fillet welds (Gomez et al., 2008).

A review of the literature relevant to this study is first presented. Subsequent sections address the experimental program, including ancillary tests and bending tests on cruciform welded specimens to investigate the out-of-plane loading condition. The data from these tests are then reviewed and analyzed along with data from prior testing programs to assess the effectiveness of the current design approach and the effect of various parameters on its applicability. An alternate model that considers the bearing effect between the plates is presented as a more suitable method to characterize the joint strength. The paper concludes by reviewing the findings and limitations of the study while outlining strategies for future research.

BACKGROUND AND OBJECTIVES

This section summarizes prior research from the early 1970s to the present, focusing on the development of test programs and analysis methods of the behavior of fillet-welded joints with out-of-plane eccentricity. While the review presented here is directly relevant to this paper, a more comprehensive background of related research (including studies on various weld configurations under concentric loading) is available in Gomez et al. (2008) and Ng et al. (2002).

Several experimental studies (e.g., Butler et al., 1972; Swannell, 1981a, 1981b; Sanaei and Kamtekar, 1988) have investigated the behavior of eccentrically loaded fillet-welded connections through experiments on lapped specimens, such as illustrated schematically in Figure 1(b). Whereas these studies have validated several theoretical approaches to predict the strength of these eccentrically loaded welded connections, they only consider situations where the eccentric load is in the plane of the weld group, such as illustrated in Figure 1(b). Experimental studies that examine situations where the eccentric load is not in the plane of the weld group, such as illustrated in Figure 1(a), are relatively scarce, and prior to the current study, only two significant documented test projects have investigated this configuration. These are reviewed first, before discussing various theoretical models for strength prediction.

The first experimental study, by Dawe and Kulak (1972), included eight specimens to investigate the behavior of weld groups subjected to out-of-plane eccentric loading. The test specimens consisted of a wide flange section with its end welded to an end plate by fillet welds along the outer side of each flange. The test configuration involved loading the wide flange sections in minor axis bending to determine the joint strength. The key variables investigated included the length of weld, the eccentricity of load and the thickness of the connected plate. Two nominal weld lengths (8 in. and 12 in.) and four load eccentricities (ranging from 8 in. to 20 in.) were considered. Since the specimens were loaded in the minor axis orientation, the effective plate bearing width was determined as twice the flange thickness of the wide flange section. Using this interpretation, five nominal bearing widths (ranging from 0.86 in. to 1.24 in.) were investigated. All specimens were fabricated from ASTM A36 steel and featured ¼-in. (nominal leg size) fillet welds deposited with AWS A5.1 E60XX compliant electrodes. Table 1 summarizes the main aspects of the test series, including test results, which will be discussed later. A detailed analysis of these data and comparison to the current study are presented in a subsequent section.

The second experimental study, by Beaulieu and Picard (1985), included a total of 24 fillet welded plate connections loaded eccentrically out-of-plane. Referring to Table 1, the

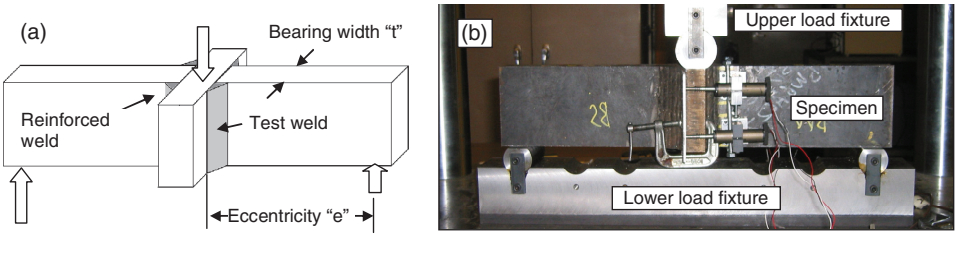

Fig. 2. Cruciform joint bending specimens: (a) schematic and (b) photograph of test setup.

Table 1. Results of Cruciform Bend Tests from Dawe and Kulak (1972) and Beaulieu and Picard (1985)

Test Program	Test #	a[a]	Nom[b] in.	t[c] in.	R_{max}[d] kips	$\frac{R_{max}}{R_n^{AISC}}$[e]	$\frac{R_{max}}{R_n^{bearing}}$[f]
Dawe and Kulak (1972)	1	1.03	¼	1.04	62.5	1.36	1.07
	2	1.53	¼	1.04	39.0	1.22	0.96
	3	2.03	¼	1.04	23.1	0.99	0.78
	4	2.56	¼	1.06	19.5	1.06	0.83
	5	2.04	¼	0.86	23.6	1.02	0.89
	6	2.02	¼	1.52	32.6	1.29	0.95
	7	1.26	¼	1.24	59.7	1.11	0.83
	8	1.69	¼	1.24	49.6	1.15	0.88
Beaulieu and Picard (1985)[g]	1	1.50	¼	0.79	50.9	1.08	1.02
	2	1.50	½	0.79	61.9	0.73	0.94
	3	0.50	¼	0.79	157.9	1.19	1.10
	4	0.50	¼	0.79	141.7	1.10	1.00
	5	0.30	¼	0.79	245.9	1.39	1.27
	6	1.51	5/16	1.58	93.5	1.27	1.03
	7	1.49	5/16	1.58	96.1	1.31	1.05
	8	1.51	⅜	1.58	61.3	0.85	0.68
	9	1.51	⅜	1.58	109.1	1.49	1.20
	10	0.50	5/16	1.58	235.7	1.35	1.08
	11	0.50	5/16	1.58	286.6	1.66	1.32
	12	0.50	⅜	1.58	266.2	1.56	1.24
	13	0.50	⅜	1.58	249.5	1.39	1.12
	14	0.30	5/16	1.58	334.6	1.68	1.45
	15	0.30	5/16	1.58	313.4	1.66	1.43
	16	0.31	⅜	1.58	381.5	1.42	1.24
	17	0.30	⅜	1.58	358.7	1.34	1.18
					Mean	**1.27**	**1.06**
					Coefficient of variation	**0.19**	**0.19**

[a] Load eccentricity ratio = load eccentricity length divided by weld group length.
[b] Nominal (specified) weld size.
[c] Plate (root notch) thickness.
[d] R_{max} = maximum eccentric force observed in experiments.
[e] R_n^{AISC} = predicted strength based on AISC approach.
[f] $R_n^{bearing}$ = predicted strength on alternate approach incorporating bearing.
[g] Only 17 of 24 tests reported; others failed by plate rupture.

key variables investigated in this study include the weld size (nominally ¼ in., ⅜ in., 5/16 in. and ½ in.), the load eccentricity (ranging between 3 in. and 14.75 in.) and the bearing width, also equal to the root notch length (0.787 in. and 1.575 in.). All specimens were fabricated from ASTM A36 steel, and the welds (all approximately 10 in. long) were deposited using AWS A5.1 E70XX electrodes. The 17 experiments included in Table 1 represent only those that exhibited weld failure and do not include other specimens that showed base metal failure due to tearing.

Building on these and other studies on lap-joint specimens (such as those briefly mentioned earlier), various theoretical methods have been proposed to determine the strength of eccentrically loaded fillet welds. Broadly, these may be classified into three categories: (1) methods that assume elastic response of all the welds, (2) methods that apply the principle of the

instantaneous center (IC) of rotation, and (3) methods that assume a predetermined form of the stress distribution in the welds and in the bearing portion of the connected plates. The elastic methods are generally understood to be highly conservative (Lesik and Kennedy, 1990; Salmon and Johnson, 1996), while those that apply the principle of the IC of rotation and an assumed stress distribution reflect more realistic response, including inelastic action in the welds. With this background, this section reviews the development of these methods.

Butler et al. (1972) developed a method to predict the strength of welded joints with in-plane eccentricity based on the approach previously proposed by Crawford and Kulak (1971) for eccentrically loaded bolted joints. This method employs the load deformation response of weld elements as a function of loading angle and relies on the assumption that the weld group, under an eccentric load, rotates about an instantaneous center of rotation. Once the location of the IC is established (through an iterative process until equilibrium of forces and moments is satisfied), the strength of the joint is calculated considering equilibrium of all the weld elements when the critical element (typically farthest from the IC) reaches its ultimate (or fracture) deformation. Various aspects of this method have been refined in subsequent years, including load-deformation relationships of the weld elements themselves, which is an important input to these methods. The original work of Butler et al. (1971) was based on a load-deformation model for fillet welds based on a series of tests on ¼-in. welds conducted by Butler and Kulak (1971). Lesik and Kennedy (1990) subsequently refined the load-deformation models based on the tests of Miazga and Kennedy (1986, 1989) on double-lapped connections. The IC method has also been adapted for eccentrically loaded joints loaded out-of-plane, where plate bearing in the compression zone may alter the stress distribution in the welds (Dawe and Kulak, 1972).

Neis (1980) simplified the ultimate weld capacity prediction procedures proposed by Dawe and Kulak (1972). The model presented by Neis assumes a stress distribution in the weld adopted from the research of Butler and Kulak (1971) for a weld loaded perpendicular to its axis ($\theta = 90°$). This approach obviates the iterative procedures typically involved in the IC methods and obtains predictions as a closed-form solution. Neis suggested seven variants of the model, which featured various combinations of stress block geometries for the welds and assumptions regarding bearing stress distribution in the compression zone. Beaulieu and Picard (1985) presented a model similar to Neis (1980) by assuming that the bearing strength is equal to the yield strength of the bearing plates. Both Neis (1980) and Beaulieu and Picard (1985) neglect shear stresses in the welds and are valid only for relatively large load eccentricities (ratio of eccentricity to weld length greater than 0.4).

The American Institute of Steel Construction (AISC, 2005) published tables (*Steel Construction Manual*, Table 8-4, "special-case") for the strength of eccentric fillet welded connections loaded out-of-plane. Figure 3 schematically illustrates the assumptions and stress distributions reflected in the AISC design tables. As indicated in the figure, the stresses in the welds are based on the IC method employing the descriptions of the fillet weld load-deformation response proposed by Lesik and Kennedy (1990). Lesik and Kennedy performed extensive analysis on test data of Miazga and Kennedy (1986, 1989) to provide algebraic expressions for the load-deformation relationships of fillet welds. As per their research, for a weld segment of leg size w and unit length (such as indicated in Figure 3) loaded at an angle θ with respect to its axis, the load-deformation relationship may be expressed as follows:

$$f(\rho) = 8.234\rho \text{ for } 0 < \rho \leq 0.0325 \quad (1)$$

$$f(\rho) = -13.29\rho + 457.32\rho^{1/2} - 3385.9\rho^{1/3} + 9054.29\rho^{1/4} - 9952.13\rho^{1/5} + 3840.71\rho^{1/6} \text{ for } \rho > 0.0325 \quad (2)$$

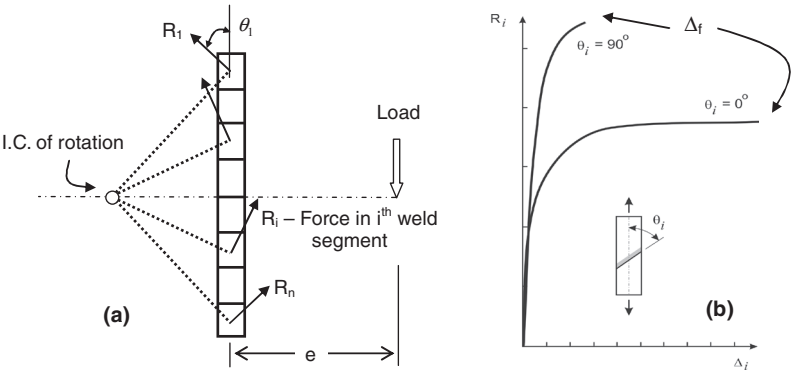

Fig. 3. Assumptions inherent in the AISC design tables: (a) weld deformation and stresses, (b) load deformation response of welds (Lesik and Kennedy, 1990).

where $f(\rho)$ is the normalized force in the i^{th} weld element, such that $f(\rho) = R_i/R_{ult}$, and:

$$R_{ult} = 0.60F_{EXX}A_w(1.0 + 0.5\sin^{1.5}\theta) \quad (3)$$

Equation 3 predicts the capacity of a fillet weld segment in terms of the electrode nominal tensile strength, F_{EXX}, the weld throat area, A_w, and the angle, θ, between the axis of the weld and the line of action of the force. The constant 0.60 is the shear stress transformation factor. The deformation quantity described in Equations 1 and 2 is normalized by the deformation at peak force such that $\rho = \Delta/\Delta_u$, where:

$$\Delta_u = 0.209(\theta + 2)^{-0.32}{}_w \quad (4)$$

As per the IC method (Butler et al., 1972), the weld group is assumed to rotate until a critical segment (typically farthest from the IC) reaches its fracture deformation, Δ_f, which is determined as follows:

$$\Delta_f = 1.087D(\theta + 6)^{-0.65}{}_w \leq 0.17_w \quad (5)$$

At this point, the equilibrium of the entire connection is considered, and the force capacity is determined. Referring to the preceding discussion and Figure 3, some of the assumptions implicit in the formulation of the AISC design tables are questionable. For example, the weld load-deformation response described by Equations 1 through 5 is based on tests of lap-joint specimens. Thus, the equations (especially Equation 5 which reflects weld fracture deformation) neglect the crack-like effect of the root notch, as shown in Figure 1(a), which may potentially impact weld strength and ductility. In this context, it is relevant to mention recent tests by Ng et al. (2002), Li et al. (2007) and Kanvinde et al. (2008) on welded cruciform joint specimens, which indicate that the ductility (and to some extent the strength) of welds is diminished when the load is applied perpendicular to the root notch. Perhaps more importantly, the approach disregards bearing between the two connected plates in the compression region and assumes that all the stresses are carried by the welds (refer to Figure 3). Thus, the actual behavior of the welds for out-of-plane loading is not reflected by the AISC approach.

In summary, prior research features limited test data with respect to eccentric weld connections loaded out-of-plane. Thus, the theoretical methods to predict the strength cannot be evaluated for a wide range of parameters. The methods themselves are based on several assumptions, outlined in the preceding discussion. Moreover, since all the methods are based on weld load-deformation relationships derived from tests on lap-joint specimens, none consider the potentially detrimental effect of the root notch on the ductility of the welds. Finally, an examination of current AISC design tables indicates that significant aspects of physical response, such as bearing between the connected plates, are not considered in their development. To address these issues, the main objectives of the current study, as discussed in the introduction, are to evaluate the applicability of the current design standards to joints with out-of-plane eccentricity and to suggest improved alternatives.

ANCILLARY TESTS

A series of ancillary tests was conducted to characterize material properties in support of the cruciform joint bending tests. Described in the next section, the cruciform joint bend specimens were fabricated from ASTM A572 Grade 50 base metal, and two different types of E70XX weld filler metals (self shielded flux-cored wires), including an AWS A5.20 (2005a) E70T-7 electrode, which is designated as a "non-toughness-rated" filler metal, and a "toughness-rated" E70T7-K2 electrode per AWS A5.29 (AWS, 2005b). Welds designated "toughness-rated" meet minimum Charpy V-Notch toughness requirements of 27 joules at –29 °C and 54 joules at 21 °C. Standard tension tests (per AWS A5.20, 2005a, and AWS A5.29, 2005b, for welds; ASTM E8, 2008, for base metal) were conducted to characterize material constitutive response. The test method for the weld materials involved creating a groove-welded assembly of two plates per AWS 5.20 (2005a), shown schematically in Figure 4, from weld electrodes used for fabrication of the cruciform bend tests. Referring to the figure, all-weld metal specimens (two for each weld material) were extracted from the groove weld region and tested under monotonic tension. Average results from these tests, including the yield and ultimate strengths and ductilities expressed in terms of the ratio of pre- to post-fracture cross section diameter d_0/d_f (and the corresponding maximum true strains at fracture), are summarized in Table 2. The mean ultimate strengths $F_{u,\ weld}$ (from quasi-static tests) for both the E70T-7 and E70T7-K2 weld metals are approximately 97 ksi, on average 40% greater than the specified minimum (70 ksi). As expected, the average ductility, d_0/d_f, for the toughness rated E70T7-K2 weld material is greater (by about 35%) as compared to the non-toughness-rated (E70T-7) weld material. Similar results from tension tests of the base metal are also

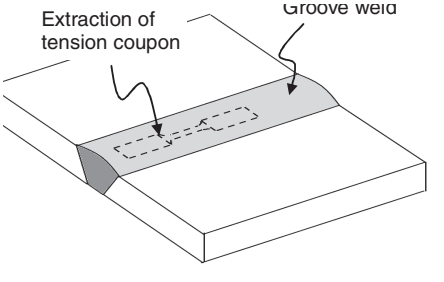

Fig. 4. Plate assembly (per AWS A5.20) indicating extraction of all-weld metal tension specimens.

Table 2. Results from Ancillary Tests Including Tension and Charpy V Notch Tests								
		Tension Tests				CVN Energy (lb-ft)		
Material	Test	F_y[a] ksi	F_u[b] ksi	d_o/d_f	ε[c]	–20 °F	70 °F	212 °F
E70T-7 (Non-toughness-rated weld)	1	75.8	97.1	1.35	0.60	5.5	19.0	41.0
	2	76.8	97.2	1.15	0.28	6.0	18.0	41.0
	Mean	**76.3**	**97.1**	**1.25**	**0.45**	**5.75**	**18.5**	**41.0**
E70T7-K2 (Toughness-rated weld)	1	82.7	97.5	1.65	1.00	30	56.0	88.0
	2	83.0	97.4	1.74	1.11	23	62.0	88.0
	Mean	**82.8**	**97.4**	**1.69**	**1.05**	**26.5**	**59.0**	**88.0**
A572 Grade 50 (Base metal)	1	52.9	71.5	2.13	1.52	CVN tests not conducted for base metal		
	2	53.9	71.8	2.08	1.46			
	Mean	**53.4**	**71.6**	**2.11**	**1.49**			

[a] Measured yield stress, based on 0.2% offset method; static value
[b] Measured ultimate strength; static value
[c] $\varepsilon = \ln(d_o/d_f)^2$ = average true strain across necked cross section of tension coupon

presented in Table 2. In addition to these mechanical tests, spectrochemical analyses were carried out for both weld metal electrodes. The analyses (archived in Roberts, 2008) indicate that none of the electrodes had an unexpected chemical composition relative to the requirements of AWS 5.20 (2005a).

Similar ancillary tests have been conducted for the other experimental programs (Dawe and Kulak, 1972; Beaulieu and Picard, 1985). Although these ancillary data are not reproduced in this paper (since they are available in the cited references), they are used in the analysis of bend test data from these programs.

EXPERIMENTAL PROGRAM

This section describes the cruciform joint bending tests in detail. Figure 2(a) illustrates the test setup and specimen schematically, whereas Figure 2(b) includes a photograph of a specimen being loaded in a three-point-bend configuration. The main variables investigated are (1) the load eccentricity, e; (2) the plate bearing width or plate thickness, t, which is also equal to the nominal root notch dimension; (3) weld size and (4) weld filler metal classification. Table 3 presents the test matrix indicating that three replicates are tested for each assembly (or test category) to obtain statistically significant data. Referring to the table, two nominal weld sizes (½ in. and 5⁄16 in. leg dimension), three load eccentricities (e = 3.0, 5.5 and 8.5 in.) and three plate widths (t = 1.25, 1.75 and 2.50 in.) were investigated for each of the two weld classifications. For economy, the test matrix represents a fractional factorial matrix; that is, not all possible parameter combinations are investigated explicitly. However, the matrix is designed to provide comparative evaluations of the effect of all parameters. The following discussion outlines the specimen preparation, test setup and procedure. Discussion of the test results is presented in a subsequent section.

Test Specimen Preparation and Test Setup

Figure 5 schematically illustrates the typical specimen geometry. As shown in the figure, for each configuration, three replicate specimens (nominally 4 in. wide) were cut out from an assembly of three plates (all A572 Grade 50 ksi steel) welded together in a cruciform configuration. The plate bearing width (i.e., the root notch length) was controlled by varying the thickness of the two outer plates. The connection was designed so that failure occurred in the test welds while the connecting plates remained elastic. The overall width of the assembly was 13 in. allowing run-on and run-off regions at either end of the assembly to ensure relatively uniform weld properties within each specimen. Each of the two filler metal types (E70T-7 and E70T7-K2) was taken from the same spool of wire to minimize variability in weld properties. Standard weld procedures (Roberts, 2008) were used, and all welding was performed using the flux cored arc welding (FCAW) process. Three weld passes were needed for the ½-in. welds, while only one pass was needed for the 5⁄16-in. welds. As indicated in Figure 5, one side of the central plate had reinforced welds (i.e., they were oversized by approximately ½ in.) to ensure failure on the predetermined "test" side, thereby minimizing instrumentation.

The loading fixture shown in Figure 2(b) was designed to enable testing of the cruciform joint specimens in bending with different load eccentricities, while also providing pinned boundary conditions. The fixture includes a steel base with smooth-cut round grooves (at multiple preset locations) in which dowel pins may be seated as the supports. A similar

dowel pin is connected to the central (upper) loading fixture. All dowel pins feature a milled flat surface to minimize local deformations of the specimen at the reaction points. The round dowels were lubricated to allow free rotation at the contact points. The eccentricity for each test, as illustrated in Figure 2(a), is defined as the distance from the centerline of the dowel to the surface of the center plate.

Using the load setup and fixture described earlier, 60 cruciform specimens were loaded quasi-statically to failure under displacement control. Qualitatively, all tests exhibited a similar response: initial elastic response followed by a period of strain hardening concluding with a drop in force. Figure 6 shows a representative load versus load-line deformation curves for Test 8 (eccentricity = 3.0 in.) and Test 52 (eccentricity = 8.5 in.). The load shown in the figure is half the load applied at the center of the symmetric three-point-bend specimen, representing the force sustained by the test weld, which is located on one side of the central loading fixture. Failure for most tests with larger eccentricities (e = 5.5 in. and 8.5 in.) was gentle, and weld rupture involved a gradual "un-zipping" of the specimen initiating at the bottom end of the weld (the tension end); see the response of Test 52 shown in Figure 6. A majority of the tests with the smaller eccentricity (i.e. e = 3.0 in.) exhibited more sudden shearing failure, corresponding to an abrupt drop in load (see response of Test 8 shown in Figure 6). Figure 7(a) shows a fractured specimen (Test 19) photographed at the conclusion of testing. Several load and deformation quantities were measured during the tests, including the peak load, R_{max} (as indicated on Figure 6), the load line displacement, the weld deformation at four locations and, in some specimens, the longitudinal surface strains. While a detailed discussion of these various quantities is presented in Gomez et al. (2008), the observed peak load, R_{max} (or connection strength), is most relevant in the context of this paper. Table 3 summarizes measured R_{max} values for all the test specimens, along with other quantities. A discussion of these results along with a graphical representation is presented in a subsequent section.

Pre- and Post-Fracture Specimen Measurements

To minimize systematic bias in the analysis of the test data, detailed measurements of the weld sizes were recorded both before and after testing. The profiles of all the test welds

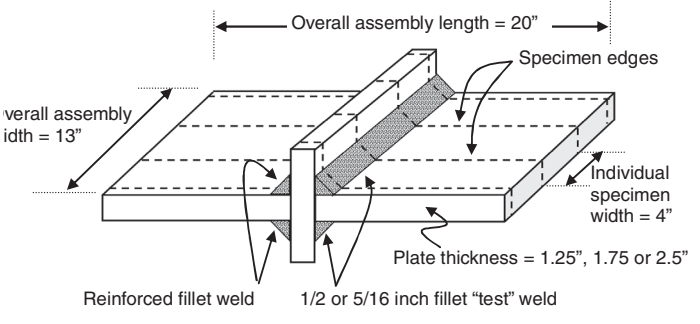

Fig. 5. Cruciform specimen assembly showing key dimensions and fabrication details.

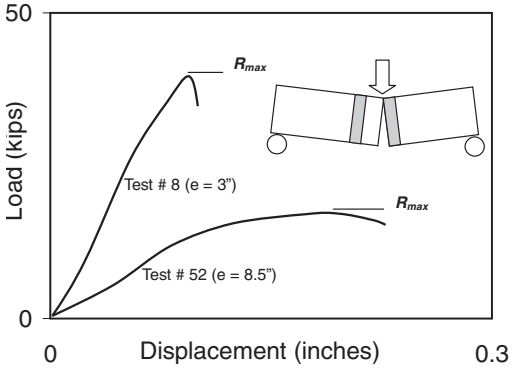

Fig. 6. Representative load-deformation curve for Test 8 and Test 52 (indicating the peak load, R_{max}).

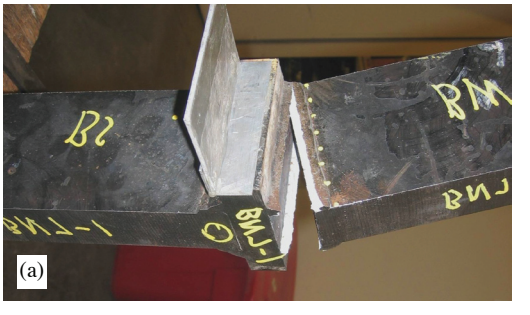

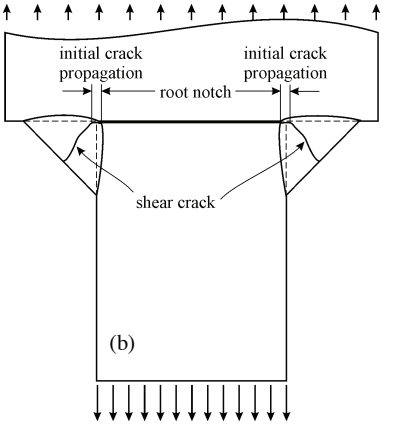

Fig. 7. (a) Representative photograph of failed specimen (Test 19); (b) schematic bottom view of specimen indicating failure pattern.

Table 3. Results of Cruciform Bend Tests from Current Study

Test No.[a]		e[b]	Weld Size (in.)			t[e]	R_{max}[f] kips		$\frac{R_{max}}{R_n^{AISC}}$[g]		$\frac{R_{max}}{R_n^{bearing}}$[h]	
			Nom[c]	w_{eff}[d]								
NT	T	in.		NT	T	in.	NT	T	NT	T	NT	T
1	31	5.5	5/16	0.400	0.427	1.25	44.4	50.5	1.41	1.58	1.19	1.36
2	32			0.399	0.426		53.7	57.4	1.68	1.75	1.42	1.50
3	33			0.411	0.421		52.5	60.8	1.63	1.95	1.39	1.67
4	34		½	0.593	0.589		73.4	82.0	1.55	1.66	1.55	1.65
5	35			0.591	0.562		72.2	84.5	1.50	1.84	1.49	1.78
6	36			0.587	0.608		71.1	98.8	1.46	1.84	1.45	1.86
7	37	3.0	5/16	0.359	0.403	1.75	120.0	165.2	2.34	2.79	1.73	2.12
8	38			0.365	0.382		119.0	160.4	2.23	2.71	1.66	2.04
9	39			0.361	0.387		123.9	155.3	2.26	2.64	1.68	1.99
10	40		½	0.551	0.583		153.4	193.2	2.02	2.17	1.68	1.84
11	41			0.555	0.580		175.0	200.0	2.14	2.30	1.79	1.94
12	42			0.570	0.563		152.1	185.4	1.94	2.17	1.63	1.81
13	43	5.5	5/16	0.367	0.445		61.7	86.7	1.95	2.31	1.42	1.80
14	44			0.366	0.424		59.7	69.8	1.90	1.94	1.39	1.50
15	45			0.371	0.360		63.0	78.0	2.08	2.53	1.52	1.84
16	46		½	0.598	0.583		90.0	99.3	1.73	2.02	1.48	1.72
17	47			0.563	0.602		76.6	90.0	1.79	1.91	1.50	1.65
18	48			0.584	0.574		79.6	86.6	1.71	1.92	1.46	1.62
19	49	8.5	5/16	0.418	0.419		39.0	45.9	1.81	1.92	1.38	1.45
20	50			0.422	0.416		30.1	46.8	1.43	2.08	1.09	1.58
21	51			0.417	0.418		33.4	46.0	1.53	2.04	1.16	1.54
22	52		½	0.585	0.588		51.9	59.3	1.57	1.78	1.35	1.52
23	53			0.576	0.601		51.3	59.9	1.57	1.83	1.34	1.57
24	54			0.622	0.631		53.0	57.1	1.53	1.82	1.35	1.61
25	55	5.5	5/16	0.405	0.381	1.25	62.0	77.9	1.73	2.42	1.18	1.62
26	56			0.403	0.398		58.7	77.0	1.76	2.34	1.20	1.58
27	57			0.396	0.407		58.3	76.4	1.66	2.32	1.13	1.59
28	58		½	0.582	0.621		86.9	110.5	1.81	2.13	1.36	1.63
29	59			0.575	0.642		101.6	112.0	1.96	2.16	1.47	1.67
30	60			0.555	0.615		94.5	110.7	1.93	2.27	1.43	1.74
								Mean	**1.79**	**2.10**	**1.43**	**1.69**
								Coefficient of variation	**0.14**	**0.15**	**0.13**	**0.11**

[a] NT = "Non-toughness–rated" (E70T7) welds; T = "toughness–rated" (E70T7-K2) welds.
[b] Load eccentricity length.
[c] Nominal (specified) weld size.
[d] Effective weld size based on average *measured* tension and shear leg dimensions, i.e., $w_{eff} = \sqrt{\frac{2}{\left(1/L_{shear}\right)^2 + \left(1/L_{tension}\right)^2}}$
[e] Specified plate (root notch) thickness.
[f] R_{max} = maximum eccentric force observed in experiments.
[g] R_n^{AISC} = predicted strength based on AISC approach.
[h] $R_n^{bearing}$ = predicted strength on alternate approach incorporating bearing.

were measured at eight locations along the length of each test weld (within each specimen), using a fillet weld gage and a caliper gage. These detailed measurements enable a more effective interpretation of the test data with respect to design equations. Figure 8 illustrates the average weld profiles (based on all the measurements for a given assembly) for all the welds. In the figure, average weld profiles from all the assemblies (corresponding to the given weld size) are overlaid on one another. Because welding of the test specimens was performed in the horizontal position, the "shear leg" and the "tension leg" had different dimensions. On average, the "shear leg" of the weld (which attaches to the large outer plate) was 38% longer than the "tension leg" (which attaches to the central plate), although this difference was slightly less pronounced in the ½-in. welds. However, in most cases, the tension leg was at least as large as the specified weld size, whereas the shear leg was on average 44% longer then the specified minimum. It is also interesting to observe the dimple shaped weld profiles for the ½-in. weld assemblies, which are produced by the multiple welding passes. The length of each weld was also measured and, in general, was determined to be within 5% of the nominal 4-in. length. It is important to emphasize that all the comparisons with the predicted values are made based on the measured weld profiles and lengths, rather than the nominal weld sizes.

Figure 7(a) shows a representative photograph of a fractured specimen (shown here for Test 19, 1.75-in. root notch, non-toughness 5⁄16-in. weld, 8.5-in. eccentricity). Referring to the figure, the fracture surface consists of a region of initial crack propagation straight ahead of the root notch (i.e., perpendicular to the principal bending stresses), before transitioning to shear type fracture at an angle. Figure 7(b) indicates this schematically. This type of failure surface was also observed for the cruciform tension tests (Kanvinde et al., 2008). In many specimens, fracture did not occur on well-defined planes, and sometimes the fracture plane changed orientation along the length of a single weld. Several measurements were conducted on the fractured specimens. Given the irregularity of the fracture surfaces, these post-fracture measurements are interesting only in a qualitative sense and cannot be directly applied to interpret the effectiveness of design guidelines.

EXPERIMENTAL DATA FROM PREVIOUS INVESTIGATIONS

As discussed previously, two other test programs have investigated the strength of welded joints with out-of-plane eccentricity. In the context of this paper, where a key objective is to examine the effectiveness of current design provisions, it is important to examine these other results to enable a comprehensive evaluation of the current design guidelines. Table 1 summarizes data from these other experimental programs (i.e., Dawe and Kulak, 1972; Beaulieu and Picard, 1985). The data are presented in a similar format as Table 3, wherein the various test parameters are presented, including the joint strength, R_{max}, along with test-to-predicted ratios per the AISC design tables. The data are also represented graphically in figures introduced in the next section. As for the tests presented in the current study, strength predictions for these prior tests are based on the measured material properties and weld profiles.

DISCUSSION OF RESULTS

The results from the present study and prior experimental programs are summarized in Tables 1 and 3. Both these tables include the measured joint strengths, R_{max}, and the test-to-predicted ratios, R_{max}/R_n^{AISC}, where R_n^{AISC} represents the strength calculated per Table 8-4 from the *Steel Construction Manual* (AISC, 2005). As discussed in a previous section, Table 8-4 in the *Manual* is based on the instantaneous center approach employing several assumptions, including (1) the weld load-deformation relationship as outlined in Lesik and Kennedy (1990), (2) no consideration of the plate bearing and the corresponding distribution of stresses in the weld, and (3) no consideration of the effect of the root notch on

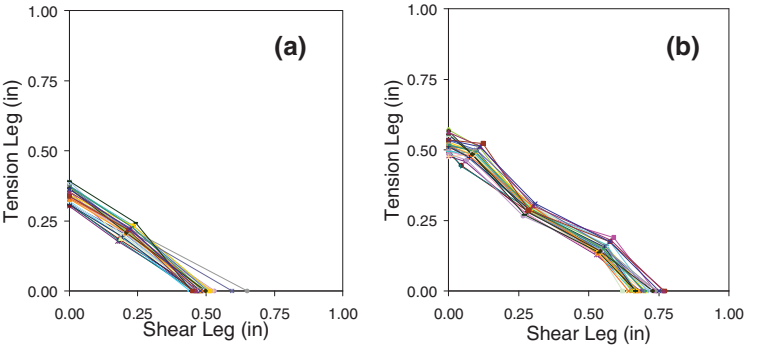

Fig. 8. Mean weld profiles for (a) all the 5⁄16-in. welds including the different filler metals and plate thicknesses, and (b) all the ½-in. welds, including the different filler metals and plate thicknesses.

weld ductility. The design table is applied through Equation 6 presented here:

$$R_n^{AISC} = CC_1dL \quad (6)$$

The coefficient C is taken directly from the *Steel Construction Manual* Table 8-4, for different load eccentricity ratios "a" (i.e., ratio of load eccentricity to weld length). The coefficient C_1 accounts for weld strength and is equal to 1.0 for E70XX electrodes. For calculations in the present study, this coefficient is modified to reflect the measured, rather than the nominal material strength. Referring to Table 2, the measured to nominal strength ratios (and hence the C_1 coefficients) for the E70T-7 and E70T7-K2 filler metals are both 1.39. The parameter L is the measured weld length. The parameter d reflects the weld size, indicating the number of sixteenths of an inch in the weld leg size. To reflect the measured weld sizes through this parameter, an effective weld leg dimension is calculated as follows:

$$w_{effective} = \left(\frac{1}{\sqrt{\left(1/L_{shear}\right)^2 + \left(1/L_{tension}\right)^2}} \right) \times \sqrt{2} \quad (7)$$

where the first term reflects the effective throat dimension based on the measured tension and shear leg dimensions of each specimen (averaged over eight measurements along the length of each weld), and the second term ($\sqrt{2}$) reflects the assumed geometrical relationship between the throat size and the effective weld size. Calculating the effective weld size in this manner is consistent with the intent of the AISC design table, such that the weld throat area corresponding to the preceding estimate of effective weld size from Equation 7 corresponds to the weld throat area of the actual specimen, which typically does not have equal leg sizes. The true throat area of the welds may be affected by other factors, such as the number of weld passes (see the irregular weld profile indicated in Figure 8) and weld penetration. However, using these estimates is not consistent with the way in which welds are designed or fabricated. Thus, only the measured leg sizes (rather than measured throat sizes) are used in the calculation of the effective weld size. Once the effective weld size w_{eff} is calculated in inches, the parameter d is conveniently determined through division by (1/16).

In addition to Table 1 and Table 3, the comparison between the experimental and predicted strength for all the specimens (including those tested in other studies) is presented graphically in Figure 9 and Figures 10(a)–(d). Figure 9 plots the experimentally measured strength, R_{max}, against the predicted strength, R_n^{AISC}, for all (85) experiments considered. For a closer examination of the trends within the data, Figures 10(a)–(d) plot the test-to-predicted ratios, R_{max}/R_n^{AISC}, against various test parameters, including the load eccentricity, nominal weld size, plate bearing width and weld toughness classification.

Referring to Figure 9, it is immediately apparent that, on average, the AISC design approach predicts strengths significantly lower than the experimental values. Based on all the experiments, the mean value of R_{max}/R_n^{AISC} is 1.75 (coefficient of variation = 0.25). While the AISC approach is significantly conservative for the test results reported in the current study (R_{max}/R_n^{AISC} = 1.94, COV = 0.17), it is relatively less conservative for the other test programs (Dawe and Kulak, 1972; Beaulieu and Picard, 1985) for which the average R_{max}/R_n^{AISC} is 1.15 and 1.32 (COV = 0.12 and 0.21), respectively. This may be attributed to two effects. First, the current study features, on average, larger bearing plate widths (between 1.25 and 2.50 in.), compared to the other test programs (between 0.787 and 1.575 in.). Since the predicted values do not incorporate the effect of bearing, one may argue that the presence of larger bearing widths within a data set may bias R_{max}/R_n^{AISC} ratios within that data set. In fact, referring to Figure 10(a), which plots bearing width versus R_{max}/R_n^{AISC} for all experiments, a general trend is observed such that larger bearing widths result in larger R_{max}/R_n^{AISC} values. When considered in this context, results from the current study appear to be more consistent with the overall trend. Second, the higher R_{max}/R_n^{AISC} values may be attributed to differences in weld metal properties between the current study and the other studies. While the measured strength values for all the studies are incorporated into the predicted strength capacities, recall that the strength estimate implicitly reflects the entire load-deformation response of the weld elements. Thus, the design tables cannot capture the effects of notch toughness (and hence weld ductility) variation between various data sets. Although toughness data (such as Charpy V-Notch energy values) are not documented for the other test programs, it is likely that the current study may result in higher strengths of the joints due to higher weld material toughness as compared to the previous

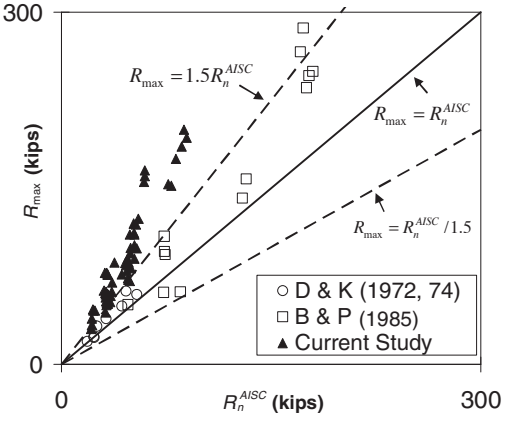

Fig. 9. Comparison between experimental joint strength, R_{max}, and joint strength predicted as per current AISC design table, R_n^{AISC}.

testing programs. However, a detailed comparative analysis (Gomez et al., 2008) between the current (UC Davis) tests and other tests (Ng et al., 2002) indicates that both the filler metals used in the current study are not unusually strong or tough when compared with similar filler metals featured in other recent tests. Thus, results from the current study may be considered only suitable to represent currently used welding materials and practices.

To examine the experimental trends in more detail, Figures 10(a)–(d) plot the R_{max}/R_n^{AISC} ratio against various test parameters for all the experiments. These are now discussed individually:

1. Figure 10(a) plots R_{max}/R_n^{AISC} against the plate bearing width, t. A trend is observed across all data sets, such that the predictions become increasingly conservative (i.e., R_{max}/R_n^{AISC} increases) as the bearing thickness of the plates increases. As discussed earlier, this may be explained based on the inability of the design tables to incorporate the effect of bearing on the stress distribution of the welds. It is relevant to note that the bearing thickness is also equal to the weld root notch length. However, based on the data (which shows a consistently increasing trend of R_{max}/R_n^{AISC} with respect to t), it appears that the root notch length does not have a significant detrimental effect on the test-to-predicted ratios, especially in the presence of the apparent benefits obtained due to simultaneous increase in bearing thickness. This is consistent with findings from a companion study (Kanvinde et al., 2008) that featured tension tests on cruciform specimens, where the results did not indicate a significant decrease in strength or ductility with an increase in the root notch length above a certain length (typically 1.0 in.).

2. Figure 10(b) plots R_{max}/R_n^{AISC} for all the tests against the weld metal classification. The only tests that feature a weld filler metal with a toughness rating are Tests 31 to 60 of the current study (with the E70T7-K2 filler metal). From the figure, it is evident that, on average, specimens featuring the toughness rated welds have higher R_{max}/R_n^{AISC} values (on average 2.09, COV = 0.15), as compared to the other specimens (on average 1.55, COV = 0.23). As described previously, the AISC design tables reflect a specific weld load-deformation relationship proposed by Lesik and Kennedy (1990), and thus do not distinguish between the tough and non-tough specimens.

3. Figure 10(c) plots R_{max}/R_n^{AISC} versus the eccentricity ratio, a, for all the experiments. From the figure, a slight trend is observed within each data set such that increasing the eccentricity ratio reduces the R_{max}/R_n^{AISC} ratios. In the absence of additional data, this trend may be analyzed only in a speculative manner. The specimens with the larger eccentricities result in weld deformations that are more tensile rather than shearing in nature. Although the length of the root notch has been observed to not affect weld strength or ductility when the root notch is longer than about 1 in. (Kanvinde et al., 2008), the *presence* of the transverse root notch produces lower strength and ductility as compared to

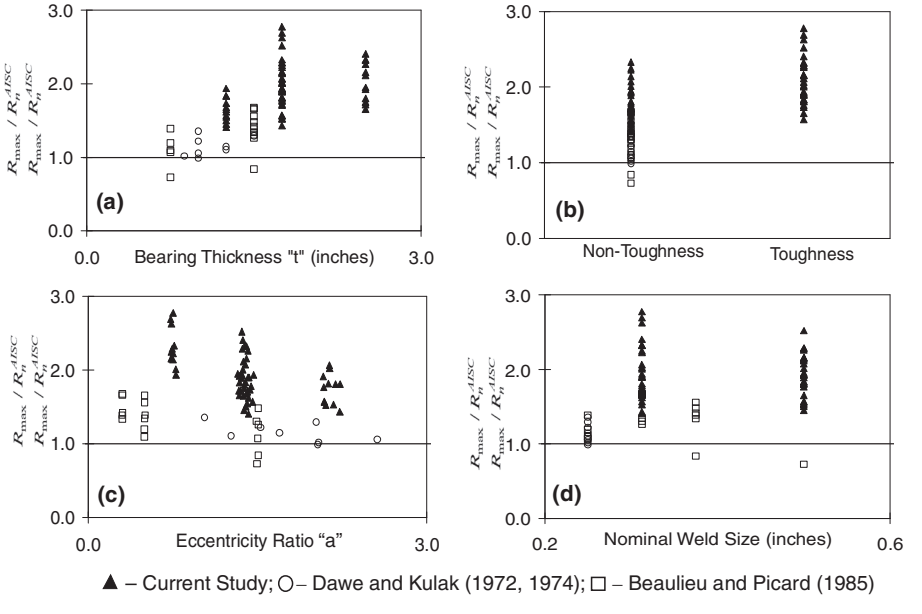

Fig. 10. Effect of various test parameters on the test-predicted ratios, R_{max}/R_n^{AISC}.

lap-joint specimens (where there is no root notch effect). For specimens with a low eccentricity ratio, the deformations are predominantly attributed to shear stresses; thus, the detrimental effect due to the presence of the root notch may be less prominent (i.e., for these connections the root notch is not transverse to the applied stress), as compared to the specimens with the higher eccentricity. In any case, it is important to emphasize that even for the higher eccentricity ratios, the R_{max}/R_n^{AISC} ratios are, on average, greater than 1.0.

4. Finally, referring to Figure 10(d), the weld size did not appear to have a significant influence on the R_{max}/R_n^{AISC} ratios.

In summary, the AISC design tables produce conservative estimates of weld strength for a large majority of the experimental data examined. A reliability analysis of all the experimental data (summarized in Gomez et al., 2008) indicates that the AISC tables, when used in conjunction with a resistance factor $\phi = 0.75$, provide a safety index $\beta = 7.2$, which is well in excess of the target safety index, typically taken as 4.0 for fracture limit states in welded connections. A closer examination of the data reveals that this conservatism may be attributed to two sources. The main issue is that the AISC design tables are based on the IC method, disregarding the effect of plate bearing, which, as discussed previously [and illustrated in Figure 10(a)], has a beneficial influence on the connection capacity. A secondary effect is related to the weld toughness (i.e., ductility). The AISC method implicitly reflects a specific and consistent load-deformation response (and, consequently, ductility) for the weld elements (based on the work on lapped specimens of Lesik and Kennedy (1990). A higher weld ductility than the implicitly assumed values will result in higher R_{max}/R_n^{AISC} ratios. The other effect disregarded by the AISC approach, that is, the existence of the "crack-like" root notch, does not appear to have a prominent effect on strength, especially in the presence of the accompanying benefit on strength due to the increased bearing width.

The next section presents an alternate approach for evaluating the strength of welded connections loaded with out-of-plane eccentricity. By explicitly incorporating bearing in the strength estimates, the aim of this alternate approach is to reduce the conservatism associated with the AISC design tables.

ALTERNATE APPROACH FOR STRENGTH PREDICTION CONSIDERING BEARING

As discussed in the previous section, the AISC design approach predicts the strength of tested welded connections with a high degree of conservatism, providing a safety index well in excess of the target value of 4.0. To address this issue, this section provides an alternate approach to characterize the strength of connections with out-of-plane eccentricity. Referring to the previous section, the AISC standard is conservative mainly due to the omission of the bearing effect between the two connected plates. Fortunately, this effect is convenient to incorporate within the framework of the IC method described previously, by assuming an appropriate stress distribution in the compressive region of the connection. With the objective of developing a refined model for predicting the strength of these joints, several alternative models were applied to the test data and examined for accuracy and consistency. These models included variations based on the IC method (e.g., Dawe and Kulak, 1972) as well as other approaches that resulted in closed form strength equations (e.g., Neis, 1980; Beaulieu and Picard, 1985). The variations in these models resulted from the use of different weld load-deformation relationships (e.g., Butler and Kulak, 1971, or Lesik and Kennedy, 1990) and the assumption of various stress distributions in the compressive bearing region and the tension region. A reliability analysis of all these models, along with a detailed discussion, is presented in Gomez et al. (2008). In the current paper, only one of these models is presented. This model provides the best agreement with the test data, while relying on assumptions that are consistent with the principles of mechanics and weld load-deformation relationships that have been demonstrated to represent measured response.

The model presented in this paper is a modified version of the approach proposed by Dawe and Kulak (1972). In concept, the approach is similar to the one used by AISC (Figure 3), except it explicitly considers bearing stresses in the compressive region of the connection. This is illustrated in Figure 11, which indicates that this method makes use of the instantaneous center of rotation assumptions in the tension zone of the connection and assumes load transfer in the compression zone by bearing of the connected plates and shear of the weld. The normal stress distribution in the compression zone is assumed to be rectangular (i.e., there is no transition from zero stress to yield stress), with the

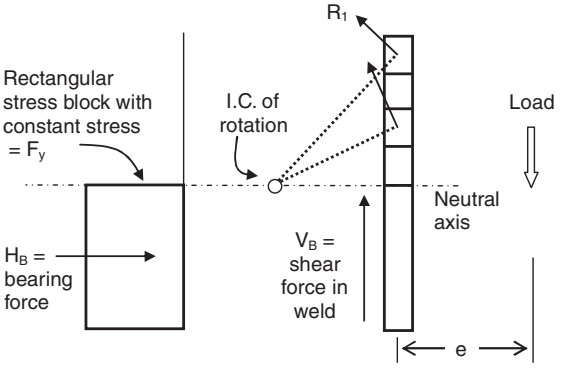

Fig. 11. Assumptions for the alternate method considering bearing.

uniform stress in this region taken as the yield strength of the plate material. As further explained in Gomez et al. (2008), this type of stress distribution reflects typical observations from strain-gaged specimens. Since the normal force in the compression zone (H_B in Figure 11) is carried by bearing between two plates, the weld in this zone is assumed to carry a vertical force, V_B, corresponding to the strength of the weld loaded at an angle, θ = 0°. It is relevant to discuss here that, in general (for more complex connection geometries), the contact between the two connected plates will be nonuniform due to the challenges associated with alignment in a fabricating shop. Thus, a gap may exist between the two connected plates. However, at the ultimate limit state, either the welds in the compression zone will yield, thereby eventually allowing contact, or the plate itself will yield in the compression zone at the toe of the weld. In either case, the assumed stress distribution is consistent with expected response. Thus, the presence of nonuniform contact is not expected to significantly alter the findings of this study.

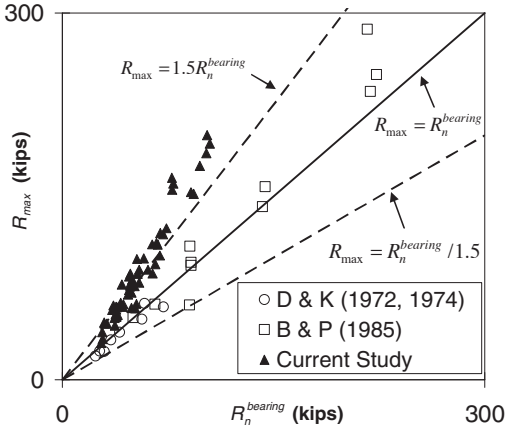

Fig. 12. Comparison between experimental joint strength, R_n, and joint strength predicted using the alternate method incorporating bearing, $R_n^{bearing}$.

In the tension region, the weld deformations are determined by applying the principle of the instantaneous center of rotation. Similar to the AISC approach, the corresponding weld load-deformation response is based on Equations 1 through 5 (Lesik and Kennedy, 1990). Finally, the strength capacity is calculated through an iterative procedure similar to the one outlined by Dawe and Kulak (1972) and the AISC approach. The resulting test-to-predicted ratios, $R_{max}/R_n^{bearing}$, for all the specimens are summarized in Table 3 (specimens from current study) and Table 1 (specimens from previous studies). Figures 12 and 13(a)–(d) are equivalent to Figures 9 and 10(a)–(d) discussed in the previous section, but instead feature the predicted strengths, $R_n^{bearing}$, based on the alternate approach that incorporates the bearing effect. Several observations may be made based on Tables 1 and 3 and Figures 12 and 13(a)–(d).

The main observation is that the average test-to-predicted ratio, $R_{max}/R_n^{bearing}$, for all the tests is 1.41 (with a COV = 0.22). This ratio is about 20% lower as compared to the $R_{max}/R_n^{bearing}$ ratios that were obtained disregarding bearing. This suggests that a consideration of bearing produces more accurate estimates of strength. This has important design implications because the method incorporating bearing will result in welds that are significantly smaller compared to those designed as

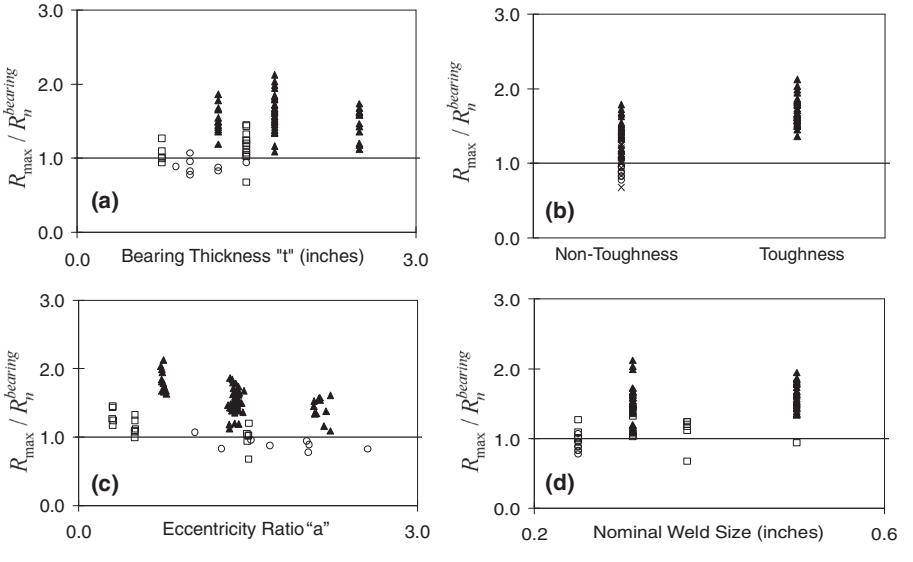

Fig. 13. Effect of various test parameters on the test-predicted ratios, $R_{max}/R_n^{bearing}$.

per the AISC table. A reliability analysis of the data (Gomez et al., 2008) demonstrates that the alternate approach, when used with a capacity factor $\phi = 0.75$, provides a safety index $\beta = 4.6$, which is still in excess of the target safety index $\beta = 4.0$. Since the determination of the weld strengths requires an iterative analysis, the results may be most conveniently presented in the form of a table similar to the current Table 8-4 of the *Steel Construction Manual* (AISC, 2005). Such a table is presented in Gomez et al. (2008).

Figures 13(a)–(d) provide a closer examination of the trends within the experimental data. Comparing Figure 13(a) to Figure 10(a) shown previously, it is apparent that the $R_{max}/R_n^{bearing}$ ratios that incorporate the bearing effect do not show a significant trend with respect to the bearing thickness within any data set. This is encouraging, because it suggests that the alternate method is able to effectively capture the bearing effect. The current tests show higher $R_{max}/R_n^{bearing}$ values on average than the tests from the other test programs, but as discussed previously, this may be attributed to the inherent material toughness of the weld filler metal used in the current study. Refer, for example, to Figure 13(b), that plots the $R_{max}/R_n^{bearing}$ versus toughness classification. Compared to the similar Figure 10(b) shown earlier, a similar trend is observed, such that the approach is on average more conservative for specimens with the toughness rated filler material. In addition to the effect of material toughness, it is relevant to note that that the other test programs had smaller plate thicknesses as compared to the current study. The lower strength observed in these programs may be attributed to weld fracture accompanied by yielding in the base metal, such as may be observed for thinner plates. However Ng et al. (2002) determined that (1) the strength of cruciform tension specimens was not significantly affected by this factor, and (2) this condition (i.e., forcing the base metal to yield before the weld, while ensuring that fracture ultimately occurs in the welds) is difficult to reproduce experimentally, because the exact strength of the weld and base metal is not known at the design stage. Thus, for the current study, thicker plates were chosen to ensure failure in the welds without tension yielding in the base metal. Figures 13(c) and 13(d) plot the $R_{max}/R_n^{bearing}$ ratios against the load eccentricity and the weld size, respectively. The trends observed here are similar to those observed for the AISC approach, and these are not discussed in detail.

It is important to point out that while the alternate method considers the effect of bearing, it does not consider the weld toughness as an input variable. Thus, it cannot distinguish between specimens featuring dissimilar filler metal toughness. The framework of the IC method allows for the convenient implementation of weld toughness, such that the weld load-deformation response (and the fracture deformation Δ_f; refer to Equation 5) may be adjusted to reflect weld toughness. However, incorporating the toughness parameter within the approach is an ambitious goal, given the difficulty in characterizing weld toughness in a quantitative manner and correlating it with the load-deformation capacity of weld elements. Thus, the alternate method described in this paper considers only the most significant effect disregarded by the AISC approach, namely, the bearing between the connected plates. In itself, this has significant cost implications for the design of welds. Possible variations and refinements to the approach described in this section may include (1) explicitly incorporating some measure of weld toughness in the strength prediction, or (2) prescribing different ϕ factors for toughness- or non-toughness-rated specimens, such that a consistent safety index is provided for each type of weld classification. These are described in greater detail in Gomez et al. (2008).

SUMMARY AND CONCLUSIONS

Current design tables (AISC, 2005) for the strength of fillet-welded joints under out-of-plane eccentric loading do not consider two effects that may potentially impact their accuracy. First, they disregard the contribution of bearing between the two connected plates, and second, they do not incorporate the effect of the root notch on weld ductility and strength. The majority of test data that have governed the development of the design tables were obtained from experiments on lapped-splice connections in which neither of these effects are present. This paper presents data from 60 bending tests on cruciform specimens and ancillary tests to investigate the strength of welded connections with an out-of-plane load eccentricity. These specimens feature connections with three different plate bearing thicknesses (1.25, 1.75 and 2.50 in.), two nominal weld sizes (½ in. and 5⁄16 in.), three load eccentricities (3.0, 5.5 and 8.5 in.) and two filler metal classifications ("non-toughness-rated" E70T-7 and "toughness-rated" E70T7-K2). Three replicate tests are conducted for each parameter set. In addition to the tests conducted as part of this study, the analysis of data includes results from other test programs that feature similar experiments.

The experimental results of all documented tests indicate that current design tables (AISC, 2005) are considerably conservative when applied to fillet-welded joints loaded with out-of-plane eccentricity, such that on average, the test-predicted ratio, R_{max}/R_n^{AISC}, is 1.75 (coefficient of variation = 0.25). A closer analysis of the data indicates that this conservatism may be attributed to a bearing mechanism between the connected plates, which is not incorporated in methods used for the development of the AISC design tables. In the presence of this beneficial effect, the accompanying influence of the root notch (whose length is equal to the bearing plate thickness) is minor. The toughness of the filler metal is also determined to contribute to the conservatism of the design approach.

To address these issues, an alternate approach is presented to predict the strength of the welded connections. The approach is similar to the AISC approach (i.e., it is based on the IC method), but it directly incorporates the bearing effect by including an appropriate bearing stress distribution in the

compressive region of the connection. Strength predictions based on this approach are significantly less conservative as compared to the AISC approach, such that on average, $R_{max}/R_n^{bearing}$ is determined to be 1.41 (with a COV = 0.22), an approximate 20% decrease with respect to the AISC approach. This has potentially beneficial cost implications since welds designed using the alternate approach will be significantly smaller as compared to welds designed as per the current (AISC) approach. When used with a resistance factor ϕ = 0.75, the alternate approach provides an acceptable safety index β = 4.6. Since application of the alternate approach involves an iterative procedure, the method may be most suitably applied through a design table.

However, the alternate approach does not incorporate all aspects of joint response—especially the weld toughness, which is determined to have an influence on the test-to-predicted ratios. Incorporating the weld toughness as a design parameter may be an ambitious goal, given the subjectivity in characterizing it in a quantitative manner. To incorporate these effects, variations to the method are briefly discussed and refinements are proposed for future work. In addition, the effects of weld profile irregularity cannot be explicitly considered within the scope of this study. For example, the deviation between ideal and true weld profiles, as well as the extent of weld root penetration may have a proportionally dissimilar effect for welds of different sizes. Finally, the results of this study are based on all documented test data on fillet welds with out-of-plane eccentricity. Unfortunately, limited test data (i.e., only three experimental programs) are available for this type of welded detail. There is the possibility of the test data being influenced by unusual material properties or other aspects of the test setup. While the authors have sought to incorporate these effects into their analysis to the extent possible (e.g., by comparing the current test data with other similar data to examine its applicability), the generalization of the results (and possible incorporation into design guidelines) must be accompanied by a fair degree of caution and engineering judgment.

ACKNOWLEDGMENTS

This project was funded by the American Institute of Steel Construction (AISC). The authors gratefully acknowledge Mr. Tom Schlafly of AISC and Dr. Duane Miller of Lincoln Electric, who provided valuable advice and reviewed the welding and shop procedures. Marshall Roberts, graduate student at UC Davis, assisted with the experimental setup, and Jorge Camacho, undergraduate researcher at UC Davis, assisted with the specimen measurements; the authors are thankful for their efforts. The assistance of Mr. David DeBlasio of Gayle Manufacturing Company in preparing the specimens is greatly appreciated. The authors also acknowledge Bill Sluis, laboratory technician at UC Davis, for assistance with design of the test setup.

NOTATION

a	=	load eccentricity ratio $a = e/L$
A_{throat}	=	throat area based on average measured leg dimensions
A_w	=	weld throat area
C	=	coefficient tabulated in AISC Table 8-4
C_1	=	electrode strength coefficient
d	=	number of sixteenths-of-an-inch of fillet weld size
d_0/d_f	=	ratio of initial to final (fracture) diameter of tension coupon
e	=	load eccentricity
$f(\rho)$	=	normalized force in the i^{th} weld element
F_{EXX}	=	electrode tensile strength
F_u	=	ultimate strength of plate or weld
F_y	=	yield strength of plate or weld
H_B	=	normal force in connection compression zone
L	=	length of weld group
L_{shear}, $L_{tension}$	=	mean measured shear and tension leg dimensions, respectively
Nom	=	nominal (specified) weld size
R_i	=	resultant force in the i^{th} weld element
R_{max}	=	experimentally observed maximum strength
R_{ult}	=	ultimate force of weld element
R_n^{AISC}	=	strength calculated as per AISC design table
$R_n^{bearing}$	=	strength calculated as per the method considering bearing
t	=	plate bearing width (also equal to nominal root notch length)
V_B	=	shear force in connection compression zone
w	=	weld segment leg size
w_{eff}	=	effective weld size
β	=	safety index
Δ	=	deformation of weld element
Δ_f	=	fracture deformation of weld
Δ_u	=	deformation of weld at ultimate strength
ε	=	average true strain across cross section of tension coupon
θ	=	angle between weld axis and line of action of load
ρ	=	normalized weld deformation in the i^{th} weld element
ϕ	=	resistance factor

REFERENCES

AISC (2005), *Steel Construction Manual*, 13th Ed., American Institute of Steel Construction, Chicago.

ASTM E-1820 (2008), "Standard Test Methods for the Measurement of Fracture Toughness," ASTM International, West Conshohocken, PA.

ASTM E-8 (2008), "Standard Test Methods for Tension Testing of Metallic Materials," ASTM International, West Conshohocken, PA.

AWS (2005a), "Specification for Carbon Steel Electrodes for Flux Cored Arc Welding," ANSI/AWS A5.20/A5.20M, American Welding Society, Miami.

AWS (2005b), "Specification for Low-Alloy Steel Electrodes for Flux Cored Arc Welding," ANSI/AWS A5.29/A5.29M, American Welding Society, Miami.

Beaulieu, D. and Picard, A. (1985), "Résultats d'essais sur des assemblages soudés excentriques en flexion (Test Results on Eccentrically Loaded Welded Joints in Bending)," *Canadian Journal of Civil Engineering*, Vol. 12, No. 3, 494–506.

Butler, L.J. and Kulak, G.L. (1971), "Strength of Fillet Welds as a Function of Direction of Load," *Welding Journal, Welding Research Supplement*, Vol. 36, No. 5, 231–234.

Butler, L.J., Pal, S. and Kulak, G.L. (1972), "Eccentrically Loaded Welded Connections," *Journal of the Structural Division,* ASCE, Vol. 98, No. 5, 989–1005.

CISC (2007), *Handbook of Steel Construction,* 9th Ed., Canadian Institute of Steel Construction, Willowdale, Ontario.

Clark, P.J. (1971), "Basis of Design for Fillet-Welded Joints Under Static Loading," *Proceedings, Conference on Improving Welded Product Design*, The Welding Institute, Cambridge, England, Vol. 1, 85–96.

Crawford, S.F. and Kulak, G.L. (1971), "Eccentrically Loaded Bolted Connections," *Journal of the Structural Division,* ASCE, Vol. 97, No. ST3, 765–783.

Dawe, J.L. and Kulak, G.L. (1972), "Behavior of Welded Connections under Combined Shear and Moment," Structural Engineering Report 40, Department of Civil and Environmental Engineering, University of Alberta, Edmonton.

Dawe, J.L. and Kulak, G.L. (1974), "Welded Connections under Combined Shear and Moment," *Journal of the Structural Division,* ASCE, Vol. 100, No. ST4, 727–741.

Gomez, I.R., Kwan, Y.K., Kanvinde, A.M. and Grondin, G.Y. (2008), "Strength and Ductility of Fillet Welds Subjected to Out-of-Plane Bending," Technical Report submitted to the American Institute of Steel Construction, Chicago.

Kanvinde A.M., Gomez I.R., Roberts M., Fell B.V. and Grondin, G.Y, (2008—accepted), "Strength and Ductility of Fillet Welds with Transverse Root Notch," *Journal of Constructional Steel Research,* Elsevier.

Lesik, D.F. and Kennedy, D.J.L. (1990), "Ultimate Strength of Fillet Welded Connections Loaded in Plane," *Canadian Journal of Civil Engineering*, Vol. 17, No. 1, 55–67.

Li, C. (2007), "Reliability Analysis of Concentrically Loaded Fillet Welds," MSc thesis, Department of Civil and Environmental Engineering, University of Alberta, Edmonton, Alberta, October.

Ligtenburg, F.K. (1968), "International Test Series, Final Report. IIW Document XV-242-68," International Institute of Welding.

Miazga, G.S. and Kennedy, D.J.L. (1986), "Behavior of Fillet Welds as a Function of the Angle of Loading," Structural Engineering Report 133, Department of Civil Engineering, University of Alberta, Edmonton.

Miazga, G. S. and Kennedy, D.J.L. (1989), "Behaviour of Fillet Welds as a Function of the Angle of Loading," *Canadian Journal of Civil Engineering*, Vol. 16, No. 4, 583–599.

Neis, V.V. (1980), "Factored Resistance of Welded Connections Subject to Shear and Moment," *Canadian Journal of Civil Engineering*, Vol. 7, No. 1, 84–92.

Ng, A.K.F., Driver, R.G., and Grondin, G.Y. (2002), "Behavior of transverse fillet welds," Structural Engineering Report 245, Department of Civil and Environmental Engineering, University of Alberta, Edmonton.

Pham, L. (1983), "Co-ordinated Testing of Fillet Welds Part 1—Cruciform Specimens—AWRA Contract 94, AWRA Document P6-35-82," *Australian Welding Research*, Vol. 12, 16–25.

Roberts, M. (2008), "Experimental and Analytical Investigations of the Strength and Ductility of Fillet Welds with Transverse Root Notch," Masters Thesis, Department of Civil and Environmental Engineering, University of California, Davis.

Salmon, C.G. and Johnson, J.E. (1996), *Steel Structures, Design and Behavior*, Fourth Edition, Chapter 16, HarperCollins College Publishers, New York.

Sanaei, E. and Kamtekar, A.G. (1988), "Experiments on Some Arbitrarily Loaded Fillet Welds." *Welding Journal*, Welding Research Supplement, Vol. 67, No. 5, 103–109.

Swannell, P. (1981a). "Rational Design of Fillet Weld Groups," *Journal of the Structural Division,* ASCE, Vol. 107, No. ST5, 789–802.

Swannell, P. (1981b). "Weld Group Behavior," *Journal of the Structural Division,* ASCE*,* Vol. 107, No. ST5, 803–815.

Tide, R.H.R. (1980), "Eccentrically Loaded Weld Groups—AISC Design Tables," *Engineering Journal,* AISC, Vol. 17, No. 4, 90–95.

DISCUSSION

Designing Compact Gussets with the Uniform Force Method

Paper by Larry S. Muir
(First Quarter, 2008)

Discussion by Ramon F. Arias

The writer submits this discussion with some trepidation as he recognizes that the author of the paper is a well-known authority in the design of connections, and who has made valuable contributions to the AISC codes and to books on the subject.

Prior to discussing the substance of the author's paper, a typo should be corrected as follows:

The author's equation (8) reading $\Sigma F_x = 0 = H_c - H_c$ should read $\Sigma F_x = 0 = P\sin\theta - (H_b + H_c)$. This correction does not affect the author's analysis.

The first point of discussion is the author's approach. It appears that the author's solution to the compact gusset corresponds to one of two boundary conditions that would frame the actual solution.

In discussing this, two geometric points should be noted: point B_o on the beam axis at the column flange and point C_o on the column axis at the level of the top of the beam. In the traditional Uniform Force Method (UFM), the force (H_b, V_b) passes through point B_o and the force (H_c, V_c) passes through point C_o. In other words, the moment M_{bo} of the forces H_b and V_b relative to point B_o and the moment M_{co} of the forces H_c and V_c relative to point C_o are both zero.

In the author's solution to the compact gusset, the force (H_b, V_b) passes through B_o but the force (H_c, V_c) is left to drift away from C_o and all of this in such a way that the equations of equilibrium are satisfied. In other words, $M_{bo} = 0$ and M_{co} differs from zero. Under these conditions, expressions are derived for H_c, V_b, H_b and V_c as exhibited by the author's equations (10), (11), (12) and (13), respectively.

Ramon F. Arias is a principal civil engineer with Babcock Hitachi K.K., Kure Division, Vancouver, BC.

Additionally, the moments M_{bo} and M_{co} defined earlier are:

$$M_{bo} = 0 = H_b e_b - V_b \alpha \quad (13.1)$$

$$M_{co} = H_c \beta - V_c e_c \quad (13.2)$$

Equations 13.1 and 13.2 are not in the author's paper, but they can be easily derived from his analysis.

The other boundary condition consists of letting the force (H_b, V_b) drift away from point B_o while keeping the force (H_c, V_c) through C_o and satisfying the equations of equilibrium. That is to say, $M_{co} = 0$ while M_{bo} differs from zero. Under these conditions the analysis gives the following results:

$$H_c = e_c P\{\cos\theta - e_b \sin\theta/(e_c + \alpha)\}/\beta \quad (10a)$$

$$V_b = e_b P\sin\theta/(e_c + \alpha) \quad (11a)$$

$H_b = P\sin\theta - H_c$ (same as the author's equation 12)

$V_c = P\cos\theta - V_b$ (same as the author's equation 13)

$M_{bo} = H_b e_b - V_b \alpha$ (same as 13.1 above)

$M_{co} = 0 = H_c \beta - V_c e_c$ (same as 13.2 above)

If the author's approach is correct, the solution of the problem created by the compact gusset should be located between these boundary conditions. In this solution, both M_{bo} and M_{co} are different from zero. These moments are relatively small. M_{co} is usually neglected and M_{bo} can be easily accommodated in the beam to column connection.

Table 1a shows a comparison between the two boundaries and includes a solution consisting on a weighted sum of the values from the boundary conditions. The weight factor for the boundary 1 values is $k_1 = d_c/(d_b + d_c)$ and for boundary 2 is $k_2 = d_b/(d_b + d_c)$, where d_b and d_c are the distances from points B (centroid of the beam-to-column connection)

Table 1a. Comparison between Muir's solution (Boundary 1), Boundary 2, and a Weighted Solution			
Parameters	**Boundary 1**	**Boundary 2**	**Weighted Solution**
V_b	50.3	46.0	47.9
H_b	60.2	69.7	65.4
V_c	7.09	11.4	9.46
H_c	21.7	12.2	16.5
M_{bo}	0.0	175.0	96.8
M_{co}	91.4	0.0	40.8

and *C* (centroid of the column-to-gusset connection) to the working point (WP) or point of intersection of the beam and column axes. Then,

$$V_b = k_1 V_{b1} + k_2 V_{b2}$$

$$H_b = k_1 H_{b1} + k_2 H_{b2}$$

and so on, where V_{b1}, H_{b1}, V_{b2} and H_{b2} indicate the reaction values corresponding to boundaries 1 and 2.

Of course, the two boundary conditions and the weighted solution satisfy $\Sigma F_x = 0$, $\Sigma F_y = 0$ and $\Sigma M = 0$.

A second point of discussion is the approach adopted by the author and continued in this discussion, in which geometric constraints are imposed to determine the connection forces.

The solution to the compact gusset cannot be any of the two boundary conditions or the weighted solution because they contain geometric restrictions that are imposed by the designer (the forces must pass through certain points and must be oriented in certain directions). However, the behavior of the connection under the axial force does not have to follow arbitrary geometric constraints.

Since the forces are concurrent and their sum is zero, it follows as a result that the sum of their moments relative to any point is also zero. This approach is arbitrary as it gives solutions without having to make implicit or explicit reference to the moment caused by the local eccentricity of the brace axial force relative to the centroid *G* of the connections of the gusset to beam and column. The fact that the sum of moments is zero should be a condition of the problem, not a result of imposed geometric constraints. In other words, the analysis must reflect the behavior of the connection, and the geometric constraints must be relaxed accordingly.

A third and final point of discussion is the adoption by the author of a force, ΔV_b, to manipulate force, V_b, resulting in a moment, M_b, assigned to the beam to gusset connection and given by the author's equation (14). Actually, what is adopted is a couple, (ΔV_b, α), with forces, ΔV_b, oriented vertically so that they only affect V_b and V_c, acting at points *B* and *C*. The results of this manipulation are shown in Table 1 of the author's paper (refer to the column entitled "Modified UFM with ΔV_b" in this table). The adoption of a couple of forces that act in the vertical direction and applied at points that do not fall in a horizontal line is arbitrary. The forces should be oriented perpendicular to line *BC* and it should affect all connection forces.

Additionally, the author does not explain why the moment, M_b, required to balance the couple, (ΔV_b, α), is applied to the beam-to-gusset interface. Presumably, the reason is that this connection is more rigid than the column-to-gusset connection. However, it could be argued that the design of a more compact gusset with a larger β, as in the author's example, results in an increased rigidity of the column-to-gusset connection compared to the concentric gusset connection case. Based on this increase, the moment should be assigned to the column-to-gusset connection. Furthermore, assigning the moment M_b to the beam-to-gusset connection interface appears to defeat the purpose of the author's solution as this moment must also be applied to the beam to column connection.

The writer feels that if there is a need to manipulate the results, an alternative is to introduce a moment, M_{bc}, affecting all four connection forces. The moment, M_{bc}, should consist of a couple, (ΔF, d_{bc}), where d_{bc} is the distance between *B* and *C* ($d_{bc}^2 = \alpha^2 + \beta^2$). The force, ΔF, would be selected so as to result in the desired values of the connection forces. Then, a balancing moment, $-\Delta M$, would have to be assigned to one of the two connections.

In summary, the author has identified a boundary condition to the solution of the compact gusset. However, this boundary condition has been reached by adopting geometric constraints that appear to invalidate it. This also applies to the second boundary condition and the weighted solution presented here. Some of the resulting connection forces in the boundary conditions, including the author's solution, could be underestimated. The introduction by the author of a force, ΔV_b, to manipulate the results of his analysis also seems arbitrary.

A solution to the compact gusset design should (1) be based on the UFM, (2) with the equations of equilibrium as condition of its solution, (3) include in the analysis the local eccentricity of the brace force relative to the centroid *G*, (4) be reduced to the traditional UFM solution under the right circumstances, (5) not include arbitrary geometric constraints, and (6) be easily expanded to accept small eccentricities created by the brace axial force not passing through WP. This solution would have M_{bo} and M_{co} different from zero, except for the special case where the centroid *G* is located on the axis of the brace.

NOTATION

d_b = distance from the beam-to-gusset connection to the working point

d_c = distance from the column-to-gusset connection to the working point

d_{bc} = distance between the beam-to-gusset and column-to gusset connection centroids

e_b = one-half the depth of the beam

e_c = one-half the depth of the column

k_1, k_2 = weight factors

B = centroid of the beam-to-gusset connection

B_o = centroid of the beam-to-column connection

C = centroid of the column-to-gusset connection

C_o = point on the column axis at the level of the top of the beam

G = centroid of the combined beam-to-gusset and column-to-gusset connections

H_b, H_{b1}, H_{b2} = shear force on the beam-to-gusset connection

H_c, H_{c1}, H_{c2} = tension force on the column-to-gusset connection

M_b = moment on the beam-to-gusset connection

M_{bc} = moment introduced to manipulate the reactions

M_{bo} = moment on point B_o

M_{co} = moment on point C_o

V_b, V_{b1}, V_{b2} = tension force on the beam-to-gusset connection

V_c, V_{c1}, V_{c2} = shear force on the column-to-gusset connection

WP = point of intersection of the beam and column axes

α = distance from face of column to centroid of beam-to-gusset connection

β = distance from face of beam flange to centroid of column-to-gusset connection

ΔF = force adopted to manipulate all reactions ($\Delta F = M_{bc}/d_{bc}$)

ΔV_b = change in the distribution of vertical reactions

(X, Y) = force resulting from the vector addition of forces X an Y

(X, y) = pair for forces X acting in opposite directions and at a distance

CLOSURE

Designing Compact Gussets with the Uniform Force Method

Paper by Larry S. Muir
(First Quarter, 2008)

Closure by Larry S. Muir

I would like to begin by thanking Mr. Arias for his interest in and comments regarding my paper. I believe that an open and vigorous discourse is the best way to advance our understanding and practice of engineering.

Mr. Arias addresses three separate issues, which I will try to restate:

1. I have found only one of a number of possible solutions to the problem.

2. I have applied arbitrary geometric constraints to the analysis, and my analysis does not reflect the behavior of the connection.

3. I present an alternative that uses ΔV_b to arbitrarily manipulate the distribution of vertical forces in the connection.

I agree with all three of Mr. Arias' points enumerated here. However, I disagree with the conclusions developed from these points. It is my understanding that Mr. Arias's main problem with the approach presented in my paper is that it is arbitrary and does not accurately reflect the true behavior of the connection. From this he concludes that the procedure may result in inadequate designs and that the traditional UFM more accurately reflects the behavior of the connection and therefore results in safer designs.

Larry S. Muir is the president of Cives Engineering Corporation and chief engineer at Cives Steel Company, Roswell, GA.

I contend that no one—not Mr. Arias, not myself, not Dr. Thornton, the originator of the UFM—can accurately predict the behavior of any connection. That is why all connection design—and, in all likelihood, virtually all structural steel design—is accomplished based, either implicitly or explicitly, on the Lower Bound Theorem. The Lower Bound Theorem states that the applied external forces in equilibrium with the internal force field are less than or, at most, equal to the applied external force that would cause failure, provided that all the limit states are satisfied and sufficient ductility exists to allow redistribution of the forces. In other words, as long as sufficient ductility is present and all applicable limit states are satisfied, design can safely proceed based on any arbitrary distribution of forces, as long as the distribution satisfies equilibrium. If this was not true, designs would quickly grind to a halt as we constructed and calibrated, through physical testing, highly complex finite element models for every detail and possible load case for our designs.

Mr. Arias brings up many arguments that are certainly true. There will undoubtedly be some moment present in the physical connection at the beam-to-column interface. However, this moment will be limited to some value less that the ultimate strength of the beam-to-column connection. As the loads imposed on the connection approach the connection strength, the elements will begin to yield and therefore shed load to stiffer elements. As it turns out, neglecting the rotational stiffness of this connection and the resulting imposed moments in the analysis actually adds to, and not subtracts from, the safety of the connection. Any additional restraint will serve to strengthen, not weaken, the structure.

As Mr. Arias states, increasing the β dimension of the connection will tend it make it more rigid at the gusset-to-column interface. This will, as Mr. Arias asserts, draw moment from the gusset-to-beam interface. The prediction that no moment exists at the gusset-to-column interface is most certainly incorrect, as are all the other forces predicted by the proposed procedure. Some of the predicted forces are too

high, some are too low, but still the resulting design is safe and will carry the loads, or else the Lower Bound Theorem is wrong and so too are countless structures in service.

This same logic justifies the use of ΔV_b to manipulate the distribution of the forces in the connection. The use of ΔV_b predates my paper and has been present in the AISC *Manual* for many years. It is used primarily where the beam end connection is subjected to a high shear load due to gravity loads, so that it cannot resist the additional load imposed by the bracing with a typical connection. In some instances, the additional shear induced by the bracing may be such that the beam web itself is overstressed when subjected to the forces predicted by the UFM. If the beam and its connections maintained their stiffness throughout loading and then suddenly snapped like glass, it would be inappropriate to apply ΔV_b—but this is not how steel behaves.

Finally, Mr. Arias suggests that the traditional UFM is inherently superior to the procedure presented in the paper. Based on his previous arguments regarding the generalized UFM presented in the paper, this implies he feels the traditional UFM is less arbitrary than the generalized method. In fact, it could be argued that the traditional UFM is actually more arbitrary in the constraints it chooses to impose on the force distribution. When he derived the traditional UFM, Dr. William Thornton arbitrarily chose to pass the forces V_c and H_c through a point at the intersection of the top of steel and the face of the column. This ensured that no moment would exist in a section cut through the column at the top of steel. This choice was based in part on figures shown in Blodgett's *Design of Welded Structures*. It resulted in more elegant-appearing equations for the interface forces than my proposed generalized method, but actually contained one additional arbitrary geometric constraint than the generalized procedure.

In conclusion, the procedure presented in my paper was never intended to accurately predict the forces present in the connection. It was intended instead as an improvement to an existing tool by which an admissible force distribution can be obtained that has been proven through use to produce safe and economical designs.

Current Steel Structures Research

REIDAR BJORHOVDE

Research is not always tied to industrial or societal needs, and sometimes not even closely related to such needs. This is most unfortunate, especially for all of engineering, since it would appear that if a study does not have any practical applications and ultimately does not end up in the form of real-life projects, why should it be undertaken in the first place? Of course, it is always interesting and challenging to solve complex problems, but for engineers there is a clear missing link if the subject has not emanated from a practical need. Nevertheless, esoteric subjects form the basis of many projects, and the key to satisfactory solutions is to maintain a levelheaded view of progress and goals.

On this background, it is a fact that research around the world tends to progress in waves and cycles. The initial idea may have come from a study in the United States or any other country, but reports and publications and interpersonal relationships communicate with the research community at large. A good idea is a good idea anywhere, and elements of the broad subject matter that lend themselves to additional study get picked up by students or professors or practicing engineers and eventually to solutions that address real needs. As a "for instance," the entire subject matter dealing with robust structures, structural integrity and resistance to disproportionate (progressive) collapse is currently being addressed by researchers in a dozen or more countries. To a certain extent, these studies are tied to the seismic performance of structures and connections. Five years ago, research on robustness was essentially nonexistent. Thus, three of the studies presented in this paper deal with robust performance in one or another form, and the analyses and applications demonstrate degrees of sophistication the attest to levels of advanced knowledge that even a few years ago was limited to very few institutions.

The performance of various types of industrial structures is now being addressed by groups in the United States, Switzerland and South Africa, to mention three efforts. This includes a novel framing system that has broad applications within certain industries, not because of the complex nature of the frames themselves but because manufacturing companies need them. A new seismic standard has in fact been developed to reflect the design needs of these frames.

Work on numerous applications of hollow structural sections is actively pursued in a number of countries, for structural as well as architectural reasons. Finally, an interesting project is focusing on imperfections of various kinds, using an optimization approach to determine the most unfavorable combination of imperfections in certain types of structural elements.

References are provided throughout the paper, whenever such are available in the public domain. However, much of the work is still in progress, and reports or publications have not yet been prepared for public dissemination.

Reidar Bjorhovde is the Research Editor of AISC's *Engineering Journal.*

ROBUST STRUCTURAL PERFORMANCE AND STRENGTH UNDER SEISMIC LOADS

Robustness of Seismically Resistant Multi-Story Frames with Accidental Column Loss Scenarios: This project has been conducted at the Polytechnic University of Timisoara in Timisoara, Romania, with Professor Dan Dubina as the director, in collaboration with the Timisoara Branch of the Romanian Academy of Sciences.

Several projects over the past few years have suggested that seismically resistant framing systems also will provide significant robustness against disproportionate collapse. In particular, the study of Hayes et al. (2005) showed that special moment frame detailing of structures led to improved response to blast and similar loading conditions, in comparison with the performance of ordinary moment frames under the same type of loading conditions. Further, the capacity design approach that forms the basis for the seismic criteria of Eurocode 8 (CEN, 2005b) emphasizes energy dissipation in certain members (normally beams and girders) and structural overstrength in the columns. This design philosophy achieves satisfactory ductility and prevents failure modes that involve soft story mechanisms (Dinu and Dubina, 2009).

The current project has specifically examined the progressive collapse resistance of certain types of multistory frames that have been designed for seismic performance. Various failure scenarios were investigated, specifically by looking at the structural behavior for cases of loss of interior columns and loss of corner columns, located at mid-height of the frame or at the first floor level. The building in question is shown in Figure 1— it is a 26-story structure that had been designed for seismic accelerations of 0.24-g and a multilevel performance requirement with a ground acceleration of

0.36 g. The building is located in the high seismicity region of Bucharest in Romania; it was completed in 2007.

Three performance levels were used in the evaluation of the structure: (1) serviceability limit state, (2) ultimate limit state, and (3) collapse prevention limit state. Nonlinear dynamic analyses were used for an accurate performance assessment of the structure as a whole. For the column removal evaluations, two cases were used, as follows: Case 1 involved the loss of the first floor interior columns; Case 2 examined the performance of the frame with the loss of the 14th-floor interior columns. The columns were removed one by one, and three-dimensional nonlinear static analysis was used to examine the response of the structure. The nonlinear modeling incorporated material as well as geometric effects.

The analyses of Case 1 showed that the structure was able to carry the gravity loads when as many as 15 to 20% of the 1st-floor interior columns were removed (five columns). Plastic hinges developed in the beams of the 1st through the 13th stories, with plastic rotations up to 0.015 radian. For Case 2, the structure was stable after the loss of five columns, but the rotations were no larger than 0.007 radian. The researchers note that the rotation demands associated with the loss of 15 to 20% of the columns is similar to what would be expected for a strong earthquake. They also observe that columns in high-strength steel [yield stress of 65 ksi (460 MPa)] may further improve the structural performance.

Finally, any effects of strain hardening, different strain rates and overstrength of the steel have not been examined. Similarly, the dynamic (i.e., brittle) effects of column removal have not been studied; this would be an important addition to the state of the art. It is anticipated that these topics will be addressed in further studies.

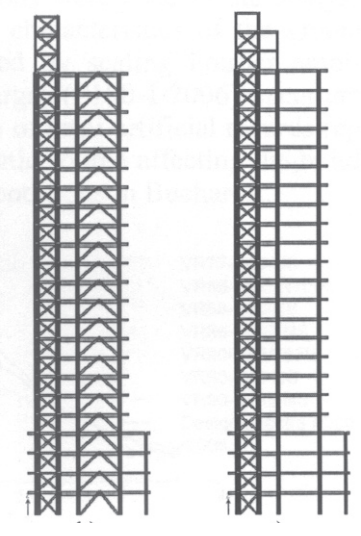

Fig. 1 (a). Elevation of frame for column removal study (courtesy of Professor Dan Dubina).

Robustness of Parking Garages against Localized Fire: This three-year project is a major collaborative study, involving universities, companies and research centers in five European countries. The lead institution is the University of Liège in Liège, Belgium; the other institutions are Imperial College in London, England; University of Coimbra in Coimbra, Portugal; the steel producer ArcelorMittal in Luxembourg; and CTICM, the French steel construction institute. Funding has been provided by the Research Fund for Coal and Steel of the European Commission. Professor Jean-Pierre Jaspart of the University of Liège is the director of the project.

The project was recently started, so any results are not yet available. However, input from the research partners and access to the European fire research database will be critical to the success of the work. The effects of nonuniform temperature distributions, connection behavior and other aspects of the response of the parking structures to localized fires will be examined, with the aim of providing practical design criteria and realistic performance descriptions.

It is interesting to observe that a parking garage fire test was conducted by the American Iron and Steel Institute (AISI) in Scranton, Pennsylvania, in 1972, using a full-size American car as the source of the fire (Gage-Babcock, 1973; Harris, 1979). The steel structure had no fire protective materials for any components. The garage and its members behaved very well, with no local or overall member or structural failure.

Robust Structures by Joint Ductility: This is a three-year collaborative research project that was completed in 2007. Involving the University of Liège in Liège, Belgium, the University of Stuttgart in Stuttgart, Germany, and the University of Trento in Trento, Italy, the industrial partner was the steel producer ARBED, Arcelor Group, from Luxembourg. Funding was provided by the Research Fund for Coal and Steel of the European Commission. Professor Ulrike Kuhlmann of the University of Stuttgart was the project director.

The project focused on how redundancy and general structural system robustness could be mobilized to prevent a local failure from progressing to overall failure of the

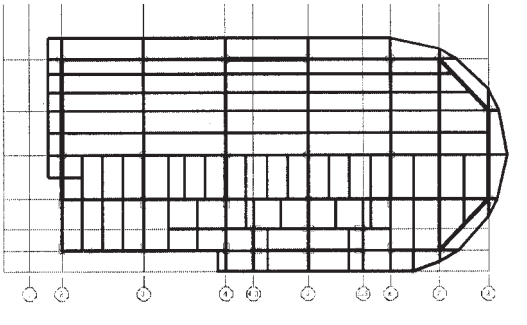

Fig. 1(b). Floor plan for building (courtesy of Professor Dan Dubina).

structure. In particular, the ductility of steel and the capacity of the connections to undergo very large deformations were examined as key elements of the stress resultant redistribution throughout the frame. The full-scale tests at the University of Liège are especially interesting, as they focused on column removal within a two-bay substructure of a composite frame, examining the robustness of the connections as well as the frame (Demonceau, 2008; Demonceau and Jaspart, 2008). Complete nonlinear finite element analyses of the structure and the substructure that was tested have been conducted, using static loads. Figure 2 shows one of the specimens after the completion of the test.

The final report of the project is not yet available. It will be published by the Science Research Development arm of the European Commission.

INDUSTRIAL STRUCTURES AND APPLICATIONS

Uplift Criteria for Unanchored Circular Tanks Subjected to Seismic Loads: This is a research project that is just getting started at the Swiss Federal Institute of Technology in Lausanne, Switzerland. The project director is Professor Alain Nussbaumer.

The European experience with circular silos and tanks has shown that there may be significant risk for uplift and failure of the welded bottom connections when these structures are subjected to seismic loads. The design criteria are provided by Eurocodes 3 and 8 (CEN, 2005a; 2005b); analyses have shown that the anchoring for many of the silos and tanks need to be strengthened to ensure satisfactory performance. Various models for uplift have been developed, but the problems are highly complex and are not completely understood. The results also vary a great deal and do not provide consistent predictions for slender and stocky tanks alike. The project aims at resolving the technical issues as far as behavior and strength are concerned, including questions related to low-cycle fatigue of the welded base plate to tank connections. It is also anticipated that improved code criteria will be developed.

Based on finite element analyses, Figure 3 gives an example of the relationship between the uplift force (V), the vertical displacement (w) and the uplift length of the base (L) for a tank with a height to radius aspect ratio of H/R = 0.5 (Scharf, 1989).

Geometric Nonlinear Analysis of Slender Structures: This is a major collaborative research and development project involving universities in Germany, Russia and South Africa, with Professor Peter Dunaiski of the University of Stellenbosch in Stellenbosch, South Africa, as the project director and lead researcher. The project has been under way for some time, and a book that will feature the nonlinear techniques and software that have been developed will be published by the University of Stellenbosch in 2009.

As an example, the approach to nonlinear analysis has been applied to a study of slender, long-span trusses that has been conducted at Stellenbosch. Coupled with full-scale tests, among other findings is the observation that the effective lengths of truss verticals and diagonals are significantly smaller than the system lengths. Figure 4 shows one of the trusses that was analyzed. Another study examined the design of slender portal frames, determining that serviceability governs these structures as opposed to strength.

Seismic Response of Cold-Formed Steel Structural Systems in Special Bolted Moment Frames: This project was conducted at the University of California at San Diego, with

Fig. 2. Robustness test of two-span composite beam with column removed (courtesy of Jean-François Demonceau).

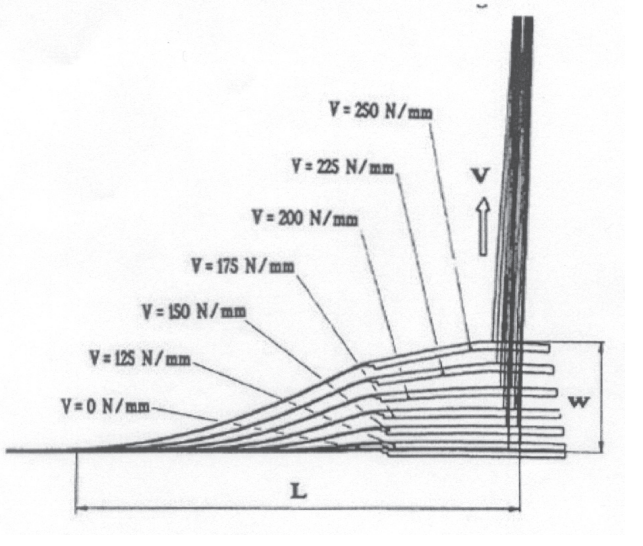

Fig. 3. Tank uplift force in relation to displacement and uplift length (Scharf, 1989) (courtesy of Professor Alain Nussbaumer).

Professor Chia-Ming Uang as the director. The study was funded by the American Iron and Steel Institute and was completed in 2007, including the development of a new AISI/ANSI design standard for these types of frames (AISI, 2007; Sato and Uang, 2008). A notable achievement, it is emphasized that this is the first time a seismic standard has been developed for use with cold-formed members.

These special bolted moment frames (SBMF) are commonly one story only and are used as mezzanine or platform structures within other structures typically industrial installations. They are very common and economical solutions for unique needs and are used a great deal in California and other seismically active areas. The SBMF uses HSS columns with cold-formed C-shape beams, as shown in Figure 5. The connections are bolted, as shown, most commonly with 1-in.-diameter HS bolts; these are installed as snug-tight bolts only.

The project examined the response of the frames to a large number of ground motions and determined that most of the energy absorption took place in the connections. Nine full-scale tests were conducted (Sato and Uang, 2008), and no local or overall buckling occurred during the tests. Using a capacity design approach in the development of the connection model, the analyses also predicted such behavior. It is interesting to observe the hysteretic response of the connection and compare this to what is commonly seen for many hot-rolled connections. An example is shown in Figure 6, demonstrating very different behavior but excellent connection rotation and energy absorption capacity.

Fig. 4. Long-span slender truss (courtesy of Professor Peter Dunaiski).

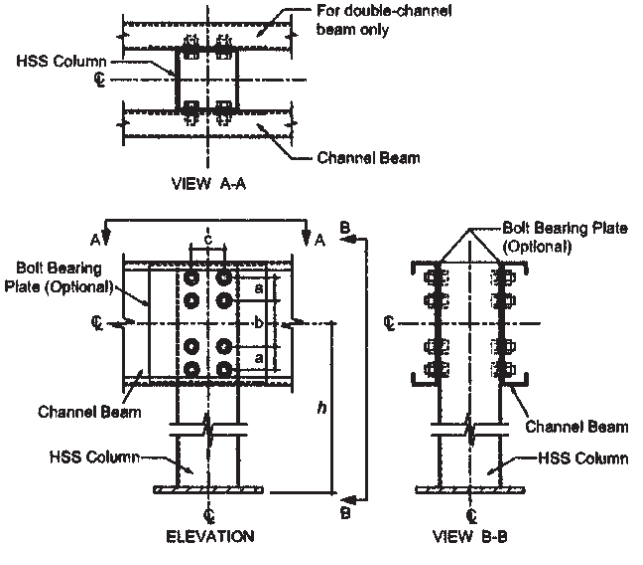

Fig. 5. Connection for special bolted moment frames with cold-formed beams (courtesy of Professor C.-M. Uang).

ANALYSIS OF STEEL STRUCTURES

Application of Optimization Techniques to Assess Effects of Imperfections: This study has been conducted at the University of Ljubljana in Ljubljana, Slovenia, with Professor Joze Korelc as the project director.

Many structures are imperfection sensitive, especially structures with very slender members such as cold-formed elements and certain plate girders with very thin webs. It is important to find the most critical types, locations and orientation of the imperfections and to determine the ultimate limit state(s) that is governed by each of these. Using optimization philosophy, an algorithm has been developed that takes into account nonlinear primal and first-order sensitivity analysis to arrive at the moist suitable objective function

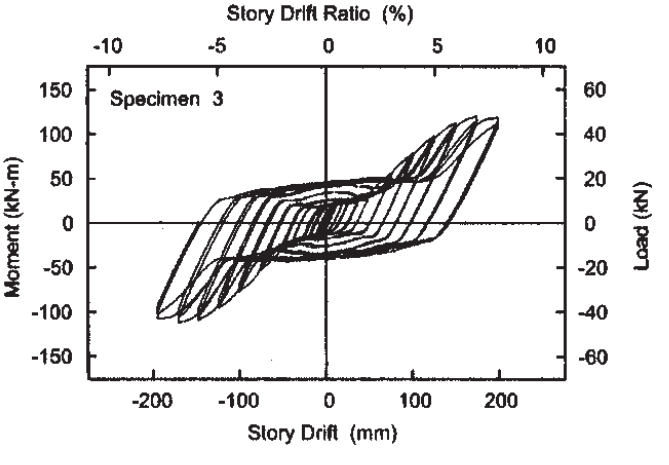

Fig. 6. Hysteresis characteristics for the connection of a special bolted moment frame (courtesy of Professor C.-M. Uang).

(Kristanic and Korelc, 2008). The method is capable of dealing with a range of imperfection magnitudes, using linear combinations of certain basic types. Constraints can be set to allow for the selection of various basic shapes, including selection of boundary conditions and characteristic shapes.

It has been found that if only the amplitude of the imperfections is constrained, the solution gives significantly lower ultimate loads than what is found in physical experiments. Part of the problem is that some of these imperfection shapes are, in fact, technically impossible. Although the method is very powerful, it is, therefore, important to ensure that the imperfection shape is realistic. The magnitude of the imperfections must also be controlled, to avoid getting unrealistic, very low ultimate loads.

Figure 7 shows a girder with exaggerated (for illustration purposes) imperfections, but the form of the deflections is realistic. The method is very efficient for computations.

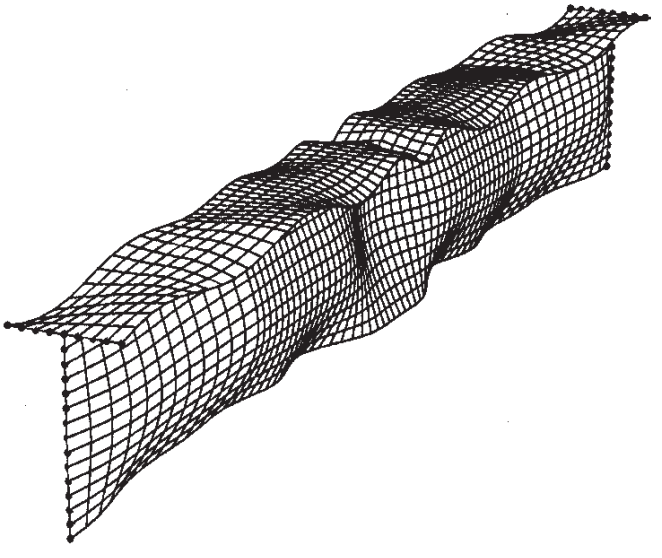

Fig. 7. Girder with the optimized governing imperfections (courtesy of Professor Joze Korelc).

REFERENCES

American Iron and Steel Institute (AISI) (2007), *Standard for Seismic Design of Cold-Formed Steel Structural Systems—Special Bolted Moment Frames*, AISI/ANSI Standard No. S110-07, AISI, Washington, DC.

CEN (Comité Européen de Normalisation) (2005a), *Eurocode 3—Design of Steel Structures—EN 1993-1*, CEN, Brussels, Belgium.

CEN (Comité Européen de Normalisation) (2005b), *Eurocode 8—Design Provisions for Earthquake Resistance of Structures—EN 1998-1*, CEN, Brussels, Belgium.

Demonceau, Jean-François (2008), "Steel and Composite Building Frames: Sway Response under Conventional Loading and Development of Membrane Effects in Beams Further to an Exceptional Action," Ph.D. Dissertation, University of Liège, Liège, Belgium.

Demonceau, Jean-François and Jaspart, Jean-Pierre (2008), "Robustness of Structures—Behaviour of Composite Joints," in *Connections in Steel Structures VI*, R. Bjorhovde, F. S. K. Bijlaard and L. F. Geschwindner, Editors, AISC, Chicago, 467–477.

Dinu, F. and Dubina, D. (2009), "Robustness of Seismic Resistant Multistory Frame Buildings in Case of Accidental Column Loss Scenarios," Proceedings, STESSA Conference, Philadelphia, Pennsylvania.

Gage-Babcock & Associates (1973), "Automobile Burn-Out Test in an Open-Air Parking Structure," Report No. 7328, Gage-Babcock & Associates, Westchester, Illinois, January.

Harris, Leslie (1979), "1979 Update of the Survey of Fire Experience in Automobile Parking Structures in the United States and Canada," Marketing Research Associates, Teaneck, New Jersey, January.

Hayes, J. R., Woodson, S. C., Pekelnicky, R. G., Pohland, C. D., Corley, W.G., and Sozen, M. (2005), "Can Strengthening for Earthquake Improve Blast and Progressive Collapse Resistance?" *Journal of Structural Engineering*, ASCE, Vol. 131, No. 8, 1157–1177.

Kristanic, Niko and Korelc, Joze (2008), "Optimization Method for the Determination of the Most Unfavorable Imperfection of Structures," *Computational Mechanics*, Vol. 42, No. 6, 859–872.

Sato, Atsushi and Uang, Chia-Ming (2008), "Application of Instantaneous Center of Rotation Concept for Cyclic Modeling of Bolted Connections in Special Bolted Moment Frames," in *Connections in Steel Structures VI*, R. Bjorhovde, F. S. K. Bijlaard and L. F. Geschwindner, Editors, AISC, Chicago, 231–242.

Scharf, K. (1989), "Beiträge zur Erfassung des Verhaltens von Erdbebnerregten, Oberirdischen Tankbauwerken," Ph. D. Dissertation, University of Wien, Austria.

ACKNOWLEDGMENTS

Special thanks are due the following members of the International Structural Steel Research Advisors (ISSRA) who provided input to this paper:

Darko Beg, University of Ljubljana, Ljubljana, Slovenia

Dan Dubina, Technical University of Timisoara, Timisoara, Romania

Hennie DiClercq, Southern African Institute of Steel Construction, Johannesburg, South Africa

Jean-Pierre Jaspart, University of Liège, Liège, Belgium

Ulrike Kuhlmann, University of Stuttgart, Stuttgart, Germany

Alain Nussbaumer, Swiss Federal Institute of Technology, Lausanne, Switzerland

Additional assistance has been provided by Jean-François Demonceau, University of Liège, Liège, Belgium; Peter Dunaiski, University of Stellenbosch, Stellenbosch, South Africa; Atsushi Sato, Kyoto University, Kyoto, Japan; and Chia-Ming Uang, University of California—San Diego, La Jolla, California.

GUIDE FOR AUTHORS

SCOPE: The ENGINEERING JOURNAL is dedicated to the improvement and advancement of steel construction. Its pages are open to all who wish to report on new developments or techniques in steel design, research, the design and/or construction of new projects, steel fabrication methods, or new products of significance to the uses of steel in construction. Only original papers should be submitted.

GENERAL: Papers intended for publication must be submitted by mail to the Editor, Cynthia J. Duncan, ENGINEERING JOURNAL, AMERICAN INSTITUTE OF STEEL CONSTRUCTION, One East Wacker Drive, Suite 700, Chicago, IL, 60601-1802.

The articles published in the *Engineering Journal* undergo peer review before publication for (1) originality of contribution; (2) technical value to the steel construction community; (3) proper credit to others working in the same area; (4) prior publication of the material; and (5) justification of the conclusion based on the report.

All papers within the scope outlined above will be reviewed by engineers selected from among AISC, industry, design firms, and universities. The standard review process includes outside review by an average of three reviewers, who are experts in their respective technical area, and volunteers in the program. The maximum number of papers sent to a single reviewer is three per year, with a frequency of not more than one per quarter. Papers not accepted will be returned to the author. Published papers become the property of the American Institute of Steel Construction, Inc. and are protected by appropriate copyrights. No proofs will be sent to authors. Each author receives three copies of the issue in which his contribution appears.

MANUSCRIPT PREPARATION: Manuscripts must be provided on PC-formatted media, such as a CD-ROM, in Microsoft Word format. A laser-quality proof must accompany your submittal. Fonts and spacing must be suitable for easy reading and reproduction (for the peer-review process). Do not embed photographs, diagrams, illustrations, charts or graphs within the electronic manuscript files. Only equations may be embedded within the flow of the text. Specific requirements for electronic graphics are outlined below. *Engineering Journal* reserves the right not to publish a submittal if suitable graphics cannot be provided by the author.

Title and By-Line: Exact name, title and affiliation of the author or authors are required to appear on the first page of the manuscript.

Body Text: Please restrict font usage to Times, Helvetica, Times New Roman, Arial, and Symbol (for Greek and mathematical characters.)

Headings: All headings should be typed flush left, using upper and lower case, with two line spaces above.

Tables: Each table should appear on its own page. Footnotes to tables should appear below the table, identified by superscripted lower case letters (a, b, c, etc.).

Equations: Whenever possible, equations should be set using Microsoft Equation Editor or MathType (www.mathtype.com). Please set equations using Times New Roman, Times, and/or Symbol fonts.

Captions: Captions should be typed, double-spaced, and located at the end of the electronic manuscript. All photos and graphics must be clearly marked to indicate their corresponding caption.

References: Should be noted clearly in the text and listed, double-spaced, on a separate page in the following sample format.

In text: (Doe, 1992)

In Reference List:

Doe, J.H. (1992), "Structural Steel," *Engineering Journal*, AISC, Vol. 100, No. 1, 1st Quarter, pp. 2–10.

Footnotes: Footnotes should be noted clearly in the text with a superscript asterisk, and should appear at the bottom of the text page, in the following style:

*For a detailed discussion, see...

Graphics (other than photographs): Provide a clear $8\frac{1}{2}$ in. × 11 in. laser-quality proof of each graphic element. Graphics should reproduce cleanly in black-and-white format. Graphics may be submitted and reproduced in color at the Editor's discretion. Please restrict font usage to Helvetica, Arial or Symbol, in sizes suitable for at least 50% reduction (12 pt. minimum). Line weights must be suitable for 50% reduction. When possible, provide each graphic element in a separate electronic file. TIF or EPS file formats are preferred, with a minimum resolution of 300 dots per inch.

Photographs: Provide either original photographs or high-quality electronic files and laser-quality proofs. Electronic photographs may be submitted as grayscale TIF or JPG images, one photograph per file. Photographs may be submitted and reproduced in color at the Editor's discretion. Minimum image resolution is 300 dots per inch. Photographs should be a minimum of 4 in. wide, so the minimum image width is 1200 pixels. Detailed photographs may require resolutions up to 1200 dots per inch. Photos embedded in word-processing documents are not acceptable.

There's always a solution in steel.

ENGINEERING JOURNAL
American Institute of Steel Construction
One East Wacker Drive, Suite 700
Chicago, IL 60601